Silicon photonic micro-ring resonators to sense strain and ultrasound

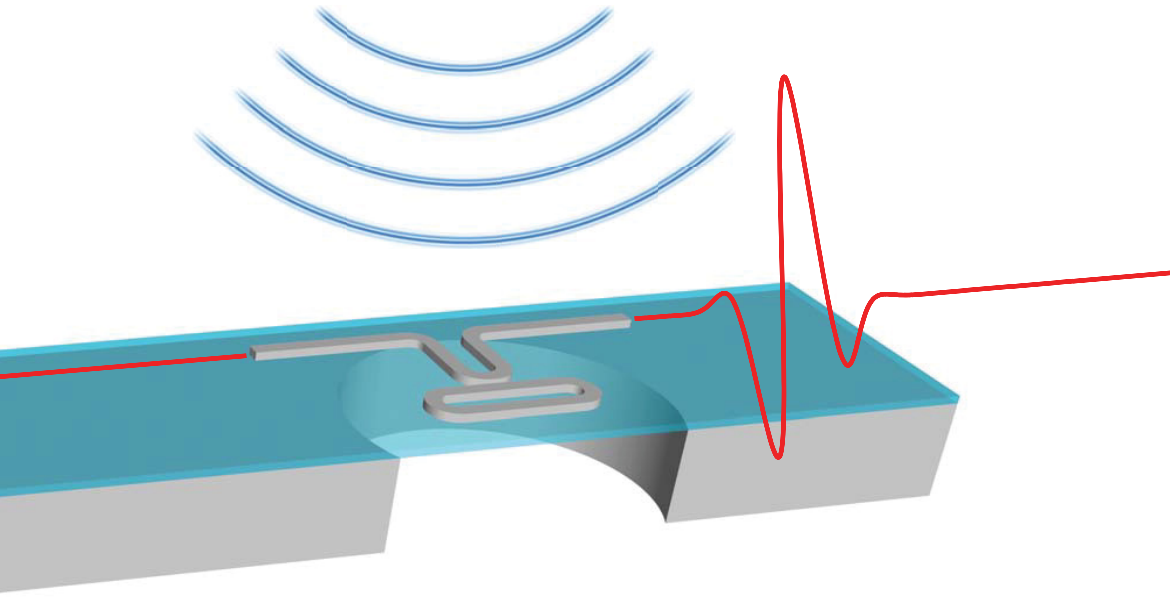

Wouter Westerveld

This thesis is about silicon photonic micro-ring resonators that are employed to sense deformation and ultrasound. The front cover illustrates a new type of ultrasound microphone, consisting of a silicon micro-ring resonator on a silicon-dioxide membrane. Ultrasonic pressure waves deform the membrane and thus the resonator. The light in the waveguide, which closely passes the resonator, is thereby modulated with the ultrasonic signal. In this thesis, we prove the operation principle and we measured a minimal detection level below 1 Pa (at 0.75 MHz), which is already on the same order of magnitude as the state-of-the-art of traditional PZT transducers. This new microphone may cause a breakthrough in array transducers for ultrasonography; first because optical multiplexing allows array interrogation via a single optical fiber and second because the silicon-on-insulator technology allows cost-effective fabrication. To understand this microphone, all of its components are studied: analytical theory for the photonic resonators, experimental characteristics of the resonators, and the effect of a static deformation of the resonator.

Pagina vii bevat een Nederlandse samenvatting.

ISBN 978-94-6259-079-3

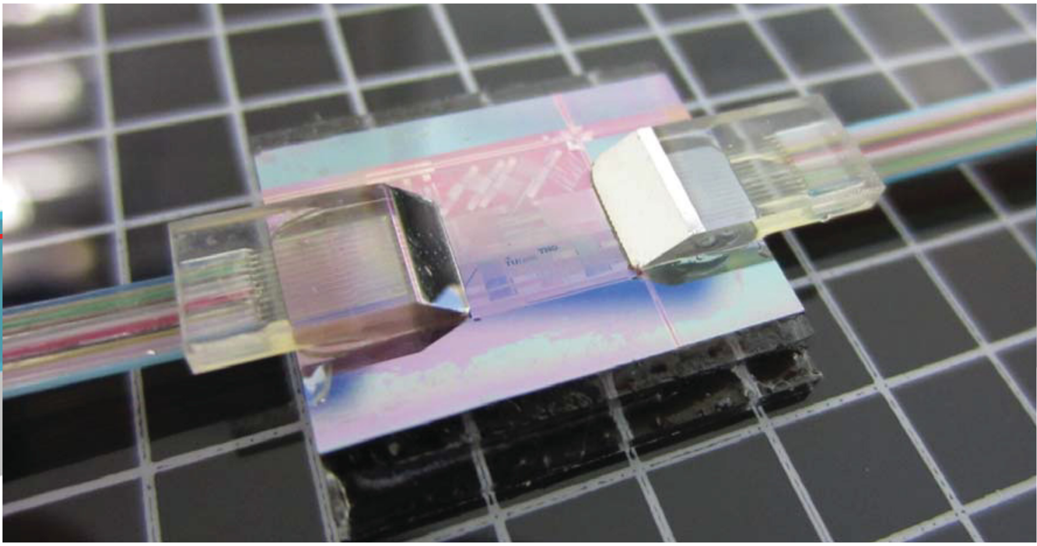

Silicon Photonic Micro-Ring Resonators to Sense Strain and Ultrasound

Proefschrift

ter verkrijging van de graad van doctor
aan de Technische Universiteit Delft,
op gezag van de Rector Magnificus prof. ir. K.C.A.M. Luyben,
voorzitter van het College voor Promoties,
in het openbaar te verdedigen op woensdag 19 maart 2014 om 12:30 uur

door

Wouter Jan WESTERVELD

natuurkundig ingenieur
geboren te Goes

Dit proefschrift is goedgekeurd door de promotor:
prof. dr. H. P. Urbach

Samenstelling promotiecommissie:

Rector Magnificus,	voorzitter
prof. dr. H. P. Urbach,	Technische Universiteit Delft, promotor
prof. dr. G. T. Reed,	University of Southampton
prof. dr. A. Melloni,	Politecnico di Milano
prof. dr. ir. F. van Keulen,	Technische Universiteit Delft
prof. dr. ir. A. Gisolf,	Technische Universiteit Delft
dr. M. Yousefi,	Photonic Sensing Solutions
dr. J. Pozo,	TNO
prof. dr. ir. N. de Jong,	Technische Universiteit Delft / Erasmus MC, reservelid

This research was supported by the IOP Photonic Devices programme of NL-Agency of the Dutch Ministry of Economic Affairs (project number IPD100026) and by TNO.

This free electronic version of this thesis can be downloaded from:
http://repository.tudelft.nl

ISBN 978-94-6259-079-3

Copyright © 2014 by W. J. Westerveld

All rights reserved. No part of this publication may be reproduced, stored in a retrieval system or transmitted in any form or by any means: electronic, mechanical, photocopying, recording or otherwise, without prior written permission of the author.

Printed in The Netherlands.

Summary

Silicon photonic micro-ring resonators to sense strain and ultrasound

We demonstrated that photonic micro-ring resonators can be used in micro-machined ultrasound microphones. This might cause a breakthrough in array transducers for ultrasonography; first because optical multiplexing allows array interrogation via one optical fiber and second because the silicon-on-insulator technology allows cost-effective fabrication. To understand this microphone, all of its components were studied: fundamental theory of the photonic resonators, experimental characteristics of the resonators, and the effect of a static deformation of the resonator.

The most familiar use of ultrasound is observing unborn children but ultrasonography is widely used in medical and industrial applications. Today's clear ultrasonic images are made by digital focusing which requires an array of transducers that records the sound at a number of positions spaced less than a wavelength. Typical sound frequencies are $1 - 40$ MHz with corresponding wavelengths of $0.04 - 1.5$ mm in water.

Conventional ultrasound transducers employ piezo-electric material to convert sound pressure to an electronic signal. An array requires individual fabrication, placement and wiring of these transducers. Last decades, micro-machined ultrasound transducers (MUTs) have received large interest. Array MUTs are fabricated and wired directly as a single silicon "chip". This micro-machining technology leverages the cost-effective wafer-scale CMOS technology that was developed by the semiconductor industry. A MUT consists of a flexible membrane that is sensitive to ultrasonic pressure waves, like a drumhead. The membrane deformation is most commonly measured by recording the electrical capacitance between the membrane and a fixed bottom plate. Unfortunately, these MUTs do not meet the sensitivity of piezo-electric transducers. Moreover, electrical transducers normally require a coaxial wire for each array element. The size of this wire bundle is, for example, problematic in medical intravascular ultrasonography (IVUS), where atherosclerosis is diagnosed from a high-resolution ultrasonograph of the artery wall that is obtained by catheter which is brought inside the blood vessel.

We propose a new type of ultrasound microphone that consists of a silicon photonic micro-ring resonator integrated in the membrane of a MUT. Incident ultrasonic pressure waves deform the membrane and thus deform the resonator, thereby shifting its optical resonance frequencies. This shift is accurately recorded by an external interrogation system. Next to the resonators, it is possible to integrate tiny optical multiplexers on the same chip so that many resonators can

be simultaneously interrogated via a single optical fiber. Moreover, the all-optical sensor can be used in MRI scanners.

We proved the operation principle of this new ultrasound microphone. The designed, fabricated and characterized microphone consists of a photonic racetrack-shaped resonator (footprint 50 μm by 10 μm, height 0.220 μm) that is integrated in an acoustically resonant silicon-dioxide membrane (diameter 0.124 mm, height 2.5 μm). Fabrication of the microphone demonstrated successful integration of silicon photonic circuits in silicon micro-mechanical systems. First the photonic circuit was fabricated in a semi-industrial CMOS line. Second the membrane was fabricated by etching a hole from the back-side of the wafer using a Bosch etch process. The photonic micro-ring resonator was interrogated using a laser and a photo-receiver, providing a minimal detectable wavelength shift of 36 fm. We measured a ultrasonic minimal detection level (noise equivalent pressure) below 1 Pa which is on the same order of magnitude as the state-of-the-art of PZT piezo-electric based transducers. The microphone showed an acoustical resonance around 0.75 MHz with a -6 dB bandwidth of 20%. We only studied the most simple configuration of this microphone and there is a lot of room for improvement.

The relation between a deformation of the micro-ring resonator and the shift in the resonance wavelengths was studied in a well-defined static mechanical setup. Depending on the width of the waveguide and the orientation of the silicon crystal, the linear wavelength shift per applied strain varies between 0.5 and 0.75 pm/microstrain for infrared light around 1550 nm wavelength. The influence of the increasing ring circumference is about three times larger than the influence of the change in the propagation speed of the light through the waveguide (effective index), and the two effects oppose each other. The strong dispersion in silicon subwavelength waveguides (400 nm by 220 nm) accounts for a decrease in sensitivity of about a factor two.

The optical characteristics of the micro-ring resonators and their components were extensively studied. Different methods to characterize directional couplers (direct and in ring-resonators) gave similar results. An interesting observation was that directional couplers introduce a large coupling-induced phase delay when nearly all light couples from one waveguide to the other.

Most properties of silicon ring resonators and their components can be computed using approximate analytical theories. Many theories on integrated optics were originally derived for low-index-contrast waveguides like optical fibers ($\Delta n < 0.1$). We reviewed and revised those theories for application to silicon-on-insulator waveguides which have a very high index contrast ($\Delta n \approx 2$). This work is formulated such that it can be used in a university course with only basic theory of electrodynamics as prerequisite. Analytical theories provide insight and allow fast computation of the behavior of photonic devices and circuits.

In conclusion, we studied silicon photonic micro-ring resonators and their application in mechanical sensing. Application of these sensors in micro-machined ultrasound transducers opens new opportunities for ultrasonic array technology.

Samenvatting

Silicium optische micro-ring-resonatoren voor het meten van rek en ultrageluid

In dit proefschrift tonen we aan dat fotonische micro-ring-resonatoren kunnen worden gebruikt in ultrageluid microfoons. Dit kan een doorbraak betekenen in matrix transducenten (luidsprekers/microfoons) voor ultrasone echografie. Ten eerste kunnen meerdere microfoons worden uitgelezen via één optische glasvezel. Ten tweede kunnen de microfoons kosteneffectief worden gemaakt. Om de werking van de microfoon te begrijpen, hebben we alle onderdelen bestudeerd: fundamentele theorie van optische resonatoren, experimentele karakterisering van de resonatoren en het effect van een statische deformatie van de resonator.

Ultrasone echografie wordt gebruikt in medische en industriële toepassingen. De meest bekende toepassing is de echo van een foetus. Moderne, hoge-kwaliteit afbeeldingen worden gemaakt door digitale focussering. Hiervoor is een matrix van ultrageluid transducenten nodig die minder dan een golflengte van elkaar liggen. Typische frequenties zijn 1–40 MHz met golflengtes 0.04–1.5 mm (in water).

In conventionele ultrageluid transducenten wordt piëzo-elektrisch materiaal gebruikt om geluidsdruk om te zetten in een elektrisch signaal. Voor een matrix transducent is individuele fabricage, plaatsing en elektrische aansluiting van elk element nodig. In de afgelopen twintig jaar zijn micro-gefabriceerde ultrageluid transducenten (MUTs) ontwikkeld. Matrix MUTs worden direct als één silicium “chip” gemaakt met micro-fabricage technologie. Deze technologie is gebaseerd op de kosteneffectieve CMOS-technologie die is ontwikkeld door de halfgeleider industrie. Een MUT bestaat uit een flexibel membraan dat wordt bewogen door geluidsgolven, zoals bij een trommelvlies. De beweging wordt meestal gemeten door uitlezing van de elektrische capaciteit tussen het membraan en een vaste grondplaat. Helaas is de gevoeligheid van MUTs lager dan die van piëzo-elektrische transducenten. Elektrische matrix transducenten hebben een coaxkabel per element nodig en hiervoor is niet altijd ruimte. Dit is bijvoorbeeld het geval bij de medische diagnosticering van aderverkalking. Hierbij worden echo’s van de kransslagader gemaakt vanuit een katheter (ø 1 mm) die in de ader wordt gebracht.

We introduceren een nieuw type ultrageluid microfoon. Deze bestaat uit een silicium optische micro-ring-resonator die is geïntegreerd in het membraan van een MUT. Ultrageluidgolven vervormen het membraan en dus de resonator, waardoor zijn optische resonantiefrequenties verschuiven. Deze verschuivingen kunnen nauwkeurig worden gemeten met externe uitleesapparatuur. Naast de resonatoren kan een optische multiplexer worden geïntegreerd die, door gebruik te maken van verschillende kleuren licht, ervoor zorgt dat verschillende resonatoren tegelijk kunnen worden uitgelezen via één glasvezel. Deze microfoon kan ook worden ingezet in MRI-scanners.

We hebben de werking van deze nieuwe ultrageluid microfoon aangetoond. Het ontworpen, gefabriceerde en experimenteel gekarakteriseerde prototype bestaat uit een optische, atletiekbaan-vormige, ring-resonator (oppervlakte 50 bij 10 μm^2, hoogte 0.220 μm) die is geïntegreerd in een akoestisch resonant membraan (diameter 0.124 mm, hoogte 2.5 μm). De fabricage van het prototype bewijst de succesvolle integratie van de optische schakelingen in micro-mechanische systemen. Als eerste heeft IMEC, een onderzoekscentrum in Leuven, met hun semi-industriële CMOS-technologie de optische schakelingen gemaakt op een silicumschijf (wafer). Hierna hebben wij het membraan gefabriceerd door vanaf de achterkant van de siliciumschijf een gat te etsen (Bosch ets). Het optische uitleessysteem bestaat uit een laser en een fotodiode en geeft een detecteerbare golflengteverschuiving van 36 fm. Het detecteerbare ultrageluidniveau van deze sensor ligt onder 1 Pa. Dit is dezelfde ordegrootte als 's werelds beste piëzo-elektrische PZT transducenten. De microfoon heeft een akoestische resonantie bij 0.75 MHz en een -6 dB bandbreedte van 20%. We hebben de meest eenvoudige uitvoering bestudeerd en er is nog veel ruimte voor verbetering van deze sensor.

In een mechanisch goed gedefinieerde opstelling hebben we de invloed van de vervorming van een micro-ring op de verschuiving van zijn optische resonanties gemeten. De resonantiegolflengte verschuiving ligt tussen de 0.5 en 0.75 pm/microrek voor licht met een golflengte van 1550 nm. De verschuiving is afhankelijk van de breedte van de golfgeleider en van de silicium kristaloriëntatie. De resonantieverschuiving komt vooral door de verlenging van de golfgeleider. De invloed van de verandering van de fasesnelheid van het licht in de golfgeleider (effectieve index) is een factor drie kleiner en werkt in tegengestelde richting. De sterke dispersie in sub-golflengte silicium golfgeleiders (400 bij 220 nm^2) halveert de verschuiving.

De optische eigenschappen van de micro-ring-resonatoren en hun componenten hebben we uitvoerig bestudeerd. Verschillende methoden voor de karakterisering van directionele koppelaars, die licht naar de ring koppelen, geven vergelijkbare resultaten (direct en in ring-resonatoren). Een interessant gemeten effect is de grote faseverandering die deze koppelaars introduceren wanneer nagenoeg al het licht van de ene naar de andere golfgeleider koppelt.

De meeste eigenschappen van silicium ring-resonatoren kunnen worden berekend met benaderende analytische theorie. Deze theorieën zijn meestal ontwikkeld voor golfgeleiders met een laag brekingsindexcontrast, zoals glasvezels ($\Delta n < 0.1$). We hebben deze theorieën nagekeken en, waar nodig, aangepast voor silicium golfgeleiders, die juist een hoog brekingsindexcontrast hebben ($\Delta n \approx 2$). Analytische theorieën geven fysisch inzicht en kunnen worden gebruikt in snelle simulaties van grote fotonische schakelingen. Voor het lezen van dit proefschrift is basiskennis van elektrodynamica voldoende. Hoofdstuk 2 kan worden gebruikt als onderdeel van een vak op universitair niveau.

Dit proefschrift beschrijft ons onderzoek naar silicium fotonische micro-ring-resonatoren en hun toepassing als mechanische sensoren. Het gebruik van zulke resonatoren in micro-gefabriceerde ultrageluid transducenten (MUTs) biedt nieuwe mogelijkheden voor ultrasone matrix technologie.

Contents

Preface

thesis, project, team, acknowledgments

As the title suggests, this thesis is about silicon photonic micro-ring resonators to sense strain and ultrasound. To some readers, this title clearly states what I did while this title will sound alien to others. Basically, I used photons (light) to measure deformation (strain) and high-frequent sound. I have tried to address all readers. Chapters 1 and 6 should be readable to anyone with an interest in technology (and a good level of English). The technical Chapters 2 to 5 contain abstracts that address scientific peers. Anybody with a basic knowledge of electrodynamics should be able to read this thesis without consulting other literature – provided that you read the thesis from front to back. Chapters 4 and 5 are directly accessible to mechanical and acoustical engineers. Whatever your background, I hope that you enjoy the reading, that you learn something, and that you get as enthusiastic as I am about these new sensors.

I got the idea of this ultrasound sensor when I was doing my Masters' thesis project in the field of silicon photonics (Dec. 2008). This project was collaboration between the Optics Research Group of Delft University of Technology (TU Delft) and TNO (Delft). At TNO, there was a project to develop a pressures sensor based on silicon photonic micro-ring resonators. I had done my bachelor's project in the acoustics group (of TU Delft) and my industrial internship on ultrasonic imaging of oil pipes (at Applus RTD, Rotterdam). I realized that TNO's pressure sensors could also measure ultrasound when interrogated fast enough and that this would have substantial benefits for microphone arrays in hard-to-reach locations such as oil pipes or the human artery. My supervisors, prof. Paul Urbach of TU Delft and dr. Mirvais Yousefi of TNO decided that this would be an interesting project for me to carry out as a PhD student in their groups.

This project was initially funded by TNO while we wrote a research proposal. The codename of the project was "Photonic NanoPhone" because we were working towards a very small and sensitive optical microphone. Dr. Koen van Dongen of the acoustical wavefield imaging group (TU Delft) joined the project. His team was developing a piezo-electric transducer array for ultrasonic imaging inside blood vessels (IVUS). Prof. Ton van der Steen of the Thorax Center of the Erasmus MC (Rotterdam) found the project interesting and promising but decided not to join because the microphone would not go to the clinic within the duration of this project. He was very right about that - although size of the actual microphone we report in this thesis is smaller than the diameter of a human hair, this microphone is in a package of a few centimeters. Something I would not like in my

artery. We wrote the proposal and I would like to acknowledge the IOP Photonic Devices programme of NL-Agency of the Dutch Ministry of Economic Affairs for the grant. This project fits well in their research programme which focuses on intensive collaboration between multidisciplinary research groups and industry. This new microphone has a huge potential for applications in industry while there were many fundamental issues unknown and there was no proof of the principle. The project started March 2011. Next to TNO, Technobis Fibre Technologies (Uitgeest) and HQ sonics (Waalre) joined as industrial partners to work on the electro-optic interrogation and on the ultrasonic testing, respectively. Ir. Suzanne Leinders joined as PhD student in the acoustics group with a focus on the acoustics of the sensor and the application to ultrasonic imaging. We collaborated a lot. In November 2011, Mirvais Yousefi left TNO and dr. Jose Pozo took over as my direct supervisor. In April 2013, dr. Martin Verweij and prof. Nico de Jong took over as supervisors of Suzanne. Nico de Jong is also with the Erasmus MC. With this thesis, I leave the project but the research continues by Suzanne and her supervisors and possible by other PhD students that join this research activity.

This project has been performed in close collaboration between the partners and I have experienced an open-door policy. I had the luxury of having two and sometimes even three desks in the same building. One at TNO, one at TU Delft, and occasionally one in the acoustics group to efficiently work together. I have used two labs: the photonics lab of TNO for the measurements of Chapters 3 and 4 and we have built the setup for Chapter 5 in a lab of the TU Delft acoustics group. The micro-mechanical fabrication was performed by TNO in the Van Leeuwenhoek Laboratory, a joined lab of TU Delft and TNO. We received large interest from Technobis - I hope that we did not drive them crazy by asking for different specs every time we met. Henk Huynen was always critical about the specs of the microphone and with Chapter 5, we can finally answer his questions. Positively.

As should be clear by now, I have many people to acknowledge: Paul Urbach, Mirvais Yousefi and Jose Pozo for the guidance, insightful discussions, and their open-door attitude; Suzanne for the open discussions, her practical mindset about technical and non-technical issues and her jokes; Koen van Dongen for the collaboration on the research proposal; Martin Verweij and Nico de Jong for the guidance of Chapter 5's research.

At TNO, I would like to acknowledge Hans van den Berg for the micro-fabrication: the PECVD deposition and the micro-fabrication of the membranes in the ultrasound sensors (Appendices A and D); Peter Harmsma, Remco Nieuwland and Jos Groote Schaarsberg for the help and training in the photonics lab; Emile van Veldhoven for the helium ion microscope (HIM) images; Pim Muijlwijk (then intern at TNO and now employee) for the work on Chapter 4 including automation of the setup; Teun van den Dool and Erik Tabak for the development of the strain tool and the discussions on Chapter 4; Martin Lemmen for the discussions on mechanics; Ruud Schmits for the fabrication of the first silicon photonic resonators (not reported in this thesis); Paul van Neer for the discussions about ultrasound sensors; Dario Lo Cascio, Michael Engelmann, Jan-Leendert Joppe, and Roland van Vliet ("let's do cool stuff") for the management support.

I would like to acknowledge TU Delft's technical and support staff, Yvonne van Aalst, Henry den Bok, Gerrit van Dijk, Dennis van Doorn, Roland Horsten, Emile Noothout, Rob Pols, Thim Zuidwijk. I would like to thank the staff of the Van Leeuwenhoek Laboratory / Kavli NanoLab Delft for the help with the metrology and fabrication of the membranes. I would like to acknowledge Olaf Janssen sharing the layout template of his thesis.

I would like to acknowledge the ePIXfab consortium for the fabrication of the photonic chips; Pieter Dumon, Amit Khanna and their team at IMEC (Leuven, Belgium) for the technical support; Bradley Sneyder and Peter O'Brien of the Tyndall National Institute (Cork, Ireland) for the non-trivial packaging of the photonic microphones; Khalid Chougrani of Applus RTD (Rotterdam) for Figure 1.1b; Anne-Sophie Bonnet-Ben Dhia, Omar El Gawhary, Kevin van Hoogdalem, Adrianus T. de Hoop, Steven Johnson, Wim van Horssen, Jos Thijssen, and Ad Verbruggen for the input on Chapter 2; Vincent Brulis of Photon Design (Oxford, UK) for his support on their software; the user committee of the project for their interest and their constructive feedback during our meetings. I would like to acknowledge my doctoral committee (see page iv).

I would like to thank my colleagues at both TU Delft and TNO for the fruitful discussions, the fruitless discussions, and the laughters. I would also like to thank all the people with whom I have had interesting discussions or good times at scientific conferences. Special thanks to the people of Southampton's ORC who I was always welcome to join for dinner and drinks when I was visiting conferences by myself. I have become good friends with my TU Delft long-term office mates: Nitish and Adonis, I enjoyed sharing thoughts about technical and non-technical topics. I am indebted to my friends, my family, my parents, my sisters, and especially to my girlfriend, Mirjam, for their enduring trust and support. Thank you very much.

Chapter 1

Introduction

This thesis is about photonic ring resonators to be used as ultrasound microphones (Sec. 1.2) or strain gauges (Sec. 1.3). Hereafter we first explain how these new sensors work and the research we carried out to make them work (Sec. 1.1). Recent technological developments in the semiconductor industry make (mass-) production of these silicon devices possible (Sec. 1.4). The outline of this thesis is presented in Sec. 1.5.

1.1 The aim: photonic ring resonators to sense ultrasound

This thesis is about the research that has been carried out towards a new ultrasound microphone based on silicon photonic ring resonators. In this photonic microphone, light is guided through a waveguide to a photonic resonator and the light that passes the resonator is recorded using a photo-receiver. The photonic resonator is made to modulate the light with the ultrasonic pressure. We used a photonic ring resonator which consists of a looped waveguide, forming a closed cavity that has specific optical resonances. This resonator was integrated in a thin membrane. The operation principle is as follows: ultrasonic pressure waves deform the membrane and thus deform the photonic ring resonator. This deformation shifts of the resonance frequencies of the ring resonator. These shifts are measured by recording the light that passes the ring resonator. We have investigated these microphones in silicon-on-insulator (SOI) technology, because it allows for cheap and reliable fabrication of both the photonic circuits and the micro-mechanics of the devices.

The aim of this research project was to proof the operation principle of this new type of microphone and to study the feasibility for application in ultrasonic imaging. We have chosen to also develop thorough understanding of the components and principles on which this sensor is built, so that the obtained knowledge is useful for many other applications as well.

Therefore the first objective was to review and, when necessary, extend fundamental theory of silicon photonic micro-ring resonators (Chapter 2). The second objective was to characterize and understand the optical behavior of the resonator, thus without applied deformation (Chapter 3). The third objective was to understand the relation between an applied deformation of the resonator and the corresponding shift in the resonance wavelength, as little was known in literature about this relation (Chapter 4). In Chapter 5, we reach the final goal of this research and we demonstrate the operation principle of the new type of ultrasound microphone that is based on silicon photonic micro-ring resonators. The demonstrated sensor has a sensitivity that is already similar to the state-of-the-art of conventional ultrasound sensors despite the fact that we report on the most basic configuration and that there is much room for optimization and improvement.

The chapters of this thesis are relevant to different fields of scientific research. Therefore we have reviewed the literature in the introductory section of each chapter, and not in this Chapter 1 as is often done. The history and rationale behind silicon photonics is introduced in Sec. 2.2 while the state-of-the-art is summarized in Sec. 3.1. This introductory Chapter 1 motivates the research reported in this thesis from a more general perspective.

1.2 A new microphone for (medical) ultrasound

This thesis demonstrates the working principle of a new type of microphone with important benefits for medical and industrial ultrasonography. In this section, we first introduce ultrasonography and traditional microphones. Then we present the new microphone. We conclude this section with two applications: medical intravascular ultrasonography (IVUS) and non-destructive testing (NDT) of industrial pipes.

Ultrasonography is a technique in which high-frequent sound waves are used to image something which is not visible with light. Well known are the images of a fetus, which are made with an ultrasonic transducer placed on the belly of a pregnant woman. Sound waves are emitted downwards into the belly, partially reflect upwards on the structure of interest (the fetus), and these *echoes* are recorded by the transducer. The technique is similar to sonar used by some animals such as bats. Today's clear ultrasonic images are made with an array of transducers, which record the sound waves at a number of positions spaced at distances smaller than the wavelength. The recordings are transformed to images by digital focusing, using a computer to generate an acoustical image similar to what a lens does with visible light.

Conventional ultrasound transducers employ piezo-electric material. As a sound (pressure) wave compresses this material, the piezo-electric effect generates an electric voltage. The resulting electrical signal is a direct measure of the incoming sound pressure. Last decades, micro-machined ultrasound transducers (MUTs) have received a lot of interest. Arrays of traditional piezo-electric transducers require individual fabrication, placement and wiring of the piezo-electric elements, while micro-machined transducers are fabricated with optical lithography in which all array elements are made simultaneously. This may result in an huge reduction of the price of such transducer arrays. In MUTs, sound pressure deforms a flexible membrane, similar to the human eardrum. The most popular MUT is a capacitive MUT (cMUT) in which the vibrating deflection is measured by recording the electrical capacitance between the membrane an a bottom plate. The high-frequency signal of the electrical transducers is transmitted via a coaxial wire. Despite the low capacitance of these cables, the capacitance still limits the cable length.

In this thesis, we investigate and prove the principle of an ultrasound microphone based on integrated photonic resonators, in which photons rather than electrons, carry information (Chapter 5). We demonstrate a microphone for operation at 0.75 MHz with a minimal detection level (NEP) as low as 1 Pa. This is already on the same order of magnitude as the state-of-the-art of piezo-electric transducers while there is much room for improvement. One sensor consists of an optical resonator integrated in the membrane of a micro-machined ultrasound transducer. The deflection of the membrane caused by the ultrasonic waves shift the optical resonance frequencies. This shift of resonance can be optically monitored by an external interrogator system. Next to the resonators, it is possible to integrate optical multiplexers[1] directing specific wavelengths to individual resonators (wavelength-division-multiplexing, WDM). In the literature, various types of multiplexers in silicon-on-insulator technology have been demonstrated with footprints below 1 mm^2 [1,2]. This allows simultaneous reading of multiple sensors with one optical fiber. Fabrication of the devices is done with optical lithography for photonics and micromechanics, exploiting the high-tech fabrication technology developed in the semiconductor industry. Another major advantage of the all-optical sensor that we investigate is that it does not suffer from electromagnetic interference (EMI).

A limitation of this new type of transducer is that it only records but does not generate sound. Acoustical imaging with digital focusing only requires an array of microphones, while one omnidirectional source suffices. This source can be a single traditional piezo-electric transducer. Alternatively, all-optical solutions use the photo-acoustic effect, either in a well-defined structure in the catheter [3–7], or in the imaged medium (this has additional advantages, see [8]).

Ultrasonography is used in medical diagnostics for the imaging of different subcutaneous body structures. Lately, it has been recommended as an effective tool for the diagnoses of atherosclerosis (intravascular ultrasonography, IVUS) [10–12]. By bringing the ultrasonic transducer, mounted on the tip of a catheter, into the artery an image of the vessel wall can be obtained (see Fig. 1.1a for an example of an IVUS image). However, respiratory motion can displace the catheter tip as much as 6 mm, resulting in serious blurring and artifacts in the images. To improve the image quality, it is advantageous to use an array of many transducers in the arterial direction. This was demonstrated by our collaborators of the acoustical wavefield imaging laboratory [13]. Although possible to a certain extent, it is difficult to wire many electronic transducers with coaxial cables through the artery. In contrast, when the optical MUT is used, the signals of many sensors can be transmitted via one optical fiber[2]. Moreover, the insensitivity to EMI allows the ultrasound microphone to be used inside MRI-scanners, combining two complementing imaging modalities. Our research has received large interest from the

[1] Multiplexing is the simultaneous transmittance of multiple signals via one cable.

[2] An alternative approach is placing a micro-chip on the catheter tip, pre-processing the signal to limit the amount of data to be transmitted through the coaxial wires. This is explored in the STW-project "Miniature ultrasound probe for real-time three-dimensional imaging and monitoring of Cardiac interventions".

(a) (b)

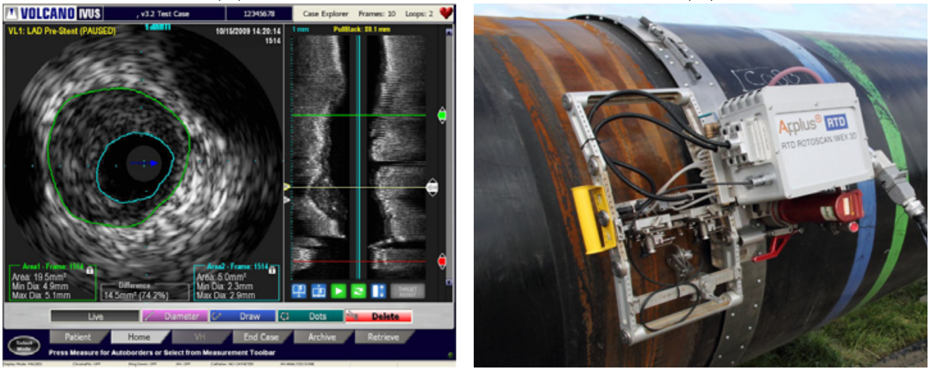

Figure 1.1: Applications of ultrasonography. **(a)** Intravascular imaging. Ultrasonograph of the cross-section of a blood vessel (main image), scan along the longitudinal direction of the blood vessel (right image). Screenshot illustrating VH®IVUS of Volcano Corporation (San Diego, California, USA) [9]. **(b)** Ultrasonic inspection of the girth welds of industrial pipes. RTD Rotoscan IWEX 3D equipment of Applus RTD (Rotterdam, The Netherlands). Photograph courtesy of Applus RTD (mr. Khalid Chougrani).

biomedical engineering group of the Thorax center of the Erasmus Medical Center in Rotterdam, who pioneered and developped ultrasonic diagnostic techniques for vulnerable plaque detection.

Ultrasonography is also used for non-destructive testing (NDT) of industrial vessels or pipes as applied in the petrochemical and oil&gas industries. A major application is the inspection of grith welds of new pipelines. Welding of metal pipes is not straightforward, and industrial use requires strong and defect-free welds. One can imagine that these issues are especially important when a pipe is to be submerged to the bottom of the sea. In today's ultrasonic NDT, array technology with over one hundred elements is employed. Applus RTD, a Rotterdam based company, is leading in ultrasonic inspection of such welds. In their state-of-the-art IWEX 3D imaging technology, the electronical processing unit is located close to the actual ultrasound transducers, in order to limit the length of the ultrasonic signal cables (see Fig. 1.1b). This unit is relatively large and heavy compared to the size of the transducer. In contrast, our optical transducers allow the processing to be done kilometers from the inspected structures by using optical fibers originally developed for long-haul telecommunication. Moreover, the all-optical system cannot ignite gas explosions.

In this thesis, we have given a proof-of-the-principle of an micro-machined ultrasound microphone based on integrated optical resonators. This microphone is very promising for various fields of ultrasonography, varying from medical to industrial applications.

1.3 A new strain sensor for micro-mechanical systems

Microscale displacement sensors are widely used in micro electro-mechanical systems (MEMS) to measure strains such as those induced by force, acceleration, pressure or (ultra)sound (Refs [14] and [15] and review MEMS and Piezoresitive devices in particular, respectively). MEMS mechanical sensors are, for example, used in the iPhone 4 which is equipped with a MEMS accelerometer and a MEMS gyroscope to provide the feature of automatic recognition whether the phone is held horizontally or vertically. Another example is in cars, where the air-bags are usually triggered by a MEMS accelerometer. Although the aim of our research was to obtain a micromechanical all optical ultrasound sensor, the sensor that is studied in this thesis is actually more generally applicable.

Traditional MEMS sensors are based on a capacitor or on piezoresistive material to transduce a displacement into an electrical signal. Alternatively, we propose to use optical resonators as sensing element, which provides particular benefits: high-speed readout, small sensor size, small multiplexer size (1 mm^2), insensitivity to electromagnetic interference, and no danger of igniting gas explosions by electric sparks.

Integrated optics technology allows the optical sensors, as well as their multiplexing circuit, to be integrated with MEMS. The sensing elements and their multiplexers can often be fabricated in a single processing step. Silicon-on-insulator (SOI) has emerged as one of the focus platforms for integrated optics, and is relatively straightforward to integrate with MEMS, since MEMS are most commonly made of silicon.

Any change in the size or in the refractive index of a silicon integrated optical resonator shifts its resonance frequencies, and this shift can be accurately recorded. Several groups have reported on sensor MEMS that are based on silicon integrated optical ring resonators, such as strain gauges [16–18], or pressure sensors [19–22]. In Chapter 4, we will study in detail the relation between an applied strain and the shift in the optical resonance frequency.

1.4 Silicon photonic and micromechanical fabrication technology

We have chosen to develop opto-mechanical sensors in silicon-on-insulator technology, to profit from 50 years of development in semiconductor fabrication technology.

The electronic integrated circuit (IC) industry has tremendously improved micro-fabrication technologies. Many innovations of the last 50 years were due to the desire to reduce the cost, size, and power consumption of ICs (computer chips), for application in computers, internet, cruise control, mobile phones, etc. The heart of semiconductor fabrication is photolithography, where the patterns that have to be realized are projected in a photosensitive layer. This layer is transferred into the actual material using an etch process. (Reference [23] introduces ICs.) Next to the fabrication of ICs, the micro-fabrication technology has been extended to the fabrication of micro-mechanical systems (MEMS) and photonic integrated circuits (PICs). (See Refs. [14] and [24], respectively).

Standardized technology platforms have been developed because accurate and reproducible fabrication takes many years to develop. Such a platform restricts to a wafer with layers of specific materials, and uses specific processes to fabricate structures in these wafers. The fabrication platforms are offered by semiconductor fabrication plants (fabs) worldwide.

We have chosen the silicon-on-insulator technology platform in which both micromechanics and integrated photonics are fabricated. (A more detailed motivation for this choice of material platform is given in Sec. 5.2.) Silicon technology is the most developed platform, and is offered by many fabs. Fabrication of silicon devices is reproducible and mass-production is relatively cheap. Silicon is a strong material and the common material in MEMS. The optical properties of silicon are good enough to meet the requirements of our resonator. The very high refractive index contrast confines the light strongly inside the silicon, allowing devices with a small footprint (ring resonators with diameters down to 6 μm). However, silicon photonics also has some drawbacks. First, silicon does not electronically generate or detect light at the used telecommunication wavelengths (~1550 nm). Other groups have solved this by adding active materials, but, in our case, we actually prefer light to be transmitted to and from the chip via an optical fiber to an external read-out system. Second, silicon waveguides have relatively high loss, reducing the quality factor of the resonators and thus their theoretical sensitivity. Third, the thermo-optic effect is quite large in silicon, which causes relatively large thermal noise [25]. Our ultrasound signals have, however, a small and well known bandwidth so that filtering drastically reduces this noise to acceptable values.

Integrated photonics requires a higher fabrication accuracy than is needed for MEMS membranes that we use. We ordered the photonic integrated circuits via the EU-funded ePIXfab consortium at IMEC (Leuven, Belgium) [24, 26]. IMEC fabricated the devices in their CMOS line with deep-UV lithography. We successfully post-processed these chips in-house with MEMS fabrication processes, without damaging the photonic circuits.

1.5 Outline of this thesis

In this chapter, we introduced the concept of strain and ultrasound sensing with silicon photonic micro-ring resonators. We motivated this research by presenting applications of this sensor in ultrasound detection and in microscale strain sensors. These sensors are widely used in the medical market, the oil & gas industry, the petrochemical industry, the automotive industry and the consumer electronics market. The remainder of this thesis is about the advances in theory and technology that we made, starting with a theoretical and experimental studies of the ring itself, followed by a study of the relation between strain and the resonances of the optical micro-rings and then presenting the proof-of-the-principle of the ultrasound sensor. Each chapter contains an introduction in which we compare the presented work with the state-of-the-art.

Chapter 2 presents fundamental theories on silicon photonic micro-rings, including waveguides, couplers and resonators. It includes the fundamentals of integrated optics so that it can be used as additional material in a university course on electrodynamics. We assume the book Electrodynamics by Griffiths as prerequisite. The chapter reviews theories in the literature from the perspective of high-index-contrast (silicon-on-insulator waveguides have a high index contrast). It includes new extensions and revisions of existing theories to the regime of high-index-contrast.

Chapter 3 provides a methodology for characterization of micro-ring resonators and their components (waveguides and directional couplers). It reports on the obtained characteristics of the resonators that are used as mechanical sensors in the chapters thereafter. Directional couplers are used to couple light to and from the micro-ring resonators. An interesting observation is that these couplers introduces a significant additional phase delay in the regime that nearly all light is coupled to/from the ring. We observed this as a significant change in the resonance wavelengths of a micro-ring; this change was caused by a tiny difference between the waveguides of the directional coupler.

Chapter 4 studies the shift in the optical resonance frequencies of silicon ring resonators due to an applied static mechanical strain. It presents a methodology to characterize strain sensors in silicon photonic technology, including a novel mechanical setup. Different design choices are investigated such as width of the waveguides and orientation of the resonator with respect to the orientation of the silicon crystal. The influence of different physical effects is analyzed: elongation of the track circumference, a change in the size of the cross-section of the waveguides due to Poisson's effect, the change in the refractive index of the silicon and silicon-dioxide due to the photo-elastic effect, and the dispersion that is introduced by the waveguide. These figures and insights are necessary for the design of strain and ultrasound sensors based on silicon waveguides.

Chapter 5 presents the proof-of-the-principle of ultrasound detection with optical silicon ring resonators integrated in an acoustical resonant membrane. It presents the design, fabrication and characterization of this microphone. The characterization shows a minimal detection level (NEP) below 1 Pa which is already on the same order of magnitude as the state-of-the-art of piezo-electric transducers. The chapter concludes with a number of suggestions to improve the detection limit even further.

Chapter 6 concludes the thesis with a summary of the previous chapters and an outlook to the future.

Chapter

2

Fundamental theory of silicon micro-rings: waveguides, couplers and resonators

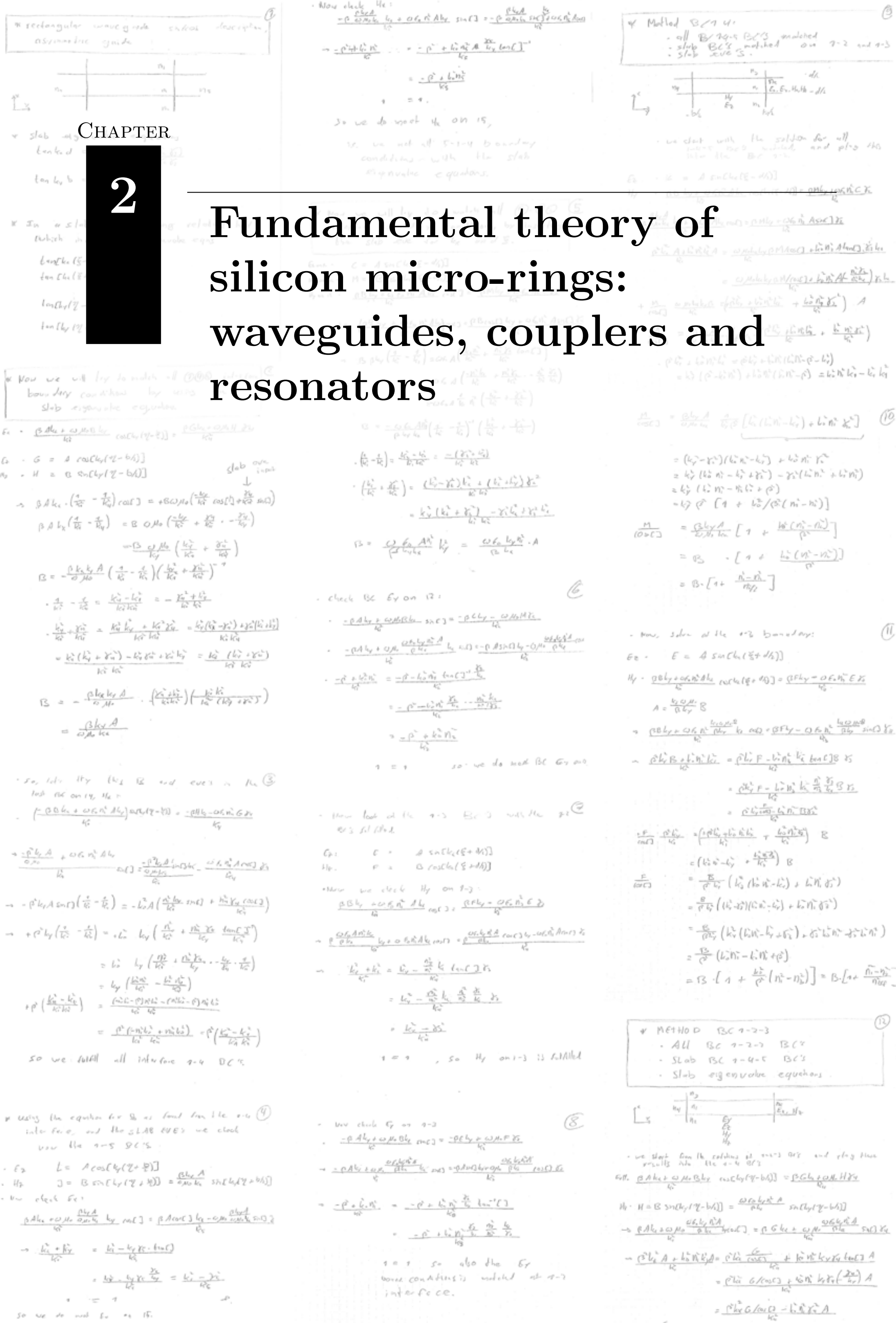

Abstract – many theories on integrated optics were originally derived for low-index-contrast ($\Delta n < 0.1$) waveguides while contemporary SOI waveguides have a high-index-contrast ($\Delta n \approx 2$). In this chapter, we review theories in the literature from the perspective of high-index-contrast and we extend the theories where necessary. We describe general properties of light propagation through waveguides following the work of Kogelnik [27] and Marcuse [28, 29] (Secs. 2.4-2.6). We extend Marcatili's approximate analytical method for rectangular waveguides to the regime of high-index-contrast [30] (Sec. 2.7). We find that Marcatilis eigenvalue equation for the propagation constant is also valid for SOI waveguides and we improve the method by adjusting the amplitudes of the components of the electromagnetic fields. Our method shows much better agreement with rigorous simulations of SOI waveguides. Furthermore, we derive expressions for the effective group index and we study the avoided crossing of TE- and TM-like modes. We present three calculations for directional couplers, based on coupled mode theory, eigenmode expansion and FDTD (Sec. 2.10). We review and reformulate the coupled mode theory of Hardy and Streifer [31,32] to show that this theory is, despite the high index contrast, applicable to silicon directional couplers (Sec. 2.10.3). We introduce out-of-plane grating couplers, including a new simulation scheme for 1-D grating couplers and a brief review of more advanced out-of-plane grating couplers (Sec. 2.11). We present Yariv's formulation of ring resonators, but with exact equations for the extinction ratio and the full-width at half-max (FWHM, Sec. 2.12). We design, as example, racetrack-shaped ring resonators for strain and ultrasound sensing (Sec. 2.13).

2.1 Introduction

This chapter presents fundamental theories that describe photonic micro-ring resonators in silicon-on-insulator (SOI) technology. Waveguides in SOI technology have a high index contrast (i.e., a large difference between the refractive index of the core of the waveguide and the cladding of the waveguide). In the early days of integrated optics, mainly low index contrast waveguides were used, and many theories stem from this time [27–38]. Unfortunately, these theories are not always applicable to high-index-contrast. This chapter presents theories for high-index-contrast silicon waveguides, including two theories newly derived in the scope of

Section 2.7 is based on W.J. Westerveld, S.M. Leinders, K.W.A. van Dongen, H.P. Urbach, and M.Yousefi, "Extension of marcatili's analytical approach for rectangular silicon optical waveguides," *Journal of Lightwave Technology*, vol. 30, no. 14, pp. 2388–2401, 2012.

Section 2.11 is based on W.J. Westerveld, H.P. Urbach, and M. Yousefi, "Optimized 3-D simulation method for modeling out-of-plane radiation in silicon photonic integrated circuits," *IEEE Journal of Quantum Electronics*, vol. 47, no. 5, pp. 561–568, May 2011.

A free open-source Matlab implementation of the methods in Sec. 2.7 has been published online as "RECTWG: Matlab implementation of the extended Marcatili approach for rectangular dielectric optical waveguides", distributed in *RECTWG package for Matlab – Version 0.1*, Mar. 2013. This package is maintained by W.J. Westerveld, R.C. Horsten, J. Pozo, and H. P. Urbach. Available at `http://waveguide.sourceforge.net`.

this thesis, and a review of existing theories. The scope of this chapter is limited to photonic components in the silicon-on-insulator technology with subwavelength rectangular waveguides. Nowadays, this is one of the most used platforms. Other technologies, such as rib waveguides, are not included here and the reader is referred to, for example, Ref. [39]. This chapter includes fundamentals so that it can be used as extra material in a university course on electrodynamics (such as Ref. [40]).

This chapter first introduces the concepts of integrated optics and silicon-on-insulator technology (Secs. 2.2 and 2.3). Then it states Maxwell's Equations, describes the modal propagation of light through slab waveguides, and derives general properties of modes (Secs. 2.4, 2.5 and 2.6). After this, a new approximate method for rectangular SOI waveguides is derived, folllowed by a short introduction to numerical mode-solvers and typical properties of SOI waveguides (Secs. 2.7, 2.8 and 2.9). The chapter continues with components: directional couplers, out-of-plane grating couplers, and ring resonators (Secs. 2.10, 2.11 and 2.12). The chapter is concluded with our rationale behind the design of racetrack resonators for sensing of mechanical strain and ultrasound (Sec. 2.13).

2.2 Silicon Photonics

This section briefly introduces photonics, integrated photonics, silicon photonics, and the state-of-the-art of silicon photonic fabrication techniques. Recent scientific advancements are further detailed in Sec. 3.1.

In photonics, light is used as carrier of information, likewise electrons are used in electronics. Photonics as a field began with the invention of the laser in 1960. Other developments followed, including: the laser diode, optical fibers for transmitting information, and the Erbium-doped fiber amplifier. These inventions formed the basis for the telecommunications revolution of the late 20th century and provided the infrastructure for the internet [41]. Photonics is not limited to telecommunications, for example, in this thesis we work on optical sensors. A number of optical components are required: laser sources, modulators to encode the light with an (electronic) signal, detectors, and splitters to redirect signals to the designated users.

The concept of integrated optics, already proposed in the late 1960's, is to fabricate all these optical components in a single on-chip integrated circuit [42]. These chips usually use dielectric materials to confine and guide light (like optical fibers). The size of a single-mode-waveguide depends strongly on its refractive index contrast, i.e., the difference in refractive index between the core of the waveguide and is cladding. For example, optical fibers have a low index contrast (∼0.05) with a core of ∼8.2 μm [43], and silicon waveguides with a SiO_2 cladding have a high index contrast (∼2) and core of ∼0.5 μm. In the early days of integrated optics, only low index contrast waveguides could be fabricated. Development of integrated photonic components has always gone hand-in-hand with development of lithographic fabrication processes. Devices and waveguides require dimensions on the order of the wavelength with a much higher accuracy, demanding the most of micro-fabrication techniques. Over the last decades, a number of more-or-less standardized platforms have been developed, comprising a set of material combinations, fabrication processes, and typical optical components.

One of the most promising platforms for integrated photonics is the silicon-on-insulator platform, often referred to as *Silicon Photonics*. Silicon photonic components have first been reported in the mid 1980's [44] and silicon-on-insulator waveguides were reported few years later [45, 46]. Photonics has been driven by the telecommunication industry and the vision of a "superchip" combining electronics and photonics, presented in the early 1990's, has inspired many researchers since [47, 48]. A review of the field of silicon photonics may be found in Refs. [39] and [49]. Large companies such as Intel, IBM, Molex, and Teraxion have announced and launched products in silicon photonic technology, for example optical interconnects for high-speed communication [50–55]. A major advantage of this platform is that photonic integrated circuits can be fabricated in the existing CMOS infrastructure of the semiconductor industry, allowing for low cost and stable mass-fabrication. Moreover, silicon is a strong material and its high refractive index contrast allows for small devices. Silicon is a passive material with no direct semiconductor band gap around 1550 nm free-space wavelength, thereby it cannot be used to electronically detect or generate light. Germanium or silicon-germanium alloys are added to provide this functionality, while this processing is still possible in CMOS fabrication lines [56–59]. Alternatively, III-V materials can be integrated into silicon photonic integrated circuits [60, 61].

Integrated photonic circuits have different requirements than electronic circuits. Typical critical dimensions of silicon waveguides (100 nm - 500 nm) are fairly large in today's high-end CMOS tools; however, optical components require the dimensions to be accurate within nanometers and consist of diverse features (ranging from isolated waveguides to dense arrays of holes). Existing CMOS processes have been tailored to these demands of integrated photonics, and a silicon photonics platform is offered for about a decade by the ePIXfab consortium [24]. Today, wafer-scale fabrication in (semi) industrial fabrication plants (fabs) is offered by various parties[1]. Photonic components in today's silicon platforms are often based on rectangular silicon waveguides on a SiO_2 *burried oxidie* (BOX) substrate, and with an air or SiO_2 cladding. Waveguides have a typical height around 220 nm and width around 450 nm.

This chapter presents a selection of theories that are applicable to integrated photonic components in SOI technology. We assume light with a free-space wavelength λ around 1.55 μm. Telecommunications often works with this wavelength, and many components (sources, detectors, fibers, etc) are relatively cheap available for this wavelength, making this wavelength also attractive for other applications.

[1] In Europe, the EU-funded ePIXfab consortium offers fabrication at IMEC (Leuven, Belgium), CEA-LETI (Grenoble, France) or IHP (Frankfurt an der Oder, Germany) [24, 26]. A similar service is offered by the OpSIS project based at the University of Washington in Seattle and the University of Delaware in Newark, a consortium including the Institute of Microelectronics (IME, Singapore), Luxtera (headquarter in Carlsbad, California), and STMicroelectronics (headquarter in Geneva, Switzerland) [62].

2.3 Fabrication technology for optical designers

Fabrication of the small waveguides in silicon-on-insulator technology is not straightforward, only last decade's high-end technology is accurate enough. The rules that apply to macro-fabrication do generally not apply to micro-fabrication. To illustrate this, we compare the fabrication of a photonic chip in a fab against the fabrication of a wooden table by a craftsman. Asking a fab to make a device from a slightly different material might a decade of development, whereas a wood craftsman could easily work with a slightly different type of wood. On the contrary, it would be almost impossible for a craftsman to fabricate a million tables, while a fab easily fabricates a millions devices

We briefly explain the fabrication concept. First, the optical designer makes a construction plan based on the technology which is offered by a fab. The fab starts with a clean silicon-on-insulator wafer. A photo-sensitive layer is spun upon the wafer. This layer is illuminated with the pattern that has to be written in this layer. (You can compare this with a traditional photography, where an image created by light falling on a photographic film.) Then the photosensitive layer is developed such that it transforms into a mask protecting only the illuminated patterns. The actual fabrication is done using etching, a chemical process a in which a plasma "eats" the unprotected silicon. Then the wafer is cleaned, removing the residue of the mask. Most chips require more than one of these fabrication sequences, for example for the fabrication of out-of-plane grating couplers (see Sec. 2.11), which basically is a grating etched in the top surface of a wide waveguide.

In reality, micro-fabrication is a rough process on the micro-scale. We will illustrate this with some examples, most appreciated when one realizes that the width of a waveguide (500 nm) is about one hundredth of the diameter of a human hair. In the illumination, the imaging has to be accurate within a few nanometers over a surface of about 1 cm^2 (the chip). Multiple layers have to be aligned to each other, so after fabrication of the first layer, the wafer has to go back into the lithography machine and the image of the second layer has to be aligned to the patterns on the wafer with an accuracy of a few tens of nanometers. Also the etching is notably rough. The top of the patterns is protected with a mask, but the formation of the sides is controlled in the etch process. The unprotected areas of the chip consume the etchant in a higher rate than the protected patterns, giving a variation of the etchant over the wafer. Etching small deep features is especially difficult as "fresh" etchant has difficulty arriving at the bottom.

This gives a number of differences between the fabricated devices and the designed ones and we list the most important differences. (1) The world-leading manufacturer of SOI-wafers, Soitec (Bernin, France), specifies the variation of the height of the silicon light-guiding layer as 20 nm, 10% of the typical height of 220 nm [63]. (2) Variations in illumination may cause all devices to be larger or smaller than designed. (3) The lithography can be optimized for only one feature size [24]. For example, when 450 nm wide waveguides are according to specification, then other widths are not. (4) The sides of the pattern (waveguide) are not perfectly straight but have an angle of about 10 degrees [64]. (5) The sides of the patterns are not smooth, but have nanometer-scale roughness [65].

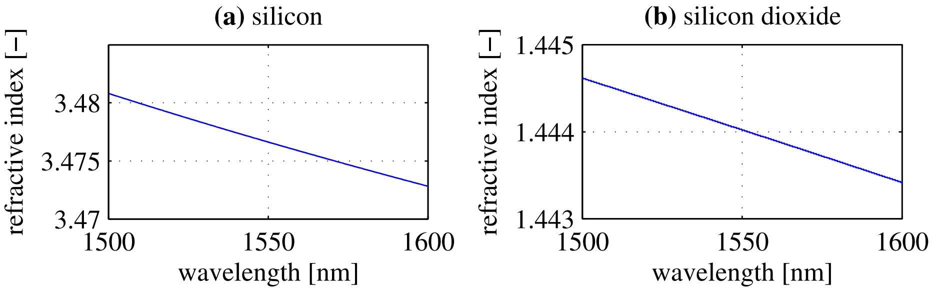

Figure 2.1: Refractive index n of **(a)** silicon and **(b)** silicon dioxide, plotted as a function of wavelength.

For an optical designer, it is necessary to design the devices such that they remain functional regardless the fabrication-induced variations. There are two approaches to address these fabrication-variations. For known fabrication-induced differences, it is possible to design the pattern not to be identical to the desired pattern, but to make it such that it will be fabricated as the desired pattern. For example, when one knows the relation between the designed and fabricated width of a waveguide, it is easy to draw the waveguide with a width that will be fabricated as the desired width. Another example is the placement of the grating in out-of-plane grating couplers on top of a wide waveguide. The width of the grating can be designed larger than the waveguide (the part which extends further than the waveguide has little effect on the light in the guide), and the length of the wide waveguide can be chosen longer than the length of the grating. An unintentional offset between the waveguide and the grating will then not affect the optical properties of the device. For unknown fabrication variations, it is necessary to design the device such that it is tolerant against fabrication variations, i.e., to design it such that the optical functionality remains acceptable. An example here is in the design of ring resonators, see Sec. 2.13.

2.4 Maxwell's equations for linear, passive materials

Maxwell's equations generally describe the propagation of light in terms of the electric field $\boldsymbol{\mathcal{E}}$ and the magnetic field $\boldsymbol{\mathcal{H}}$. This section presents Maxwell's equations in a convenient form to describe passive components in silicon-on-insulator technology.

Typical passive optical components in silicon-on-insulator technology consist of silicon (Si), silicon-dioxide (SiO_2) and air (see Fig. 2.1 for refractive indices). These materials have no direct band-gap around the telecom wavelength (1550 nm), therefore active components use different materials to generate and detect (absorb) the light. The active components are typically located far away (hundreds of wavelengths) from the passive components. The passive components have no free carriers or currents, so we can neglect these terms in Maxwell's equations.

Unless intentionally modified, silicon and SiO_2 can be approximated as linear dielectrics (i.e., approximating the material polarization proportional to the electric field $\boldsymbol{\mathcal{E}}$). The linear and nonlinear susceptibilities $\chi^{(i)}$ of silicon are well described in Ref [66]. The magnetic susceptibility of the dielectrics can be neglected (i.e., approximating the permeability μ as the vacuum permeability μ_0). In this work, all optics is presented for monochromatic light with angular frequency ω and vacuum wavelength $\lambda = \omega/c$, with c the speed of light in vacuum. This is not a limitation, as all linear systems can equally be described in terms of time t or angular frequency ω via the Fourier transform.

We describe the physical electromagnetic fields in terms of their complex amplitudes $\boldsymbol{\mathcal{E}}$ and $\boldsymbol{\mathcal{H}}$. The physical (and thus real) electromagnetic fields are the real components of these complex amplitudes, i.e., $\mathrm{Re}\{\boldsymbol{\mathcal{E}}\}$ and $\mathrm{Re}\{\boldsymbol{\mathcal{H}}\}$, respectively. Maxwell's complex equations for monochromatic light in an isotropic linear dielectric medium without charges are given by [40]

$$\nabla \times \boldsymbol{\mathcal{E}} = -\imath\mu_0\omega\boldsymbol{\mathcal{H}}, \tag{2.1}$$
$$\nabla \times \boldsymbol{\mathcal{H}} = \imath\omega\epsilon\boldsymbol{\mathcal{E}}, \tag{2.2}$$
$$\nabla \cdot \epsilon\boldsymbol{\mathcal{E}} = 0, \tag{2.3}$$
$$\nabla \cdot \boldsymbol{\mathcal{H}} = 0, \tag{2.4}$$

with vacuum permeability μ_0, and permittivity ϵ. The latter two equations (2.3) and (2.4) are not independent and follow directly from the first two equations (2.1) and (2.2), as the divergence of the curl of a vector is zero. The refractive index $n = \sqrt{\epsilon/\epsilon_0}$, with ϵ_0 the vacuum permittivity. The permeability $\epsilon(x, y, z)$ profile describes how the devices (e.g., waveguides, couplers, ec) look like, and how the electromagnetic fields behave.

Electromagnetic fields in a homogeneous isotropic medium obey the wave equations

$$(\nabla^2 + n^2k^2)\boldsymbol{\mathcal{E}} = 0, \tag{2.5}$$
$$(\nabla^2 + n^2k^2)\boldsymbol{\mathcal{H}} = 0, \tag{2.6}$$

with $k = \omega/c$ the free-space propagation constant [40, Ch. 9]. When using the wave equation for homogeneous media, it is necessary to apply interface conditions to ensure that the solutions also obey Maxwell's equations across interfaces. These four conditions are that the tangential components of the electric $\boldsymbol{\mathcal{E}}$ and magnetic $\boldsymbol{\mathcal{H}}$ fields are continuous [40, Ch. 7].

2.5 Dielectric Slab waveguides

Dielectric waveguides consist of a beam of a material that has a refractive index higher than its surrounding. Light can be guided along the long direction of such a beam. In typical[2] silicon-on-insulator technology, the silicon beam is rectangular and fabricated on top of a SiO_2 layer with a cladding of either SiO_2 or air. The easiest waveguide to describe is a slab waveguide. This basic structure demonstrates the concept of modes, and our description of rectangular waveguides (Sec. 2.7) is

[2] Different waveguide types are possible in SOI, but rectangular ones are often used today (see Sec. 2.9).

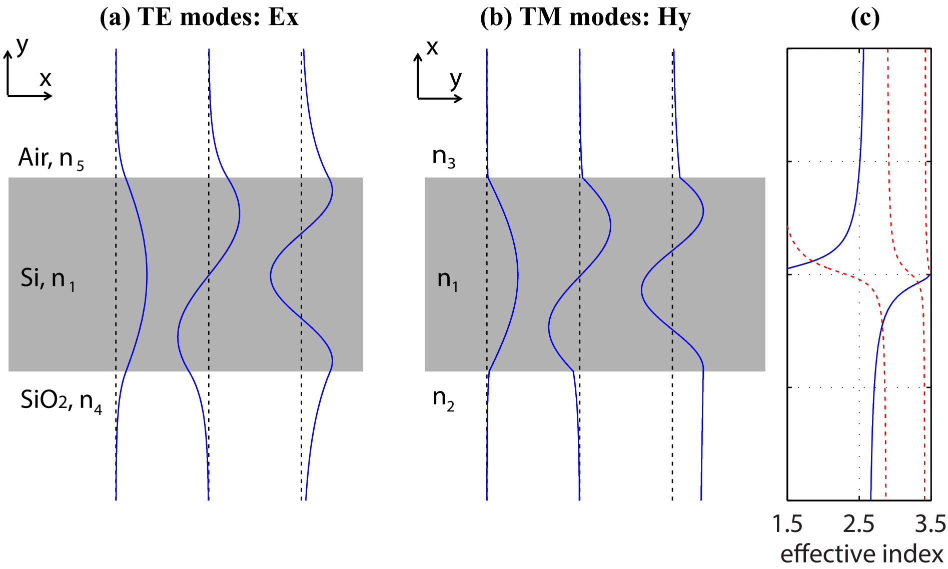

Figure 2.2: Silicon-on-insulator slab waveguide with height 600 nm. **(a,b)** Sketches of cross sections. **(a)** TE-modes. Coordinate frame. Electric fields of the three supported guided modes. **(b)** TM-modes. Coordinate frame. Magnetic fields of the three supported guided modes. **(c)** Graphical method to solve Eq. (2.17) for TE modes. Tangential term (dashed line) and fraction term (solid line) both plotted versus the effective index n_e ($k_y = \sqrt{k^2 n_1^2 - k^2 n_e^2}$). The three crossings correspond to the solutions plotted in (a). In Sec. 2.5, $n_2 = n_4$ and $n_3 = n_5$. We chose different labels of the cladding refractive indices for the TE- and TM-modes (n_4, n_5 and n_2, n_3) because that will be useful in Sec. 2.7.

strongly related to the equations derived here. A slab waveguide is a layer with a sandwiched between two layers with a lower refractive index. Light propagation through slab waveguide is surprisingly well described with ray optics, despite the waveguide height being only half a wavelength (see [27, 28, 67]). We, however, directly use the more complete wave optics.

Figure 2.2 depicts a slab waveguide. For now, we stick to the coordinate frame in Fig. 2.2a, in which we chose a coordinate frame with the z-direction along the direction of propagation of the wave and the y-direction normal to the slab. In Sec. 2.5.2 (Fig. 2.2b), we will use a different coordinate frame because that will be useful in the description of rectangular waveguides (Sec. 2.7). We simplify the analysis by assuming that there is no variation of the electromagnetic fields in the transversal x-direction ($\partial/\partial x = 0$), i.e., we assume an infinitely wide waveguide. Maxwell's equations (2.1-2.4) actually include 8 equations as Faraday's law (2.1) and Ampère's law (2.2) are vectorial. Substituting $\partial/\partial x = 0$ in these equations shows that they decouple in equations either with $\mathcal{E}_x$, $\mathcal{H}_y$ and $\mathcal{H}_z$, or with $\mathcal{H}_x$, $\mathcal{E}_y$ and $\mathcal{E}_z$. Solutions to the first set of equations are classified as transverse electric

(TE) modes because the electric field $\boldsymbol{\mathcal{E}} = \mathcal{E}_x\hat{\boldsymbol{x}}$ is transverse to the direction of propagation. Solutions of the second set of equations are classified as transverse magnetic (TM) modes because $\boldsymbol{\mathcal{H}} = \mathcal{H}_x\hat{\boldsymbol{x}}$.

2.5.1 TE modes

Figure 2.2a sketches the TE-modes in a 600 nm high silicon-on-insulator slab waveguide. Transverse electric modes have only three non-zero field components: $\mathcal{E}_x$, $\mathcal{H}_y$ and $\mathcal{H}_z$. The magnetic components can be computed from the electric component, so that $\mathcal{E}_x$ uniquely defines the electromagnetic fields. We look for monochromatic propagating wave solutions, i.e. solutions in the form

$$\boldsymbol{\mathcal{E}} = E_x(y)e^{\imath(\omega t-\beta z)}\hat{\boldsymbol{x}}, \tag{2.7}$$

with propagation constant β. Subsituting this in Eq. (2.5) gives

$$\frac{\partial^2 E_x}{\partial y^2} = (\beta^2 - k^2n^2)E_x. \tag{2.8}$$

Depending on the sign of $(\beta^2 - k^2n^2)$, the solutions of this equation are either standing waves or exponentially decreasing fields towards $\pm y$. Exponentially increasing solutions are not physical. The slab acts as a waveguide for $k^2n_1^2 > \beta^2 > k^2n_4^2, k^2n_5^2$. In this case, the electric field inside the core (n_1) is a standing wave, while the field exponentially decay in the cladding. The light is thus confined in the core. For $\beta^2 > k^2n_1^2$, the wave is above the material cutoff of all of the materials and does not propagate. For $\beta^2 < k^2n_4^2, k^2n_5^2$, the wave propagates in the upper/lower cladding and is not confined to the core. For guided waves, Eq. (2.8) has the solutions

$$E_x = \begin{cases} C\ \exp[-\gamma_5(y-b/2)], & \text{upper cladding} \quad y > b/2, \\ A\ \cos[k_y(y+\eta)], & \text{core} \quad b/2 \geq y \geq -b/2, \\ B\ \exp[\gamma_4(y+b/2)], & \text{lower cladding} \quad y < -b/2, \end{cases} \tag{2.9}$$

with

$$k_y = \sqrt{k^2n_1^2 - \beta^2}, \tag{2.10}$$

$$\gamma_j = \sqrt{\beta^2 - k^2n_j^2} = \sqrt{k^2(n_1^2 - n_j^2) - k_y^2}, \quad j = 4, 5. \tag{2.11}$$

Equation (2.9) obeys Maxwell's equations in all three layers of the slab, but it also has to obey these equations at the interfaces. Electromagnetic interface conditions demand continuity of the tangential electromagnetic field components. Continuity of $\mathcal{H}_z$ in combination with Faraday's law (2.1) and $\partial/\partial x = 0$ demands continuity of $\partial E_x/\partial y$. We first calculate the relations which follow from these conditions and then discuss their meaning.

$$\frac{\partial^2 E_x}{\partial y^2} = \begin{cases} -\gamma_5 C\exp[-\gamma_5(y-b/2)], & \text{upper cladding}, \\ -k_y A\ \sin[k_y(y+\eta)], & \text{core}, \\ \gamma_4 B\exp[\gamma_4(y+b/2)], & \text{lower cladding}. \end{cases} \tag{2.12}$$

From the interface conditions at the lower interface ($y = -b/2$), we find

$$A\cos[k_y(\eta - b/2)] = B, \tag{2.13}$$
$$\tan[k_y(\eta - b/2)] = -\gamma_4/k_y, \tag{2.14}$$

and at the upper interface ($y = b/2$), we find

$$A\cos[k_y(\eta + b/2)] = C, \tag{2.15}$$
$$\tan[k_y(\eta + b/2)] = \gamma_5/k_y. \tag{2.16}$$

In the description of the modal electric field, Eq. (2.9), B and C follow from Eqs. (2.13) and (2.15), respectively. The amplitude factor A is a normalization factor, describing the amount of light in the mode, and should not follow from the interface conditions. Note that the propagation constant β is not free as it directly follows from k_y via Eq. (2.10). Equations (2.14) and (2.16) define k_y and η. After some algebra[3], we find

$$F(k_y, k, n_1, n_4, n_5, b) \equiv \tan[k_y b] - \frac{k_y(\gamma_4 + \gamma_5)}{k_y^2 - \gamma_4\gamma_5} = 0. \tag{2.17}$$

For a given slab waveguide (n_1, n_4, n_5, b) and angular frequency ($k = \omega/c$), Maxwell's equations thus demand k_y to obey Eq. (2.17). Depending on the slab waveguide, this equation has zero or more solutions for guided waves with β between $n_1 k$ and the higher value of $n_4 k$ and $n_5 k$. The tangential term is periodic, due to which multiple solutions might exist (see Fig. 2.2c). We hereby demonstrated that a waveguide has a distinct number of modes given a certain frequency. Each mode has its own distinct propagation constant β and with modal field $\boldsymbol{E}(y)$.

2.5.2 TM modes

Transverse magnetic modes have the magnetic field transversal to the propagation direction in the waveguide. Although annoying now, we switch to a different coordinate frame in which the x-direction is normal to the slab (see Fig. 2.2b). In this frame, non-zero electromagnetic field components are $\mathcal{H}_y$, $\mathcal{E}_x$, and $\mathcal{E}_z$. The waveguide is infinitely wide in the y-direction and $\partial/\partial y = 0$. Analogue to the derivation of TE modes, we look for propagating wave solutions

$$\boldsymbol{\mathcal{H}} = H_y(x)e^{\imath(\omega t - \beta z)}\hat{\boldsymbol{y}}, \tag{2.18}$$

obeying the wave equation (2.6), so that

$$\frac{\partial^2 H_y}{\partial x^2} = (\beta^2 - k^2 n^2)H_y. \tag{2.19}$$

[3] $\tan[k_y b] = \tan[k_y(b/2+\eta) + k_y(b/2-\eta)] = \frac{\tan[k_y(b/2+\eta)]+\tan[k_y(b/2-\eta)]}{1-\tan[k_y(b/2+\eta)]\tan[k_y(b/2-\eta)]} = \frac{\gamma_4/k_y+\gamma_5/k_y}{1-\gamma_4\gamma_5/k_y^2}$, using [68, Eq. (2.174)] for the 2nd equality sign and Eqs. (2.14) and (2.16) for the 3rd equality sign.

Guided waves have $k^2n_1^2 > \beta^2 > k^2n_2^2, k^2n_3^2$, hence the solutions of Eq. (2.19) are

$$H_y = \begin{cases} \tilde{C}\ \exp[-\gamma_3(x-d/2)], & \text{upper cladding} \quad x > d/2, \\ \tilde{A}\ \cos[k_x(x+\xi)], & \text{core} \quad d/2 \geq x \geq -d/2, \\ \tilde{B}\ \exp[\gamma_2(x+d/2)], & \text{lower cladding} \quad x < -d/2, \end{cases} \tag{2.20}$$

with

$$k_x^2 = k^2n_1^2 - \beta^2, \tag{2.21}$$

$$\gamma_j^2 = \beta^2 - k^2n_j^2 = k^2(n_1^2 - n_j^2) - k_x^2, \quad j = 2, 3. \tag{2.22}$$

The interface conditions demand continuity of the tangential electromagnetic field components (i.e., $\mathcal{H}_y$). Inspecting Ampère's law (2.2) in the z-direction and using $\partial/\partial y = 0$ gives

$$\imath\omega\mathcal{E}_z = \frac{1}{n^2}\frac{\partial\mathcal{H}_y}{\partial x} = \frac{1}{n^2}\frac{\partial H_y}{\partial x}e^{\imath(\omega t - \beta z)}, \tag{2.23}$$

demanding continuity of the right-hand-side of this equation because $\mathcal{E}_z$ is continuous. Time and z-position evolution are identical in all layers of the slab, hence continuity of the following term is demanded

$$\frac{1}{n^2}\frac{\partial^2 H_y}{\partial x^2} = \begin{cases} -\gamma_3/n_3^2\,\tilde{C}\exp[-\gamma_3(x-d/2)], & \text{upper cladding,} \\ -k_x/n_1^2\,\tilde{A}\ \sin[k_x(x+\xi)], & \text{core,} \\ \gamma_2/n_2^2\,\tilde{B}\exp[\gamma_2(x+d/2)], & \text{lower cladding.} \end{cases} \tag{2.24}$$

The four interfaces conditions, continuity of $\mathcal{H}_y$ and $\mathcal{E}_z$ at $x = -d/2$ and $x = d/2$, demand

$$\tilde{A}\cos[k_x(\xi - d/2)] = \tilde{B}, \tag{2.25}$$

$$\tan[k_x(\xi - d/2)] = -\frac{n_1^2}{n_2^2}\frac{\gamma_2}{k_x}, \tag{2.26}$$

$$\tilde{A}\cos[k_x(\xi + d/2)] = \tilde{C}, \tag{2.27}$$

$$\tan[k_x(\xi + d/2)] = -\frac{n_1^2}{n_3^2}\frac{\gamma_3}{k_x}. \tag{2.28}$$

Combining[4] Eqs. (2.26) and (2.28) gives the condition for the propagation constant β (in terms of k_x)

$$G(k_x, k, n_1, n_2, n_3, d) \equiv \tan[k_x d] - \frac{n_1^2 k_x(n_2^2\gamma_3 + n_3^2\gamma_2)}{k_x^2 n_2^2 n_3^2 - n_1^4\gamma_2\gamma_3} = 0. \tag{2.29}$$

2.6 General properties of modes in dielectric waveguides

This section is about general properties of dielectric waveguides. Some important characteristics such as the finite and discrete number of modes in a waveguides

[4] $\tan[k_x d] = \tan[k_x(d/2+\xi) + k_x(d/2-\xi)] = \frac{\tan[k_x(d/2+\xi)] + \tan[k_x(d/2-\xi)]}{1 - \tan[k_x(d/2+\xi)]\tan[k_x(d/2-\xi)]}$, using [68, Eq. (2.174)] for the second equality sign.

were already observed in the slab waveguide, and this section derives properties and equations for guided modes in a general waveguide with a two-dimensional refractive index profile $n(x, y)$ (or permittivity profile). A dielectric waveguide is fully described by its permittivity profile $\epsilon(x, y)$ which is invariant in the z-direction, the direction in which the light propagates. We look for propagating wave solutions in the from

$$\boldsymbol{\mathcal{E}}(x, y, z, t) = \boldsymbol{E}(x, y)e^{\imath(\omega t - \beta z)}, \qquad \boldsymbol{\mathcal{H}}(x, y, z, t) = \boldsymbol{H}(x, y)e^{\imath(\omega t - \beta z)}. \tag{2.30}$$

The propagation constant β is often expressed in terms of the effective index

$$n_e \equiv \frac{\beta}{k}, \tag{2.31}$$

with free-space propagation constant $k = 2\pi/\lambda$ and free-space wavelength λ. The first-order dispersion in the effective index n_e can be expressed in terms of the effective group index n_g

$$n_g \equiv \frac{\partial \beta}{\partial k} = n_e - \lambda \frac{\partial n_e}{\partial \lambda}, \tag{2.32}$$

where the last equality follows from Eq. (2.31). In the case that we only use small wavelength span around a center wavelength λ_c, it is often possible to approximate the wavelength-dependence of the effective index $n_e(\lambda)$ as linear, so that

$$\beta(\lambda) \approx 2\pi \left[\frac{n_e(\lambda_c) - n_g(\lambda_c)}{\lambda_c} + \frac{n_g(\lambda_c)}{\lambda} \right]. \tag{2.33}$$

2.6.1 Maxwell's equations in E_x, E_y, H_x and H_y: an eigenvalue problem

With electromagnetic fields in the form of Eq. (2.30), Maxwell's equations (2.1) and (2.2) may be written as[5]

$$\nabla_\beta \times \boldsymbol{E} = -\imath\omega\mu_0 \boldsymbol{H}, \tag{2.34}$$

$$\nabla_\beta \times \boldsymbol{H} = \imath\omega\epsilon \boldsymbol{E}, \tag{2.35}$$

with

$$\nabla_\beta = \frac{\partial}{\partial x}\hat{\boldsymbol{x}} + \frac{\partial}{\partial y}\hat{\boldsymbol{y}} - \imath\beta\hat{\boldsymbol{z}}. \tag{2.36}$$

We may describe the propagation of light through waveguides as an eigenvalue problem with the propagation constant β as eigenvalue. By eliminating the longitudinal components E_z and H_z from Maxwell's equations, one obtains the following eigenvalue problem for the transverse components only

$$\left(\hat{O} - \beta\right) \begin{pmatrix} E_x(x,y) \\ E_y(x,y) \\ H_x(x,y) \\ H_y(x,y) \end{pmatrix} = \begin{pmatrix} 0 \\ 0 \\ 0 \\ 0 \end{pmatrix}, \tag{2.37}$$

---

[5] As components, $\begin{pmatrix} \frac{\partial E_z}{\partial y} + \imath\beta E_y \\ -\imath\beta E_x - \frac{\partial E_z}{\partial x} \\ \frac{\partial E_y}{\partial x} - \frac{\partial E_x}{\partial y} \end{pmatrix} = \begin{pmatrix} -\imath\omega\mu_0 H_x \\ -\imath\omega\mu_0 H_y \\ -\imath\omega\mu_0 H_z \end{pmatrix}$, and $\begin{pmatrix} \frac{\partial H_z}{\partial y} + \imath\beta H_y \\ -\imath\beta H_x - \frac{\partial H_z}{\partial x} \\ \frac{\partial H_y}{\partial x} - \frac{\partial H_x}{\partial y} \end{pmatrix} = \begin{pmatrix} \imath\omega\epsilon E_x \\ \imath\omega\epsilon E_y \\ \imath\omega\epsilon E_z \end{pmatrix}$.

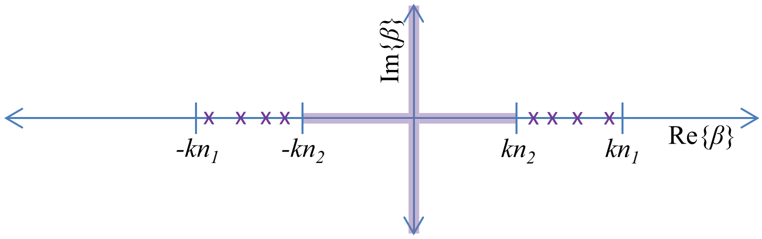

Figure 2.3: Sketch of Eigenvalues β of the eigenvalue problem in Eq. (2.37 with 2.40) showing guided, radiation and evanescent modes. Waveguide with cladding refractive index n_2 and core refractive index n_1. Light with free-space propagation constant k. The discrete number of guided modes are marked **x**, lay on the real axis, and have $kn_2 > |\beta| > kn_1$. The continuum of radiation modes lays on the real axis and have $|\beta| \leq kn_2$. The continuum of evanescent modes lays on the imaginary axis. Solutions with general complex β may exist as well. See Refs. [29, 33].

with $\hat{O}$ a second-order partial differential operator with respect to transverse variables x and y. From the z-components of Faraday's law (2.34) and Ampère's law (2.35), we respectively find

$$H_z = \frac{\imath}{\omega\mu_0}\left(\frac{\partial E_y}{\partial x} - \frac{\partial E_x}{\partial y}\right), \tag{2.38}$$

$$E_z = \frac{\imath}{\omega\epsilon}\left(\frac{\partial H_x}{\partial y} - \frac{\partial H_y}{\partial x}\right). \tag{2.39}$$

Substituting Eq. (2.39) in the x- and y-components of Faraday's law (2.34) and substituting Eq. (2.38) in the x- and y-components of Ampères law (2.35) gives a set of four equations which are linear in E_x, E_y, H_x and H_y. Rearranging these equations to the form of Eq. (2.37) gives

$$\hat{O} = \begin{pmatrix} 0 & 0 & 0 & \omega\mu_0 \\ 0 & 0 & -\omega\mu_0 & 0 \\ 0 & -\omega\epsilon & 0 & 0 \\ \omega\epsilon & 0 & 0 & 0 \end{pmatrix} + \begin{pmatrix} 0 & 0 & -\frac{\partial}{\partial x}\frac{1}{\omega\epsilon}\frac{\partial}{\partial y} & \frac{\partial}{\partial x}\frac{1}{\omega\epsilon}\frac{\partial}{\partial x} \\ 0 & 0 & -\frac{\partial}{\partial y}\frac{1}{\omega\epsilon}\frac{\partial}{\partial y} & \frac{\partial}{\partial y}\frac{1}{\omega\epsilon}\frac{\partial}{\partial x} \\ \frac{1}{\omega\mu_0}\frac{\partial^2}{\partial x \partial y} & \frac{-1}{\omega\mu_0}\frac{\partial^2}{\partial x^2} & 0 & 0 \\ \frac{1}{\omega\mu_0}\frac{\partial^2}{\partial y^2} & \frac{-1}{\omega\mu_0}\frac{\partial^2}{\partial y \partial x} & 0 & 0 \end{pmatrix}. \tag{2.40}$$

The solutions of the eigenvalue problem Eq. (2.37 with 2.40) are called modes and the eigenvalues β are called propagation constants. Different types of modes are associated with different eigenvalues β (see Fig. 2.3). We consider a waveguide with core refractive index n_1 and cladding refractive index n_2. Similar to the slab waveguide, guided modes propagate along the guide in the z direction. This finite number of guided modes have real propagation constants β with $kn_2 > |\beta| > kn_1$. There is a continuum of radiation modes which have real propagation constants β with $|\beta| \leq kn_2$. There is a continuum of evanescent modes with imaginary propagation constants β. There may also be solutions with general complex β. The total electric (or magnetic) field may be written as a superposition of the electric (or magnetic) fields corresponding to these modes.

It is relevant to note that the operator, $\hat{O}$, and the eigenvalues of guided modes, β, are real. Therefore, we may choose the eigenfunctions of guided modes (E_x, E_y, H_x, H_y) to be real[6]. Hence all their transversal electromagnetic field components are in phase.

2.6.2 Maxwell's equations in E_z and H_z: few unknowns

Alternatively, it is possible to formulate Maxwell's equations in terms of the longitudinal field components E_z and H_z. This formulation has only two unknown field components, and it will be used in the description of rectangular waveguides (Sec. 2.7). Solving Eqs. (2.34) and (2.35) for the transversal field components gives[7] [28]

$$E_x = \frac{-\imath}{K^2}\left(\beta\frac{\partial E_z}{\partial x} + \omega\mu_0\frac{\partial H_z}{\partial y}\right), \tag{2.41}$$

$$E_y = \frac{-\imath}{K^2}\left(\beta\frac{\partial E_z}{\partial y} - \omega\mu_0\frac{\partial H_z}{\partial x}\right), \tag{2.42}$$

$$H_x = \frac{-\imath}{K^2}\left(\beta\frac{\partial H_z}{\partial x} - \omega\epsilon_0 n_j^2\frac{\partial E_z}{\partial y}\right), \tag{2.43}$$

$$H_y = \frac{-\imath}{K^2}\left(\beta\frac{\partial H_z}{\partial y} + \omega\epsilon_0 n_j^2\frac{\partial E_z}{\partial x}\right), \tag{2.44}$$

with

$$K(x, y) = \sqrt{n(x, y)^2k^2 - \beta^2}. \tag{2.45}$$

All components, and hence in particular the longitudinal components E_z and H_z, satisfy the reduced wave equation (here given for E_z) [28]:

$$\frac{\partial^2 E_z}{\partial x^2} + \frac{\partial^2 E_z}{\partial y^2} + K^2E_z = 0. \tag{2.46}$$

This equation is found by substituting the modal electromagnetic field, Eq. (2.30), in the wave equation (2.5).

---

[6] Proof: Let a real number β be the eigenvalue of a real operator $\hat{O}$ with a corresponding complex eigenfunction $\boldsymbol{u} = \boldsymbol{u}' + \imath\boldsymbol{u}''$, with real $\boldsymbol{u}'$ and $\boldsymbol{u}''$. Then the eigenproblem $(\hat{O} - \beta)\boldsymbol{u} = \mathbf{0}$ separates into $(\hat{O} - \beta)\boldsymbol{u}' = \mathbf{0}$ and $(\hat{O} - \beta)\boldsymbol{u}'' = \mathbf{0}$. As both equations are identical, they span the same eigenspace, and we may thus choose the real eigenspace as basis.

[7] Eq. (2.41) follows from solving the y-component of Eq. (2.34) for H_y, and substituting this in the x-component of Eq. (2.35). Eq. (2.42) follows from solving the x-component of Eq. (2.34) for H_x, and substituting this in the y-component of Eq. (2.35). Eq. (2.43) follows from solving the y-component of Eq. (2.35) for E_y, and substituting this in the x-component of Eq. (2.34). Eq. (2.44) follows from solving the x-component of Eq. (2.35) for E_x, and substituting this in the y-component of Eq. (2.34).

2.6.3 Orthogonality

We will derive the orthogonality relation which modes in a waveguide obey. Consider two modes in the form of Eq. (2.30), labelled 1 and 2. First we use a vector identity[8] to find

$$\nabla \cdot (\boldsymbol{\mathcal{E}}_1 \times \boldsymbol{\mathcal{H}}_2^*) = \boldsymbol{\mathcal{H}}_2^* \cdot (\nabla \times \boldsymbol{\mathcal{E}}_1) - \boldsymbol{\mathcal{E}}_1 \cdot (\nabla \times \boldsymbol{\mathcal{H}}_2^*) \tag{2.47}$$

(* denotes the complex conjugate). Then we use Faraday's law (2.1) and Ampère's law (2.2) on the first and second terms on the right-hand-side of Eq. (2.47), respectively, to arrive at

$$\nabla \cdot (\boldsymbol{\mathcal{E}}_1 \times \boldsymbol{\mathcal{H}}_2^*) = \imath\omega(\epsilon \boldsymbol{\mathcal{E}}_1 \cdot \boldsymbol{\mathcal{E}}_2^* - \mu_0 \boldsymbol{\mathcal{H}}_1 \cdot \boldsymbol{\mathcal{H}}_2^*), \tag{2.48}$$

Now we exchange labels 1 and 2 in Eq. (2.48), take the complex conjugate, and add the result to Eq. (2.48) to obtain

$$\nabla \cdot (\boldsymbol{\mathcal{E}}_1 \times \boldsymbol{\mathcal{H}}_2^* + \boldsymbol{\mathcal{E}}_2^* \times \boldsymbol{\mathcal{H}}_1) = 0. \tag{2.49}$$

Modes 1 and 2 are waveguide modes with the form of Eq. (2.30), substituting this in Eq. (2.49) gives

$$\nabla \cdot (\boldsymbol{E}_1 \times \boldsymbol{H}_2^* + \boldsymbol{E}_2^* \times \boldsymbol{H}_1) e^{\imath(\beta_2 - \beta_1)z} = 0, \tag{2.50}$$

or, using the differentiation product rules[9],

$$\nabla \cdot (\boldsymbol{E}_1 \times \boldsymbol{H}_2^* + \boldsymbol{E}_2^* \times \boldsymbol{H}_1) + (\boldsymbol{E}_1 \times \boldsymbol{H}_2^* + \boldsymbol{E}_2^* \times \boldsymbol{H}_1) \cdot \hat{\boldsymbol{z}}\, \imath(\beta_2 - \beta_1) = 0. \tag{2.51}$$

The phase term $e^{\imath(\beta_2-\beta_1)z}$ is never zero thus was divided out this equation. We now apply a special case of the divergence theorem[10] in which we choose a plane S as a cross-section of the waveguide, i.e., an entire plane in (x,y). Integrating Eq. (2.51) over this plane, and applying the divergence theorem, gives

$$\begin{aligned} &\oint_{\partial S} (\boldsymbol{E}_1 \times \boldsymbol{H}_2^* + \boldsymbol{E}_2^* \times \boldsymbol{H}_1) \cdot \hat{\boldsymbol{n}}\, \mathrm{d}S \\ &\qquad + \iint_S (\boldsymbol{E}_1 \times \boldsymbol{H}_2^* + \boldsymbol{E}_2^* \times \boldsymbol{H}_1) \cdot \hat{\boldsymbol{z}}\, \mathrm{d}x\mathrm{d}y\, \imath(\beta_2 - \beta_1) = 0, \end{aligned} \tag{2.52}$$

with $\hat{\boldsymbol{n}}$ the unit vector in the (x,y) plane being perpendicular to the curve ∂S. The first term is a contour integral over an infinitely large curve enclosing the waveguide. This term vanishes as the fields of guided modes decay exponentially towards infinity. Equation (2.52) thus reduces to the orthogonality relation

$$\frac{1}{4} \iint_{-\infty}^{+\infty} (\boldsymbol{E}_1 \times \boldsymbol{H}_2^* + \boldsymbol{E}_2^* \times \boldsymbol{H}_1) \cdot \hat{\boldsymbol{z}}\, \mathrm{d}x\mathrm{d}y = 0, \qquad \text{or,} \qquad (\beta_2 - \beta_1) = 0. \tag{2.53}$$

[8] $\nabla \cdot (\boldsymbol{a} \times \boldsymbol{b}) = \boldsymbol{b} \cdot (\nabla \times \boldsymbol{a}) - \boldsymbol{a} \cdot (\nabla \times \boldsymbol{b})$. [68, Eq. 2.53]

[9] $\nabla \cdot (f\boldsymbol{a}) = f(\nabla \cdot \boldsymbol{a}) + \boldsymbol{a} \cdot (\nabla f)$. [68, Eq. 2.50]

[10] A special case of the divergence theorem follows by specializing it to the plane instead of a volume [40, 69]. Letting S be a region in the plane with boundary ∂S, the divergence theorem then collapses to $\iint_S \left(\frac{\partial}{\partial x}\hat{\boldsymbol{x}} + \frac{\partial}{\partial y}\hat{\boldsymbol{y}}\right) \cdot \boldsymbol{a}\, \mathrm{d}A = \oint_{\partial S} \boldsymbol{a} \cdot \hat{\boldsymbol{n}}\, \mathrm{d}S$.

For two equal modes 1 and 2, the second equation is satisfied ($\beta_1 = \beta_2$) and the first equation is not. Moreover, the left-hand-side of the first equation then represents the power carried by the mode, as will be shown in Eq. (2.60). We have proved orthogonality relation (2.53) for two guided modes but this relation holds also for orhogornality between all guided, radiative and evanescent modes [27, 29, 33].

Equation (2.53) is probably the neatest orthogonality relation, but we will proceed deriving a shorter relation. The shorter relation is often used, but forward- and backward-traveling modes are not necessarily orthogonal in the shorter relation. We proceed by showing that the two terms under the integral in Eq. (2.53) vanish separately. The permittivity $\epsilon(x, y)$ is symmetric in z, so if there is a mode propagating in the positive z-direction, then we also expect a mode propagating in the negative z-direction. In fact, if there exist a forward-traveling mode (labelled 2) $\boldsymbol{\mathcal{E}}_2$ with propagation constant β_2 and transverse fields $\boldsymbol{E}_2$ and $\boldsymbol{H}_2$, then there also exists a backward-traveling mode (labelled 3) with

$$\beta_3 = -\beta_2 \tag{2.54}$$

$$\boldsymbol{E}_3 = E_{2x}\hat{\boldsymbol{x}} + E_{2y}\hat{\boldsymbol{y}} - E_{2z}\hat{\boldsymbol{z}}, \tag{2.55}$$

$$\boldsymbol{H}_3 = -H_{2x}\hat{\boldsymbol{x}} - H_{2y}\hat{\boldsymbol{y}} + H_{2z}\hat{\boldsymbol{z}}. \tag{2.56}$$

Equation (2.56) is found by substituting Eqs. (2.54) and (2.55) in Faraday's law (2.34) and comparing the result with β_2 and $\boldsymbol{E}_2$ also substituted in Faraday's law. Equations (2.54)-(2.56) also obey Ampère's law (2.35), as can be verified by first substituting β_3 and $\boldsymbol{H}_3$ in Ampère's law, then also substituting β_2 and $\boldsymbol{H}_2$ in Ampère's law, to compare the resulting equations. The fact that the modal fields of the backwards traveling mode are different from the forward traveling modes can be explained from a physics point of view. As will be shown later, the power flow of a mode is related to $\mathrm{Re}\{(\boldsymbol{E} \times \boldsymbol{H}^*) \cdot \hat{\boldsymbol{z}}\}$. Thus the fields of a backwards traveling mode should be different from fields of a forward traveling mode because the direction of the power flow should be reversed.

Once realized that only the transversal field components (x and y) contribute to Eq. (2.53), it follows that Eq. (2.53) applied to modes 1 and 3 gives

$$\frac{1}{4}\iint (-\boldsymbol{E}_1 \times \boldsymbol{H}_2^* + \boldsymbol{E}_2^* \times \boldsymbol{H}_1) \cdot \hat{\boldsymbol{z}}\, \mathrm{d}x\mathrm{d}y = 0, \qquad \text{or,} \qquad (\beta_2 + \beta_1) = 0. \tag{2.57}$$

Subtracting Eq. (2.53) from Eq. (2.57) shows that [27, 29]

$$\frac{1}{2}\iint (\boldsymbol{E}_1 \times \boldsymbol{H}_2^*) \cdot \hat{\boldsymbol{z}}\, \mathrm{d}x\mathrm{d}y = 0, \qquad \text{for} \qquad |\beta_2| \neq |\beta_1|. \tag{2.58}$$

Note that the orthogonality in Eq. (2.58) does not apply to a forward propagating mode and its backwards propagating counterpart as their propagation constants β are equal in magnitude.

2.6.4 Power flow

The energy flux density (energy per unit area per unit time) is given by the Pointing vector [40]

$$\boldsymbol{S} = \mathrm{Re}\{\boldsymbol{\mathcal{E}}\} \times \mathrm{Re}\{\boldsymbol{\mathcal{H}}\}, \tag{2.59}$$

which is defined in terms of the physical (real) electromagnetic fields. The Pointing vector of a waveguide mode is found by inserting Eq. (2.30) in Eq. (2.59) and using $\mathrm{Re}\{\boldsymbol{\mathcal{E}}\} = \frac{1}{2}(\boldsymbol{\mathcal{E}} + \boldsymbol{\mathcal{E}}^*)$ to arrive at

$$\boldsymbol{S} = \frac{1}{4}\Big((\boldsymbol{\mathcal{E}} \times \boldsymbol{\mathcal{H}}^*) + (\boldsymbol{\mathcal{E}}^* \times \boldsymbol{\mathcal{H}}) + (\boldsymbol{\mathcal{E}} \times \boldsymbol{\mathcal{H}})e^{\imath 2(\omega t - \beta z)} + (\boldsymbol{\mathcal{E}}^* \times \boldsymbol{\mathcal{H}}^*)e^{\imath 2(\beta z - \omega t)}\Big) .$$

The last two terms on the right-hand-side of this equation vanish when averaging over time. The time-averaged power P carried by the mode is found by integrating the time-averaged Pointing vector S over an infinite cross-section of the waveguide (i.e., a x,y-plane) [27, 28]

$$P = \frac{1}{4}\iint (\boldsymbol{E} \times \boldsymbol{H}^* + \boldsymbol{E}^* \times \boldsymbol{H}) \cdot \hat{\boldsymbol{z}}\, \mathrm{d}x\mathrm{d}y. \tag{2.60}$$

For guided modes, the transversal components of the electromagnetic fields are in phase, so that both terms under the integral of Eq. (2.60) are real and

$$P = \frac{1}{2}\iint (\boldsymbol{E} \times \boldsymbol{H}^*) \cdot \hat{\boldsymbol{z}}\, \mathrm{d}x\mathrm{d}y. \tag{2.61}$$

2.6.5 Mode expansion, normalization and *bra-ket* notation

The electric and magnetic fields in a waveguide may be expressed as a superposition of the modes of the waveguide. These modes are solutions of Maxwell's equations formulated as eigenvalue problem with operator $\hat{O}$, see Eq. (2.37 with 2.40). The eigenvalues of this operator are the propagation constants β and the eigenfunctions are the transverse components of the corresponding modal electromagnetic fields. Expressing the total electric field in a waveguide with core refractive index n_1 and cladding refractive index n_2 as a superposition of its modes gives

$$\begin{aligned}\boldsymbol{\mathcal{E}}(x,y,z,t) = &\underbrace{\sum_{i=0}^{N-1} a_i \boldsymbol{E}_i(x,y)e^{\imath(\omega t - \beta_i z)}}_{\text{guided}} + \underbrace{\int_{-kn_2}^{+kn_2} b(\beta)\boldsymbol{E}(\beta;x,y)e^{\imath(\omega t - \beta z)}\mathrm{d}\beta}_{\text{radiation}} \\ &+ \underbrace{\int_{-\imath\infty}^{+\imath\infty} c(\beta)\boldsymbol{E}(\beta;x,y)e^{\imath(\omega t - \beta z)}\mathrm{d}\beta}_{\text{evanescent}} \quad + \underbrace{\quad \dots \quad}_{\substack{\text{general}\\ \text{complex } \beta}} ,\end{aligned} \tag{2.62}$$

with a_i, $b(\beta)$ and $c(\beta)$ the complex amplitudes of the guided, radiation and evanescent modes, respectively, $\boldsymbol{E}$ the electric fields corresponding to the modes, and N the number of guided modes (see Fig. 2.3 on page 21). A similar expression holds for the magnetic field $\boldsymbol{\mathcal{H}}$. We introduce a short-hand notation of Eq. (2.62) by writing the second, third and fourth terms as a summation. The modal amplitudes a_i, $b(\beta)$ and $c(\beta)$, as well as the modal amplitudes of the solutions with complex β, are lumped together in a_i with infinite i. This gives

$$\boldsymbol{\mathcal{E}}(x,y,z,t) = \sum_{i=0}^{\infty} a_i \boldsymbol{E}_i(x,y)e^{\imath(\omega t - \beta_i z)}, \tag{2.63}$$

with the summation running over all modes including discrete and continuum modes. The magnetic field $\boldsymbol{\mathcal{H}}$ may be expressed in a similar expression. In this thesis, we normalize the guided waves such that they carry unit power in the positive or negative z-direction, i.e., $P = \pm 1$ in Eq. (2.60). There was no need to normalize the radiation and evanescent modes (this is not straightforward as evanescent modes carry no power in the z-direction).

A *bra-ket* notation is adopted for later use (Secs. 2.7.4 and 2.10.3). In *bra-ket* notation, transverse electromagnetic fields of a mode with label i are denoted $|i\rangle$. The operator $\hat{O}$ is not symmetric, however solutions of Eq. (2.37) are orthogonal with respect to the bilinear form derived from the power flux, Eq. (2.53). In *bra-ket* notation, Eqs. (2.37) and (2.53) read

$$\hat{O}|i\rangle = \beta_i|i\rangle, \tag{2.64}$$

$$\langle i|j\rangle \equiv \frac{1}{4}\iint_{-\infty}^{\infty} \left(\boldsymbol{E}_i \times \boldsymbol{H}_j^* + \boldsymbol{E}_j^* \times \boldsymbol{H}_i\right) \cdot \hat{\boldsymbol{z}} \,\mathrm{d}x\mathrm{d}y, \tag{2.65}$$

respectively, defining the scalar product between two solutions i and j. The guided modes are normalized such that they carry unit power, so that

$$\langle i|j\rangle = \frac{\beta_i}{|\beta_i|}\,\delta_{ij} \qquad \text{(guided modes).} \tag{2.66}$$

2.6.6 Waveguides with losses and bends

So far, we have discussed ideal waveguides, composed of lossless materials, without the slightest variation of the refractive index profile in the z-direction, and with infinite cladding. However, real waveguides are never perfect and also include bends to, for example, form a ring resonator. This section describes these phenomena in a less formal manner than the previous sections. Rigorously including all loss mechanisms leads a complication which is unnecessary for the scope of this work, and calculations are often impossible due to limited knowledge about the precise material and structural properties of the waveguides. Roughness of the side-walls of the waveguide and bends in waveguides break the assumption of z-invariance of the permittivity profile $\epsilon(x, y)$ on which the rigorous formalism is based.

Waveguide propagation loss

We include a propagation loss α_p in our description of modes in waveguides, and modify Eq. (2.30) to

$$\boldsymbol{\mathcal{E}} = e^{-\alpha_p z}\boldsymbol{E}(x, y)e^{\imath(\omega t-\beta z)}, \quad \boldsymbol{\mathcal{H}} = e^{-\alpha_p z}\boldsymbol{H}(x, y)e^{\imath(\omega t-\beta z)}. \tag{2.67}$$

This equation does not rigorously conform the mathematical framework of this section. We have assumed no absorption (already in Maxwell's equations, Sec. 2.4) and invariance of the refractive index in the z-direction, giving Eq. (2.30). Real waveguides are not perfectly invariant in the z-direction as the side-walls contain nanometer-scale roughness, the material contains nanometer-scale defects,

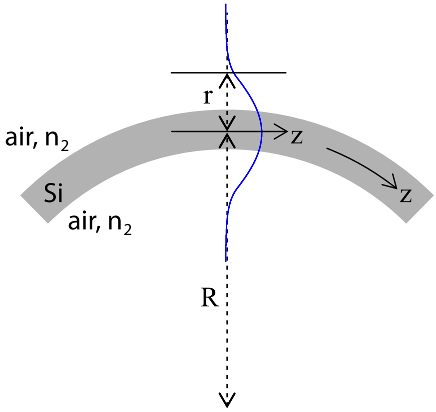

Figure 2.4: Sketch of a bent waveguide with radiation loss, top-view.

the waveguides have width variations over a millimeter length-scale, etc. This leads to coupling of the guided mode to other modes. Moreover, the materials and material interfaces of real waveguides absorb electromagnetic energy. These effects are lumped together in the propagation loss α_p. The term $\exp[-\alpha_p z]$ can be interpreted as modal amplitude, and the theories in this section remain a good approximation when this amplitude varies slow compared to the other variations of the electromagnetic fields.

Waveguide bends

For waveguide bends with radii R much larger than the width of the waveguide, it is reasonable to approximate the modes in the bend as the modes of a straight waveguide. We will illustrate that radiation loss in waveguide bends is lower when the bending radius is larger and the when refractive index contrast is higher. We assume that the phase front of a mode in a bent waveguide has an angular velocity Ω and that the velocity v_z of the light at a distance r' from the center of the waveguide reads

$$v_z = (R + r')\Omega, \tag{2.68}$$

see Fig. 2.4. We approximate the phase velocity of in the center of the waveguide by the phase velocity of the mode in a straight waveguide, i.e., $v_z = \omega/\beta$ for $r' = 0$. The phase front of a mode in a bent waveguide thus has angular velocity

$$\Omega = \frac{\omega}{\beta R}. \tag{2.69}$$

Around the waveguide, the velocity of the light, v_z, is similar, because the width of the waveguide is much smaller than the bending radius. However, this velocity increases with increasing distance from the center of the guide. At a certain distance r from the center of the waveguide, the required velocity is higher than the speed of light supported by the medium (c/n_2), leading to radiation. We find this distance r by solving $v_z = c/n_2$, Eq. (2.68) and Eq. (2.69) for r, and find

$$r = R\left(\frac{\beta - n_2 k}{n_2 k}\right). \tag{2.70}$$

The strength of the radiation scales with the amount of the modal electromagnetic field that is located further than the distance r from the center of the waveguide. Large bending radius R implies a large r, thus lower radiation loss. High index contrast waveguides have modes that are strongly confined around the waveguide and smaller field values at distances larger than r. Moreover, the difference between β and kn_2 is generally large for lower order modes in high-index-contrast waveguides. Therefore sharp bends in silicon waveguide have in general lower radiation loss than waveguides of the same geometry with lower index contrast.

2.7 Rectangular silicon waveguides: Extension of Marcatili's approach

Marcatili's famous approximate analytical description of light propagation through rectangular dielectric waveguides, which was published in 1969, gives accurate results for low-index-contrast waveguides [30]. However, silicon-on-insulator waveguides have a very high-index-contrast. In this section, we extend Marcatili's model to the regime of high-index-contrast waveguides by adjusting the amplitudes of the components of the electromagnetic fields [70, 71]. Our improved method gives the modal fields of SOI waveguides that are much closer to the solutions obtained by rigorous numerical computations than Marcatili's original approximation. The goal of this section is to clearly explain this method while the reader is referred to Ref. [70] for more details such as an extensive comparison with the literature. Aalto [72] derived an empirical relation for single mode operation of rectangular silicon waveguides was extracted from rigorous numerical simulations. Although numerical mode-solvers are available, we believe that an analytical model is useful in order to gain insight in the physics of the devices, and also for fast explorative simulations of photonic-integrated circuitry [73].

We will compare the approximate analytical approaches presented in this section with results obtained using a rigorous numerical mode solver (FMM method, see Sec. 2.8 for details). Typical silicon-on-insulator waveguides with air cladding are studied, with waveguide heights of 220 nm and 300 nm. The first height is often used because it only supports TE-like modes, whereas the second height supports both TE-like and TM-like modes.

This section starts with an *Ansatz* for the form of the modes followed by the resulting boundary conditions (Secs. 2.7.1 and 2.7.2). Then it proposes approximate solutions (Sec. 2.7.3). Last, it discusses apparent degeneracy of "TE-like" and "TM-like" modes (Sec. 2.7.4).

We have published a Matlab implementation of the methods presented in this section as a free and open-source software package entitled *RECTWG* [74].

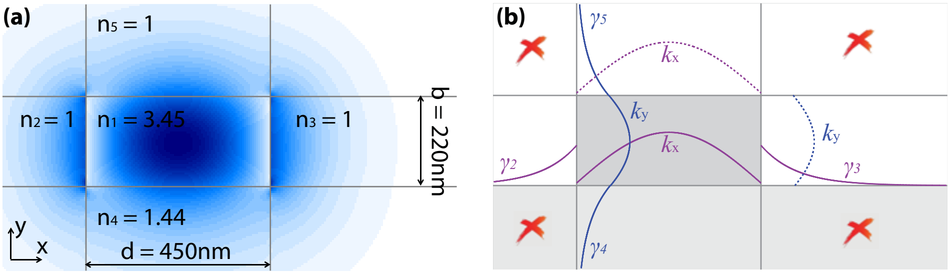

Figure 2.5: Cross-section of a SOI waveguide. **(a)** Waveguide definition. Sketch of the E_x component of the fundamental mode in color. (Dark blue represents a large field, white represents zero field.) **(b)** Outline of the approximate analytical method.

2.7.1 *Ansatz* for the shape of the field

Figure 2.5 shows a typical SOI waveguide, whose core has a higher refractive index (n_1) than its surroundings ($n_2 - n_5$). In this section, we make an *Ansatz* for the shape of the modal electromagnetic fields, inspired by the assumptions that fundamental modes have most of their energy in the center of the waveguide (such as in Fig. 2.5a), and that modes are either "TE-like" or "TM-like". For "TE-like" modes, the electric field is predominantly tangential to the upper surface of the waveguide, whereas "TM-like" modes have the electric field predominantly normal to the upper surface of the waveguide. In our analysis, we choose our coordinate frame such that E_x is the dominant electric field component. Consequently, H_y is the dominant magnetic field component of such modes. In Fig. 2.5, the width of the waveguide, d, is larger than its height b, and the mode is "TE-like" as E_x is parallel to the upper surface of the waveguide. However, in our analysis, there are no restrictions on the values of d, b, and n_1-n_5, so that the analysis equally describes a "TM-like" mode when n_2 is said to be the substrate, b the width, and d the height of the waveguide (thus $b > d$).

As derived in Sec. 2.6.2, Maxwell's equations may be formulated in terms of the longitudinal field components (E_z and H_z) only. For permittivity profiles that are invariant in the z-direction, the transverse components follow from Eqs. (2.41-2.44).

Following Marcatili's original approach, we use the following *Ansatz* for the fields of the modes. The dominant field components, $E_x(x, y)$, and $H_y(x, y)$, are proportional to $\cos[k_x(x + \xi)] \cos[k_y(y + \eta)]$, with maximum field in the center. Furthermore, outside the core, the fields decay exponentially, while the transverse profile of the field is identical to that in the core (Figs. 2.5b and 2.6a). Finally, the fields in the outer quadrants are neglected because they are small in these regions. Fig. 2.6b presents the *Ansatz* for the full field, expressed in its longitudinal components (E_z and H_z). We choose to obey Maxwell's equations in all regions 1-5, and

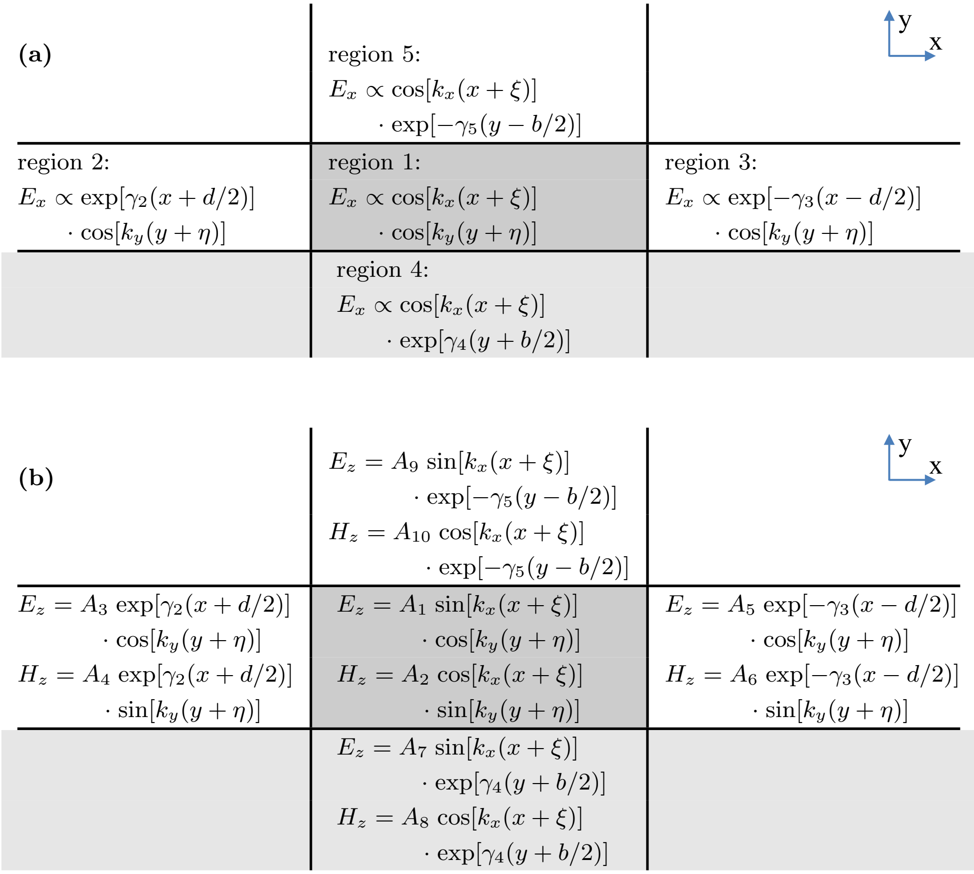

Figure 2.6: (a) Shape of the dominant electromagnetic field components E_x and H_y. **(b)** *Ansatz* describing the modal electromagnetic field in terms of E_z and H_z. The gray background color sketches the waveguide such that the mode is a "TE-like" mode.

express β, and γ_2 - γ_5 in terms of k_x and k_y employing the wave equation (2.46)

$$\beta = \sqrt{n_1^2 k^2 - k_x^2 - k_y^2}, \tag{2.71}$$

$$\gamma_2 = \sqrt{(n_1^2 - n_2^2)k^2 - k_x^2}, \quad \gamma_3 = \sqrt{(n_1^2 - n_3^2)k^2 - k_x^2}, \tag{2.72}$$

$$\gamma_4 = \sqrt{(n_1^2 - n_4^2)k^2 - k_y^2}, \quad \gamma_5 = \sqrt{(n_1^2 - n_5^2)k^2 - k_y^2}. \tag{2.73}$$

Equations (2.72) and (2.73) are identical to Eqs. (2.22) and (2.11). The errors of the approximation manifest themselves at the interfaces between the core and the cladding of the waveguide. Field amplitude A_1 is employed to normalize the mode to a power flux of unity. The remaining free parameters that still have to be determined are A_2 - A_{10}, ξ, η, k_x and k_y (thirteen in total, also see Fig. 2.6b).

2.7.2 Boundary conditions

At interfaces between the core and the cladding of the waveguide, continuity of the electromagnetic field components tangential to these interfaces is required, adding up to $4 \times 4 = 16$ electromagnetic boundary conditions. With these conditions satisfied, the normal components automatically obey Maxwell's equations.

We derive the requirements that follow from continuity of the fields at the two horizontal interfaces, to which the dominant electric field E_x is tangential. The field components E_x, H_x, E_z and H_z are tangential to these interfaces. From the four boundary conditions, we find

$$A_2 = \frac{\beta k_y}{\omega \mu_0 k_x} A_1, \tag{2.74}$$
$$A_7 = A_1 \cos[k_y(\eta - b/2)], \tag{2.75}$$
$$A_8 = A_2 \sin[k_y(\eta - b/2)], \tag{2.76}$$
$$A_9 = A_1 \cos[k_y(\eta + b/2)], \tag{2.77}$$
$$A_{10} = A_2 \sin[k_y(\eta + b/2)], \tag{2.78}$$

together with

$$\tan[k_y(\eta - b/2)] = -\gamma_4/k_y, \tag{2.79}$$
$$\tan[k_y(\eta + b/2)] = \gamma_5/k_y. \tag{2.80}$$

Equations (2.75)-(2.78) follow from the continuity of E_z and H_z. Continuity of E_x and H_x is most easily verified by substituting Eqs. (2.74)-(2.80) into the four boundary conditions corresponding to these field components at the two interfaces. It follows from Eq. (2.42) that with these field amplitudes A_2, A_7 - A_{10}, the electric field component E_y is zero in regions 1, 4 and 5. The last two equations, (2.79) and (2.80) can be recognized as the eigenvalue equations for a TE mode in a slab waveguide, namely (2.14) and (2.16), respectively. These eigenvalue equations thus do not only hold for a slab solution where $\partial/\partial x = 0$ and E_x, H_y and H_z are the non-zero field components, but also for our *Ansatz* where there is a variation in the x-direction. This observation agrees with the limit that the width of the waveguide goes to infinity $d \to \infty$, as the waveguide then becomes a slab waveguide. Eliminating η from the latter two equations gives the functional F in Eq. (2.17).

The dominant magnetic field component, H_y, is tangential to the vertical interfaces, and so are E_y, E_z and H_z. From the four boundary conditions at the two vertical interfaces, we find

$$A_2 = \frac{\omega \epsilon_0 n_1^2 k_y}{\beta k_x} A_1, \tag{2.81}$$
$$A_3 = A_1 \sin[k_x(\xi - d/2)], \tag{2.82}$$
$$A_4 = A_2 \cos[k_x(\xi - d/2)], \tag{2.83}$$
$$A_5 = A_1 \sin[k_x(\xi + d/2)], \tag{2.84}$$
$$A_6 = A_2 \cos[k_x(\xi + d/2)], \tag{2.85}$$

together with

$$\tan[k_x(\xi - d/2)] = -\frac{n_1^2}{n_2^2}\frac{\gamma_2}{k_x}, \tag{2.86}$$

$$\tan[k_x(\xi + d/2)] = \frac{n_1^2}{n_3^2}\frac{\gamma_3}{k_x}. \tag{2.87}$$

Equations (2.82)-(2.85) follow directly from the continuity of E_z and H_z. The continuity of E_y and H_y is most easily verified by substituting Eqs. (2.81)-(2.87) into the remaining electromagnetic boundary conditions. With these field amplitudes A_2 - A_6, the magnetic field component H_x is zero in regions 1, 2 and 3, as follows from Eq. (2.43). The last two equations, (2.86) and (2.87), may be recognized as the eigenvalue equations of a TM mode in a slab waveguide, despite the fact that our *Ansatz* does have variation in the y-direction.

It can be seen that the horizontal and the vertical interfaces require a different ratio A_2/A_1, i.e. a different H_z/E_z in the core. Thus the *Ansatz* has no solutions that exactly obey the boundary conditions at all interfaces simultaneously. In what follows, the 13 free parameters are chosen such that the error in the 16 boundary conditions is minimal.

2.7.3 Approximate methods

This section presents three approximate methods for rectangular waveguides, based on the previous *Ansatz*. All three methods share the same equations for the computation of the propagation constant β, but the amplitudes A_2 - A_{10} of the modal fields are computed differently. The methods for computation of the fields are based on (1) the assumption of low-index-contrast, (2) continuity of the dominant electric and magnetic field components, and (3) minimization of the discontinuity of the electromagnetic fields. The first method is Marcatili's original approach [30]. The last two methods were derived in our analysis of SOI waveguides [70].

Propagation constant β and spatial frequencies k_x, k_y

We argue that the dominant boundary conditions for determining k_y and η are at the horizontal interfaces, while the vertical interfaces influence k_x and ξ more strongly. Therefore we compute k_x from Eq. (2.29), k_y from Eq. (2.17), and β from Eq. (2.71). In Fig. 2.7a,c we compare our approximate analytical calculation with a rigorous numerical calculation and find that the effective index, $n_{\text{eff}} = \beta/k$, is accurately found within 2% for typical waveguides.

Fields (1): Marcatili's approach for low-index-contrast waveguides

Marcatili has developed a widely used analytical approach for low-index-contrast waveguides in which all refractive indices n_j have similar values [28,30]. For propagating modes in these guides, $kn_j \approx \beta$ because modes are not guided otherwise, so $k_x, k_y << kn_j$. Choosing $E_y = 0$ gives a modal field profile that is continuous

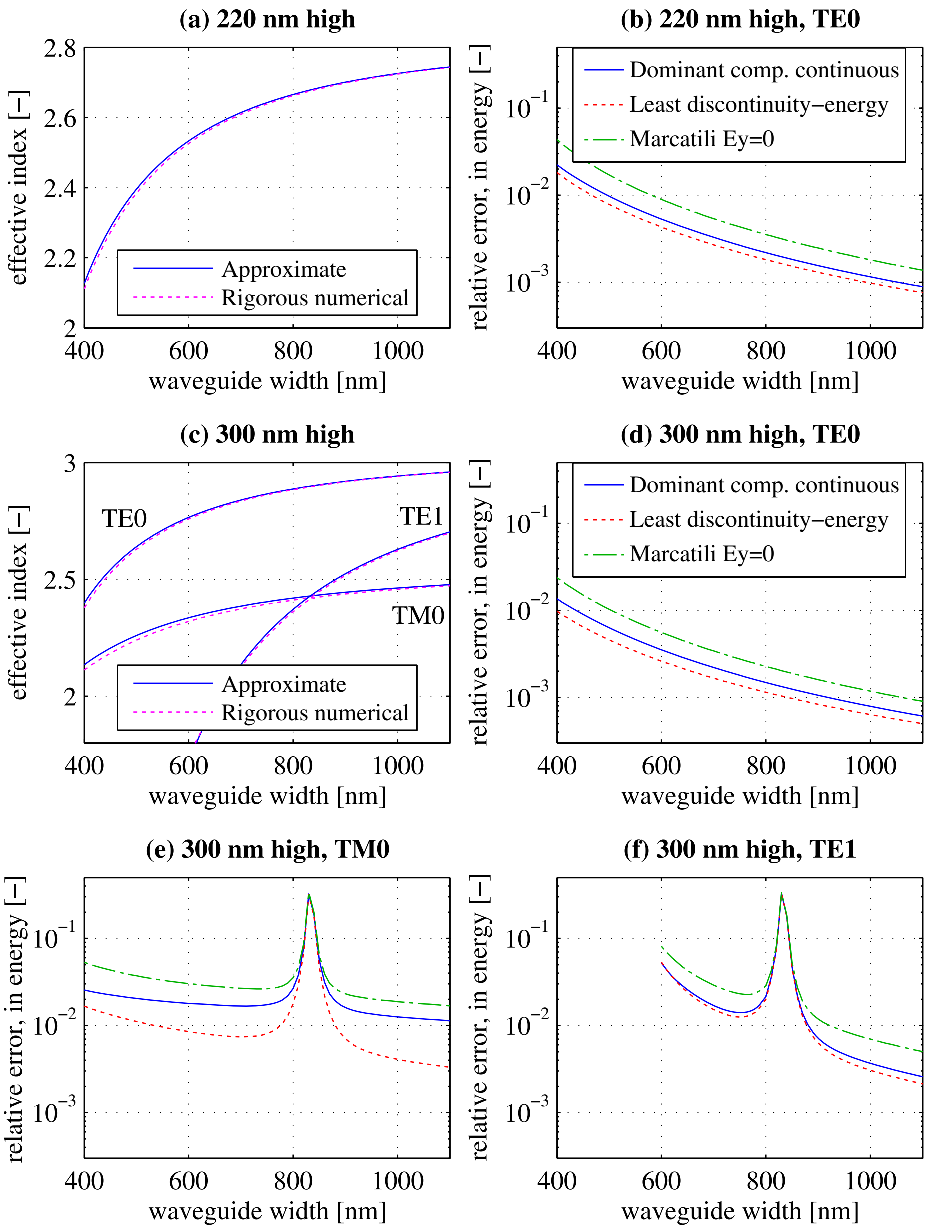

Figure 2.7: Approximate analytical model compared with rigorous mode solver (FMM method). Typical rectangular silicon-on-insulator waveguides with air cladding. **(a,b)** 220 nm high, fundamental mode. **(c-f)** 300 nm high, first 3 modes: TE0, TM0, TE1. We omitted one zero from conventional notation (e.g., TE_{00}), because our waveguides have higher-order standing waves only in the direction of the width of the waveguide. **(a,c)** Effective index. **(b,d,e,f)** Energy in the difference field between the two approximate methods and the rigorously computed field, normalized to the energy in the rigorously computed field, i.e., Eq. (2.93).

on the horizontal interfaces, while it obeys the conditions on the vertical interfaces when neglecting terms on the order of $(k_x/kn_j)^2$. However, for high-index-contrast guides, these terms can be even larger than one.

Fields (2): continuity of dominant electromagnetic field components

This method demands continuity of dominant electromagnetic field components (E_x, H_y) across all interfaces that they are tangential to. In this section, we consider the mode to be "TE-like", such as the mode depicted in Fig. 2.5. For "TM-like" modes in wide waveguides, a similar method can be derived (see our work in Ref. [70]). As typical waveguides are larger in width than in height, the height gives the strongest confinement, therefore we chose to match all boundary conditions at the horizontal interfaces. This choice is supported by the argument that the vertical sides are irrelevant for an infinitely wide waveguide. With these requirements (including k_y and k_x obtained from the slab eigenvalue equations), only one amplitude parameter is left free, although we have not yet matched E_y, E_z and H_z on the vertical interfaces. Of these field components we chose to match E_z because H_z goes to zero for infinitely wide ($b \to \infty$) waveguides and E_y is a weak field component which is largest at the corners of the waveguide. With these requirements, the free parameters in the *Ansatz* are fully determined. Parameters k_x, k_y, ξ and η are given by the slab eigenvalue equations (2.29) and (2.17). The amplitudes of the field components, A_2-A_{10}, are given by Eqs. (2.74)-(2.78), together with

$$A_3 = A_1 \sin[k_x(\xi - d/2)], \tag{2.88}$$

$$A_4 = A_2 \left(1 + \frac{k^2(n_1^2 - n_2^2)}{\beta^2}\right) \cos[k_x(\xi - d/2)], \tag{2.89}$$

$$A_5 = A_1 \sin[k_x(\xi + d/2)], \tag{2.90}$$

$$A_6 = A_2 \left(1 + \frac{k^2(n_1^2 - n_3^2)}{\beta^2}\right) \cos[k_x(\xi + d/2)]. \tag{2.91}$$

This method was first presented in Ref. [70] as *Improved* $E_y \approx 0$ *method*, because E_y is zero in regions 1, 4 and 5.

Fields (3): least-discontinuity optimization of the Ansatz parameters

We presented an *Ansatz* for the form of the electromagnetic field of modes in a rectangular waveguide. This *Ansatz* was chosen such that Maxwell's equations are satisfied in regions 1-5, so that all errors manifest themselves at the four interfaces between the waveguide core and the cladding regions. The method we propose is to minimize this error, by minimizing the discontinuity of the tangential electromagnetic field components at the interfaces. The measure we adopt to quantify this error is the average energy density that is associated with these discontinuities, defined by:

$$U_{\mathrm{mm}} = \frac{\epsilon_0}{4l} \oint (n^+ + n^-)^2 \cdot \left|\hat{\boldsymbol{\nu}} \times \left(\boldsymbol{E}^+ - \boldsymbol{E}^-\right)\right|^2 dl + \frac{\mu_0}{l} \oint \left|\hat{\boldsymbol{\nu}} \times \left(\boldsymbol{H}^+ - \boldsymbol{H}^-\right)\right|^2 dl. \tag{2.92}$$

The four interfaces of the waveguide are simultaneously described by the integral. The line integral runs along the entire circumference of the waveguide in the (x,y)-plane, and $l = 2(b + d)$ is the length of this circumference. $\boldsymbol{E}^+$ and $\boldsymbol{E}^-$ are the electric fields just outside and inside the waveguide core region 1, so that $(\boldsymbol{E}^+ - \boldsymbol{E}^-)$ represents the discontinuity of this field, and $\hat{\boldsymbol{\nu}}$ is a unit vector orthogonal to the waveguide surface. The cross product of $\hat{\boldsymbol{\nu}}$ with the discontinuity in the field just selects the tangential components. n^+ and n^- are the refractive indices just outside and inside the waveguide. At the interface, an average refractive index $(n^+ + n^-)/2$ is assumed to calculate the energy density of the electric field components. Although U_{mm} can be intuitively interpreted as an energy density, we cannot attach a rigorous physical meaning to this quantity. The discontinuity of the fields only occurs at interfaces, which have no physical volume. Therefore the energy density cannot be integrated over volume in order to obtain a total energy.

We determined the minimum U_{mm} numerically using an unconstrained nonlinear optimization as implemented in MATLAB. As initial estimate we use the modal amplitudes as computed using the previously described *Improved* $E_y \approx 0$ *method*. However, Eq. (2.92) is quadratic in the amplitudes A_2-A_{10} and the minimum can thus be found analytically. This method was first presented in Ref. [70] as *amplitude optimization method*, because the amplitudes A_2 - A_{10} are optimized.

Comparison

We have presented one approximate method to compute the propagation constant, or effective index, of the modes in rectangular waveguides. Given this propagation constant, we presented three different methods that approximate the field of these modes: (1) Marcatili's original approach, (2) a method based on continuity of the dominant electromagnetic field components, and (3) a method based on minimization of the discontinuities of the electromagnetic fields.

In Fig. 2.7b and Fig. 2.7d-f, we compare modal fields computed with the approximate methods with the fields computed with a rigorous numerical mode solver. The measure that is used to compare two electromagnetic fields is the relative energy of the difference of the fields, i.e.

$$\Delta U = \frac{\iint\limits_{\text{regions 1-5}} \left(n^2\epsilon_0|\boldsymbol{E}^A - \boldsymbol{E}^N|^2 + \mu_0|\boldsymbol{H}^A - \boldsymbol{H}^N|^2\right) \mathrm{d}x\mathrm{d}y}{\iint\limits_{\text{regions 1-5}} \left(n^2\epsilon_0|\boldsymbol{E}^N|^2 + \mu_0|\boldsymbol{H}^N|^2\right) \mathrm{d}x\mathrm{d}y} \tag{2.93}$$

where $\boldsymbol{E}^A$ and $\boldsymbol{E}^N$ are the analytically and rigorous numerically calculated fields, respectively. This integral runs over all regions that are described by the analytical solution.

It is clear that something interesting happens for waveguides with dimensions around 833 nm width by 300 nm height. This is at the point of the apparent crossing of the propagation constants of the TM0 and TE1 modes (see Fig. 2.7c), and this case is addressed in the next section. Apart from this special case, the relative errors of the method with continuity of the dominant field components is below 3%, and the relative error of the method in which the energy associated with the discontinues is minimized is even lower. Both method outperform Marcatili's original approach for these typical SOI waveguides with high index contrast. The *amplitude optimization method*, which minimizes the energy associated with the discontinuities, has the advantage that it is works for both "TE-like" and "TM-like" modes.

2.7.4 Avoided crossing of modes with similar propagation constants

Figure 2.7e,f on page 33 suggest that something interesting happens at the apparent crossing of the effective indices of the TM0-like and the TE1-like modes when the width of the guide is changed. A detailed inspection of the waveguides with widths around 833 nm is presented in Fig. 2.8. In Fig. 2.8a, it can be seen that the numerically computed effective indices of the 2nd and 3rd mode in the waveguide (counted from high to low effective index) actually do not cross each other, but show a behavior that is known in quantum mechanics as *avoided crossing* [75]. We investigate the modes that where found numerically in terms of the analytically computed approximate modes.

We denote the actual, rigorous numerically computed, modes as $\boldsymbol{E}_i^{\mathrm{N}}$ with i the number of the mode. We will verify that the actual modes $\boldsymbol{E}_2^{\mathrm{N}}$ and $\boldsymbol{E}_3^{\mathrm{N}}$ can in good approximation be written as a superposition of the approximate TM0-like, $\boldsymbol{E}_{\mathrm{TM0}}$, and TE1-like, $\boldsymbol{E}_{\mathrm{TE1}}$ modes. The TM0-like and TE1-like modes were calculated using the approximate *amplitude optimization method*. Thus

$$\boldsymbol{E}_i^{\mathrm{N}} \approx a\boldsymbol{E}_{\mathrm{TM0}} + b\boldsymbol{E}_{\mathrm{TE1}}, \tag{2.94}$$

for some real a and b, and $i = 2$ or 3. The phase of mode $\boldsymbol{E}_i$ is chosen such that coefficient b is positive. The coefficient a of the TM0-like mode can be either positive or negative. The approximate calculated modes $\boldsymbol{E}_{\mathrm{TM0}}$ and $\boldsymbol{E}_{\mathrm{TE1}}$, are in good approximation orthonormal such that normalization of the guided modes $\boldsymbol{E}_i$ in the norm of Eq. (2.66) implies $b = \sqrt{1-a^2}$.

The coefficient a of the TM0-like mode is optimized such that the difference measured using Eq. (2.93) between the left- and right-hand sides of Eq. (2.94) is minimum. The result is plotted in Fig. 2.8b, where it can be seen that mode 2 looks like a TM0-mode at the left of the crossing, while it looks like a TE1-like mode on the right-hand-side of the crossing, whereas close to the crossing the modes are an equal mixture of $\boldsymbol{E}_{\mathrm{TM0}}$ and $\boldsymbol{E}_{\mathrm{TE1}}$. In Fig. 2.8c, it can be seen that the error between the superposition $\boldsymbol{E}_i$ and the rigorous numerically calculated field $\boldsymbol{E}_i^{\mathrm{N}}$ close to the apparent crossing is small and similar to the error that was found away from the crossing (see Fig. 2.7e,f). Therefore we may indeed conclude that the field around the crossing can be written as a superposition of modes of the types that are present away from the crossing. Figure 2.9 presents the electric fields $\boldsymbol{E}_{\mathrm{TM0}}$, $\boldsymbol{E}_{\mathrm{TE1}}$, $\boldsymbol{E}_2^{\mathrm{N}}$ and $\boldsymbol{E}_3^{\mathrm{N}}$ for a 833 nm wide by 300 nm high waveguide, where $a^2 \approx b^2 \approx 0.5$.

Using this observation, we will derive a qualitative description of this *avoided crossing*. We consider forward propagating guided modes with positive β_i. The

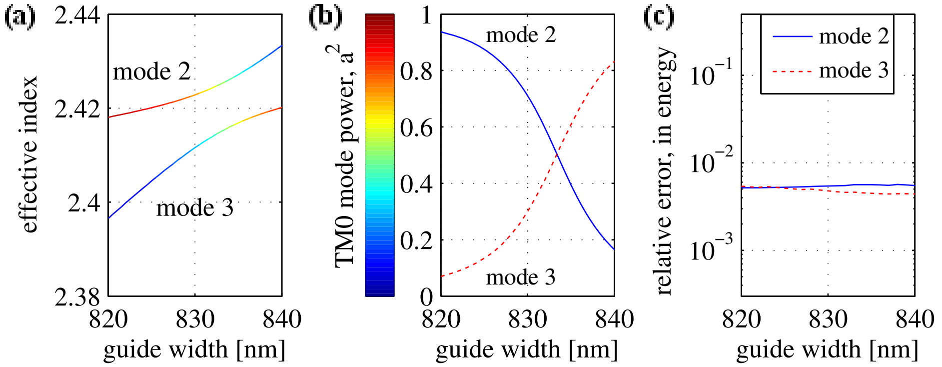

Figure 2.8: Investigation of the avoided crossing of effective indices of two modes. **(a)** Numerically calculated effective indices of the 2nd and 3rd mode, zoom-in of Fig. 2.7c. **(b)** Power in the TM0-like mode when the fields of the modes in plot (a) are written as a superposition of a TM0-like and a TM1-like mode. The curves in plot (a) are color-coded accordingly. **(c)** Relative energy in the electromagnetic difference field between the superposition and the rigorous numerically calculated fields, to be compared with Fig 2.7 (e) and (f).

guided modes modes are normalized such that they carry unit power. We employ the eigenvalue-problem formulation of Maxwell's equations for waveguides (Sec. 2.6.1) and we use the *bra-ket* notation (Sec. 2.6.5). We formulated Maxwell's equations as an eigenvalue problem, $\hat{O}|i\rangle = \beta_i|i\rangle$, with the propagation constant β_i as eigenvalue. The operator $\hat{O}$ is not symmetric. However, forward-propagating guided modes are orthonormal with respect to the scalar product given by Eq (2.65), i.e., $\langle i|j\rangle = \delta_{ij}$. We now apply the aforementioned observation that, in good approximation, the electromagnetic fields of the modes in the waveguide, also around the crossing, can be written as a superposition of the approximate fields. Hence

$$\boldsymbol{E_i} \approx a\boldsymbol{E}_{\text{TM0}} + b\boldsymbol{E}_{\text{TE1}}, \quad \text{or} \quad |i\rangle \approx a|a\rangle + b|b\rangle, \tag{2.95}$$

where $|a\rangle$ and $|b\rangle$ represent the TM0-like and TE1-like modes in the waveguide, respectively, while $|i\rangle$ represents the exact solutions of Eq. (2.64). We only consider the 2nd and 3rd approximate solutions here. As will become clear, only modes with similar propagation constants have to be taken into account around the crossing. The other modes are already accurately calculated by the approximate methods presented in Sec. 2.7.3. Substituting Eq. (2.95) in Eq. (2.64) and taking the inner product with $\langle a|$ gives

$$a\langle a|\hat{O}a\rangle + b\langle a|\hat{O}b\rangle \approx \beta_i \left(a\langle a|a\rangle + b\langle a|b\rangle\right). \tag{2.96}$$

If we also take the inner product of Eq. (2.64) with $\langle b|$ we arrive at the (2x2)-system:

$$\begin{pmatrix} \langle a|\hat{O}a\rangle & \langle a|\hat{O}b\rangle \\ \langle b|\hat{O}a\rangle & \langle b|\hat{O}b\rangle \end{pmatrix} \begin{pmatrix} a \\ b \end{pmatrix} \approx \beta_i \begin{pmatrix} \langle a|a\rangle & \langle a|b\rangle \\ \langle b|a\rangle & \langle b|b\rangle \end{pmatrix} \begin{pmatrix} a \\ b \end{pmatrix}, \tag{2.97}$$

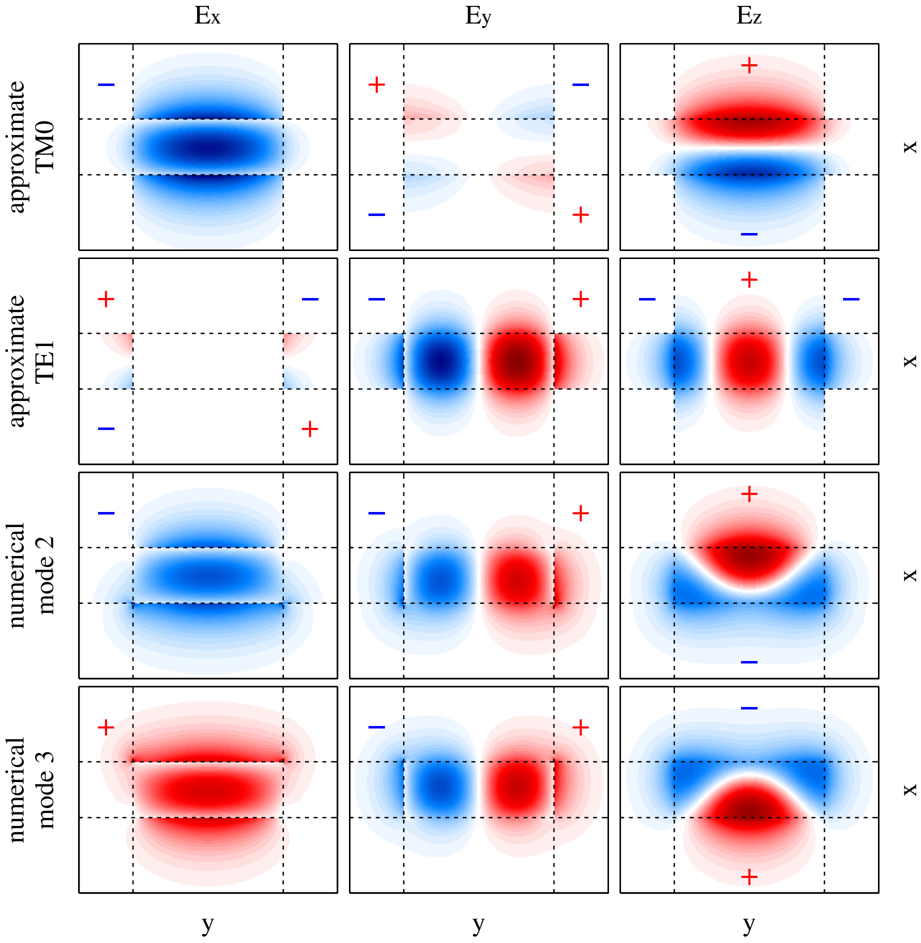

Figure 2.9: Electric fields of different modes in a 833 nm wide by 300 nm high waveguide. The dashed lines separate the different regions (see Fig. 2.5). Modes $\boldsymbol{E}_{\mathrm{TM0}}$, $\boldsymbol{E}_{\mathrm{TE1}}$, $\boldsymbol{E}_2^{\mathrm{N}}$ and $\boldsymbol{E}_3^{\mathrm{N}}$ are plotted from top to bottom. Color indicates the field strength, white regions have a low field strength. Regions with positive field strength are indicated with a plus (+) sign and red. Regions with a negative field strength are indicated with a minus sign (-) and blue.

or,

$$\frac{1}{D}\begin{pmatrix} \langle b|b\rangle\langle a|\hat{O}a\rangle - \langle a|b\rangle\langle b|\hat{O}a\rangle & \langle b|b\rangle\langle a|\hat{O}b\rangle - \langle a|b\rangle\langle b|\hat{O}b\rangle \\ -\langle b|a\rangle\langle a|\hat{O}a\rangle + \langle a|a\rangle\langle b|\hat{O}a\rangle & -\langle b|a\rangle\langle a|\hat{O}b\rangle + \langle a|a\rangle\langle b|\hat{O}b\rangle \end{pmatrix}\begin{pmatrix} a \\ b \end{pmatrix} \approx \beta_i \begin{pmatrix} a \\ b \end{pmatrix},$$

with

$$D = \langle a|a\rangle\langle b|b\rangle - \langle a|b\rangle\langle b|a\rangle. \tag{2.98}$$

The modes that we found in our approximate analysis are almost orthonormal, so $\langle a|a\rangle$ and $\langle b|b\rangle$ are approximately unity and $\langle a|b\rangle$ and $\langle b|a\rangle$ are approximately zero. Away from the crossing, we found that the approximate solutions $|a\rangle$ and $|b\rangle$ obey relation (2.64) so that $\langle a|\hat{O}a\rangle \approx \beta_a$, $\langle b|\hat{O}b\rangle \approx \beta_b$, while $\langle a|\hat{O}b\rangle$ and $\langle b|\hat{O}a\rangle$ are small. This allows us to write the Eq. (2.98) as

$$\begin{pmatrix} \beta_a + \delta_a & \delta_{ab} \\ \delta_{ba} & \beta_b + \delta_b \end{pmatrix}\begin{pmatrix} a \\ b \end{pmatrix} \approx \beta_i \begin{pmatrix} a \\ b \end{pmatrix}, \tag{2.99}$$

where δ_a, δ_b, δ_{ab}, and δ_{ba} are quantities that are much smaller than the β's. This system has the eigenvalues (labelled 2 and 3 because they correspond to the 2nd and 3rd modes of the waveguide) [75]

$$\beta_{2,3} = \frac{\beta_a' + \beta_b'}{2} \pm \frac{\sqrt{(\beta_a' - \beta_b')^2 + 4\delta_{ab}\delta_{ba}}}{2}, \tag{2.100}$$

with corresponding eigenvectors $\boldsymbol{v}_{2,3}$ (not normalized)

$$\begin{pmatrix} 2\delta_{ab} \\ -\beta_a' + \beta_b' \pm \sqrt{(\beta_a' - \beta_b')^2 + 4\delta_{ab}\delta_{ba}} \end{pmatrix}, \tag{2.101}$$

where $\beta_a' \equiv \beta_a + \delta_a$ and $\beta_b' \equiv \beta_b + \delta_b$. The two propagation constants are closest when $\beta_a' = \beta_b'$ but are always separated by a minimum distance $4\sqrt{\delta_{ab}\delta_{ba}}$, so that they never intersect. For small $\delta_a, \delta_b, \delta_{ab}, \delta_{ba} \ll |\beta_a - \beta_b|$, we find the eigenvector for $\beta_a > \beta_b$ to be $\boldsymbol{v}_2 \approx (1,0)$ and $\boldsymbol{v}_3 \approx (0,1)$. The upper propagation constant, β_2, has a TM0-like mode in this limit, while the lower propagation constant, β_3, has a TE1-like mode. For $\beta_b > \beta_a$ we find $\boldsymbol{v}_2 \approx (0,1)$ and $\boldsymbol{v}_3 \approx (1,0)$, so that the upper propagation constant now has a TE1-like mode while the lower propagation constant has a TM0-like mode. An interesting case occurs when $\beta_a' = \beta_b'$ and $\delta_{ab} = \delta_{ba}$. Then the normalized eigenvectors of this system are $\boldsymbol{v}_2 = \frac{1}{\sqrt{2}} \cdot (1,1)$ and $\boldsymbol{v}_3 = \frac{1}{\sqrt{2}} \cdot (1,-1)$, i.e., they are an equal superposition of the eigenvectors far from the crossing.

This simple description of the *avoided crossing* agrees with the observations of the numerically computed modal profiles as presented in Figs. 2.8 and 2.9.

2.7.5 Dispersion: effective group index

Having an analytical equation for the propagation constant β or effective index n_e, it is also possible to analytically calculate the dispersion in the waveguide. Linear dispersion in waveguides is often described in terms of the effective group index,

n_g, an important quantity which, for example, describes the free-spectral-range (FSR) of ring resonators and influences the sensitivity of waveguide-based sensors. Silicon-on-insulator waveguides have, in fact, a very strong modal dispersion due to the strong confinement of the light. The group index is defined by Eq. (2.32) as $n_g \equiv \partial\beta/\partial k$. From Eq. (2.71), we find

$$\frac{\partial \beta}{\partial k} = \frac{1}{\beta}\left(k n_1^2 + k^2 n_1 \frac{\partial n_1}{\partial k} - k_x \frac{\partial k_x}{\partial k} - k_y \frac{\partial k_y}{\partial k}\right). \tag{2.102}$$

The 1st and 2nd term on the right-hand-side of this equation are specified by the material refractive indices. The refractive indices $n_j(k)$ may depend on frequency and thus on $k = \omega/c$. The 3rd term is calculated from Eq. (2.29). Although k_x is only given implicitly, $\partial k_x/\partial k$ can be calculated explicitly. The total derivative of the left-hand-side of Eq. (2.29) with respect to k, dG/dk, equals zero for solutions of $G = 0$. The height d does not depend on frequency. So we get

$$\frac{dG}{dk} = \frac{\partial G}{\partial k} + \frac{\partial G}{\partial k_x}\frac{\partial k_x}{\partial k} + \frac{\partial G}{\partial n_1}\frac{\partial n_1}{\partial k} + \frac{\partial G}{\partial n_2}\frac{\partial n_2}{\partial k} + \frac{\partial G}{\partial n_3}\frac{\partial n_3}{\partial k}, \tag{2.103}$$

or,

$$\frac{\partial k_x}{\partial k} = -\frac{\frac{\partial G}{\partial k} + \frac{\partial G}{\partial n_1}\frac{\partial n_1}{\partial k} + \frac{\partial G}{\partial n_2}\frac{\partial n_2}{\partial k} + \frac{\partial G}{\partial n_3}\frac{\partial n_3}{\partial k}}{\frac{\partial G}{\partial k_x}}. \tag{2.104}$$

Similarly, the 4th term of the right-hand-side of Eq. (2.102) is calculated from Eq. (2.17) as

$$\frac{\partial k_y}{\partial k} = -\frac{\frac{\partial F}{\partial k} + \frac{\partial F}{\partial n_1}\frac{\partial n_1}{\partial k} + \frac{\partial F}{\partial n_4}\frac{\partial n_4}{\partial k} + \frac{\partial F}{\partial n_5}\frac{\partial n_5}{\partial k}}{\frac{\partial F}{\partial k_y}}. \tag{2.105}$$

The partial derivatives in Eqs. (2.104) and (2.105) are straightforward to calculate.

For the case that only the core material is dispersive, i.e. $n_1(k)$, and where the other refractive indices do not depend on the frequency, thus also not on k, we define

$$\alpha_2 \equiv \left(\frac{k_x^2}{n_1^4} + \frac{\gamma_3^2}{n_3^4}\right)\frac{1}{n_2^2\gamma_2}, \tag{2.106}$$

$$\alpha_3 \equiv \left(\frac{k_x^2}{n_1^4} + \frac{\gamma_2^2}{n_2^4}\right)\frac{1}{n_3^2\gamma_3}, \tag{2.107}$$

$$\alpha_4 \equiv \frac{k_y^2 + \gamma_5^2}{\gamma_4}, \tag{2.108}$$

$$\alpha_5 \equiv \frac{k_y^2 + \gamma_4^2}{\gamma_5}, \tag{2.109}$$

to arrive at

$$\begin{aligned}\frac{\partial k_x}{\partial k} = &\Bigg\{ k_x k\left(\alpha_2(n_1^2 - n_2^2) + \alpha_3(n_1^2 - n_3^2) + (\alpha_2+\alpha_3)\, n_1 k \frac{\partial n_1}{\partial k}\right) \qquad (2.110)\\ &+ \left(\frac{\gamma_2}{n_2^2} + \frac{\gamma_3}{n_3^2}\right)\left(\frac{4k_x^3}{n_1^5} - \frac{2k_x}{n_1}\left(\frac{k_x^2}{n_1^4} - \frac{\gamma_2\gamma_3}{n_2^2 n_3^2}\right)\right)\frac{\partial n_1}{\partial k}\Bigg\}\\ &\cdot \left\{\left(\frac{\gamma_2}{n_2^2} + \frac{\gamma_3}{n_3^2}\right)\left(\frac{k_x^2}{n_1^4} + \frac{\gamma_2\gamma_3}{n_2^2 n_3^2}\right) + k_x^2(\alpha_2+\alpha_3) + n_1^2 d\left(\frac{k_x^2}{n_1^4} - \frac{\gamma_2\gamma_3}{n_2^2 n_3^2}\right)^2 \sec^2[k_x d]\right\}^{-1},\end{aligned}$$

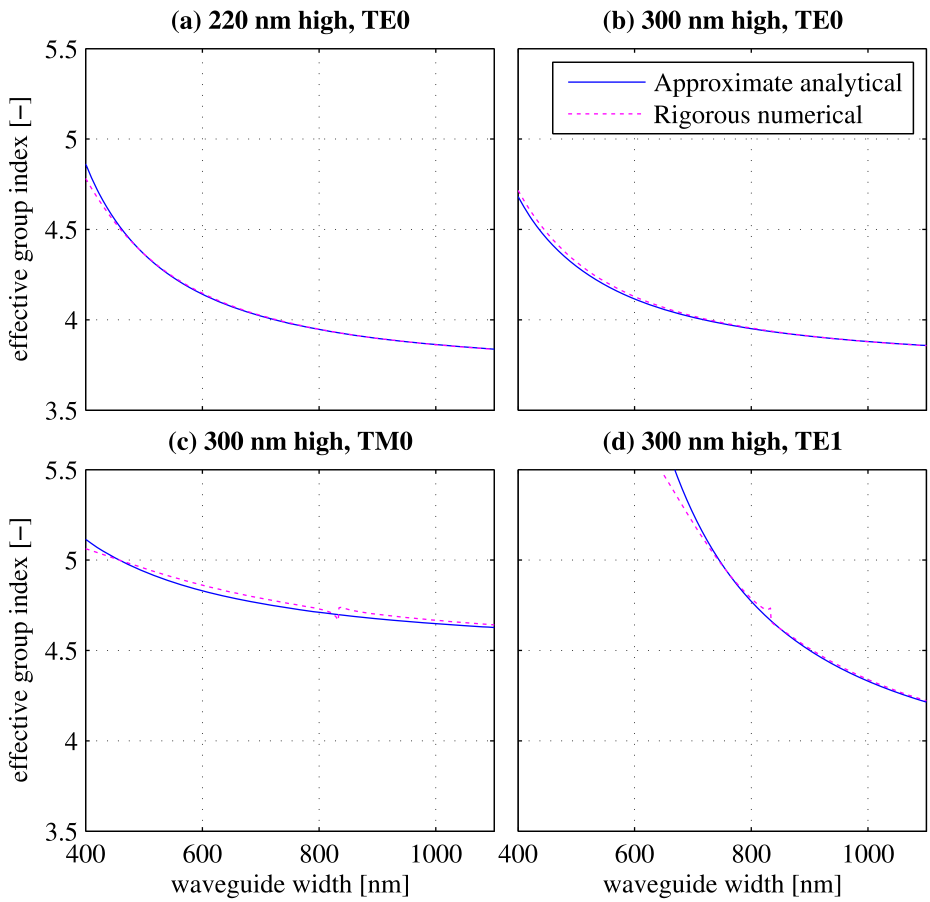

Figure 2.10: Effective group indices. Approximate analytical model compared with rigorous mode solver. Typical rectangular silicon-on-insulator waveguides with air cladding. **(a)** 220 nm high, fundamental mode. **(b-d)** 300 nm high, first 3 modes.

and

$$\frac{\partial k_y}{\partial k} = \frac{k_y k \left(\alpha_4(n_1^2 - n_4^2) + \alpha_5(n_1^2 - n_5^2) + (\alpha_4 + \alpha_5)\, n_1 k \frac{\partial n_1}{\partial k}\right)}{(\gamma_4 + \gamma_5)(k_y^2 + \gamma_4\gamma_5) + k_y^2\,(\alpha_4 + \alpha_5) + b(k_y^2 - \gamma_4\gamma_5)^2 \sec^2[k_y b]}. \quad (2.111)$$

We calculated the effective group indices of typical SOI waveguides with heights of 220 nm and 300 nm, and compared the result with a numerical mode solver. Silicon dispersion was taken into account, with $\partial n_1/\partial k = 3.147\cdot 10^8$ m^{-1}, $k = 2\pi/\lambda$ and $\lambda = 1550$ nm [76]. These results are compared with the group index that was numerically calculated using the FMM method as implemented in FimmWave. Results are presented in Fig. 2.10 where it can be seen that the error remains below 4%.

2.8 Rigorous numerical mode-solvers

Exact analytical solutions, i.e. closed form solutions, for the guided modes exist only for some waveguide shapes, such as a slab waveguides or circular waveguides. For waveguides with a rectangular cross-section, approximate models such as Marcatili's method and its modifications exist (see Sec. 2.7). However, actual waveguides might have different shapes, for example, silicon waveguides are actually trapezoidal rather than rectangular. Moreover, waveguides for evanescent field sensing have even more special shapes to maximize the overlap of the modal field with the material that is to be sensed. Rigorous numerical mode solvers can handle arbitrary shaped waveguides including losses and bends, and are therefore often used in the design of photonic waveguides.

We have used two different numerical mode solvers: the film mode-matching (FMM) method and the finite element method (FEM), both implemented in the FimmWave software package by Photon Design (Oxford, UK) [77, 78].

The FMM method is very suitable to solve waveguide geometries in which the waveguide is built up from a number of vertical slices (such as rectangular waveguides or directional couplers). In this method, the cross-section of the ridge waveguide is split in vertical slices, and 1-dimensional modes are computed analytically for each slice. The 2-D modes are found by finding a set of coefficients of the 1-D modes that will give a field profile obeying Maxell's equations everywhere. In our simulations, the area of the numerical simulation extends 2 μm from the waveguide, and 200 1-D modes are used per slice.

In the finite element method (FEM), Maxwell's equations for the modes of a waveguide are discretized and the modes are solved on the discrete grid. The FEM implementation in FimmWave uses first and second order finite elements. The triangular grid is automatically chosen such that it aligns with the waveguide structure. In our simulations, we used $\sim$210 gridpoints in both the x- and the y-directions.

For verification, we compared the FMM method with the finite element method (FEM) for the rectangular waveguides in Fig. 2.7. We found that difference (between FMM and FEM) in effective index is below 10^{-3} and the relative energy in the difference field is below 10^{-4}.

2.9 Typical silicon-on-insulator waveguides

This section details some typical characteristics of rectangular silicon-on-insulator waveguides: (1) the uncertainty in the propagation constant, (2) the effects of slightly slanted side-walls, (3) the propagation loss due to side-wall roughness, and (4) the wavelength-dependence of the effective index.

Fabrication of sub-wavelength silicon waveguides is not straightforward and real waveguides differ from the designed ones (Sec. 2.3). The most standard waveguide in SOI technology is rectangular, because it is simple and has particular advantages. The mode is strongly confined in this waveguide, allowing for sharp bends. The height of the waveguide is solely defined by the thickness of the silicon layer, and thus does not depend on etch processes which may cause variations or

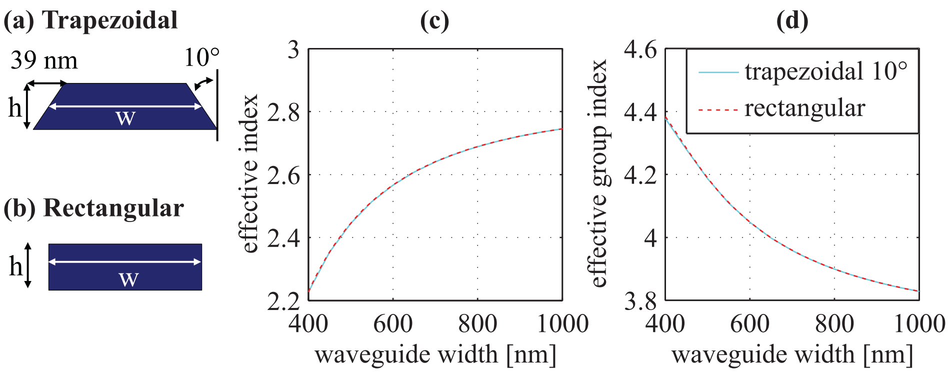

Figure 2.11: Trapezoidal waveguides with 10° side-wall angle compared with rectangular waveguides. Silicon-in-SiO_2 waveguides with a height h of 220 nm. Silicon-dioxide cladding. Film mode matching (FMM) method is used as mode-solver for the rectangular waveguids. Finite element method (FEM) is used as mode-solver for the trapezoidal waveguides because this method handles the trapezoidal structures more accurate (see Sec. 2.8). **(a)** Sketch the cross-section of a trapezoidal waveguide. **(b)** Sketch the cross-section of a rectangular waveguide, width w is equal to the average width of the trapezoidal waveguide. **(c)** Effective index. **(d)** Effective group index.

roughness. A drawback of this waveguide type is that the strong confinement also causes the effective index to be sensitive to fabrication-induced variations particularly in the width of the guides. This is a problem for some devices such as arrayed waveguide gratings.

Although the waveguides are intended to be rectangular, the side-wall angle is about 10 degrees, hence the bottom of a 220 nm high waveguide is 78 nm wider than its top (Fig. 2.11a). This is caused by the etch process in the CMOS fabrication of the waveguides. We used rigorous numerical simulations to show that the effective index and the effective group index of trapezoidal waveguides are very well approximated by rectangular waveguides that that have a width equal to the average width of the trapezoidal guide. Figure 2.11 compares trapezoidal waveguides with rectangular waveguides. For silicon waveguides embedded in silicon-dioxide with height 220 nm and widths varying from 400 nm to 1000 nm, the effective index and effective group index agree within 0.1%. Hence the effective index and the effective group index of typical trapezoidal SOI waveguides may be very well approximated by rectangular waveguides.

The propagation losses α_p of SOI waveguides have many causes: linear and non-linear absorption in the material (both in the bulk as well as at the interfaces between materials), leakage into the silicon substrate, scattering from small defects in the material, and scattering from roughness of the silicon-silica interfaces of the waveguide. Dry etching, which is used to fabricate these guides, creates sub-wavelength roughness at the sidewalls of the waveguides. This is the dominant loss mechanism in sub-wavelength silicon waveguides [79]. The high index contrast of waveguides in SOI technology allows small bending radii (3 μm) with reasonable propagation losses. These losses originate not only from radiation loss due to the curvature in the waveguide. The fields of the mode of a bend waveguide is pushed outwards towards the outer side of the waveguide. This increases losses due to side-wall roughness because the field intensity at the sidewalls is higher compared to a straight waveguide. This also increases substrate leakage because the mode is less confined. Moreover, side-walls are typically not perfectly vertical, which introduces TE/TM conversion in the bends; this conversion gives additional loss [64]. Moreover, there is a mismatch between the mode of the straight waveguide and the mode of the bend waveguide, especially for smaller bending radii. This causes at the interfaces between the straight and the curved waveguides. Therefore the loss of two 90° turns separated by a straight guide is not necessarily same as the loss of a single 180° turn. Finding the modes of an ideal waveguide without losses can be done with high accuracy, but the calculation of loss mechanisms is relatively difficult [79].

The out-of-plane grating couplers which we used to couple light to and from the chip work approximately in a 30 nm wavelength span around a center wavelength λ_c of 1550 nm. In this regime, the wavelength-dependence of the effective index can be approximated as linear, so that we may use Eq. (2.33).

2.10 Directional couplers

Directional couplers can be used to couple a fraction of the light from one waveguide to another, for example to couple light to ring resonators. This section starts with an intuitive introduction to the behavior of such couplers. Then three methods to calculate the behavior of directional couplers are presented and compared: eigenmode expansion (Sec. 2.10.1), rigorous numerical FDTD simulations (Sec. 2.10.2), and coupled mode theory (Sec. 2.10.3).

A directional coupler consists of two parallel single-mode waveguides close to each other so that power couples from one waveguide to the other (see Fig. 2.12). Describing this system with coupled mode theory, we assume that the electric field in the coupler can be approximated by a superposition of the two modes of the isolated waveguides. The amplitudes of the two modes vary while propagating through the parallel waveguides due to the coupling (i.e., light "leaks" from one mode to the other). This coupled mode theory will be derived in Sec. 2.10.3 but we present the most important results already in this paragraph. The electromagnetic field is approximated by

$$\boldsymbol{\mathcal{E}}^c(x, y, z, t) \approx \boldsymbol{E}^a(x, y)u_a(z)e^{\imath\omega t} + \boldsymbol{E}^b(x, y)u_b(z)e^{\imath\omega t}, \tag{2.112}$$

with $u_a(z)$ and $u_b(z)$ the complex modal amplitudes of waveguides a and b, respectively, $\boldsymbol{E}^a(x, y)$ and $\boldsymbol{E}^b(x, y)$ the modal electric fields of the waveguides and $\boldsymbol{\mathcal{E}}^c(x, y, z, t)$ the electric field. Let us consider the result of an excitation of mode b at $z = 0$ (i.e., all light is in waveguide b). The transmission of a coupler with length $\tilde{L}$ is given by $u_b(\tilde{L}) = \tau u_b(0)$, while the coupled light is given by $u_a(\tilde{L}) = \kappa u_b(0)$. These complex amplitudes τ and κ can be calculated using coupled mode theory

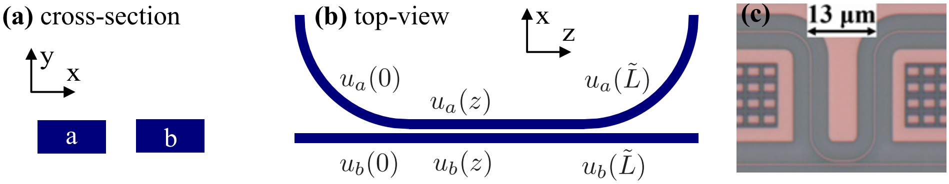

Figure 2.12: Sketch of a directional coupler consisting of two parallel waveguides. We studied couplers with an silicon-dioxide cladding because these devices were used in Chapters 3, 4 and 5. **(a)** Cross-section of the coupler. Two 440 nm × 220 nm rectangular silicon waveguides are separated 200 nm. Refractive index of the guides is n_1 and the SiO_2 cladding has index n_2. **(b)** Top-view including the bends. Upper waveguide *a* and lower waveguide *b*. **(c)** Optical microscope photo of a directional coupler in SOI. The very narrow pinkish lines are the waveguides.

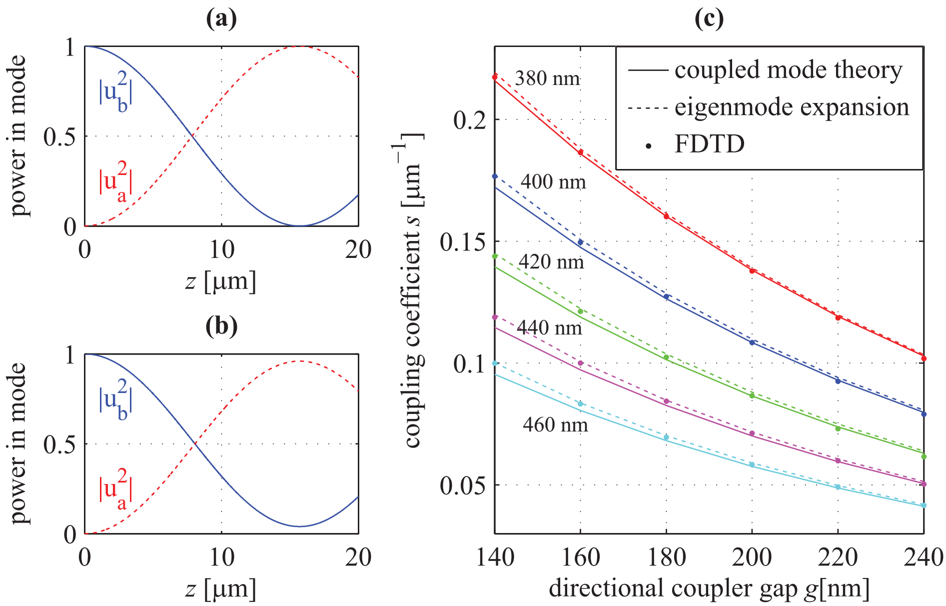

Figure 2.13: **(a and b)** Behavior of a directional coupler. Power in upper waveguide *a* and lower waveguide *b*. At $z = 0$, all power resides in the lower guide *b*. **(a)** Coupling coefficient $s = 0.1$, identical waveguides, $\delta = 0$. **(b)** Coupling coefficient $s = 0.1$, different waveguides, $\delta = 0.02$.
(c) Coupling coefficient calculated using three different methods (see legend). The five groups of lines correspond to waveguide widths: 380 nm, 400 nm, 420 nm, 440 nm and 460 nm (top to bottom). The rectangular silicon waveguides are 220 nm high and have silicon-dioxide cladding.

(see Sec. 2.10.3)

$$\tau = \left(\cos s\tilde{L} - \frac{\imath\delta}{s}\sin s\tilde{L}\right) e^{-\imath(\beta_b+\kappa_{bb}-\delta)\tilde{L}}, \tag{2.113}$$

$$\kappa = -\left(\frac{\imath\kappa_{ab}}{s}\sin s\tilde{L}\right) e^{-\imath(\beta_b+\kappa_{bb}-\delta)\tilde{L}}, \tag{2.114}$$

where β_b is the propagation constant of mode b, κ_{bb} is the correction to this propagation constant originating from the other waveguide, $\delta \equiv \frac{1}{2}(\beta_b + \kappa_{bbb} - \beta_a - \kappa_{aa})$ is the difference between the corrected propagation constants of the guides, $s = \sqrt{\kappa_{ba}\kappa_{ab} + \delta^2}$ is the coupling coefficient dominated by κ_{ab} and κ_{ba}. The guides in the coupler we study are designed to be identical, but we experimentally observed non-zero δ in our couplers. Equation (2.113) is valid for two parallel waveguides, whereas the actual coupler also includes bends to connect the parallel waveguides to the components in the circuit. We take the coupling which happens in the bends into account by re-defining the length $\tilde{L}$ in Eq. (2.113) as an effective coupling length $\tilde{L} = L + \Delta L$, with L the length of the parallel waveguides. Figure 2.13a illustrates the behavior of a directional coupler in which light "leaks" from waveguide b (power $|u_b|^2$) to waveguide a. For two different waveguides (non-zero δ), the power never fully transfers from one waveguide to the other (Fig. 2.13b). In Sec. 2.10.3, we derive Eq. (2.113) by following the approach of Hardy & Streifer [31, 32]. In the conclusion of Sec. 2.10.3, we show that this method agrees well with rigorous FDTD simulations also for high-index-contrast SOI waveguides.

When using the couplers not for a single wavelength λ_c but for a range of wavelengths, it is necessary to study how the behavior of the coupler depends on the wavelength. Dispersion is taken into account by assuming linear dispersion of the effective index (hence the propagation constant $\beta_b(\lambda)$ is given by Eq. (2.33)) and by assuming linear dispersion of the coupling $s(\lambda)$. With the definition of $\tilde{L}$, it is not necessary to include dispersion in ΔL. We found that dispersion in ΔL, and higher order dispersion in s, are small and below our numerical and experimental noise (see Sec. 2.10.2 and Chapter 3, respectively).

2.10.1 Eigenmode expansion (EME)

The directional coupler may be looked upon as one single waveguide with z-invariant refractive index profile $\epsilon_c(x, y)$ consisting of two disconnected parts. A coupler that consists of two identical single-mode waveguides has two modes: a symmetric mode (labeled 0) an an anti-symmetric mode (labeled 1). These are pure "waveguide" modes, in the form of Eq. (2.30), which propagate in the z-direction with propagation constants β_0 and β_1 and without distortion. Hence

$$\boldsymbol{\mathcal{E}}^c(x, y, z, t) = u_0\boldsymbol{E}^{(0)}(x, y)e^{\imath(\omega t-\beta_0 z)} + u_1\boldsymbol{E}^{(1)}(x, y)e^{\imath(\omega t-\beta_1 z)}. \tag{2.115}$$

The relative phase between modes 0 and 1 changes with z due to the different propagation constants β_0 and β_1. After a certain propagation distance L_π, the relative phase of the two modes is changed by π rad. In Eq. (2.115), the relation to the individual waveguides a and b is not clearly visible. However, we may

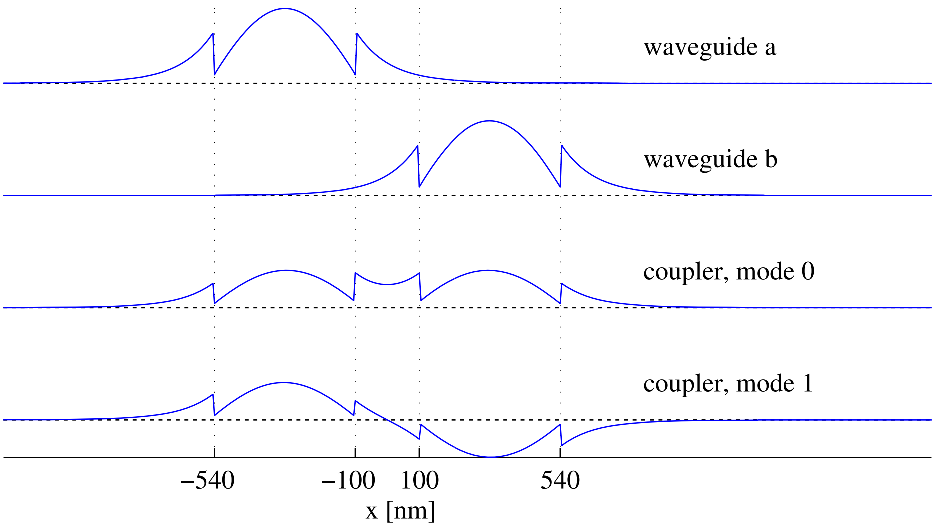

Figure 2.14: Two description of the modes in a directional coupler, modal electric field, $E_x(x, y)$ at y=0. The upper two curves show the modes of isolated waveguides a and b. The fields in the directional coupler can be approximated as a superposition of those two modes with z-dependent amplitude coefficients $u_a(z)$ and $u_b(z)$ (coupled mode theory). The lower two curves are exact solutions of the directional coupler "waveguide" (eigenmode expansion method). Symmetric mode (0) and Anti-symmetric mode (1). Modal profiles obtained using rigorous mode-solver (FMM method in FimmWave).

approximate the mode of isolated waveguide a by adding modes 0 and 1. We may approximate the mode of isolated waveguide b by subtracting mode 1 from mode 0 (see Fig. 2.14). Thus the excitation of the "mode" of waveguide b at $z = 0$ can be approximated by $u_0 = \sqrt{1/2}$ and $u_1 = -\sqrt{1/2}$. After a propagating a distance L_π, the sign of one mode 1 has effectively flipped, so that all light is now approximately in the "mode" of waveguide a. The length over which all ligth transfers from waveguide b to waveguide a is hence given by L_π.

In the coupled mode theory, Eqs. (2.112-2.114), it was found that all light transfers from mode b to mode a when $|u_b(\tilde{L})| = \cos s\tilde{L} = 0$, thus when $s\tilde{L} = \pi/2$. This length $\tilde{L}$ is thus the same length as L_π.This allows us to define a coupling coefficient s_{EME} as found with the eigenmode expansion (EME) method as

$$s_{\mathrm{EME}} = \frac{\beta_1 - \beta_0}{2}. \tag{2.116}$$

In the implemenation of the EME method, we calculated the coupling coefficients s_{EME} from the propagation constants (β_1 and β_0) that were calculated with a rigorous numerical mode-solver (FMM method). The calculated coupling coefficients s_{EME} agree well with coupled mode theory and with rigorous FDTD simulations (see Fig. 2.13c).

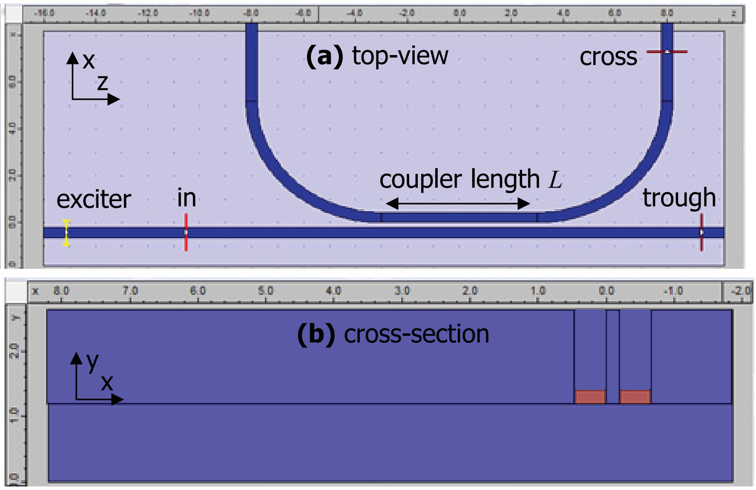

Figure 2.15: Setup of the directional coupler FDTD simulation, based on screen-shots of CyrstalWave. **(a)** Top-view with the exciter and sensors *in*, *cross*, and *through*, indicated. **(b)** Cross-section at z=0 depicting the two waveguides.

As discussed in Sec. 2.9, the side-walls of waveguides in SOI technology are not perfectly vertical but have an angle of ∼10°, hence the waveguides are trapezoidal. It was shown that the effective index index of typical trapezoidal SOI waveguides are well approximated by a rectangular waveguide with a width equal to the average width of the trapezoidal waveguide. In this paragraph, we study the influence of the side-wall angle of the waveguides in directional couplers using the EME method. We computed the coupling coefficients s_{EME} of couplers with trapezoidal and rectangular waveguides, to find that they agree within 1% (for waveguide widths varying from 380 nm to 480 nm, gaps varying from 140 nm to 240 nm, and 10° side-wall angle for the trapezoidal guides). Propagation constants β_0 and β_1 were, for both cases, computed with the finite element method (FEM) mode-solver.

2.10.2 Rigorous FDTD simulations

We have used rigorous finite difference time domain (FDTD) simulations to calculate the transmittance of light through the directional coupler. Rigorous means that we calculate the solution to Maxwell's equations without approximations. Space and time are discretized, and the behavior of the electromagnetic fields over time is calculated using Maxwell's equations. This means that the solutions are exact when using an infinitely small grid-size, an infinitely small time-step, and an infinitely accurate computer. In reality, however, computation times and computer memory are limited of course and therefore so is the accuracy that can be obtained (see Refs. [80, 81] for FDTD).

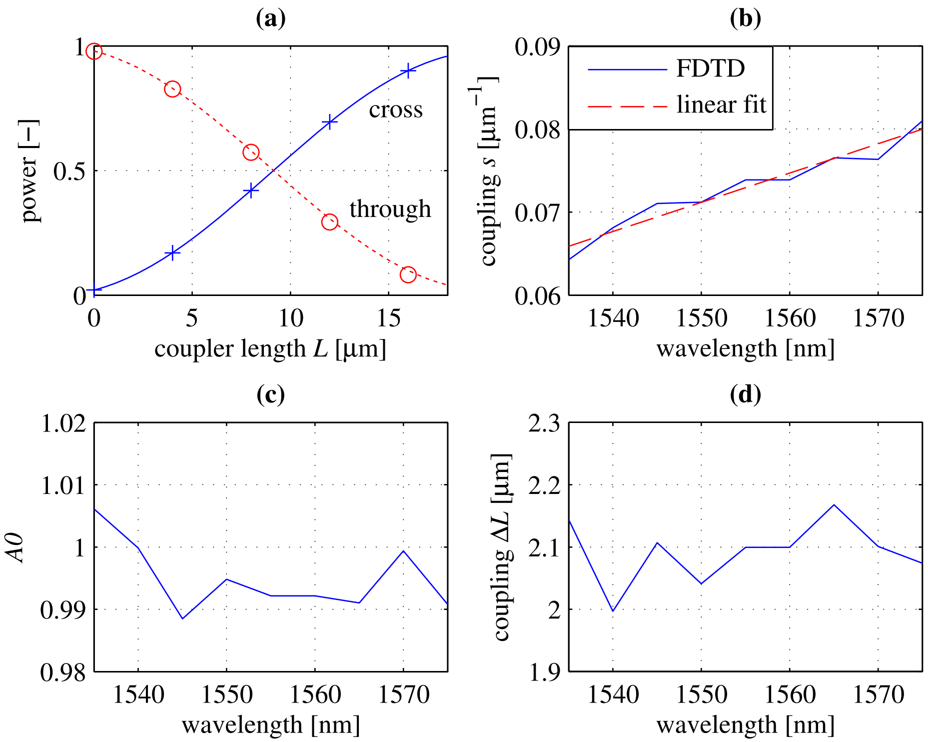

Figure 2.16: Example of FDTD simulations of a directional coupler (waveguide width 440 nm, gap 200 nm). Lengths L are: 0, 4, 8, 12, and 16 μm. **(a)** Power flow through the sensors, from FDTD (markers) and fitted (curves). **(b-c)** Fitted values of coupling coefficient s, transmittance A_0 and correction for coupling in the bends ΔL. Plotted versus wavelength to investigate both dispersion and noise.

We have used CrystalWave, a commercial FDTD implementation by Photon Design (Oxford, UK) [82]. This solver has an user-friendly interface and is designed for integrated-optical problems. The simulations were performed on a fast PC using 10 CPU-cores with a clock-speed of 2.66 GHz and 96 GBs of memory. For the simulations of the directional coupler, we used a simulation domain that extends 1 μm above and below the waveguides (see Fig. 2.15) and a grid-spacing of 20 nm for vacuum wavelengths around 1550 nm. The grid was aligned to the parallel waveguides, such that the refractive index profile in this region is not discretized or averaged. The reflections from the borders of the simulation volume was minimized using *perfectly matched layers* [82]. A TE-like mode is excited in the lower waveguide (see Fig. 2.15) with a time-pulse that consists of a sinusoidal signal (free-space wavelength 1550 nm) with an envelope that has a bandwidth of 200 nm (free-space wavelength). The electromagnetic energy flux through the rectangular surfaces of the *in*-, *through*- and *cross*-sensors are recorded (see Fig. 2.15). The sensors record the electromagnetic fields versus time and a Fourier transform is used to find the energy flux as function of frequency or free-space wavelength.

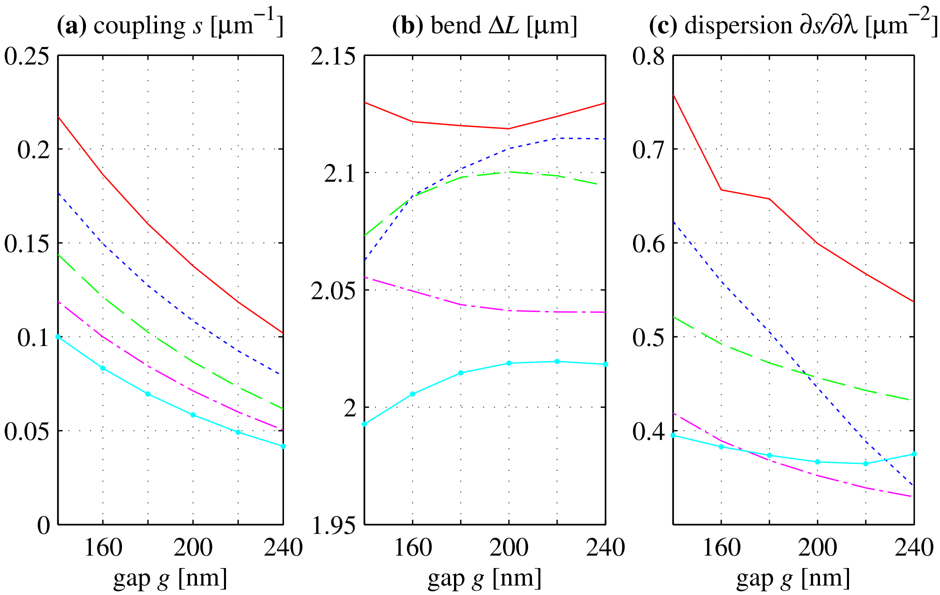

Figure 2.17: Characteristics of directional couplers with different waveguide widths and separation gaps, extracted from FDTD simulations. Labels of the y-axis are above the plots. **(a)** coupling coefficient s. Curves represent waveguide widths 380 nm, 400 nm, 420 nm, 440 nm, and 460 nm (top-to-bottom). The curves in (b) and (c) have the same color and line-style coding. **(b)** Correction for coupling in the bends ΔL **(c)** Dispersion in the coupling coefficient $\partial s/\partial\lambda$.

The power inserted in waveguide b was normalized to one using the recordings of the *in* sensor.

Equation (2.114) is used to study the behavior of the couplers. With unit power in waveguide b before the coupler, the power in waveguide a after the coupler, $|u_a(\tilde{L})|^2$, is

$$|u_a(\tilde{L})|^2 = A_0 \sin^2\left[s\,(L + \Delta L)\right]. \tag{2.117}$$

For a lossless coupler as described by Eq. (2.114), $A_0 = |\kappa_{ab}/s|^2$, but radiation loss in fact also influences A_0. We performed a series of FDTD simulations with length L varying from 0 μm to 18 μm and recorded the power in waveguide a after the coupler, $|u_a(\tilde{L})|^2$ for each length L. Then unknowns in Eq. (2.117), s, ΔL and A_0, are found by fitting this equation to the $|u_a(\tilde{L})|^2$ versus L curve. An example of the results of such a FDTD simulation and fitting is shown in Fig. 2.16a, where plusses show the FDTD results and the solid line shows the fitting. For all simulations, we found that $A_0 \approx 1$, thus radiation loss and asymmetries between the waveguides δ can be neglected. The numerical error in the FDTD computation is estimated by inspecting the results at different frequencies or free-space wavelengths (Fig. 2.16b-d). The curves in this figure are expected to be smooth, but it can be seen that the numerical error in A_0, s, and ΔL are on the order of 1%, 4% and 5%, respectively.

The power going straight through waveguide b was also recorded in the FDTD simulations (circles in Fig. 2.16a). We compare this recorded power with the parameters (s, ΔL and A_0) that were obtained using the recordings of the power coupled to waveguide a. For lossless couplers, the straight-through power in waveguide b, $|u_b(\tilde{L})|^2 = 1 - |u_a(\tilde{L})|^2$, which is plotted as the dashed line in 2.16a. This plot shows good agreement between the dashed line and the circles.

In Fig. 2.16b,d, it can be seen that the dispersion in s is linear and that the dispersion in ΔL is negligible. A linear fit is used to find linear dispersion $\partial s/\partial\lambda$ in the regime from 1525 nm to 1575 nm free-space wavelength. Figure 2.17 presents the simulated characteristics of directional couplers with different waveguide widths and separation gaps.

2.10.3 Coupled mode theory following Hardy & Streifer

This section presents the coupled mode theory as derived by Hardy and Streifer [31, 32]. This formalism requires fewer approximations than, for example, that derived by Yariv [35, 83]. Most importantly, Yariv's formalism approximates the modes as pure transverse electric (TE) or transverse magnetic (TM) which is not valid for single-mode waveguides with a high index contrast. A detailed comparison of the formalism presented here with theories reported in the literature can be found a the end of this section. We have done our best to present the derivation as clearly as possible, despite the many mathematical steps. Although the coupled mode formalism is generally applicable, we directly apply it to the directional couplers because this clarifies the description.

We consider a directional coupler consisting of two parallel rectangular waveguides (index n_1), embedded in a homogeneous cladding (index n_2), separated by a gap g (see Fig. 2.12a). For typical SOI waveguides, this gap is about 200 nm. The coupler is described by its permittivity profile $\epsilon_c(x, y) = \epsilon_0 n_c^2(x, y)$. We describe the electromagnetic fields in the coupler in terms of the modes of the two waveguides, labeled a and b. Isolated waveguide a is described by permittivity profile $\epsilon_a(x, y)$, and waveguide b is described by permittivity profile $\epsilon_b(x, y)$. We define $\Delta\epsilon_a(x, y)$ and $\Delta\epsilon_b(x, y)$ as the difference between the coupler permittivity profile and the isolated waveguide permittivity profile, i.e.,

$$\epsilon_c(x, y) = \epsilon_a(x, y) + \Delta\epsilon_a(x, y) = \epsilon_b(x, y) + \Delta\epsilon_b(x, y), \tag{2.118}$$

see Fig. 2.18. In the analysis, we assume that the mode expansion conjecture is valid. After explaining this conjecture, we go trough a long mathematical derivation to write Maxwell's equations in a form that is very useful for the description of the directional coupler. We then expand the field in terms of modes of the waveguides a and b and approximate it by only considering the modes which are important in the directional coupler, neglecting radiation and backwards-traveling modes. This results in intuitive equations for the directional coupler.

Mode expansion conjecture

The mode expansion conjecture states that, for a given frequency ω, the modes of a waveguide (including radiation modes and evanescent modes) form in every cross-

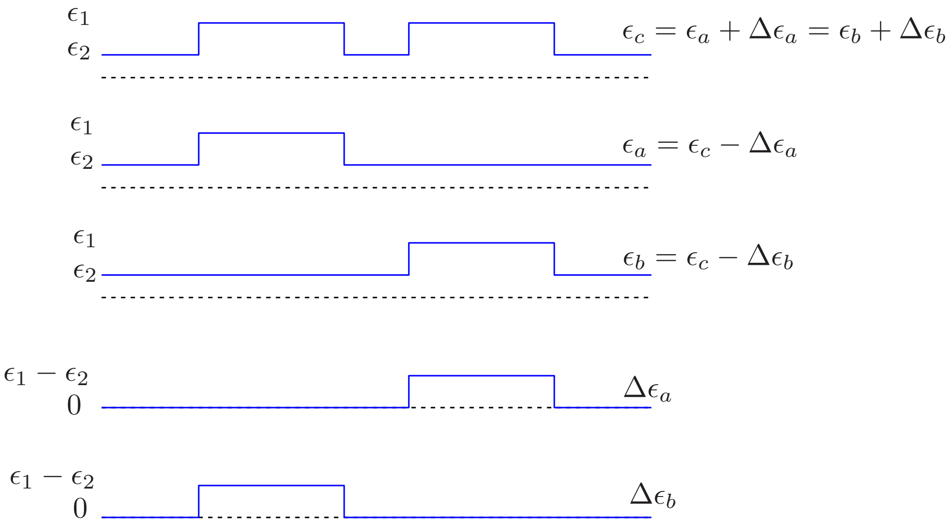

Figure 2.18: Permittivity profiles, cross-section at $y = 0$. Permittivity profiles of the directional coupler $\epsilon_c(x, y)$, isolated waveguide a $\epsilon_a(x, y)$, isolated waveguide b $\epsilon_b(x, y)$ and difference profiles $\Delta\epsilon_a(x, y)$ and $\Delta\epsilon_b(x, y)$. In typical SOI waveguides, ϵ_1 and ϵ_2 are the permittivities of silicon and silicon-dioxide, respectively.

sectional plate ($z =$ constant) a complete set; in the sense that all transversal field components for arbitrary permittivity profile can in any cross-sectional plane be written as a linear superposition of the transversal field components of the modes of the waveguide. In the example of a directional coupler, we write the time-harmonic fields of the directional coupler (permittivity $\epsilon_c(x, y)$) as a superposition of the modes of waveguide a (permittivity ϵ_a(x,y)) [28, 29, 31, 32, 84], i.e.,

$$\boldsymbol{\mathcal{E}}_t^c(x, y, z, t) = \sum_{\nu=1}^{\infty} a_\nu(z) \boldsymbol{E}_t^{a,\nu}(x, y) e^{\imath\omega t}, \tag{2.119}$$

$$\boldsymbol{\mathcal{H}}_t^c(x, y, z, t) = \sum_{\nu=1}^{\infty} a_\nu(z) \boldsymbol{H}_t^{a,\nu}(x, y) e^{\imath\omega t}. \tag{2.120}$$

where $\boldsymbol{\mathcal{E}}_t^c$ and $\boldsymbol{\mathcal{H}}_t^c$ are the transversal electromagnetic field components in coupler and with the summation over an infinite set waveguide modal profiles $\boldsymbol{E}_t^{a,\nu}(x, y)$ and $\boldsymbol{H}_t^{a,\nu}(x, y)$. Subscript t denotes the transversal field components x and y. Actually, this superposition consists of a finite sum of the guided modes and an integral over the radiation and evanescent modes, but for simplicity we will keep writing the single infinite sum (see Sec. 2.6.5). The modes of waveguide a are solutions of Maxwell's equations for permittivity $\epsilon_a(x, y)$, but they are not a solution of Maxwell's equations for the directional coupler which has permittivity $\epsilon_c(x, y)$. For example, the individual modes of waveguide a are smooth outside the core of waveguide a, whereas certain transverse components of the electromagnetic fields in the coupler are discontinuous at the interfaces of waveguide b. One might compare this expansion with spatial Fourier decomposition, in which an arbitrary function $f(x,y)$ can be written as an infinite superposition of spatial harmonic functions. So far, this conjecture has only been proven for two-dimensional lossless optical components, including TE- and TM-modes in slab waveguides [84]. This conjecture is often assumed to hold also for the general case, and is in fact often used, but a proof seems not to have been given so far. The general case of this conjecture is made plausible by the fact that the transversal components of the modes are, for given frequency ω, the eigenfields of a differential operator $\hat{O}$ defined in Eq. (2.40) with the propagation constant β as eigenvalue (see Eq. (2.37)). The fact that $\hat{O}$ is not selfadjoint makes this problem difficult because it precludes the use of some useful theories. Still, we may project the complete space on the eigenvalues of $\hat{O}$ which, for a complete set, would give identity, i.e., completeness may be formulated as

$$\lim_{|\beta|\to\infty} \oint_{\beta} \left(\beta\hat{I} - \hat{O}\right)^{-1} d\beta = \hat{I}, \tag{2.121}$$

where complex β runs along a contour in the complex plane with $|\beta| \to \infty$ and with identity operator $\hat{I}$. This projection only depends on this contour integral and not on the details in the complex plane. From Fourier theory, we know that the operator $\hat{O}$ for free-space is complete and we argue that the introduction of the waveguide can be seen as a small perturbation on the operator $\hat{O}$ which has little influence on the integral along the complex plane at infinite $|\beta|$.

The modal fields $\boldsymbol{E}^{a,\nu}(x,y)$ and $\boldsymbol{H}^{a,\nu}(x,y)$ are solutions of Maxwell's equations for a waveguide with permittivity profile $\epsilon_a(x,y)$. The z-component of the electric field follows from the transversal components of the magnetic field using Ampère's law (2.2):

$$E_z^{a,\nu}(x,y) = \frac{1}{\imath\omega\epsilon_a(x,y)}\left(\frac{\partial H_x^{a,\nu}}{\partial y} - \frac{\partial H_y^{a,\nu}}{\partial x}\right). \tag{2.122}$$

The mode expansion, Eqs. (2.119 and 2.120), concerns the transversal field components (x,y) of the electromagnetic fields in the coupler. The z-components of this field follow from Maxwell's equations. Maxwell's equations are linear so that the z-components of the electromagnetic fields ($\mathcal{E}_z^c$ and $\mathcal{H}_z^c$) are a superposition of the contributions of the individual modes of waveguide a. However, these contributions are different from $E_z^{a,\nu}$ because $\boldsymbol{\mathcal{E}}^c$ is a solution to Maxwell's equations in the coupler with permittivity ϵ_c and not a solution to the individual waveguide a with permittivity ϵ_a. We substitute the field in the form of Eq. (2.120) in the z-component of Ampère's law (2.2) and move all terms under the summation to arrive at

$$\mathcal{E}_z^c(x,y,z,t) = \sum_{\nu=1}^{\infty} a_\nu(z)\frac{1}{\imath\omega\epsilon_c(x,y)}\left(\frac{\partial H_x^{a,\nu}}{\partial y} - \frac{\partial H_y^{a,\nu}}{\partial x}\right)e^{\imath\omega t} \tag{2.123}$$

$$\equiv \sum_{\nu=1}^{\infty} a_\nu(z)\tilde{E}_z^{a,\nu}e^{\imath\omega t}, \tag{2.124}$$

where we defined $\tilde{E}_z^{a,\nu}$. From Eqs. (2.122), (2.123) and (2.124), we find

$$\tilde{E}_z^{a,\nu}(x,y) = \frac{\epsilon_a(x,y)}{\epsilon_c(x,y)} E_z^{a,\nu}(x,y). \tag{2.125}$$

The z-component of the magnetic field can be calculated from the z-component of Faraday's law (2.1). The coupler and isolated waveguide share the same permeability profile, namely μ_0, from which follows that the contribution of mode ν of isolated waveguide a does not depend on the structure (waveguide or coupler), hence is given by $H_z^{a,\nu}$.

Finally, we arrive at a description of the electromagnetic fields in the coupler, $\boldsymbol{\mathcal{E}}^c$ and $\boldsymbol{\mathcal{H}}^c$, in terms of the modes of waveguide a,

$$\boldsymbol{\mathcal{E}}^c(x,y,z,t) = \sum_{\nu=1}^{\infty} a_\nu(z) \tilde{\boldsymbol{E}}^{a,\nu}(x,y) e^{\imath\omega t}, \tag{2.126}$$

$$\boldsymbol{\mathcal{H}}^c(x,y,z,t) = \sum_{\nu=1}^{\infty} a_\nu(z) \boldsymbol{H}^{a,\nu}(x,y) e^{\imath\omega t}, \tag{2.127}$$

with

$$\tilde{\boldsymbol{E}}^{a,\nu}(x,y) = E_x^{a,\nu}(x,y)\hat{\boldsymbol{x}} + E_y^{a,\nu}(x,y)\hat{\boldsymbol{y}} + \frac{\epsilon_a(x,y)}{\epsilon_c(x,y)} E_z^{a,\nu}(x,y)\hat{\boldsymbol{z}}. \tag{2.128}$$

Adopting *bra-ket* notation for later use, Eqs. (2.126) and (2.127) read

$$|c\rangle = \sum_{\nu=1}^{\infty} a_\nu(z) |a^\nu\rangle. \tag{2.129}$$

Equation (2.65) in Sec. 2.6.5 defines the scalar product between two modes. This scalar product only depends on the transversal field components and is defined for two arbitrary modes, not necessarily two modes of the same waveguide. Two modes of the same waveguide are orthogonal (Sec. 2.6.3), but the modes of different waveguides are in general not. We will assume henceforth that the modes of waveguide a are normalized with respect to this scalar product, i.e., we assume that

$$\langle a^\mu | a^\nu \rangle = \delta_{\mu\nu}. \tag{2.130}$$

Differential equations for the modal amplitudes

We have written the electromagnetic field in the coupler as a superposition of the modes of waveguide a, with z-dependent modal amplitudes $a_\nu(z)$. We now derive differential equations that describe the z-evolution of these modal amplitudes. Later, these equations will form the basis for the coupled mode theory.

We start with two electromagnetic fields: $\boldsymbol{\mathcal{E}}^c$, $\boldsymbol{\mathcal{H}}^c$ and $\boldsymbol{\mathcal{E}}^{a,\mu}$, $\boldsymbol{\mathcal{H}}^{a,\mu}$. Both fields are monochromatic with frequency ω hence time evolution is given by $e^{\imath\omega t}$. The first fields, labeled c, are the fields in the directional coupler. The latter is mode μ

of waveguide a, which is a solution to Maxwell's equations for the waveguide with permittivity $\epsilon_a(x,y)$. Its electric field is written as

$$\boldsymbol{\mathcal{E}}^{a,\mu}(x,y,z,t) = \boldsymbol{E}^{a,\mu}(x,y)e^{\imath(\omega t - \beta_{a,\mu}z)}. \tag{2.131}$$

Fields c and a obey Ampères law (2.2) for $\epsilon_c(x,y)$ and $\epsilon_a(x,y)$, respectively,

$$\nabla \times \boldsymbol{\mathcal{H}}^c = \imath\omega\epsilon_c(x,y)\boldsymbol{\mathcal{E}}^c, \quad \nabla \times \boldsymbol{\mathcal{H}}^{a,\mu} = \imath\omega\Big(\epsilon_c(x,y) - \Delta\epsilon_a(x,y)\Big)\boldsymbol{\mathcal{E}}^{a,\mu}. \tag{2.132}$$

Similar to Sec. 2.6.3, we calculate using Faraday's (2.1) and Ampère's (2.132) laws:

$$\nabla \cdot (\boldsymbol{\mathcal{E}}^c \times \boldsymbol{\mathcal{H}}^{*\,a,\mu}) = \imath\omega\Big(\epsilon_c(x,y)\boldsymbol{\mathcal{E}}^c \cdot \boldsymbol{\mathcal{E}}^{*\,a,\mu} - \mu_0\boldsymbol{\mathcal{H}}^c \cdot \boldsymbol{\mathcal{H}}^{*\,a,\mu} - \Delta\epsilon_a(x,y)\boldsymbol{\mathcal{E}}^c \cdot \boldsymbol{\mathcal{E}}^{*\,a,\mu}\Big),$$
$$\nabla \cdot (\boldsymbol{\mathcal{E}}^{*\,a,\mu} \times \boldsymbol{\mathcal{H}}^c) = \imath\omega\Big(\mu_0\boldsymbol{\mathcal{H}}^c \cdot \boldsymbol{\mathcal{H}}^{*\,a,\mu} - \epsilon_c(x,y)\boldsymbol{\mathcal{E}}^c \cdot \boldsymbol{\mathcal{E}}^{*\,a,\mu}\Big),$$

adding up to

$$(\frac{\partial}{\partial x}\hat{\boldsymbol{x}} + \frac{\partial}{\partial y}\hat{\boldsymbol{y}} + \frac{\partial}{\partial z}\hat{\boldsymbol{z}}) \cdot (\boldsymbol{\mathcal{E}}^c \times \boldsymbol{\mathcal{H}}^{*\,a,\mu} + \boldsymbol{\mathcal{E}}^{*\,a,\mu} \times \boldsymbol{\mathcal{H}}^c) = -\imath\omega\Delta\epsilon_a(x,y)\boldsymbol{\mathcal{E}}^c \cdot \boldsymbol{\mathcal{E}}^{*\,a,\mu}.$$

Following the strategy of Sec. 2.6.3, we integrate this equation over a (x,y)-plane, and apply the two-dimensional divergence theorem to obtain

$$\frac{\partial}{\partial z}\hat{\boldsymbol{z}} \cdot \iint (\boldsymbol{\mathcal{E}}^c \times \boldsymbol{\mathcal{H}}^{*\,a,\mu} + \boldsymbol{\mathcal{E}}^{*\,a,\mu} \times \boldsymbol{\mathcal{H}}^c)\ \mathrm{d}x\mathrm{d}y = -\imath\omega \iint \Delta\epsilon_a(x,y)\boldsymbol{\mathcal{E}}^c \cdot \boldsymbol{\mathcal{E}}^{*\,a,\mu}\ \mathrm{d}x\mathrm{d}y, \tag{2.133}$$

in which we used the fact that the integral along a closed contour vanishes for increasing distance to the origin $x = y = 0$. The mode expansion conjecture states that the electromagnetic fields $\boldsymbol{\mathcal{E}}^c$ and $\boldsymbol{\mathcal{H}}^c$ may be written as a superposition of the fields of the modes of waveguide a. We will use this to formulate Eq. (2.133) in terms of the modes of waveguide a. We substitute Eqs. (2.126) and (2.127), together with Eq. (2.131) (and corresponding equation for $H^{a,\mu}$) in Eq. (2.133). We see that all time-dependencies cancel each other. We move the summation over ν outside the integrals, and we also move the z-dependencies outside the integrals, to arrive at

$$\sum_{\nu=1}^{\infty}\iint \hat{\boldsymbol{z}} \cdot \Big(\tilde{\boldsymbol{E}}^{a,\nu} \times \boldsymbol{H}^{*\,a,\mu} + \boldsymbol{E}^{*\,a,\mu} \times \boldsymbol{H}^{a,\nu}\Big)\ \mathrm{d}x\mathrm{d}y \cdot \left(\frac{\partial a_\nu(z)}{\partial z} + \imath\beta_{a,\mu}a_\nu(z)\right)e^{\imath\beta_{a,\mu}z}$$
$$= -\imath\omega\sum_{\nu=1}^{\infty} a_\nu(z)e^{\imath\beta_{a,\mu}z}\iint \Delta\epsilon_a(x,y)\tilde{\boldsymbol{E}}^{a,\nu} \cdot \boldsymbol{E}^{*\,a,\mu}\ \mathrm{d}x\mathrm{d}y. \tag{2.134}$$

The integral in the left-hand-side of the equation is the scalar product between modes ν and μ of waveguide a, which gives $\delta_{\mu\nu}$ since the modes are assumed to have been normalized (the tilde does not influence the scalar product as it only applies to the z-component). Thus the summation on the left-hand-side of this equation reduces to only one term with $\nu = \mu$. We cancel the exponential z-dependence $\exp[\imath\beta_{a,\mu}]$ and solve for $\partial a_\mu/\partial z$ to obtain

$$\frac{\partial a_\mu}{\partial z} = -\imath\beta_{a,\mu}a_\mu - \imath\sum_{\nu=1}^{\infty} a_\nu\tilde{\kappa}^a_{\nu\mu}, \tag{2.135}$$

where

$$\tilde{\kappa}^a_{\nu\mu} \equiv \omega \iint \Delta\epsilon_a(x,y)\tilde{\boldsymbol{E}}^{a,\nu} \cdot \boldsymbol{E}^{*\,a,\mu}\,\mathrm{d}x\mathrm{d}y. \tag{2.136}$$

This is a formulation of electromagnetic fields in terms of the modal fields of waveguide a, with z-dependent modal amplitudes. Equation (2.135) describes how the modal amplitudes change with z. At this point, this may seem a complicated way to write Maxwell's equations, but it will turn out to be very useful when only a limited number of modes are taken into account, such as in the case of the directional coupler.

Exact differential equations for the field in the directional coupler

Without restricting the generality, we may write the electromagnetic fields in the directional coupler (denoted $|c\rangle$) as sum of the fundamental mode of waveguide a, $|a_1\rangle$, the fundamental mode of waveguide b, $|b_1\rangle$ and a residual field, i.e.,

$$\boldsymbol{\mathcal{E}}^c(x,y,z,t) = u_a(z)\tilde{\boldsymbol{E}}^{a,1}(x,y)e^{\imath\omega t} + u_b(z)\tilde{\boldsymbol{E}}^{b,1}(x,y)e^{\imath\omega t} + \boldsymbol{E}^r(x,y,z)e^{\imath\omega t},$$

with analogous equation for $\boldsymbol{\mathcal{H}}^c$. The residual field $\boldsymbol{E}^r(x,y,z)$ may be assumed to be orthogonal to the fundamental modes of waveguides a and b, for each z, with respect to the scalar product (2.65). In *bra-ket* notation, we have

$$|c\rangle = u_a(z)|a^1\rangle + u_b(z)|b^1\rangle + |r(x,y,z)\rangle, \tag{2.137}$$

with

$$\langle a^1|r(x,y,z)\rangle = \langle b^1|r(x,y,z)\rangle = 0. \tag{2.138}$$

Taking the scalar product of Eq. (2.137) with $|a^1\rangle$ gives

$$a_1 = u_a + \langle a^1|b^1\rangle u_b, \tag{2.139}$$

where we used $\langle a^1|c\rangle = a_1$ which follows from the expansion of the field in the coupler $|c\rangle$ in terms of the modes $|a^\nu\rangle$ of waveguide a, see Eq. (2.129). Substituting Eq. (2.139) into Eq. (2.135) gives

$$\frac{\partial u_a}{\partial z} + \langle a^1|b^1\rangle\frac{\partial u_b}{\partial z} = -\imath\Big(\beta_{a1} + \tilde{\kappa}^a_{11}\Big)u_a \\ -\imath\Big(\langle a^1|b^1\rangle\beta_{a1} + \langle a^1|b^1\rangle\tilde{\kappa}^a_{11}\Big)u_b - \imath\sum_{\nu=2}^{\infty} a_\nu\tilde{\kappa}^a_{\nu 1}\,. \tag{2.140}$$

We introduce $\hat{\kappa}_{ab}$ by:

$$\hat{\kappa}_{ab} \equiv \sum_{\nu=1}^{\infty}\langle a^\nu|b^1\rangle\tilde{\kappa}^a_{\nu 1}. \tag{2.141}$$

where $\tilde{\kappa}^a_{\nu 1}$ are given by Eq. (2.136). The first term of the summation in Eq. (2.141), i.e., $\langle a^1|b^1\rangle\tilde{\kappa}^a_{11}$, is already present in the second term of the right-hand-side of

Eq. (2.140). We respectively add and subtract the other terms ($\nu = 2\ ..\ \infty$) to the second and third term of the right-hand-side of Eq. (2.140), and find

$$\frac{\partial u_a}{\partial z} + \langle a^1|b^1\rangle \frac{\partial u_b}{\partial z} = -\imath\Big(\beta_{a1} + \tilde{\kappa}^a_{11}\Big)u_a \\ - \imath\Big(\langle a^1|b^1\rangle\beta_{a1} + \hat{\kappa}_{ab}\Big)u_b - \imath\sum_{\nu=2}^{\infty}\tilde{\kappa}^a_{\nu 1}\Big(a_\nu - \langle a^\nu|b^1\rangle u_b\Big). \quad (2.142)$$

This differential equation is, in fact, the one we were looking for. Coefficient $\hat{\kappa}_{ab}$ is related to the coupling of the fundamental mode of waveguide a, $|a^1\rangle$, to the fundamental mode of waveguide b, $|b^1\rangle$. We will now simplify $\hat{\kappa}_{ab}$ and express it in terms of the modal electric fields $\boldsymbol{E}^{a,1}$ and $\boldsymbol{E}^{b,1}$ of the fundamental modes of the waveguides ($|a^1\rangle$ and $|b^1\rangle$). First we realize that we may express the transversal electric field components of $|b^1\rangle$ as a superposition of the transversal electric fields components of $|a^\nu\rangle$, i.e.

$$\tilde{\boldsymbol{E}}^{b,1} = \sum_{\nu=1}^{\infty}\langle a^\nu|b^1\rangle\tilde{\boldsymbol{E}}^{a,\nu}, \quad (2.143)$$

where we also calculated $\tilde{E}_z^{b,1}$ which is related to $E_z^{b,1}$ using Eq. (2.125) with the labels a replaced by b. Substitution of Eq. (2.136) in Eq. (2.141), and interchanging the order of the integral and the summation reads

$$\hat{\kappa}_{ab} = \omega\iint \Delta\epsilon_a(x,y)\left(\sum_{\nu=1}^{\infty}\langle a^\nu|b^1\rangle\tilde{\boldsymbol{E}}^{a,\nu}\right)\cdot\boldsymbol{E}^{*\,a,1}\,\mathrm{d}x\mathrm{d}y, \quad (2.144)$$

or, employing Eq. (2.143)

$$\hat{\kappa}_{ab} = \omega\iint \Delta\epsilon_a(x,y)\tilde{\boldsymbol{E}}^{b,1}\cdot\boldsymbol{E}^{*\,a,\mu}\,\mathrm{d}x\mathrm{d}y, \quad (2.145)$$

or, in component form and using Eq. (2.125) (for mode b)

$$\hat{\kappa}_{ab} = \omega\iint \Delta\epsilon_a(x,y)\left(E_x^{b,1}E_x^{*\,a,1} + E_y^{b,1}E_y^{*\,a,1} + \frac{\epsilon_b(x,y)}{\epsilon_c(x,y)}E_z^{b,1}E_z^{*\,a,1}\right)\,\mathrm{d}x\mathrm{d}y. \quad (2.146)$$

We derived a differential equation describing the evolution of the amplitudes (u_a and u_b) of the modal fields ($|a^1\rangle$ and $|b^1\rangle$) of the fundamental modes of waveguides a and b. We started by taking the scalar product of Eq. (2.137) with $|a^1\rangle$. Likewise, we may also take the scalar product of this equation with $|b^1\rangle$. This gives Eq. (2.142) with Eq. (2.146) but with labels a and b interchanged. We write this system of differential equations as

$$\boldsymbol{C}\frac{\partial\boldsymbol{u}}{\partial z} = -\imath\left(\boldsymbol{BC} + \hat{\boldsymbol{K}}\right)\boldsymbol{u}(z) - \imath\boldsymbol{W}(z), \quad (2.147)$$

with

$$\boldsymbol{u} = \begin{pmatrix} u_a \\ u_b \end{pmatrix}, \tag{2.148}$$

$$\boldsymbol{C} = \begin{pmatrix} 1 & \langle a^1|b^1\rangle \\ \langle b^1|a^1\rangle & 1 \end{pmatrix}, \tag{2.149}$$

$$\boldsymbol{B} = \begin{pmatrix} \beta_{a,1} & 0 \\ 0 & \beta_{b,1} \end{pmatrix}, \tag{2.150}$$

$$\hat{\boldsymbol{K}} = \begin{pmatrix} \hat{\kappa}_{aa} & \hat{\kappa}_{ab} \\ \hat{\kappa}_{ba} & \hat{\kappa}_{bb} \end{pmatrix}, \tag{2.151}$$

$$\boldsymbol{W}(z) = \begin{pmatrix} \sum_{\nu=2}^{\infty} \tilde{\kappa}^a_{\nu 1} \left(a_\nu - \langle a^\nu|b^1\rangle u_b \right) \\ \sum_{\nu=2}^{\infty} \tilde{\kappa}^b_{\nu 1} \left(b_\nu - \langle b^\nu|a^1\rangle u_a \right) \end{pmatrix}, \tag{2.152}$$

with $\hat{\kappa}_{aa} \equiv \tilde{\kappa}^a_{11}$, $\hat{\kappa}_{bb} \equiv \tilde{\kappa}^b_{11}$, $\hat{\kappa}_{ab}$ given by Eq. (2.146), and $\tilde{\kappa}^a_{\nu 1}$ given by Eq. (2.136).

Equation Eq. (2.147) may be rearranged to

$$\frac{\partial \boldsymbol{u}}{\partial z} = -\imath \left(\boldsymbol{B} + \boldsymbol{K} \right) \boldsymbol{u}(z) - \imath \boldsymbol{C}^{-1} \boldsymbol{W}(z), \tag{2.153}$$

with

$$\boldsymbol{K} = \begin{pmatrix} \kappa_{aa} & \kappa_{ab} \\ \kappa_{ba} & \kappa_{bb} \end{pmatrix}, \tag{2.154}$$

$$\kappa_{aa} = \frac{1}{1 - \langle a^1|b^1\rangle\langle b^1|a^1\rangle} \left(\hat{\kappa}_{aa} - \langle a^1|b^1\rangle \hat{\kappa}_{ba} + \langle a^1|b^1\rangle\langle b^1|a^1\rangle \left(\beta_{a,1} - \beta_{b,1} \right) \right),$$

$$\kappa_{bb} = \frac{1}{1 - \langle a^1|b^1\rangle\langle b^1|a^1\rangle} \left(\hat{\kappa}_{bb} - \langle b^1|a^1\rangle \hat{\kappa}_{ab} + \langle a^1|b^1\rangle\langle b^1|a^1\rangle \left(\beta_{b,1} - \beta_{a,1} \right) \right),$$

$$\kappa_{ab} = \frac{1}{1 - \langle a^1|b^1\rangle\langle b^1|a^1\rangle} \left(\hat{\kappa}_{ab} + \langle a^1|b^1\rangle \left(\beta_{a,1} - \beta_{b,1} - \hat{\kappa}_{bb} \right) \right),$$

$$\kappa_{ba} = \frac{1}{1 - \langle a^1|b^1\rangle\langle b^1|a^1\rangle} \left(\hat{\kappa}_{ba} + \langle b^1|a^1\rangle \left(\beta_{b,1} - \beta_{a,1} - \hat{\kappa}_{aa} \right) \right).$$

Note that these equations are exact (provided the mode expansion conjecture is correct). That is, these are Maxwell's equations in an alternative representation, which is suitable for coupled-mode analysis.

Approximations and solutions of the differential equations

We approximate the analysis of the directional coupler by neglecting $\boldsymbol{W}$ in Eq. (2.153). This term is related to the other modes of the system, not being the fundamental mode of waveguide a or b. More specifically, we assume that for higher-order modes ($\nu \geq 2$), $\tilde{\kappa}^a_{\nu 1} a_\nu$ and $\tilde{\kappa}^a_{\nu 1}\langle a^\nu|b^1\rangle$ are much smaller then $\hat{\kappa}_{aa}$, $\hat{\kappa}_{ab}$, and $\beta_{a,1}$ (and a similar requirement with a and b interchanged). This assumption is justified by the results of rigorous FDTD simulations, discussed in Sec. 2.10.2, which show that directional couplers in SOI technology have little loss, i.e., almost all energy resides in the modes of waveguides a and b.

The fundamental modes of waveguides a and b are almost orthogonal which allows to neglect all terms involving $\langle a^1|b^1\rangle$ or $\langle b^1|a^1\rangle$. When neglecting these terms, $\boldsymbol{C}$ reduces to the identity matrix and $\hat{\boldsymbol{K}} = \boldsymbol{K}$. The results obtained with this additional approximation did not differ appreciably from keeping these terms in the model. We nevertheless kept the terms with $\langle a^1|b^1\rangle$ or $\langle b^1|a^1\rangle$ in the equations.

By neglecting $\boldsymbol{W}$, i.e, neglecting the coupling to higher-order (radiation, evanescent and backwards-traveling) modes, Eq. (2.153) becomes

$$\frac{\partial \boldsymbol{u}}{\partial z} = -\imath\left(\boldsymbol{B} + \boldsymbol{K}\right)\boldsymbol{u}(z). \tag{2.155}$$

We consider a coupler in which all energy resides in waveguide b at $z = 0$, i.e. $\boldsymbol{u} = (0, 1)$. Solving Eq. (2.155) for this initial condition gives[11]

$$u_a(z) = -\frac{\imath\kappa_{ab}}{s}\sin(sz)\, e^{-\imath(\beta_{b,1}+\kappa_{bb}-\delta)z}, \tag{2.156}$$

$$u_b(z) = \left(\cos sz - \frac{\imath\delta}{s}\sin sz\right) e^{-\imath(\beta_{b,1}+\kappa_{bb}-\delta)z}, \tag{2.157}$$

$$\delta = \frac{1}{2}\left(\beta_{b,1} + \kappa_{bb} - \beta_{a,1} - \kappa_{aa}\right), \tag{2.158}$$

$$s = \sqrt{\kappa_{ab}\kappa_{ba} + \delta^2}. \tag{2.159}$$

These equations describe the behavior of the parallel waveguides in a directional coupler, when all the field is in the fundamental mode of waveguide b at $z = 0$. These equations are identical to Eqs. (2.113) and (2.114) that were previously presented and explained (but not derived) in the beginning of Sec. 2.10.

Comparison with Literature

We have followed the approach of Hardy & Streifer [31] from 1985, together with the unified notation presented by Hardy in 1998 [32]. In comparison with their derivation, we introduced a few changes. Our analysis is fully based on the orthogonality relation (2.53) rather than relation (2.58). Forward- and backwards-traveling modes are orthogonal in this relation, so that we may use a single summation over all forward- and backwards traveling modes. In the directional coupler, excitation of the backwards traveling modes can be neglected, and these modes

[11] We write Eq. (2.155) as $\partial\boldsymbol{u}/\partial z = -\imath\boldsymbol{M}\boldsymbol{u}(z)$, with $\boldsymbol{M} = \begin{pmatrix} m_a & \kappa_{ab} \\ \kappa_{ba} & m_b \end{pmatrix}$, $m_a = \beta_{a,1} + \kappa_{aa}$, and $m_b = \beta_{b,1} + \kappa_{bb}$. We look for solutions in the form $\boldsymbol{u}(z) = \boldsymbol{a}^{\pm}\exp[-\imath\lambda^{\pm}z]$. Substituting this in the differential equation gives $\lambda^{\pm}\boldsymbol{a}^{\pm} = \boldsymbol{M}\boldsymbol{a}^{\pm}$, which we recognize as the eigenvalue equation for $\boldsymbol{M}$ with eigenvalues $\lambda^{\pm}$. This equations has solutions when $\det|\boldsymbol{M} - \boldsymbol{I}\lambda^{\pm}| = 0$, from which we find the eigenvalues $\lambda^{\pm} = \frac{1}{2}(m_a + m_b) \pm \frac{1}{2}\sqrt{(m_a + m_b)^2 - 4(m_a m_b - \kappa_{ab}\kappa_{ba})}$ $= \frac{1}{2}(m_a + m_b) \pm \sqrt{\frac{1}{4}(m_b - m_a)^2 + \kappa_{ab}\kappa_{ba}} = \frac{1}{2}(m_a + m_b) \pm s$, with s and δ defined in Eqs. (2.159) and (2.158). From the eigenvalue equation of $\boldsymbol{M}$, we find eigenvectors $\boldsymbol{a}^{+} = (\kappa_{ab}, \delta + s)$ and $\boldsymbol{a}^{-} = (\kappa_{ab}, \delta - s)$. If we solve the general solution of the differential equation, $\boldsymbol{u}(z) = c^{+}\boldsymbol{a}^{+}\exp[-\imath\lambda^{+}z] + c^{-}\boldsymbol{a}^{-}\exp[-\imath\lambda^{-}z]$, for initial condition $\boldsymbol{u}(0) = (0, 1)$, we find $c^{-} = -c^{+}$ and $c^{+} = 1/2s$, giving Eqs. (2.156) and (2.157).

lumped together with the radiative and evanescent modes in the residual field $\boldsymbol{E}^r(x, y, z)$. We have assumed a lossless material with real permittivity $\epsilon_c(x, y)$. In the description of the fields in terms of the modes of waveguide a, we followed Kogelnik [27] and started our derivation with the orthogonality relation (2.53) including the complex conjugates, which led to a slightly different notation for $\tilde{\kappa}^a_{\nu\mu}$, Eq. (2.136), and $\hat{\kappa}_{ab}$, Eq. (2.146). With real transversal fields, the longitudinal (z) component of the field is imaginary, which indeed causes a minus sign in the definition of $\hat{\kappa}_{ab}$ in Refs. [31] and [32]. The derivation here is for two parallel waveguides without z-dependency in the permittivity. However, the derivation is extendable to the more general case by changing $\epsilon_c(x, y)$ to $\epsilon_c(x, y, z)$, leading to z-dependence of $\tilde{E}^{a,\nu}_z$, $\tilde{E}^{b,\nu}_z$, $\tilde{\kappa}^a_{\nu\mu}$, $\tilde{\kappa}^b_{\nu\mu}$, $\hat{\kappa}_{ab}$, $\hat{\kappa}_{ba}$, $\hat{\kappa}_{aa}$, $\hat{\kappa}_{bb}$, $\hat{\boldsymbol{K}}$, and $\boldsymbol{K}$. In Ref. [32] it is stated that neglecting the radiation and the backwards propagating waves may not be justified in the case of waveguides with high refractive index contrast. Our comparison with rigorous FDTD simulations show that by far the most energy indeed resides in the fundamental modes of the waveguides, such that neglecting the residual fields is allowed for parallel waveguides. In contrast, gratings in silicon introduce strong scattering, which will not only couple the fundamental mode to another mode, but couple to a spectrum of modes. We have tried to formulate the approach of Hardy & Streifer as clear as possible, with consistent notation, and including all steps.

In comparison with the work of Yariv, Refs. [35] and [83], the most important difference is in contrast to our approach is that Yariv approximate the modes as pure TE or pure TM. Typical typical SOI-waveguides have relevant longitudinal components of the electromagnetic fields, and neglecting them underestimates the coupling between waveguides. Furthermore, Ref. [83], approximates the fundamental modes of isolated waveguides a and b to be orthogonal, which is admittingly a good approximation for typical SOI waveguides.

Implementation and comparison with other methods

We implemented the coupled mode theory in Matlab, in which we used the modal fields as computed with a numerical mode-solver (FMM method in FimmWave), using a discretization grid of 5 nm. In Fig. 2.13c on page 45, we compare the calculated coupling coefficient s with other methods. It can be seen that there is a good agreement between the methods, so that the use of the coupled mode theory is justified for typical directional couplers in high-index-contrast silicon waveguides.

2.11 Out-of-plane grating couplers

Silicon photonic integrated circuits have a large refractive index contrast allowing for small device footprint, which is convenient for most applications. However, it makes in-and-out coupling of light into the photonic integrated circuit (PIC) very difficult, since one has to match a $\sim$9 μm fiber core with a $\sim$0.5 μm waveguide. The use of out-of-plane grating couplers circumvent this problem by employing a grating that redirects the light from the waveguide upwards. Radiation occurs

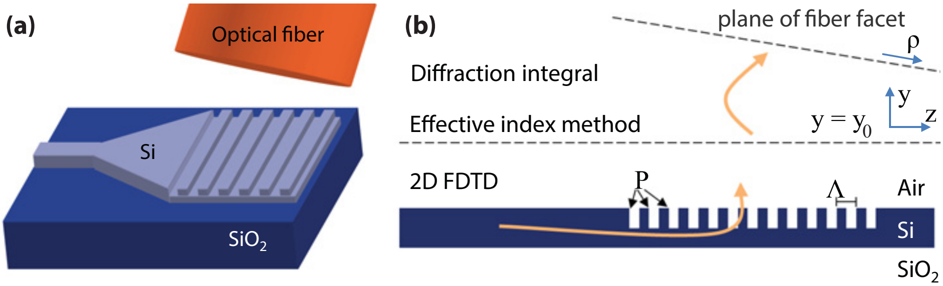

Figure 2.19: Sketches of out-of-plane grating coupler. Silicon layer height 220 nm and grating etch depth 70 nm. Waveguide width is 450 nm. Grating Coupler width 10 μm, and grating length is $\sim$15 μm. **(a)** Impression. **b** Cross-section of the grating coupler. An efficient simulation method (2D FDTD, effective index method and diffraction integral) is outlined.

from an area on the top surface of the PIC, allowing for a coupler with the same dimensions as the fiber core (Fig. 2.19a). Dielectric grating couplers date from the 1970's, and designs for SOI technology have been presented over the last decade by, among others, Gent University [85–88]. The large tolerance of the alignment of the optical fiber with respect to the couplers and the relatively straightforward CMOS fabrication make these coupler often preferable over end-fire-coupling or butt-coupling, both for characterization of integrated photonic components in labs, as well as for fiber-pig-tailing silicon integrated photonic devices. The devices reported in this thesis all have basic out-of-plane grating couplers, with a coupling efficiency of about -5 dB (30%), although more advanced grating coupler designs exist today (see Sec. 2.11.2). One of the interesting features of sensing with (ring-) resonators is that transmission loss does not have a large influence on the sensitivity.

2.11.1 Basic grating couplers

A basic grating coupler consists of a very wide (10 μm) waveguide with a grating etched in its top surface. We define a *basic* grating coupler as a one-dimensional grating in a wide waveguide with all identical and rectangular grating grooves. Advanced couplers may, for example, have a concentric cylindrical gratings, different profiles of the grooves or teeth of the grating, or an apodized grating period (see Sec. 2.11.2). For basic grating couplers, the variations of the electromagnetic fields in the x-direction are slow with respect to the variations in the y- and z-directions (see Fig. 2.19b). In and near the coupler, we may approximate the shape of the electromagnetic fields in the x-direction as the shape of the fundamental mode of the waveguide. In Ref. [89], we have justified this approximation and also proposed an efficient simulation method for out-of-plane grating couplers in which the propagation through air is computed with a two- or three-dimensional diffraction integral.

The behavior of the coupler can intuitively be understood by considering all the tall-to-short interfaces on the edge of the grating grooves as "point-source" which have a phase difference dictated by the propagation speed of the light through the waveguide (a few of such point-sources are indicated by P in Fig. 2.19b). The effective (refractive) index of the grating can be estimated as the spatially weighted average of the effective indices of the fundamental modes in the tall and short parts of the waveguide. The fields emitted by these point-sources constructively interfere to a far field that is a plane wave propagating under a certain angle θ_q w.r.t. the y-axis. This angle is given by

$$n_3 \sin(\theta_q) = n_e - q\frac{\lambda}{\Lambda}, \tag{2.160}$$

where n_3 is the refractive index of the upper medium (air in Figure 2.19), n_e is the averaged effective index of the grating, q is the diffraction order and Λ is the grating period. For perfect vertical coupling, $\theta_q = 0°$, Eq. (2.160) describes the second order resonance of a distributed Bragg reflector (DBR), which very efficiently reflects the forward propagating light in the waveguide backwards, rather than radiating it upwards. For low index contrast waveguides, Eq. (2.160) has been derived using coupled mode theory; treating the grating as a perturbation of the waveguide and calculating the coupling coefficient between the waveguide mode and a plane wave radiating with angle θ_q [36, 37]. To our knowledge, the validity of this perturbation approach has not been verified for high-index-contrast guides, and it is common to use numerical methods (e.g., FDTD). We have compared Eq. (2.160) with the strongest far-field radiation angle, and found good agreement for etch depths up to 110 nm for a free-space wavelength of 1550 nm. For efficient coupling to a fiber, the grating should be designed such that only one coupling order ($q = 1$) is allowed, and the coupling strength should be designed between strong upwards coupling and low backwards reflections. The ratio between upwards and downwards radiation is strongly influenced by the height of the buried oxide (BOX) layer.

We have developed an efficient scheme for numerical simulation of such out-of-plane grating couplers. This scheme consists of four steps: a 2D FDTD simulation which describes the propagation from the waveguide to a plane just above the coupler. Then, the effective index method is applied to calculate the lateral profile of the field, based on the width of the grating in this plane, resulting in a 3D field profile. Thereafter, Rayleigh-Sommerfeld diffraction is used to propagate the field from this plane to the plane of the fiber facet and finally an overlap integral is used to calculate the coupling into the fiber mode. In what follows, we will detail the theory behind each of these steps.

Two-dimensional calculations and the effective index method

A two-dimensional (y,z) analysis can be used in the vicinity of the coupler up to approximately one wavelength above the grating. To obtain the lateral profile in a plane just above the coupler, we apply a method similar to the effective index method (EIM) by approximating the field $\mathcal{E}_x$ as $\mathcal{E}_x(x, y, z) = \mathcal{E}_x^{2D}(y, z) \cdot E_x^{\mathrm{mode}}(x)$, where $\mathcal{E}_x^{2D}$ is the electric field as calculated using two-dimensional analysis (assuming invariance in the x-direction) and lateral field profile $E_x^{\mathrm{mode}}(x)$ is approximated from the lowest order mode in the waveguide.

Propagation into the upper-half space

To obtain the electromagnetic field radiated into the homogeneous half space $y > y_0$ by a finite aperture or source in the plane $y = y_0$ one can use the Rayleigh-Sommerfeld diffraction integral [90]. In our case, the finite aperture is a sufficiently large part of the plane just above the grating coupler such that the electromagnetic fields outside this aperture are small and hence may be neglected. The medium above y_0 is air. The diffraction integral for monochromatic light is written as [90]:

$$U(x,y,z) = \iint\limits_{\text{aperture}} U(x',y_0',z')G(x,y,z;x',y_0',z')dx'dz', \tag{2.161}$$

where

$$G = \frac{(1+\imath kr)}{2\pi}\frac{(y-y_0')}{r}\frac{\exp(-\imath kr)}{r^2}, \tag{2.162}$$

$$r = \sqrt{(x-x')^2+(y-y_0')^2+(z-z')^2}, \tag{2.163}$$

and U is any electric or magnetic field component in phasor notation with time dependence given by $e^{i\omega t}$. The Greens' function G is the sum of the fields of two in-phase point sources that are images of each other with the plane $y = y_0'$ as mirror. This choice of Greens' function allows the field in the air to be described as a function of the field in the aperture, not requiring knowledge of the normal derivative of the field. When the field is calculated for a horizontal plane (y constant), G depends on $x - x'$ and $z - z'$, so Eq. (2.161) is a 2D convolution, which can be very efficiently calculated using fast-fourier-transforms (FFTs) [91]. When the plane is tilted along the x-direction, the inner integral over x' is a convolution and can be calculated using FFTs. The 2D equivalent of Eq. (2.161), where $U = U(y,z)$, is obtained by integrating Eq. (2.161) along x', resulting in [92]:

$$U(y,z) = \int\limits_{\text{aperture}} U(y_0',z')G(y,z;y_0',z')dz', \tag{2.164}$$

where

$$G = \frac{-\imath k}{2}\frac{(y-y_0')}{r}H_1^{(2)}(kr), \tag{2.165}$$

$$r = \sqrt{(y-y_0')^2+(z-z')^2}, \tag{2.166}$$

where $H_1^{(2)}(kr)$ is the first Hankel function of the second kind, i.e. $H_1^{(2)}(kr) = J_1(kr) - \imath Y_1(kr)$ where J_1 and Y_1 are the first order Bessel functions of the first and second kind, respectively.

Coupling into a fiber

The power flux through the plane S just before the fiber can be calculated using Eq. (2.59) integrated over the plane of the fiber-end. The power coupling efficiency for TE-like modes can be estimated by [38]:

$$\eta_{\text{overlap}} = \frac{|\iint \mathcal{E}_x^i(x,\rho) \cdot \mathcal{E}_x^f(x,\rho) d\mathbf{S}|^2}{\iint |\mathcal{E}_x^i(x,\rho)|^2 d\mathbf{S} \cdot \iint |\mathcal{E}_x^f(x,\rho)|^2 d\mathbf{S}}, \tag{2.167}$$

where $\mathcal{E}_x^i$ is the x-component of electric field incident on the fiber facet. Coordinates x and ρ are in the tilted plane, parallel to the fiber facet (see Fig. 2.19). The fiber mode of a standard single-mode fiber can be approximated by a Gaussian beam [93]. Details of coupling from air into the fiber are neglected since there is a small refractive index step and a small angle of incidence of the incoming wave. When the field $\mathcal{E}_x^i$ can be separated in x and ρ dependence, i.e $\mathcal{E}_x^i(x,\rho) = \mathcal{E}_x^{i,x}(x) \cdot \mathcal{E}_x^{i,\rho}(\rho)$, then the overlap η_{overlap} can also be separated, i.e. $\eta_{\text{overlap}} = \eta_{\text{overlap},x} \cdot \eta_{\text{overlap},\rho}$.

2.11.2 Advanced grating couplers

The basic grating coupler has four major of drawbacks, which are to a large extend solved by new grating coupler designs. First, in 220 nm high waveguides, light is directed not only upwards but also in the unwanted downwards direction, accounting for 35% to 45% of loss [94]. This problem can be solved by increasing the height of the waveguide such that the downwards reflections in the grating coupler cancel each other, thereby directing the light predominantly upwards. Such grating couplers can be fabricated in wafer-scale CMOS processes by depositing an amorphous silicon layer on top of the 220 nm waveguide layer [88, 94]. In this way, efficiencies up to -1.6 dB (69%) have been reported for the of coupling of electromagnetic power from a 220 nm high silicon waveguide to a standard single-mode optical fiber. Alternatively, mirrors can be included in the substrate, but this approach has not been demonstrated in wafer-scale CMOS processes. The second drawback is that the radiation is strongest from the first grating tooth and decays exponentially with larger distance z from the beginning of the grating. Hence the radiation profile has poor mode-matching with the Gaussian-shaped mode of an optical fiber (contributing to ~20% of efficiency loss) [94]. An apodized grating can match the radiation profile to the optical fiber (Ref. [95] reported the efficiency record of -1.2 dB or 76%), but these fine grating structures can not be fabricated in today's wafer-scale CMOS technology (the first groove in Ref. [95] is 44 nm wide). The third drawback is that the adiabatic taper from the small waveguide to a the wider waveguide is a few hundred microns long and thus occupies a substantial footprint on the photonic chips. This drawback can be overcome by using a focusing grating coupler, in which the light at the end of the straight waveguide diffracts because the waveguide rapidly tapers in width (angle of 27°) [96]. For such a cylindrical wave-front, it is possible to design a cylindrical grating that couples the light to a single mode fiber. The fourth drawback of the basic grating structure is that it introduces reflections (below 6%) from the connecting waveguide back into the device, forming an undesired Fabry-Pèrot cavity between the input and the output grating couplers of the device. The focused grating coupler can be designed such that the light reflecting back from the cylindrical grating does not focus on the waveguide, but just next to it. By this reflections are reduces while the efficiency remains on the order -5 dB, similar to the efficiency of the basic grating couplers [97, 98]. Probably the most favorable grating coupler design is reported in Ref. [99]. It is wafer-scale CMOS compatible, and combines the reflectionless focused grating couplers with increased upwards directivity using a grating that has a higher waveguide, thereby providing -2.2 dB (60%) coupling efficiency with -40 dB (0.01%) back-reflections.

2.12 Ring and racetrack resonators

In Fig. 2.20, racetrack-shaped ring resonators are shown which are coupled to one or two waveguides. In this section we study the power $|b_1|^2$ that is transmitted to the output waveguide and the power $|a_d|^2$ in the so-called *drop port* of the configuration in which the ring resonator is coupled to two waveguides, the so-called *add-drop* configuration.

First the configuration with a single coupler is considered (Fig. 2.20a,b). All waveguides are single-mode and the complex amplitudes of the traveling modes in the waveguides (a_1, a_2, b_1 and b_2) are normalized such that their squared magnitude corresponds to the power in the mode. A lossless coupler without reflections is generally described by[12]

$$\begin{pmatrix} b_1 \\ b_2 \end{pmatrix} = \begin{pmatrix} \tau^* & \kappa \\ -\kappa^* & \tau \end{pmatrix} \begin{pmatrix} a_1 \\ a_2 \end{pmatrix}, \tag{2.168}$$

with $|\tau|^2 + |\kappa|^2 = 1$. This matrix does not depend on the specific type of coupler. After one round-trip through the racetrack, the wave has experienced a phase

[12] We will use power conservation to show that we may write the lossless transmission matrix $\boldsymbol{U}$ in the notation of Eq. (2.168) with only two unknowns τ and κ. First we will show that the transmission matrix is unitary, i.e., that its inverse equals the transpose of its complex conjugate, $\boldsymbol{U}^{-1} = \boldsymbol{U}^{*T}$, so that $\boldsymbol{U}^{*T}\boldsymbol{U} = \boldsymbol{I}$ (with identity matrix $\boldsymbol{I}$). The general transmission matrix equation for a system without reflections is

$$\begin{pmatrix} b_1 \\ b_2 \end{pmatrix} = \begin{pmatrix} A & \kappa \\ B & \tau \end{pmatrix} \begin{pmatrix} a_1 \\ a_2 \end{pmatrix}.$$

We express b_1 and b_2 in terms of a_1 and a_2, and compute

$$b_1 b_1^* + b_2 b_2^* = (AA^* + BB^*)a_1 a_1^* + (\kappa\kappa^* + \tau\tau^*)a_2 a_2^* + (A\kappa^* + B\tau^*)a_1 a_2^* + (A^*\kappa + B^*\tau)a_1^* a_2.$$

This power flow out of the coupler, $|b_1|^2 + |b_2|^2$, should be equal to the power flow into the coupler, $|a_1|^2 + |a_2|^2$, for arbitrary a_1 and a_2. Hence

$$(AA^* + BB^*) = 1, \quad (\kappa\kappa^* + \tau\tau^*) = 1, \quad (A\kappa^* + B\tau^*) = 0, \quad (A^*\kappa + B^*\tau) = 0$$

We use these relations to compute $\boldsymbol{U}^{*T}\boldsymbol{U}$ and find $\boldsymbol{U}^{*T}\boldsymbol{U} = \boldsymbol{I}$. The lossless transmission matrix $\boldsymbol{U}$ is thus unitary. Now using $\boldsymbol{U}^{-1} = \boldsymbol{U}^{*T}$ gives

$$\frac{1}{D}\begin{pmatrix} \tau & -\kappa \\ -B & A \end{pmatrix} = \begin{pmatrix} A^* & B^* \\ \kappa^* & \tau^* \end{pmatrix},$$

with $D = A\tau - \kappa B$. Hence $|D| = 1$, $A = D\tau^*$, and $B = -D\kappa^*$. Arbitrarily choosing $D = 1$ gives Eq. (2.168).

delay ϕ_r and a loss:

$$a_2 = \alpha e^{\imath\phi_r} b_2, \tag{2.169}$$

where α^2 is the power that is transmitted through one round-trip of the ring (i.e., $\alpha = 1$ means no loss). The power in the output waveguide, $|b_1|^2$, is obtained by solving Eqs. (2.168) and (2.169) for $|b_1|$. First we substitute Eq. (2.169) in the last row of Eq. (2.168) to find

$$b_2 = \frac{-\kappa^*}{1 - \tau\alpha e^{\imath\phi_r}} a_1. \tag{2.170}$$

Subsituting this consecutively in Eq. (2.169) and in the first row of Eq. (2.168) gives

$$b_1 = \left(\tau^* - \frac{\kappa\kappa^*\alpha e^{\imath\phi_r}}{1 - \tau\alpha e^{\imath\phi_r}}\right) a_1. \tag{2.171}$$

We define $\tau = |\tau|e^{\imath\phi_\tau}$ and use $\tau\tau^* + \kappa\kappa^* = 1$ to rewrite Eq. (2.171) as

$$b_1 = \frac{-\alpha + |\tau|e^{-\imath(\phi_r+\phi_\tau)}}{e^{-\imath\phi_r} - \alpha|\tau|e^{\imath\phi_\tau}} a_1 \tag{2.172}$$

Finally we compute $b_1 b_1^*$ and use $2\cos\theta = \left(e^{\imath\theta} + e^{-\imath\theta}\right)$ to arrive at [100]

$$|b_1|^2 = \frac{\alpha^2 + |\tau|^2 - 2\alpha|\tau|\cos\theta}{1 + \alpha^2|\tau|^2 - 2\alpha|\tau|\cos\theta}|a_1|^2, \tag{2.173}$$

where θ is the net phase delay of traveling through the ring and coupler

$$\theta = \phi_r + \phi_\tau. \tag{2.174}$$

In the case of two bus waveguides with identical couplers (Fig. 2.20c), Eqs. (2.169) and (2.173) still apply, provided we include the transmission through the second coupler in the track round-trip by replacing α by $\alpha|\tau|$, giving

$$|b_1|^2 = \frac{\left(\alpha^2 + 1 - 2\alpha\cos\theta\right)|\tau|^2}{1 + \alpha^2|\tau|^4 - 2\alpha|\tau|^2\cos\theta}|a_1|^2, \tag{2.175}$$

and Eq. (2.174) changes to

$$\theta = \phi_r + 2\phi_\tau. \tag{2.176}$$

The amplitude of the mode in the *drop* output waveguide is

$$a_d = \sqrt{\alpha}|\kappa|e^{\imath(\phi_r/2+\phi_\kappa)} b_2, \tag{2.177}$$

in which the *drop* bus waveguide is exactly located symmetric to the *input* bus waveguide, so that the wave travels half a round-trip from b_2 to the second coupler. Solving Eqs. (2.168), (2.169), and (2.177) for $|a_d|^2$ gives

$$|a_d|^2 = \frac{(1 - |\tau|^2)^2\alpha}{1 + \alpha^2|\tau|^4 - 2\alpha|\tau|^2\cos\theta}|a_1|^2 \tag{2.178}$$

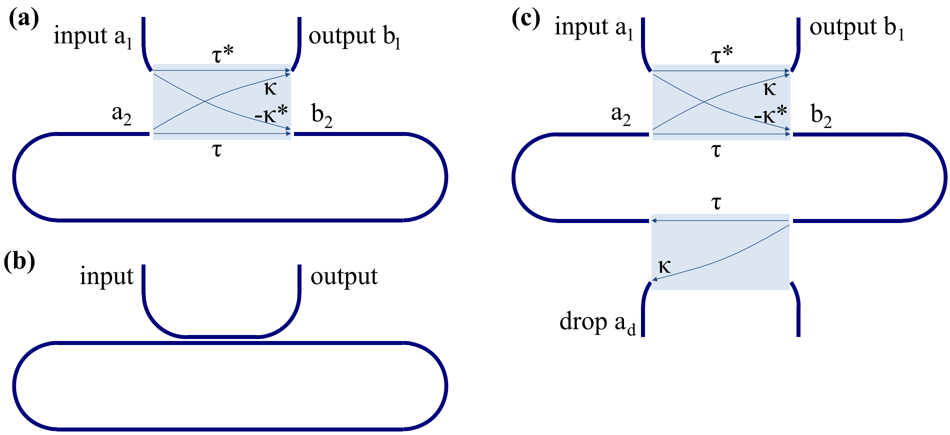

Figure 2.20: Racetrack-shaped ring resonator with one and two coupler(s). **(a)** Sketch with the coupling described by a general transmission matrix. **(b)** Layout of a racetrack resonator with 450 nm wide waveguides, a straight track of 40 μm, a bend radius of 5 μm, and a coupler as in Fig. 2.12a. **(c)** Sketch of a racetrack with two couplers (add-drop configuration).

2.12.1 Silicon ring resonators with directional couplers

We now apply the general ring theory to the racetrack resonators with directional couplers in add-drop configuration with two coupled waveguides (Fig 2.20c). The racetrack including the couplers has lenght l. The transmission τ through the directional couplers with effective length $\tilde{L}$ is given by Eq. (2.113). The phase delay due to propagation through a waveguide with length $l - 2\tilde{L}$ is, according to Eq. (2.67), equal to $\phi_r = -\beta(l - 2\tilde{L})$. Hence the total phase delay of the ring is

$$\theta = -\beta l + 2\delta\tilde{L} - 2\kappa_{bb}\tilde{L} + 2\arg\left\{\cos s\tilde{L} - \frac{\imath\delta}{s}\sin s\tilde{L}\right\}. \tag{2.179}$$

For typical silicon-on-insulator racetrack resonators, the second and third term at the right-hand-side of this equation are small ($\delta, \kappa_{bb} \ll \beta$). The uncertainty in the propagation constant β due to imperfect fabrication is larger than δ and κ_{bb}. The last term of Eq. (2.179) is usually small as the real part of the complex number of which the argument is taken is much larger than the imaginary part that is proportional to δ/s. This term can also be close to π when the real part is negative. However, in the particular case that nearly all light is coupled from/to the resonator, $\cos s\tilde{L} \approx 0$ and the argument is then close to $\pi/2$ rad. We recall that the dispersion in the effective index n_e and in the directional coupler coefficient s can considered to be linear, while the dispersion in $\tilde{L}$ is negligible (see Secs. 2.6 and 2.10, respectively). For a coupler with two identical waveguides, neglecting the κ_{bb}, and with linear dispersion of the effective index, Eq. (2.179) reduces to

$$\theta = -\beta l = -2\pi\left[\frac{n_e - n_g}{\lambda_c} + \frac{n_g}{\lambda}\right] l, \tag{2.180}$$

with n_e and n_g evaluated at the center wavelength λ_c.

The loss in the coupler can be approximated by the loss in the isolated waveguide, thus the round-trip transmittance $\alpha = e^{-\alpha_p l}$ where α_p is the propagation loss of the waveguide.

2.12.2 Ring resonator resonances

In this section, we compute some relevant characteristics of the transmission spectra that are described by Eq. (2.173). The relations derived in this section give insight in the behavior of racetrack resonators and are useful to the designers of such resonators. For simplicity, we consider ring and racetrack resonators with only one connected waveguide. The transmission spectrum of the connected waveguide is given by $|b_1|^2$ as a function of wavelength. It shows dips for $\theta = 2\pi m$, with m an integer number. For the case of two identical waveguides in the coupler (i.e., $\delta = 0$) and neglecting κ_{bb}, the resonance wavelengths λ_m are

$$m \cdot \lambda_m = n_\mathrm{e}(\lambda_m) \cdot l. \tag{2.181}$$

The free spectral range (FSR) is the difference between the resonance wavelengths of two adjacent resonances m and $m+1$. The FSR may be approximated by linearizing the relation between m and $\lambda(m)$, i.e., $m = (n_e(\lambda) \cdot l)/\lambda$, and then computing $|\Delta\lambda|$ for $\Delta m = 1$. This gives

$$\Delta\lambda_\mathrm{FSR} = \left|\frac{\partial\lambda}{\partial m}\right| \cdot 1 = \frac{\lambda^2}{\left(n_e - \lambda\frac{\partial n_e}{\partial\lambda}\right) l} = \frac{\lambda^2}{n_g l}, \tag{2.182}$$

where it was useful to compute $\partial\lambda/\partial m$ via $(\partial m/\partial\lambda)^{-1}$. The last equality sign follows from Eq. (2.32).

At resonance, $\cos\theta = 0$ and Eq. (2.173) becomes

$$|b_1|^2 = \frac{(\alpha - |\tau|)^2}{(1-\alpha|\tau|)^2}|a_1|^2. \tag{2.183}$$

From Eq. (2.183) it is observed that there is no transmission at the wavelengths of the dips when $|\tau| = \alpha$, hence when the round-trip loss of the racetrack is equal to the power coupled to the racetrack. This condition is called *critical coupling*. The minimum, $|b_1|^2_\mathrm{min}$, and maximum, $|b_1|^2_\mathrm{max}$, transmitted power occur at resonance and in between the resonances, respectively. The extinction ratio $r \equiv |b_1|^2_\mathrm{min}/|b_1|^2_\mathrm{max}$ and the full-width at half-max (FWHM) of the dips in Eq. (2.173) are

$$r = \frac{(\alpha - |\tau|)^2(1+\alpha|\tau|)^2}{(\alpha + |\tau|)^2(1-\alpha|\tau|)^2}, \tag{2.184}$$

and

$$\Delta\lambda_\mathrm{FWHM} = \frac{\lambda^2}{\pi l n_g}\cos^{-1}\left[\frac{2\alpha|\tau|}{1+\alpha^2|\tau|^2}\right]. \tag{2.185}$$

The relation for $\Delta\lambda_\mathrm{FWHM}$ is found by solving[13] Eq. (2.173) for $\cos\theta$ at half-max, i.e. with $|b_1|^2 = (|b_1|^2_\mathrm{max} + |b_1|^2_\mathrm{min})/2$, and then employing the linearized relation

[13] The full-width at half-max in terms of phase θ is $\Delta\theta_\mathrm{FWHM} = 2\cos^{-1}\left[\frac{2\alpha|\tau|}{1+\alpha^2|\tau|^2}\right]$.

between the phase delay and vacuum wavelength. The relations in Eq. (2.184) and Eq. (2.185) explicitly show the shape of the resonances as a function of the waveguide and coupler properties, and are very useful in the design of resonators. The FWHM depends on the losses in the resonator (transmittance $\alpha|\tau|$), and it scales with the free spectral range (FSR), while the extinction ratio r scales with $(\alpha - |\tau|)^2$ so that critical coupling is most important. The equations in this section, Eqs. (2.181 - 2.185), are also valid for the case of two couplers when α is replaced by $\alpha\tau$, i.e., the second coupler acts as an additional source of loss.

2.12.3 Ring resonators with a non-uniform waveguide

It is sometimes advantageous to use a ring resonator in which the width of the waveguide varies. The fundamental mode of wider waveguides have a lower group index, giving a higher sensitivity of rings employed as sensors; however, these guides support multiple lateral modes which are exited when the waveguide is bent. Adiabatically tapering the wide waveguide to a single-mode waveguide before the bends of the resonator prevents the excitation of the higher modes. For ring resonator with a varying waveguide width and of which the coupler(s) consist of two identical waveguides (i.e., $\delta = 0$), the phase delay of one round-trip is

$$\theta = -\oint \beta(\rho, \lambda_m)\mathrm{d}\rho, \tag{2.186}$$

in which the integral runs over the circumference of the track. We have neglected κ_{bb}. Comparing Eq. (2.186) with Eq. (2.180) shows that the previously presented theory for uniform guides remains applicable provided that the track-averaged effective indices are used

$$\langle n_e \rangle = \frac{1}{l}\oint n_e(\rho)\mathrm{d}\rho, \tag{2.187}$$

$$\langle n_g \rangle = \frac{1}{l}\oint n_g(\rho)\mathrm{d}\rho. \tag{2.188}$$

2.13 Design of racetrack resonators for strain and ultrasound sensing

This section presents the rationale behind the design of the racetrack resonators for the sensing of strain and ultrasound. The size and shape of these sensors is determined by acoustical/mechanical requirements.

The strains sensors are long racetracks with straight track lengths varying from 250 μm to 1000 μm. Having long resonators allows to neglect the mechanical effects at the bends of the racetracks. Hence the mechanical properties in the resonator can be considered homogeneous. The strain sensors are interrogated using a broadband light source and an optical spectrum analyzer. The full transmittance spectrum is recorded and fitting can be used to obtain an accuracy below the resolution bandwidth of the spectrum analyzer. However, such measurements

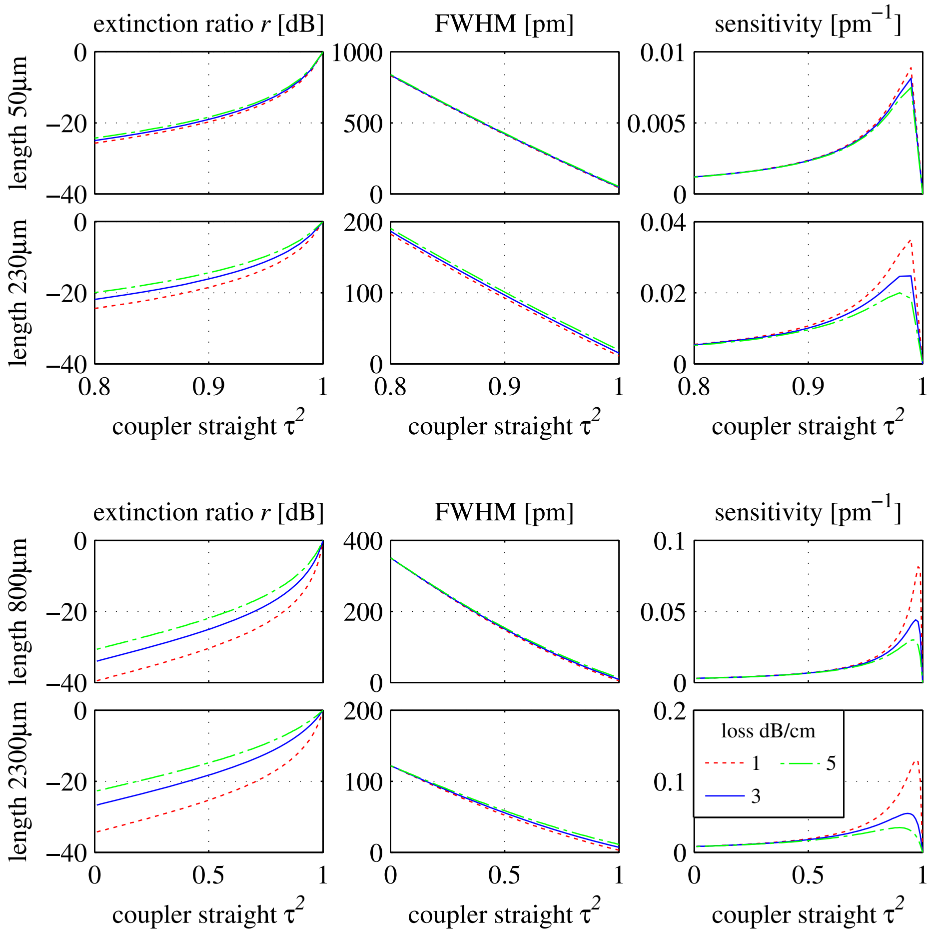

Figure 2.21: Design of the directional couplers for racetrack resonators. Horizontal axis: straight-through power $|\tau|^2$ (coupled power $|\kappa|^2 = 1 - |\tau|^2$). Upper two rows: racetracks for ultrasound sensors. Lower two rows: racetracks for strain sensors. First and second columns are calculated using Eq. (2.184) and (2.185), repectively. The losses in the racetracks are 1 dB/cm, 3 dB/cm and 5 dB/cm plus an additional 0.1 dB for the bends (legend in right-bottom plot). The effective group index $n_g = 4.28$ and free-space wavelength $\lambda_c = 1550$ nm. Sensitivity (right column) is estimated as the extinction ratio devided by the FWHM ($r/\Delta\lambda_{\mathrm{FWHM}}$).

are rather slow (minutes). To be sure of good interrogation, we designed the resonators with an extinction ratio of at least -10 dB (i.e. transmission at a resonance is maximum 10% of the off-resonant transmission).

The ultrasound sensors are placed on acoustical resonant membranes. Using wafer-scale fabrication by IMEC via the ePIXfab consortium, many chips with the same photonic circuitry were fabricated simultaneously. Then the the wafers were diced so that each *die* (piece of a silicon wafer) contained one or more chips. Later, membranes of different sizes were fabricated in the different dies. This was done by etching holes in the silicon substrate from the back-side of the chip. As we had not finalized the acoustical design when fabricating the photonic circuity, we decided to place different racetrack resonators in the chip design, with straight-track lengths varying from 10 μm to 100 μm. Ultrasonic measurements require a high interrogation speed, therefore we used a different interrogation method than the optical spectrum analyzer. We tuned the wavelength of a laser to the flank of a resonance dip of an acoustical sensor, and recorded the transmitted power at high speed (20 MHz). A shift of the resonance dip changes the transmitted laser intensity. The steeper the flank of the resonances, the more sensitive the sensor. We estimate the sensitivity of the optical resonator in the sensor as the extinction ratio divided by the FWHM ($r/\Delta\lambda_{\text{FWHM}}$) which has the unit relative power per (wave-) length.

As the shapes of the sensors were fixed by mechanical requirements, only the couplers were still free to choose. When designing the chip, there was a high uncertainty in the coupling coefficient s of directional couplers, thus also in the power $|\tau|^2$ being coupled from and to the ring resonator. This was due to the fabrication process and also because we it was the first chip design with directional couplers that was fabricated by our team. Hence we had no experimental figures on the characteristics of the directional couplers. However, it can be assumed that two couplers with identical design behave approximately the same, as differences caused by the fabrication vary only little over one chip. Also the waveguide loss was not exactly specified when we designed the chip. IMEC specified a typical waveguide loss of 3 dB/cm but IMEC did not specify the tolerance in this number, i.e. the range in which waveguide loss will certainly lay. In the last years, the ePIXfab platform has matured and many of these numbers are now better known.

We have designed the racetrack resonators with two identical couplers. Although this design has a poor FWHM of the resonance dips, it is robust against fabrication variations. When a single coupler is used, critical coupling requires that the loss in the ring is compensated by the power coupled to the ring. Because the loss and coupled power are known only to a certain extent, there is a large change of ending up with a poor extinction ratio. When two couplers are used, the power coupled to and from the ring can be chosen such that it is larger than the loss in the ring. To realize strain sensors with a good extinction ratio, we chose a design with directional couplers that coupler 50% of optical power to and from the ring (i.e., $|\tau|^2 = 0.50$). A large deviation in the relative power that is coupled to the ring will still give an acceptable extinction ratio (Fig. 2.21, lower two rows). For ultrasound sensors, we chose to couple 5% of power to the ring (i.e., $|\tau|^2 = 0.95$). The highest sensitivity would be obtained with a coupling of only 2%, but these designs have the disadvantage that a slight increase of coupling quickly reduces the sensitivity (see the upper two rows of Fig. 2.21).

2.14 Conclusion

In photonic integrated circuits (PICs), light is guided through waveguides and components that are in a planar chip. Silicon-on-insulator is one of the most promising technologies because PICs can be fabricated in the same CMOS infrastructure as electronic integrated circuits (ICs). Moreover, silicon PICs are small and strong. One of the key component in silicon PICs is a ring resonator which can be employed as filter or modulator.

Most properties of silicon ring resonators and their components (waveguides and directional couplers) can be computed using approximate analytical theories. Many theories on integrated optics were originally derived for low-index-contrast waveguides like optical fibers ($\Delta n < 0.1$). We reviewed and revised those theories for application to silicon-on-insulator waveguides which have a very high index contrast ($\Delta n \approx 2$).

Analytical theories allow fast computation of the behavior of photonic devices and circuits. This is especially important when considering large circuits that consist of many components. Moreover, we believe that analytical theories provide insight in the physics of the system that is difficult to reveal with brute-force numerical simulations.

Chapter

3 Characterization of silicon micro-ring resonators

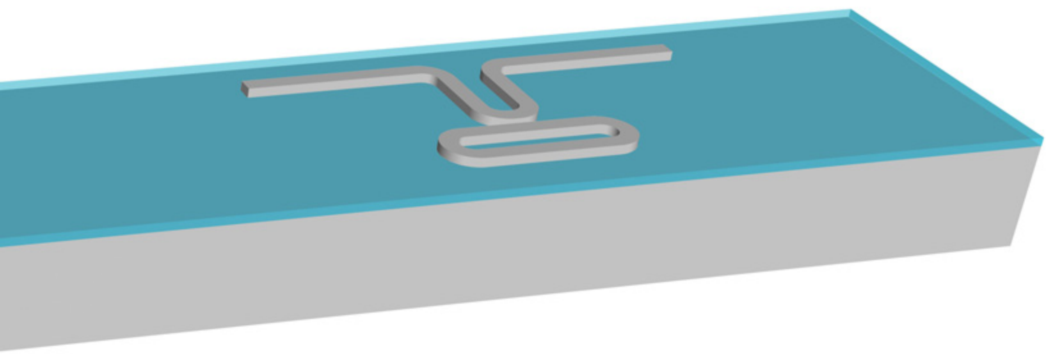

Abstract – Silicon micro-ring resonators are widely used and studied as filters in the field of optical communication and as sensitive elements in the field of sensing. This chapter provides a methodology for the characterization of micro-ring resonators and their components (waveguides and directional couplers) and reports on the obtained characteristics of a chip that was fabricated via the ePIXfab platform. Wavelength dependency and loss of the components is incorporated in the characterization. Different characterization methods for directional couplers are compared, such as power transmission measurements and methods based on ring resonator transmittance spectra. Good agreement is found between the methods. It is shown that the performance of directional couplers depends significantly on the wavelength. Moreover, we theoretically and experimentally demonstrate a large coupling-induced phase delay that occurs when nearly all light is coupled from one waveguide to the other, i.e., when the coupler operates as a cross-coupler. In this regime, ring resonators in add-drop configuration showed a change of 28% in the free-spectral-range which could be explained by a difference of only 0.1% in the propagation constants of the two waveguides. Last, the measured coupling-coefficients of directional couplers are compared with numerical simulations and significant disagreement is found. This is possibly due to imperfect deposition of the SiO_2 cladding between the waveguides of the directional couplers.

3.1 Introduction

This chapter is about the optical characteristics of the resonators that we apply as strain- and ultrasound sensors in the chapters hereafter.

One of the key components in silicon integrated circuits are micro-rings, which are used as resonant filters for the routing and modulation of tele-communication signals, and also as sensing element (biomedical-) sensors [101–103]. The field of silicon photonic micro-ring resonators and their applications has recently been reviewed in Refs. [79, 104–106].

In this work, we detailedly characterize silicon micro-ring resonators which were fabricated in modern CMOS processes. All components of the resonator, such as the waveguides, the bends, and the couplers, are fully characterized. We describe

The results presented in Sec. 3.7 were published as W. J. Westerveld, J. Pozo, S. M. Leinders, M. Yousefi, and H. P. Urbach, "Demonstration of large coupling-induced phase delay in silicon directional cross-couplers," *IEEE Journal of Selected Topics in Quantum Electronics*, vol. 20, no. 4, 2014, *to appear*.

The results presented in Sec. 3.9 were published by W.J. Westerveld, J. Pozo, M. Yousefi, H.P. Urbach as "Critical coupling of optical microring resonators for opto-mechanical sensors" in Europractice IC Service Activity Report 2011, pp. 22-23, 2012. These results were also presented in April 2012 at the 16th European Conference on Integrated Optics (ECIO) in Barcelona (talk nr. 187) and in September 2012 at the European Optical Society Annual Meeting (EOSAM) in Aberdeen (talk nr. 5995).

the micro-ring resonators with simple analytical models that include all the observed effects. Wavelength-dependency is taken into account in all measurements.

Silicon photonic devices and components have been extensively reported and characterized in literature [64,79,107–110]. In this chapter, we report on a methodology to characterize the properties of silicon ring-resonator based photonic integrated circuit (PICs). This chapter features, to the best of our knowledge, some analyses that have not been reported before.

In particular, we compared four different methods to characterize directional couplers. These methods are based on two different types of devices: sole directional couplers and directional couplers that are loaded with ring resonators. The latter devices are studied in more detail and equations are presented that include all the phenomena that we observed in the transmission spectra. This includes the effect of wavelength-dependency of the coupling coefficient and the effect of a minute asymmetry between the waveguides of the coupler. In Refs. [79, 110], a Mach-Zehnder based device was used to characterize the coupler; however, asymmetry and phase delay of the coupler were not measured. In the mathematical description, we included the coupling which occurs in the bends into account as a delta length (rather than a delta coupling as in [79, 110]), which allowed us to neglect wavelength dependency of this term.

We studied the phase delay that is introduced by directional couplers. For a coupler with two identical waveguides and with effective length $\tilde{L}$ shorter than the length L_π for which all power transfers from one waveguide to the other, the phase delay may be approximated by the phase delay of an isolated waveguide ($\beta_b \tilde{L}$). However, there has been recent interest in a more precise characterization of the couplers. Ref. [111] reported on a Mach-Zehnder interferometer with a ring coupled to one of its arms. It was shown that correcting the length of the other arm for the coupler-induced phase delay significantly improves the filter response. Ref. [112] reported on a theoretical and numerical study of the influence of the coupling-induced phase delay on a cascade of ring resonators. A modified design for cascaded resonators was presented in which the rings were adjusted to compensate for the coupling induced phase delay. We observed the additional phase delay that is introduced by directional couplers in the cross-coupling regime, i.e., when nearly all light couplers from one waveguide to the other. To the best of our knowledge, we were the first to report on the fact that a ring resonator with two couplers in the cross-coupling regime is particularly sensitive to the difference between the two waveguides.

This chapter is organized as follows. In Sec. 3.3, we describe the process of the fabrication and metrology of the devices in silicon-on-insulator technology. In Secs. 3.5, 3.6 and 3.8, we present the characterizations of the waveguides loss, directional couplers and waveguide group indices (guide widths 310 nm to 860 nm), respectively. In Sec. 3.7, we demonstrate that directional couplers introduce a large additional phase delay when nearly all light is coupled from one waveguide to the other. In Sec. 3.9, we illustrate the influence of critical coupling by studying the spectra of small racetrack-shaped ring resonators that have high losses due to their small bending radius of 3 μm. In Sec. 3.10, we compare measured coupling-coefficients of directional couplers with numerical simulations and we find significant disagreement. This is possibly due to imperfect deposition of the silicon-dioxide cladding layer between the waveguides of the directional couplers. We intended to provide a dateset for the designers of silicon photonic resonators, but the uncertainty in the cladding precludes the use of this dataset for future designs. In Sec. 3.11, we conclude the chapter.

3.2 Theory

For the convenience of the reader, we summarize the theory of Chapter 2 that is needed to describe the behavior of light in the devices we characterize in this chapter.

3.2.1 Waveguides (summary of Sec. 2.6)

Waveguides in silicon-on-insulator technology consist of a rectangular silicon rod embedded in silica (see Fig. 2.5 on page 29). We use infrared light around vacuum wavelength λ_c to excite "TE-like" modes of the waveguides. For a guide in the z-direction (i.e., with a refractive index $n(x, y)$), such a mode is described by Eq. (2.67):

$$\boldsymbol{\mathcal{E}}(x, y, z, t) = \boldsymbol{E}(x, y)e^{\imath\omega t - \imath\beta z - \alpha_p z}, \tag{3.1}$$

with modal electric field profile $\boldsymbol{E}(x, y)$, angular frequency ω, time t, modal propagation constant β, and propagation loss α_p. In this thesis, we approximate the wavelength dependency of the effective index by a linear relation, so that we may express the propagation constant $\beta(\lambda)$ around center wavelength λ_c in terms of the effective index $n_e(\lambda_c)$ and effective group index $n_g(\lambda_c)$, as given by Eq. (2.33) or Eq. (3.8). Henceforth, we drop the explicit (λ_c) notation and assume that n_e and n_g without explicit wavelength dependency are evaluated at λ_c.

3.2.2 Directional couplers (summary of Sec. 2.10)

A directional coupler consists of two parallel waveguides that are so close that power couples from one waveguide (labeled a) to the other (labeled b, see Fig. 2.12 on page 45) via the evanescent fields of the modes. Describing this system with coupled mode theory, the electric field in the coupler is approximated by a superposition of the two modes of the isolated waveguides. The amplitudes of the two modes, $u_a(z)$ and $u_b(z)$, vary while propagating through the coupler. Upon excitation of mode b at te left-hand-side of the coupler, the amplitude of mode b after propagation through the lossless coupler is given by $u_b(\tilde{L}) = \tau u_b(0)$, with τ given by Eq. (2.113):

$$\tau(\lambda) = e^{-\imath(\beta_b(\lambda)+\kappa_{bb}-\delta)\tilde{L}} \left(\cos\left[s(\lambda)\tilde{L}\right] - \frac{\imath\delta}{s(\lambda)} \sin\left[s(\lambda)\tilde{L}\right] \right), \tag{3.2}$$

with $\beta_b(\lambda)$ the propagation constant of waveguide b, κ_{bb} a small correction on β_b due to the vicinity of the other waveguide, 2δ the difference between the corrected propagation constants of the two waveguides, $s(\lambda)$ the coupling coefficient, and

$\tilde{L}$ the effective length of the coupler. This length $\tilde{L} = L + \Delta L$, with L the length of the two parallel waveguides and ΔL a correction for the coupling in the bends (see Secs. 2.10, 2.10.3 and Eqs. (2.156-2.159)). Ref. [79] incorporates the coupling in the bends using a correction in the phase rather than a correction in the length. We believe that a correction ΔL in the length is more useful because we showed that this term is relatively wavelength independent and that it is only weakly sensitive to details of the geometry of the coupler. The correction of the propagation constant κ_{bb} is very small compared to the propagation constant β_b and we did not observe it due to fabrication-induced uncertainty in β_b. Therefore we neglect $\kappa_{bb} \ll \beta_b$ in the remainder of this thesis. Moreover, we study waveguides that are designed to be identical, but observed a very small asymmetry $\delta \ll s, \beta_b$. (Ref. [79] neglects this asymmetry.)

As throughout this work, we assume linear dispersion of the effective index so that $\beta_b(\lambda)$ is given by Eq. (2.33) or Eq. (3.8). We also assume linear dispersion in the coupling coefficient s, i.e.,

$$s(\lambda) = s_c + s_c' \cdot (\lambda - \lambda_c), \tag{3.3}$$

with $s_c \equiv s(\lambda_c)$ and $s_c' = \partial s/\partial\lambda$ at λ_c. We neglect dispersion in ΔL, which is validated by the fact that the obtained relations accurately describe the measured spectra. The numerical analysis in Sec. 2.10.2 also showed that the wavelength dependency of ΔL may be neglected.

3.2.3 Ring resonators with two couplers (summary of Sec. 2.12)

The behavior of light in micro-ring resonators with two couplers was introduced in Sec. 2.12. Figure 2.20c on page 67 shows the schematics of a ring resonator with length l and two identical couplers (i.e., with drop waveguide). The rings are described in terms of the straight-through amplitude of the couplers τ, the round-trip amplitude transmittance α ($\alpha = 1$ means zero loss), and round-trip phase delay θ. The latter consists of the the phase delay due to propagation through the waveguide of the ring $\phi_r = -(l - 2\tilde{L})\beta_b$, and twice the phase delay due to the coupler $\phi_\tau = \arg\{\tau\}$. We excite the rings with infrared light in the input waveguide (modal amplitude a_1) and measure power in the output waveguide (modal amplitude b_1) and in the drop waveguide (modal amplitude a_d). Equations (2.175), (2.176), and (2.178) describe the powers at the output waveguide, $|b_1|^2$ and drop waveguide, $|a_d|^2$ in terms of the power in the input waveguide $|a_1|^2$:

$$|b_1|^2 = \frac{\left(\alpha^2 + 1 - 2\alpha\cos\theta\right)|\tau|^2}{1 + \alpha^2|\tau|^4 - 2\alpha|\tau|^2\cos\theta}|a_1|^2, \tag{3.4}$$

$$|a_d|^2 = \frac{(1 - |\tau|^2)^2\alpha}{1 + \alpha^2|\tau|^4 - 2\alpha|\tau|^2\cos\theta}|a_1|^2, \quad \text{with} \tag{3.5}$$

$$\theta = \phi_r + 2\phi_\tau.$$

Note that α, τ, and especially θ are wavelength dependent, so that these equations describe transmission spectra.

Employing the full equation of the directional coupler, Eq. (3.2), to compute the straight through transmitted power in the coupler $|\tau|^2$ and to compute the total phase delay θ of a racetrack round-trip gives

$$|\tau(\lambda)|^2 = \cos^2 s(\lambda)\tilde{L} + \left|\frac{\delta}{s(\lambda)}\right|^2 \sin^2 s(\lambda)\tilde{L}, \tag{3.6}$$

$$\theta(\lambda) = -\beta_b(n_e, n_g, \lambda)l + 2\delta\tilde{L} + 2\arg\left\{\cos s(\lambda)\tilde{L} - \frac{\imath\delta}{s(\lambda)}\sin s(\lambda)\tilde{L}\right\}, \tag{3.7}$$

with

$$\beta_b(\lambda) = 2\pi\left(\frac{n_e - n_g}{\lambda_c} + \frac{n_g}{\lambda}\right), \tag{3.8}$$

$$\tilde{L} = L + \Delta L, \tag{3.9}$$

$$s(\lambda) = s_c + s_c' \cdot (\lambda - \lambda_c), \tag{3.10}$$

with n_e and n_g evaluated at λ_c, i.e. the explicit (λ_c) is dropped from the notation and $n_e \equiv n_e(\lambda_c)$ and $n_g \equiv n_g(\lambda_c)$. Equation (3.8) is copied from Eq. (2.33).

3.2.4 Neglecting coupler asymmetry and wavelength-dependency

It is often possible to neglect the small asymmetry between the waveguides in the coupler, i.e., $\delta = 0$. Moreover, is often possible to neglect the wavelength dependency of the coupler coefficient $s(\lambda)$, i.e., $s(\lambda) = s_c$ and $s' = 0$.

In this case, the power transmitted straight through the directional coupler $|\tau|^2$ is, from Eq. (3.6),

$$|\tau|^2 = \cos^2[s_c(L + \Delta L)]. \tag{3.11}$$

The total phase delay of a round-trip through the ring with two couplers, θ as given by Eq. (3.7), reduces to

$$\theta = -\beta_b l = -2\pi\left[\frac{n_e - n_g}{\lambda_c} + \frac{n_g}{\lambda}\right] l, \tag{3.12}$$

with ring circumference l. The propagation constant depends on wavelength and is expressed in terms of n_e and n_g at λ_c via Eq. (3.8). When the racetrack consists of a waveguide width a varying width, the track-averaged effective index $\langle n_e\rangle$ and group index $\langle n_g\rangle$ may be used in this equation, see Eqs. (2.187 and 2.188). The resonance wavelengths of a ring resonator λ_m, i.e., the wavelengths with minimal transmission, are given by

$$m\lambda_m = n_e(\lambda_m) \cdot l = \left[\frac{\lambda_m}{\lambda_c} n_e + \left(1 - \frac{\lambda_m}{\lambda_c}\right) n_g\right] l, \tag{3.13}$$

with resonance number m and using Eqs. (2.181) and (2.32).

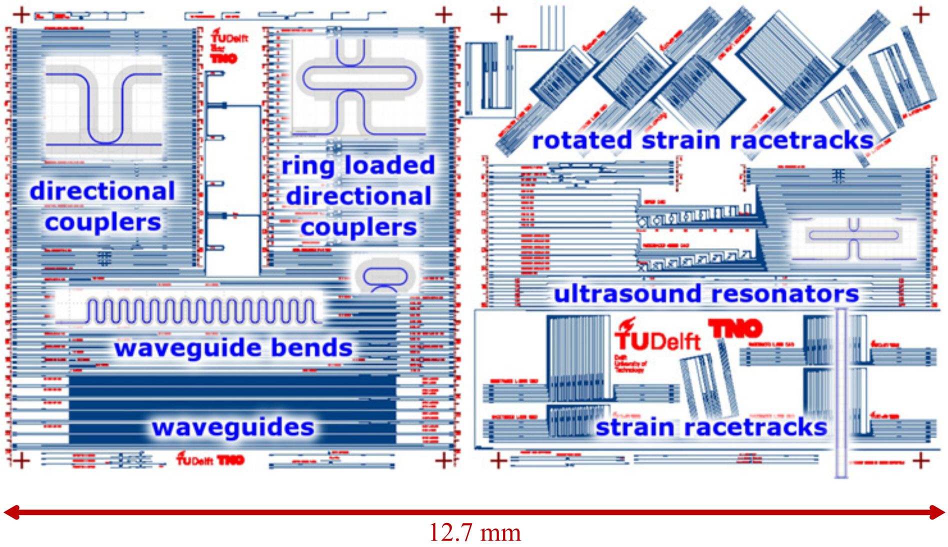

Figure 3.1: Chip-design with a few hundred devices. Showing original GDSII computer-aided-design file with overlaying examples of devices.

3.3 Technology and metrology

All experimental results in this thesis are obtained from one chip design containing a few hundred devices (Fig. 3.1). These integrated optical devices were fabricated in silicon-on-insulator technology, with 220 nm thick rectangular waveguides of mono-crystalline silicon embedded in silica.

The devices were fabricated via the ePIXfab consortium at IMEC (Leuven, Belgium) [24,26]. IMEC fabricated the devices in their semi-industrial CMOS line with 193 nm deep-UV lithography. The diameter of the wafers was 200 mm. We submitted our design for the IMEC08 multi-project-wafer shuttle (October 2011) meaning that the designs of different users are simultaneously fabricated to reduce cost. We briefly report on this participation, but we warn the reader that this is the short story. Good and frequent communication with the fab (IMEC in our case) is essential to successful participation and we gratefully knowledge IMEC's support throughout the process. First we registered for the run and booked an area on the optical mask (chip size 12.7 × 6.3 mm^2). We asked for three wafers, two with the normal thickness and two that were thinned from the back for the fabrication of the ultrasound sensors (this is not a standard option and was kindly provided by IMEC). Then we designed the photonic circuits. We used L-Edit (Tanner EDA, Monrovia, California) to draw the designs and convert them to proper drawings in the GDSII file format. However, more suitable tools dedicated to photonic designs are available today.[1] The drawings in the GDSII-files have to obey a certain set of

[1] ePIXfab supports, among others, the PhoeniX Suite (Phoenix BV, Enschede, The Netherlands) and IPKISS (Ghent University, Belgium).

rules to ensure proper fabrication. This is verified by a design rule check (DRC). It is advisable to do a DRC as early as possible in the process, for example after a typical device has been designed and drew. Our final design did not fully pass the DRC due to the non-standard resonators in the <100> crystalline direction (rotated 45°). However, we agreed with IMEC that the reported violations where due to the check and actually not in the design itself. After a few months, the devices were fabricated and wafers were shipped to us. The wafer with the normal thickness was *diced* (cut) in-house because we required some chips to be diced along the non-standard <110> direction (for the strain sensors, see Ch. 4). We characterized devices with the nominal lithography dose.

The dimensions of the fabricated devices typically differ from the designed sizes. This is especially the case when the patterns have a large variation in the typical dimensions, which is the case for integrated optical devices in a multi-project-wafer [24]. The directional coupler is the most critical pattern on our chip design, as it has a small gap (∼200 nm) between the two waveguides. The widths of the gap and surrounding waveguides might differ from the designed ones due to the optical proximity effect in the lithography or due to the lag effect in the etching. The waveguides are not perfectly rectangular but slightly trapezoidal because the etch process causes slanted side walls with a ∼10° angle. This corresponds to a significant difference of 76 nm between the widths at the top and at the bottom of the waveguide. Throughout this thesis, we refer to the average width of the waveguide. Sections 2.9 and 2.10.1 numerically show that behavior of light in such trapezoidal waveguides is very well approximated by the behavior in rectangular waveguides with the average width. We compared trapezoidal waveguides with rectangular waveguides and found agreement within 1% for the effective index n_e of waveguides, the effective group index n_g of waveguides, and for the the coupling constants s of directional couplers.

The height of the waveguides was designed to be 220 nm and we have measured that the variation is below three nanometers. This was measured using a surface profiler (Bruker Dektak XT from Bruker, Billerica, Massachusetts, USA). This is much more accurate than the specified variation of 10%.

We have measured the dimensions of the fabricated waveguides and couplers with a helium-ion-microscope (HIM, Zeiss Orion Plus from Carl Zeiss SMT, Oberkochen, Germany) [113–115]. In a helium ion microscope, a beam of positively charged helium ions is focused to a sub-nm area of the surface of the chip, where it extracts electrons, which are then detected. The beam scans the surface of the chip, and extracts few electrons at the silicon-dioxide layer, more electrons at the silicon structures, and even more electrons at the side-walls of these structures. A directional coupler is depicted in Fig. 3.2. Imaging silicon-on-insulator structures with charged particles (ions or electrons) suffers from accumulation of charge in the silicon devices, as they are isolated by the silicon-dioxide layer. This charging deteriorates the images as the charged devices repel the incoming particle beam. To overcome this problem, the HIM is equipped with a *flood gun* which uses a coarse electron beam to discharge the positively charged devices while imaging. The interpretation of the images and sizing of the devices was done by an experienced operator. Figure 3.2 show an example of a HIM image with the sizing of the

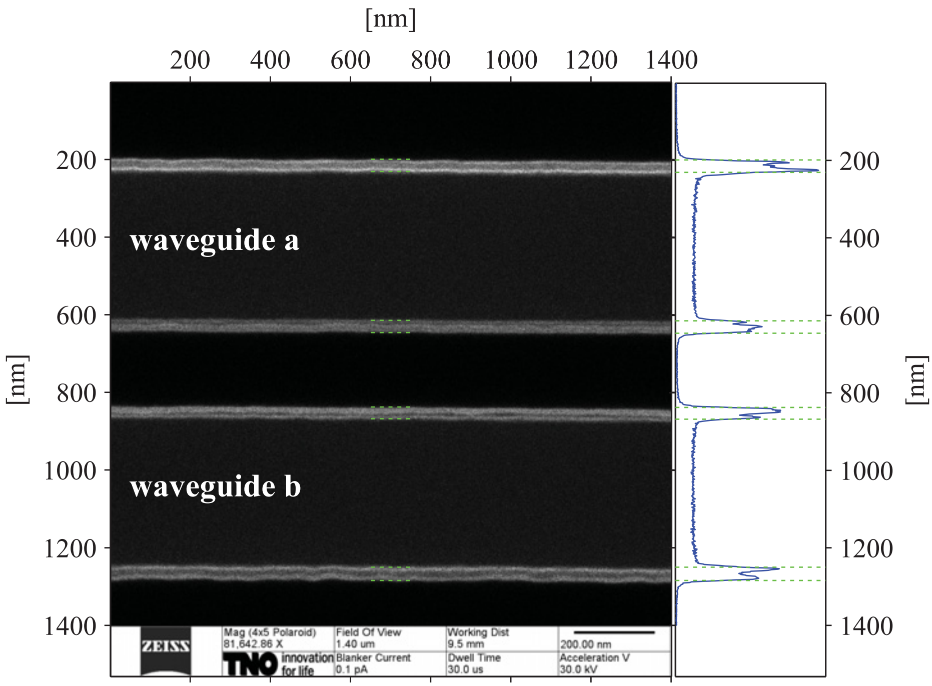

Figure 3.2: Helium ion microscope image of directional coupler (HIM, Zeiss Orion plus of Carl Zeiss SMT). The waveguides have a trapezoidal shape; the side-walls of the waveguides have an angle of ∼10°. The high-intensity "lines" are the four side-walls of the two guides. Right graph shows the average intensity of a 100 nm wide strip in the center of the image. Light-green dashed lines show the sizing of the upper and lower edges of the waveguides.

waveguides and the gap of a directional coupler. The accuracy of measurements of the widths of the waveguides and gaps was estimated below 15 nm.

We characterized the functionality of the chip before we preformed the metrology on the device dimensions. The metrology was performed on a different chip of the same wafer with the same nominal lithography dose because we had deposited the SiO_2 cladding on the original chip. The isolated waveguides (widths ranging from 309 nm to 860 nm) show a linear relation between the designed width and the measured width of the fabricated waveguide (see Fig. 3.3). The devices are 10% smaller than designed. The waveguide with 450 nm designed width was fabricated as 397 nm. IMEC performed metrology on 5 wafers in the IMEC8 run (not including our chip wafers). A waveguide with a design width of 450 nm was fabricated at an average width of 410 nm (mean of all wafers) with a variation of 8 nm [116]. This agrees with our measurements within the measurement accuracies. We measured the waveguides in directional couplers with a designed width of 450 nm as 391 nm, 392 nm, and 394 nm, similar to the width of the isolated

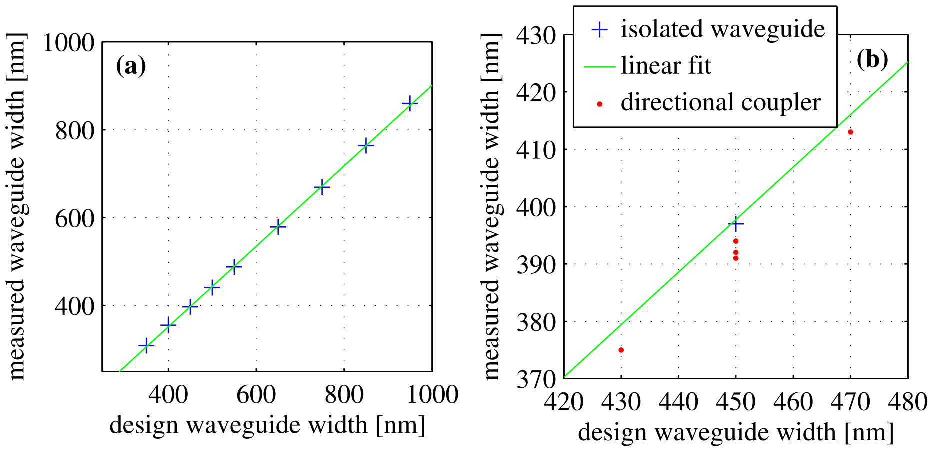

Figure 3.3: Metrology of the waveguide sizes with helium ion microscope (HIM), showing the average width of the top and bottom of the waveguides. (b) is a zoom-in of (a). Isolated vertical waveguides (blue plusses). Linear fit of the measured width versus the designed width of the isolated waveguides, tangent 0.92 nm/nm (solid green line). Horizontal waveguides in directional couplers (red dots, in (b)).

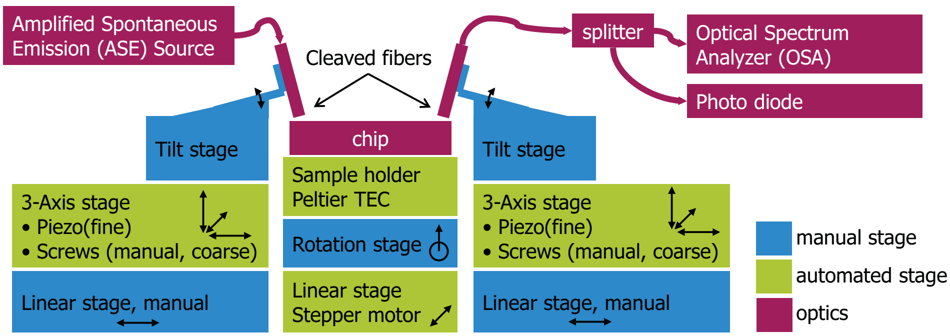

Figure 3.4: Schematics of the measurement setup. See Sec. 3.4 for description. The small arrows indicate in which direction the mechanical stages can move. The thick arrows in the top of the figure indicate optical fibers. Photos of the setup can be found in Appendix B.

waveguide (397 nm). The optical proximity effect and the lag effects did thus not significantly affect the fabrication of the directional couplers.

We have deposited the SiO_2 cladding using plasma-enhanced chemical vapor deposition (PECVD). However, the disagreement between the measured coupling of directional couplers and the simulated coupling suggests that our PECVD is imperfect. The main concern is the deposition of SiO_2 in the small gap between the waveguides, as imperfect deposition might not completely fill the gap. The PECVD process is detailed in Appendix A.

3.4 Measurement setup

The photonic circuitry has out-of-plane grating couplers to couple the light from the waveguides to optical fibers which are positioned above the photonic chip, and vice versa [89, 93]. The alignment tolerances of these couplers is large compared to the alignment tolerance with butt coupling. The fibers are positioned under an 8 degree angle with respect to the normal on the chip surface.

The measurements of the chip are automated in order to provide a high repeatability of the alignment. The setup consists of a vacuum chuck on which the chip is placed, and two 3-axis positioning stages which hold the fibers (Fig. 3.4). The chuck has a Peltier element to control the temperature. The chip is manually positioned on the chuck, and the height of the in/output fibers is manually adjusted to approximately a few hundred microns above the chip surface. We used standard single-mode fibers for a wavelength of 1550 nm (similar to Ref. [43]). The grating couplers of adjacent devices are placed next to each other with a minimum spacing of 25 μm and the chuck is placed on a motorized linear stage which moves the required device coarsely to the position below the fibers. In-plane alignment of the fibers is done automatically with piezo-electric actuators in the positioning stages, which have sub-micron resolution. The active alignment is achieved by maximizing the transmitted power through the to-be measured device, while sequentially scanning the 4 in-plane axis of the two fibers. The piezo-electric actuators showed high repeatability (without hysteresis) when the movement was always done downwards from the maximum voltage. Note that the device-to-device difference in alignment for a set of devices is thus only from the automated alignment, as the manual alignment is not changed anymore. We performed ten repetitive measurements of the devices that are used for loss characterization and we found that the maximum deviation in the transmitted power in a 5 nm wavelength span was below 0.3 dB.

We used an amplified spontaneous emission source (Opto-link ASE) to emit 50 mW of light in the C-band with an emission spectrum between 1528 nm and 1565 nm. No more than 12 mW of light is coupled to the chip (the grating couplers have a theoretical efficiency of about -3 dB for input with the right polarization, and we use unpolarized light giving an additional 3 dB of loss). The light coupled to the devices is thus constant during the measurement, in contrast to the use of a scanning laser in which the power residing in a ring resonator will vary during the scan. Light leaves the chip via the output grating coupler to an optical fiber. Part of this light is coupled to a photo-diode for the active alignment. The spectrum is recorded with an optical spectrum analyzer (Yokogawa AQ6370B OSA), which has a resolution bandwidth of 20 pm and a sampling accuracy of 4 pm.

The out-of-plane grating couplers reflect a small fraction of the light back in the waveguide, thereby causing Fabry-Pérot fringes. We have simulated these reflections with FDTD and found that the reflected power is below 6%, which is much lower than the reflection from a waveguide-air interface which is between 20% and 40% [89, 117]. In the analysis of resonators and directional couplers, the recorded spectra are normalized to the transmission spectrum of a single-mode waveguide. In order to remove the Fabry-Pérot reflections in this reference spectrum, it was smoothed by a convolution with a Gaussian window with a full-

Table 3.1: Waveguide propagation loss. Waveguide width 397 nm x height 220 nm. Mean values taken over an interval of 25 nm around 1550 nm vacuum wavelength. Measurement-to-measurement differences all below 2% (12 repetitions).

	dB/180°	dB/cm
straight waveguide	x	2.50
bent waveguide, radius 5 μm	0.024	15.29
bent waveguide, radius 3 μm	0.036	38.73

width at half-max (FWHM) of 1 nm. Datapoins in the ring transmission spectrum below -80 dB/nm were clipped as this is the noise floor of the OSA.

3.5 Waveguide and bend losses

The losses in straight waveguides are characterized by comparing the transmission of waveguides with different lengths, as shown in Fig. 3.5a. The number of bends in these structures and the length of the connecting waveguides is identical for all of them, so that only the length l' of the straight waveguides is varied from 20 μm to 4380 μm, adding up to a length variation of 5 cm. The measured spectra of the four structures are shown in Fig. 3.6a, in which the effect of the Fabry-Pérot reflections from the out-of-plane grating couplers is visible as "noise" on the spectra. The average of 5-nm wavelength spans was used to remove this effect, as indicated by the black crosses. The loss per unit length around specific wavelengths is obtained from a linear fit of the intensity versus waveguide length plot (Fig. 3.6). The average loss over the 25 nm wavelength span is 2.50 dB/cm and there is only a weak wavelength dependence. This loss is slightly higher than the values reported in literature [79, 107], which might be attributed to (1) the fact that our waveguides are smaller (397 nm here and 460 nm in Ref. [79, 107]), and (2) the fact that we have not optimized our PECVD deposition of the SiO_2 cladding.

Losses in the waveguide bends are characterized by comparing the transmission through waveguides with different numbers of bends. The structures used for this analysis consist of 180° bends which are separated by a 20 μm straight waveguide (Fig. 3.5b). We assume that this is long enough to describe propagation from the bend to an arbitrary long waveguide. The loss in two 90° bends is generally not identical to twice the loss of one 180° bend. This is because there is a mismatch between the mode in the straight waveguide and the mode in the bend waveguide. In Ref. [107], a significant decrease in the bending loss of bends with 3 μm radius is shown when the first and last 10° of the circular bend are replaced by a spline shape. Figure 3.7 presents the measured spectra (5 μm and 3 μm bending radii) and the wavelength-dependent bend losses (plot c). Table 3.1 presents the averages over a wavelength span of 25 nm. We observed a strong wavelength dependency of the loss in the 3 μm bends (Fig. 3.7c); the loss around a wavelength of 1560 nm is 1.7 times higher than the loss around 1540 nm. This information is useful for

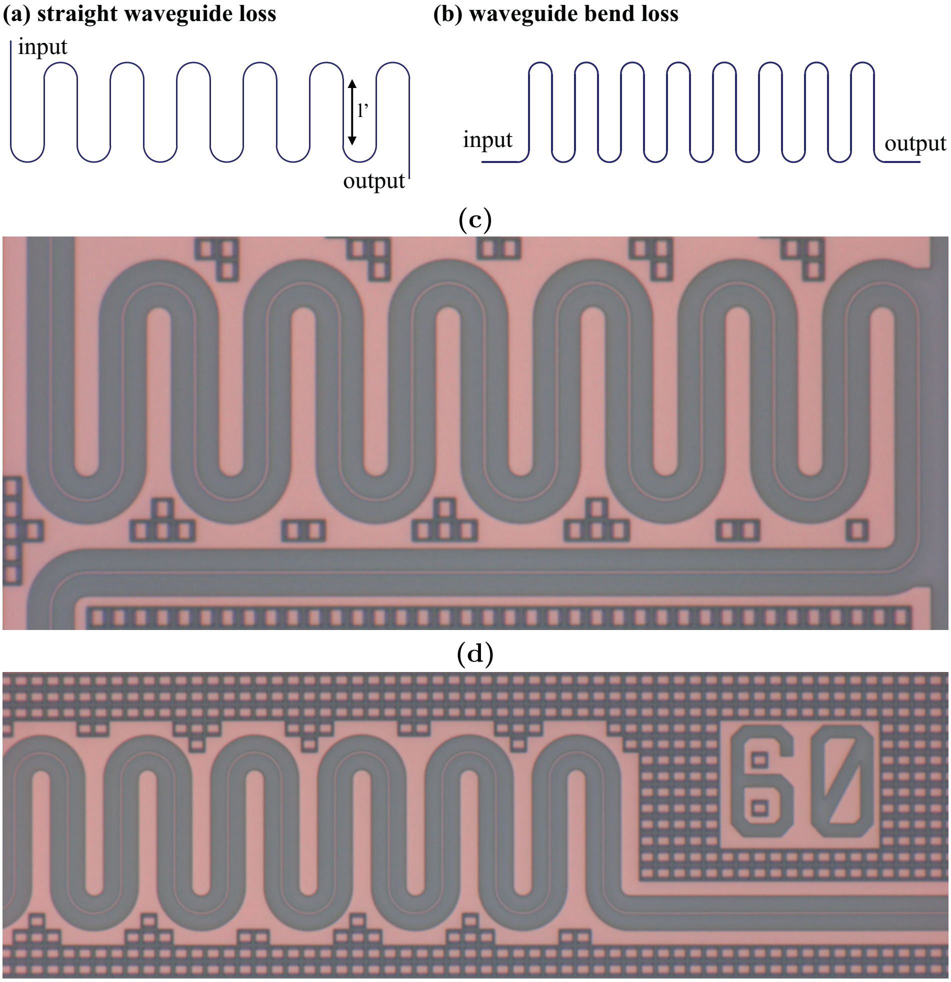

Figure 3.5: Layout of the structures for measuring waveguide loss. Waveguide width 397 nm and height 220 nm. **(a)** Structure to measure straight waveguide loss. The length of the straight waveguide l' is varied (20 μm, 1500 μm, 2900 μm, 4380 μm) while each structure contains the same bends and length of the connecting waveguides. **(b)** Structure to measure waveguide bend loss. The structures have bends of 180° separated by a straight section of 20 μm. The depicted bend radius is 3 μm. The actual structures contain 1, 119, 239, or 359 bends, and have bending radii of 3 μm and 5 μm. **(c)** and **(d)** Microscope photographs of the designs in (a) and (b), respectively. Pinkish color is the silicion light-guiding layer and greenish color is the SiO_2 BOX layer. The very narrow line is the waveguide, which is surrounded by a broad 2 μm wide trench. Far away from the structure, a "tile" pattern is written to improve the uniformity of the etch process in the CMOS fabrication.

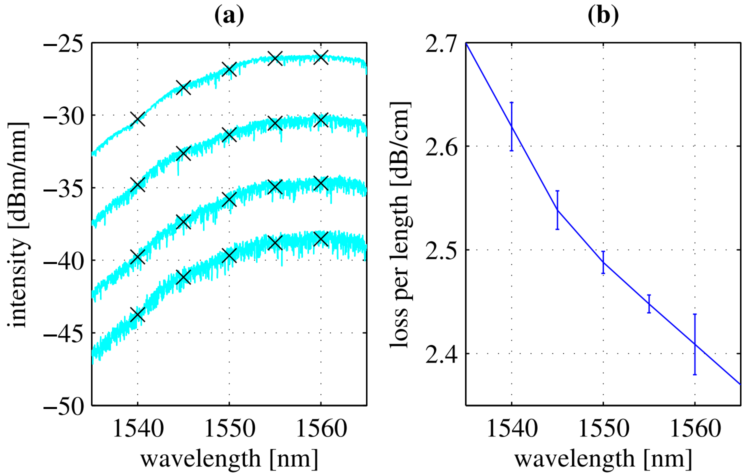

Figure 3.6: **(a)** Transmission spectra of 397 nm wide waveguides with lengths 0.240 mm, 18.000 mm, 34.800 mm, and 52.560 mm. Black crosses indicate the average of a 5 nm span. **(b)** Waveguide loss per centimeter, obtained from a linear fit of the data of (a). The lines between the datapoints are linearly interpolated/extrapolated. Error bars indicate the standard deviation of the 12 repetitive measurements.

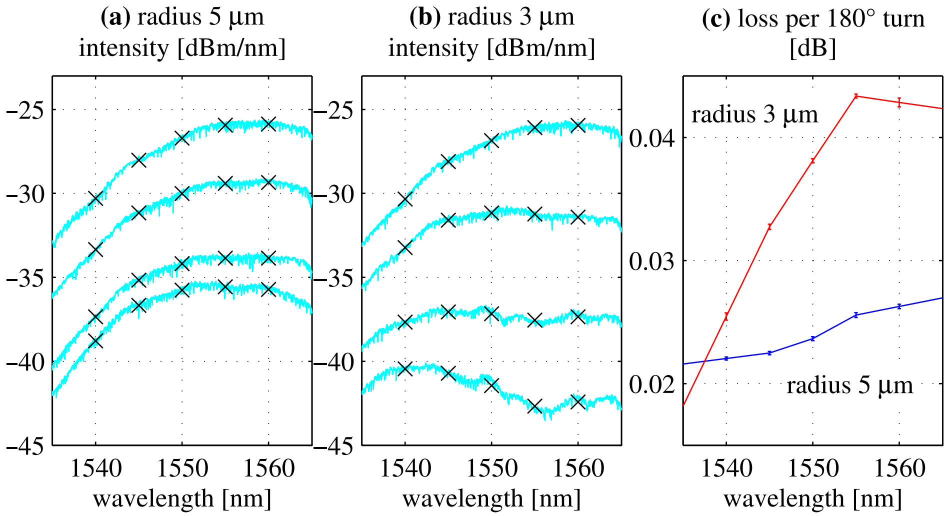

Figure 3.7: Labels of y-axes are above the plots. **(a)** and **(b)** Transmission spectra of 397 nm wide waveguides with a number 180° bends. From high to low transmission, the number of bends is 1, 119, 239, and 359. **(a)** 5 μm bend radius. **(b)** 3 μm bend radius. **(c)** Loss per 180° bend, obtained from a linear fit of the data of (a) and (b). The numbers are corrected for the loss in the straight waveguides. Error bars indicate the standard deviation of the 12 repetitive measurements. The lines between the datapoints are linearly interpolated/extrapolated. The crossing around 1538 nm wavelength is caused by extrapolation and we do not expect it in reality.

design; for example, one could tune a device to critical coupling by selecting the resonance where the losses are similar to the coupling.

3.6 Methods of characterizing directional couplers

We describe four methods for characterizing directional couplers and compare these methods. Five sets of directional couplers with different waveguide widths and gaps are characterized.

The first method is based on direct measurement of the coupler power transmission (*DCM1, transmitted power*), the other methods are based on the recorded transmission spectra of ring resonators with two identical couplers. The rings are racetrack-shaped resonators consisting of two 40 μm long straight waveguides and two 180° bends with radius 5 μm (see Fig. 2.20 on page 67). The second method uses the output spectrum of the ring, and neglects dispersion and asymmetries in the couplers (*DCM2, ring simple*). The third and fourth methods use the output and drop spectra of the ring, respectively, and include dispersion (wavelength dependency) and asymmetry in the coupler (*DCM3, ring* and *DCM4, ring drop*). Method *DCM1* depends on the repeatability of the alignment of the optical fibers with respect to the chip and method *DCM2* depends on fitting of the spectra that have noise and spurious reflections. From the results of this section, it can be concluded that both methods can be used for the characterization of directional couplers in SOI technology.

Five sets of directional couplers were characterized, each with one straight waveguide and one waveguide which is bend to form a section with two parallel waveguides (Fig. 2.12 on page 45). The bending radius is 5 μm and the length of the parallel section is varied from 0 μm to 18 μm. The five sets have a different waveguide widths and gaps. The nominal coupler has waveguide width ∼400 nm and gap ∼220 nm. Three couplers have a different waveguide width (375 nm, 391 nm, and 413 nm) but similar gap and three couplers have a different gap (168 nm, 195 nm and 222 nm) with waveguide width ∼400 nm (see Table 3.2).

In this section, we first present the four different methods (Secs. 3.6.1-3.6.4). Then we compare the methods and study their applicability and accuracy in the determination of the different properties of the directional couplers (Sec. 3.6.5). We conclude with the typical characteristics of directional couplers in SOI technology such as strong wavelength dependency (Sec. 3.6.6). Section 3.7 hereafter is about the large coupling-induced phase delay of directional couplers in the regime of cross-coupling.

3.6.1 Transmitted power measurement (*DCM1*)

In each set of directional couplers, the length L of the parallel waveguide section was varied. We measured the transmitted power going straight through the waveguides the coupler. Both the power going straight through the upper waveguide a as well as the power going straight through the lower waveguide b were recorded (see Fig. 2.12 on page 45 for a sketch of the directional couplers).

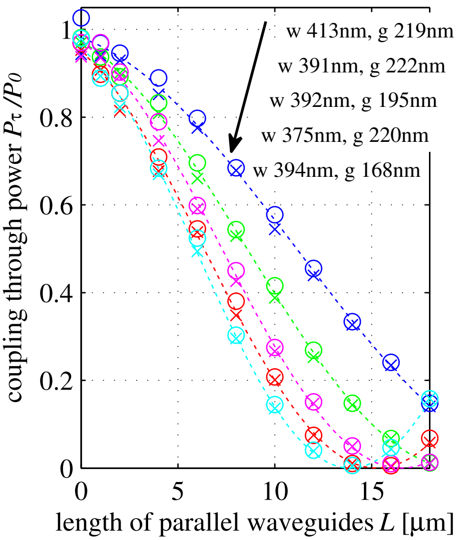

Figure 3.8: Characterization of five sets of directional couplers with different waveguide width (w) / gap (g) combinations. Power transmitted through the upper (indicated "x", a in Fig. 2.12) and lower (indicated "o", b in Fig. 2.12) waveguides is plotted versus the length L of the parallel waveguides section of the directional coupler. The power is recorded in a wavelength span of 25 nm around 1550 nm. The lines are obtained by fitting P_0, s, and ΔL in Eq. (3.14) to the measured data. The data is in this plot normalized to the fitted value of P_0.

In this characterization method, it was assumed that the couplers are lossless, that both waveguides are identical (i.e., $\delta = 0$), and that the coupling coefficient does not depend on wavelength (i.e., $s = s_c$ and $s_c' = 0$). These assumptions are listed in Sec. 3.2.4. This method is based on Eq. (3.11) which describes the transmitted power of the directional coupler. We denote the power transmission of a straight waveguide without coupling P_0 and we denote the straight-through power transmission of a directional coupler P_τ. The loss of the connecting waveguides is the same for the case with or without the coupler, hence $P_\tau/P_0 = |u_b(L+\Delta L)|^2/|u_b(0)|^2 = |\tau|^2$. From Eq. (3.11) we hence find

$$P_\tau = \cos^2[s_c(L+\Delta L)] \cdot P_0. \tag{3.14}$$

The transmitted power P_τ was measured for different coupler lengths L. From these measurements, the unknowns in Eq. (3.14); P_0, s_c, and ΔL; were fitted (see Fig. 3.8). The results are presented in Table 3.2.

3.6.2 Ring spectra analysis neglecting asymmetry and dispersion in the coupler (*DCM2*)

This method is based on the transmittance spectra of ring resonators. In contrary to the previous *DCM1*, it does not strongly depend on the repeatability of the fiber-chip coupling. As in *DCM1*, we neglect asymmetry in the coupler (i.e., $\delta = 0$) and wavelength-dependency of the coupling coefficient (i.e., $s = s_c$ and $s_c' = 0$). We recorded a set of transmission spectra of racetrack resonators in add-drop configuration for different coupler lengths L (see Fig. 2.20c on page 67 for a sketch of the device). Examples of recorded spectra are shown in Fig. 3.9 on page 93 (solid cyan curves). This method consists of two steps. In the first step, we considered the measured spectra individually and we fitted the unknowns in Eq. (3.4 with 3.12) to

Table 3.2: Directional coupler characterization. x denotes that a certain quantity is not measured or taken into account in that type of analysis. *DCM1*: average over 2 repetitions, *DCM2* and *DCM2*: average over 5 repetitions, *DCM4*: average over 2 repetitions.

		s_c [μm^{-1}]	ΔL [μm]	s'_c [μm^{-2}]	δ [μm]	n_g
waveguide width 391 nm, gap 222 nm						
transmitted power	*DCM1*	0.072	2.377	x	x	x
ring, approximate	*DCM2*	0.071	2.297	x	x	4.317
ring	*DCM3*	0.073	2.134	0.339	0.0006	4.319
ring drop	*DCM4*	0.072	2.287	0.352	0.0034	4.320
waveguide width 413 nm, gap 219 nm						
transmitted power	*DCM1*	0.058	2.416	x	x	x
ring, approximate	*DCM2*	0.057	2.213	x	x	4.292
ring	*DCM2*	0.057	2.285	0.277	0.0014	4.288
ring drop	*DCM3*	0.057	2.316	0.351	0.0002	4.287
waveguide width 375 nm, gap 220 nm						
transmitted power	*DCM1*	0.088	2.562	x	x	x
ring, approximate	*DCM2*	0.089	2.245	x	x	4.321
ring	*DCM3*	0.091	2.343	0.372	0.0027	4.351
ring drop	*DCM4*	0.089	2.408	0.416	0.0078	4.346
waveguide width 392 nm, gap 195 nm						
transmitted power	*DCM1*	0.085	1.977	x	x	x
ring, approximate	*DCM2*	0.082	2.288	x	x	4.232
ring	*DCM3*	0.084	2.118	0.411	0.0048	4.319
ring drop	*DCM4*	0.082	2.329	0.332	0.0047	4.319
waveguide width 394 nm, gap 168 nm						
transmitted power	*DCM1*	0.098	2.136	x	x	x
ring, approximate	*DCM2*	0.099	1.992	x	x	4.247
ring	*DCM3*	0.099	2.053	0.414	0.0042	4.313
ring drop	*DCM4*	0.100	2.019	0.436	0.0046	4.318

each spectrum. From this fitting, we obtained the transmittance of the directional coupler $|\tau_L|$ as a function of the coupler length L ($|\tau_L|$ denotes τ for given L). In the second step, we fitted the unknowns in Eq. (3.11) to the $|\tau_L|$ versus L curve, obtaining the characteristics of the directional coupler.

In the first step, we fitted the unknowns in Eq. (3.4 with 3.12) to each recorded spectrum. In the fitting, the resolution bandwidth of the optical spectrum analyzer was incorporated by convoluting the calculated spectrum with a Gaussian curve with a FWHM of 20 pm. We independently measured α (wavelength-averaged, using the numbers for waveguide width ∼400 nm in Table 3.1). Fitting α is difficult for the configuration of racetrack resonators with two couplers and large coupling (small $|\tau|$ with respect to transmittance α) because the the transmittance spectrum only weakly depends on the value of α. Although the spectra were corrected for a reference spectrum, it was necessary to also fit the inserted power in the device, $P_0 = |a_1|^2$, to correct for the fiber-chip alignment repeatability. Knowing the transmittance α and track circumference l, the fitted unknowns in Eq. (3.4 with 3.12) are thus $|\tau_L|^2$, n_e, n_g and P_0.

An accurate initial estimate of n_e and n_g (defining the resonance wavelengths λ_m via Eq. (3.13)) is necessary as starting point for the fitting. Therefore, the resonance wavelengths in the spectrum were first estimated using the *findpeaks* algorithm as implemented in Ref. [118]. This algorithm is capable of detecting peaks or valleys in signals with random noise by using a priori information about the peaks such as the expected width and amplitude. The group index n_g was estimated from the average free-spectral-range (FSR) between the resonances, using $n_g = \lambda_c^2/(\mathrm{FSR} \cdot l)$. The integer resonance number m was estimated from the resonance equation (3.13) at λ_c, $m \approx n_e l/\lambda_c$, where the effective index n_e was calculated using a mode solver (FMM mode solver, rectangular silicon-in-silica waveguide). The estimated n_e is then corrected such that the resonance equation (3.13) is obeyed for the resonance λ_m closest to λ_c with λ_m obtained using *findpeaks*, and using the previously estimated n_g and integer number m. With this accurate initial estimate, the fitting converged properly. The fitting of the parameters in Eq. (3.4 with 3.12) to the measured spectra was done by minimizing the root-square difference between the computed transmission spectrum, $|b_1(\lambda)|^2$, and the measured spectrum. We used the Matlab implementation of the Levenberg-Marquardt optimization algorithm [119]. The fitting of Eq. (3.4 with 3.12) to the measured spectra was done in two iteration, first fitting $|\tau_L|^2$ and P_0, and then fitting all unknowns.

In the second step, we fitted the unknowns in Eq. (3.11) to the $|\tau_L|^2$ versus L curve that was obtained in the first step. Equation (3.11) describes the behavior of the directional coupler. The fitted unknowns are the coupling coefficient s_c and the correction for the coupling in the bends ΔL.

Using the *DCM2* method as presented in this section, we obtained s_c, ΔL, and n_g (we used the fitted n_g of the $L = 0$ μm spectrum). Results for the five types of couplers are presented in Table 3.2. Figure 3.9 depicts the measured spectra (solid cyan lines) and, for clarity, only the fitting results of the next Section 3.6.3. For lengths $L = 0$ and $L = 4$, the results of this *DCM2* method were indistinguishable in this plot from the depicted results of the *DCM3* method (black dashed lines).

The measured spectrum with $L = 14$ is not well described by the theory in this section, as the FSR, or spacing between the resonance wavelengths, is wavelength-dependent. These effects are addressed in the next Section 3.6.3.

3.6.3 Full analysis of ring spectra (*DCM3*)

This section presents our most complete characterization of the directional couplers. The dispersion in the couplers (i.e., the wavelength dependency of $s(\lambda)$) and the effect of an asymmetry δ between the waveguides of a coupler are taken into account in this analysis while these effects were neglected in the previous *DCM2*. As follows from this analysis and as will be described in Sec. 3.6.6, dispersion in the coupler is significant and can thus not be neglected when designing photonic integrated circuits in SOI technology. As will be described in Sec. 3.7, this analysis led to the observation that an asymmetry between the waveguides of the coupler introduces a significant phase delay when nearly all light couplers from one waveguide to the other.

This analysis is based on the transmission spectra of ring resonators. We measured the transmission spectra of a set of eleven directional couplers in racetrack-shaped ring resonators (see Fig. 2.20c on page 67), in which the length of the parallel waveguides L was varied from 0 to 18 μm. Fig. 3.9 presents the measured transmittance spectra for a waveguide width width 394 nm and a gap width of 168 nm.

Equation (3.4 with 3.6 - 3.10) was fitted to the recorded spectra and the details of this fitting will be described in this paragraph. The spectra of the set of resonators with varying length of the coupler L were used simultaneously in the fitting. We had independently measured the wavelength-dependent losses of straight and bend waveguides to calculate the round-trip transmittance $\alpha(\lambda)$ (using the numbers for waveguide width ∼400 nm as plotted in Figs. 3.6 and 3.7). We have used single values for s_c, s'_c, ΔL, δ and n_g, i.e., single values were used to simultaneously describe all measured spectra in the set. The resonance wavelengths depend strongly on the effective index, which varies from device to device due to fabrication. This can be seen in the upper three plots of Fig. 3.9, in which the resonances are not exactly at the same wavelength. Therefore device-specific effective indices were used in the fitting, $\{n_e\}$, with the curly brackets indicating that this is a set of numbers. The input powers, $\{P_0\} = \{|a_1|^2\}$, were also fitted from measurement-to-measurement as it depends on the alignment of the optical fibers with respect to the chip. The simultaneously fitted unknowns in Eq. (3.4 with 3.6-3.10) are thus: coupling coefficient s_c, dispersion in the coupler s'_c, asymmetry in the coupler δ, effective group index n_g, the correction for coupling in the bends ΔL, a set of effective indices $\{n_e\}$, and a set of input powers $\{P_0\}$.

The unknowns in Eq (3.4 with 3.6-3.10) were fitted to the spectra by minimizing least-square difference between the computed transmission, $|b_1(\lambda)|^2$, and the measured spectra. Each datapoint (wavelength) in this minimization is weighted with $1/I$, where I is the average intensity in a 5 nm wavelength span around this wavelength. This 5 nm corresponds to approximately one FSR. The fitting is done in the intensity domain (not in the logarithmic dB scale that is used in the plotting of the figures). The noise (or spurious reflections) in the $L = 0$ μm have a stronger intensity than the signal in the $L = 14$ μm spectrum. Without weighting, the noise in the $L = 0$ μm spectrum would thus have more influence than the signal in the $L = 14$ μm spectrum. The Matlab implementation of the Levenberg-Marquardt optimization is used for the fitting [119].

An accurate initial estimate is required as starting point for the fitting to converge properly. The properties of the coupler s_c and ΔL and n_g are estimated from the *DCM2* method neglecting asymmetry and dispersion in the coupler. This less complete method gave an accurate estimate, close to the values obtained in this *DCM3* method. An accurate initial estimate of the resonance wavelengths λ_m was required. Therefore, λ_m were first found using the *findpeaks* algorithm [118]. Similar to *DCM2* method, the effective index n_e was first estimated by the mode-solver. Then the resonance number m was estimated for all dips from Eq. (3.13) using λ_m from *findpeaks*, n_g from *DCM2*, and n_e from the mode-solver. The resonance numbers of the dips in the spectra were, when needed, corrected to be consecutive integers. Then for each resonance in the recorded spectrum, the effective index is calculated from Eq. (3.13) (using λ_m from *findpeaks* and n_g from *DCM2*) and the mean effective index over all 5 or 6 resonances is used as initial estimate of n_e. As initial estimate, we chose $s'_c = 0$ μm^{-2} and $\delta = 0.002$ μm^{-1} (this gave best convergence). This procedure provided an initial estimate that is accurate enough for the fitting to converge.

Figure 3.9 shows that the fitted spectra agree very well with the measured spectra, indicating that Eq. (3.4 with 3.6 - 3.10) indeed contains all important physical effects. Length $L = 14$ μm is of special interest as it contains the cross-coupling regime. This causes the change in FSR from 5.0 nm to 6.4 nm as will be explained in Sec. 3.7. The results of *DCM3* are listed as “ring” in Table 3.2.

3.6.4 Full ring spectral analysis at the drop port (*DCM4*)

The transmittance spectra of the drop ports of the racetrack resonators were also analyzed using a method similar to the previous method *DCM3*. This is done to verify the theory of Eq. (3.5); moreover, it is useful to know whether the spectrum of the drop port can be used for the analysis of the directional couplers, because the output port is not necessarily available in all chip designs. As in *DMC3*, the wavelength dependency of $s(\lambda)$ is described by a linear model and the asymmetry between the waveguides of the coupler is taken into account by parameter δ.

The analysis is analogue to *DCM3*, but with the spectra described by Eq. (3.5) instead of Eq. (3.4). Both methods share Eqs. (3.6 - 3.10). Instead of finding dips at resonance wavelengths, the spectrum of the drop ports show peaks at the resonance wavelengths (see Fig. 3.10). Equation (3.5 with 3.6 - 3.10) was fitted to the measured drop-port spectra. Unlike *DCM3*, the spectra were not weighted in the fitting because maximal transmission of the peaks of the drop ports is around unity for all spectra, while only the off-resonant transmittance depends strongly on the amount of light coupled to the ring. Similar to *DCM3*, the initial estimates of s_c, ΔL and n_g were obtained from an analysis analogue to *DCM2* but using the

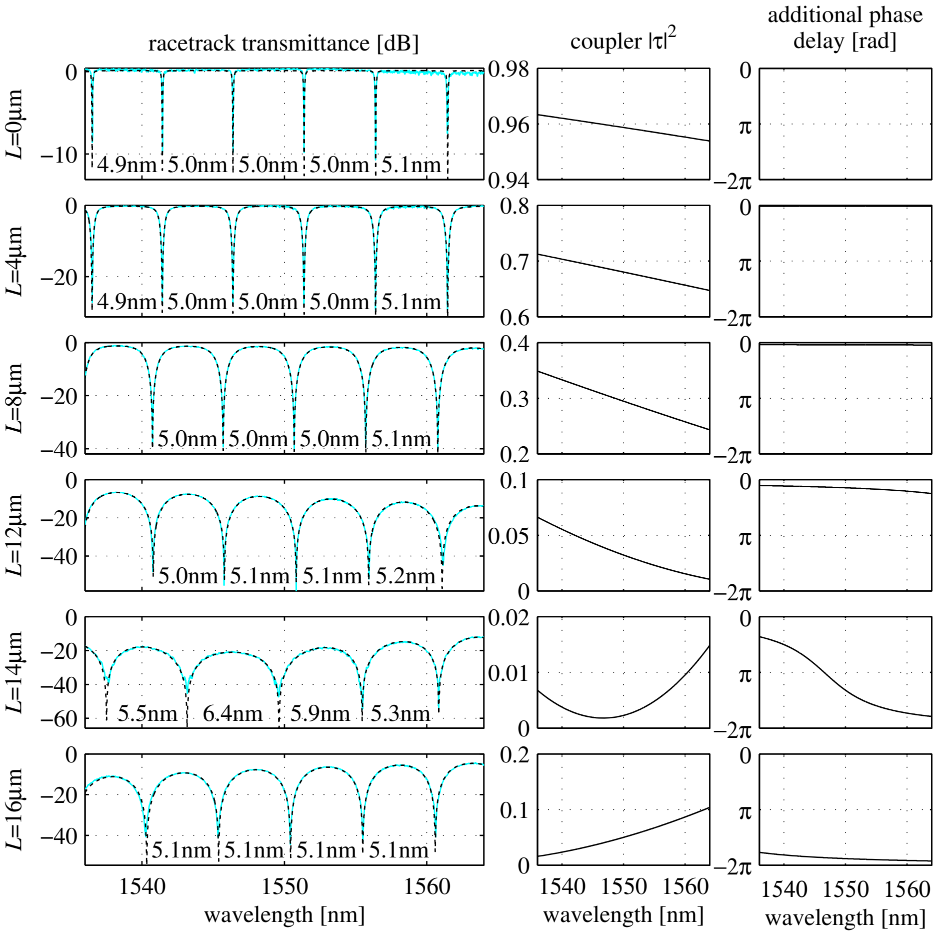

Figure 3.9: Characterization of a set of racetrack resonators with two identical couplers. Racetrack consists of two 40 μm long straight waveguides and two 180° bends with 5 μm radius. The couplers have waveguide width 394 nm and gap 168 nm. Each row shows a different length L of the parallel waveguides in the coupler. The fitted transmissions of method *DCM3*, including all effects, are shown. **Left column**: measured transmittance spectrum (solid cyan lines) and fitted transmission function $|b_1|^2$ given by Eq. (3.4 with 3.6 - 3.10) (dashed black lines). **Middle column**: Fitted value of the straight-through power in the coupler $|\tau(\lambda)|^2$. **Right column**: Fitted value of the additional phase shift due to asymmetry, $2\arg\{\cos s(\lambda)\tilde{L} - \frac{\imath\delta}{s(\lambda)} \sin s(\lambda)\tilde{L}\}$, see Eq. (3.15). This term is hardly visible in the two uppermost graphs (lengths 0 μm and 4 μm) because the curve coincides with the upper border of the graph. Lengths 1 μm, 2 μm, 6 μm, 10 μm, and 18 μm are also taken into account in the fitting but are not shown here.

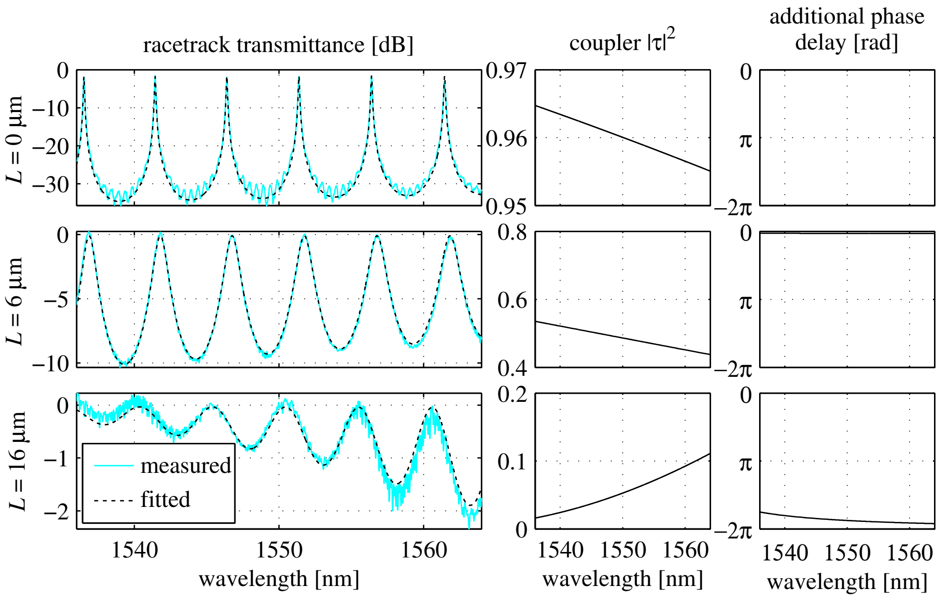

Figure 3.10: Characterization of a set of racetrack resonators with two identical directional couplers by analyzing the drop ports. Waveguide width 394 nm and gap 168 nm. Each row shows a different length L of the parallel waveguides of the couplers. The fitted transmissions of method *DCM4*, including all effects, are shown. Labels of y-axes are above the plots. **Left column**: measured transmittance spectrum (solid cyan lines) and fitted transmission function $|a_d|^2$ (dashed black lines). **Middle column**: Fitted value of the straight-through power in the coupler $|\tau(\lambda)|^2$. **Right column**: Fitted value of the additional phase shift due to asymmetry, $2\arg\{\cos s(\lambda)\tilde{L} - \frac{\imath\delta}{s(\lambda)} \sin s(\lambda)\tilde{L}\}$. This term is hardly visible in the two uppermost graphs (lengths 0 μm and 4 μm) because the curve coincides with the upper border of the graph.

measured spectra of the drop port and Eq. (3.5, again with 3.12). Initial estimates $s'_c = 0\ \mu\text{m}^{-2}$ and $\delta = 0.002\ \mu\text{m}^{-1}$ were identical to the ones in *DCM3*.

In the case that almost all light is coupled to and from the ring ($|\tau|^2 \approx 1$), the resonance peaks in the drop port spectra were not visible, while noise or spurious reflections dominated these spectra. Therefore 7 spectra out of the 55 measured spectra were not used in the analysis. Of the five waveguide width/gap combinations in Table 3.2, the following datapoints were not used: $L = 0$ (misaligned fiber); $L = 18$; $L = 16$ and $L = 14$; $L = 18$ and $L = 16$; and $L = 14$; respectively. Figure 3.10 shows an example of recorded spectra with the fitted transmission, which are in good agreement. The results of the fitting of all parameters to the spectra of the drop ports is listed as “ring, drop” in Table 3.2.

Table 3.3: Differences between directional coupler characterization methods. Derived from the data in Table 3.2. The maximum observed difference for all five sets directional couplers is presented. **Middle block:** Relative differences of the parameters. **Right block:** the maximum difference in $|\tau|^2$ for couplers with lengths L between 0 μm and 18 μm. At wavelength $\lambda_c = 1550$ nm (first column) and the maximum over a wavelength span from 1535 nm to 1565 nm (second column). **Methods:** direct measurement of transmitted power (*DCM1*), ring spectra analysis neglecting dispersion and asymmetry (*DCM2*), full ring spectra analysis (*DCM3*), full ring drop port spectra analysis (*DCM4*).

compared	relative difference					$\|\tau\|^2$ difference	
methods	s	ΔL	s'	δ	n_g	at λ_c	at $\lambda_c \pm 15$ nm
DCM1 vs *DCM2*	4%	15%	x	x	x	0.020	x
DCM2 vs *DCM3*	3%	8%	x	x	3%	0.026	x
DCM3 vs *DCM4*	3%	10%	24%	140%	1%	0.018	0.028

3.6.5 Comparison of different methods

This section compares the different methods and studies their applicability to the characterization of directional couplers. The results of the different methods are presented in Fig. 3.11a and compared in Table 3.3. For each method-to-method comparison in this Table, the maximum difference over all width/gap combinations is shown. The first row compares the two methods that neglect dispersion and asymmetry (i.e., for which $s(\lambda) = s_c$, $s'_c = 0$ and $\delta = 0$): the direct transmitted power method (*DCM1*) and the approximate fitting of the ring spectra method (*DCM2*). The methods in the second row are both based on the recorded spectra of the ring output port, and the influence of neglecting dispersion and asymmetry is compared. The methods in the third row are both based on the full directional coupler analysis, and the difference between the analysis of the output and drop ports is shown. The middle block shows the relative differences of the fitted parameters, and the right block shows the maximum difference in the transmitted power of the directional coupler $|\tau|^2$ (see Fig. 3.11).

The differences between the methods are all of the same order of magnitude, and we could not attribute the differences to a specific reason. In general, it can be seen that the difference in the fitted parameters is quite large, but that the net influence on the directional coupler is low (the difference in $|\tau|^2$ is below 0.03). This indicates that the combination of the parameters is more accurate than an individual parameter. The value of δ could only be accurately obtained for the directional couplers with smaller gaps of 195 nm and 168 nm, as seen by comparing the results of the ring (*DCM3*) and ring drop (*DCM4*) in Table 3.2. We believe this is because the measured spectra have the point of minimal transmission $|\tau|^2$ in the middle of a recorded spectrum, such that asymmetry-induced widening of the FSR is included in this fitting. For the directional couplers with gaps of ~220 nm, the coupler with waveguides widths 391 nm and 413 nm have this point for lengths

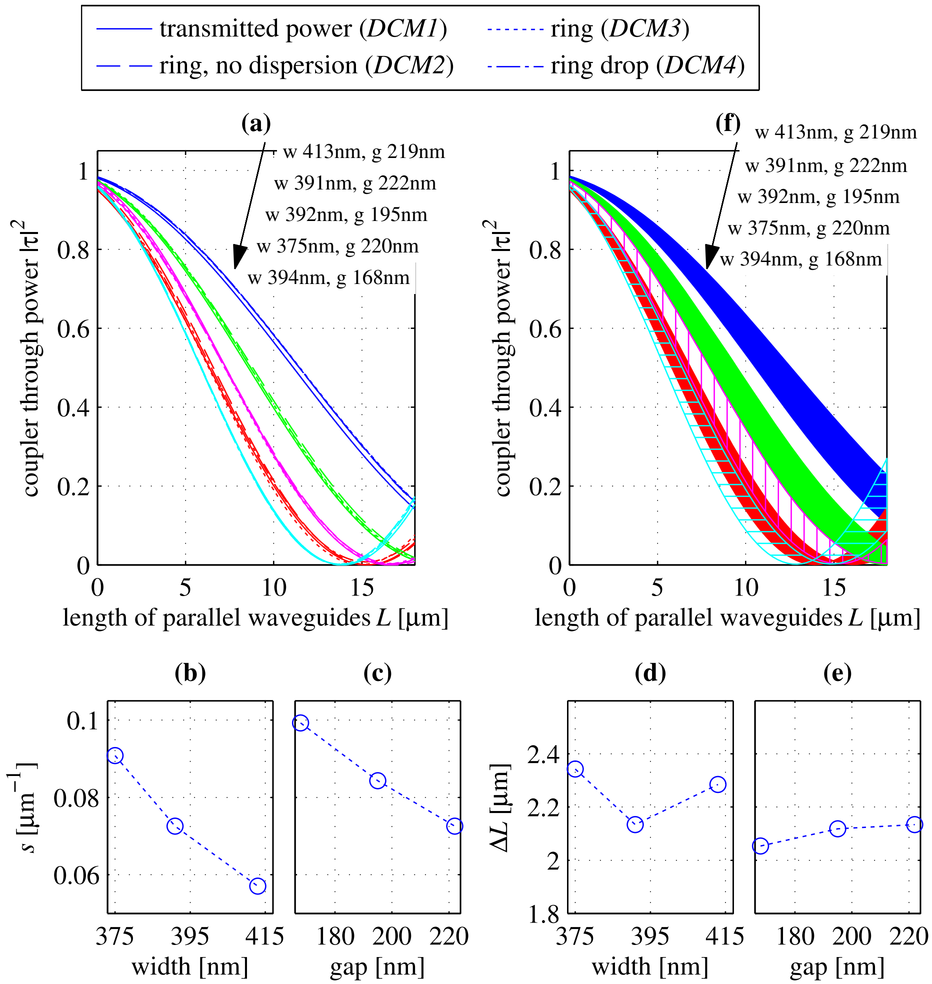

Figure 3.11: (a) Comparison of the different methods for characterizing the directional couplers. Results are shown for the center wavelength $\lambda_c = 1550$ nm. Five width/gap (w/g) combinations are shown. For each combination, four different characterization methods are shown: transmitted power (*DCM1*), ring output port spectra neglecting asymmetry and dispersion (*DCM2*), ring output port spectra (*DCM3*) and ring drop port spectra (*DCM4*). **(b,c)** Effect of the waveguide width and gap on the coupling coefficient s. **(d,e)** Effect of the waveguide width and gap on the correction ΔL of the coupling length due to the bends. **(b-e)** Couplers in plots (b) and (d) have similar gaps ∼220 nm. Couplers in plots (c) and (e) have similar waveguide width ∼390 nm. **(f)** Analysis of the effect of dispersion in the couplers, using data of the "ring" analysis (*DCM3*). Five width/gap (w/g) combinations are shown. For each type of coupler (w/g), an area is plotted that is bounded by the maximum and the minimum transmission $|\tau(\lambda)|^2$ over a wavelength span from $\lambda = 1535$ nm to $\lambda = 1565$ nm.

longer than 18 μm, while the coupler with waveguide width 375 nm has this point around a length of 15 μm which was not in our set of lengths (minimal $|\tau|^2$ was at the edge of the spectra of the resonators with coupler lengths 14 μm and 16 μm).

In general, it can be concluded that all methods give similar results and that the different methods agree fairly well with each other. A set of directional coupler parameters (s_c, ΔL, s'_c and δ) obtained from the same characterization method should be used together, because the net differences in the transmission are lower than the differences in the individual parameters.

The characteristics of directional couplers in SOI technology can be obtained from direct measurements of the directional couplers (*DCM1*) and also from the analysis of the spectra of ring resonators (*DCM2*). The values of $|\tau|$ obtained from s_c and ΔL agree for both methods.

We extensively studied the analysis employing racetrack resonators and also measured the dispersion in the coupler by fitting the linear model of $s(\lambda)$ of Eq. (3.3). Both the output port as well as the drop ports of the ring can be used in the analysis (*DCM3* and *DCM4*, respectively). To characterize the difference between the waveguides of the couplers, δ, it is best to use the output port of the ring resonator because noise or spurious reflections dominate the spectra in the drop port of the devices where the effect of δ is most visible. The good agreement between the measured spectra and the theory suggests that the equations that are used in *DCM3* and in *DCM4* in include all relevant physics. Dispersion in ΔL and nonlinear dispersion in $s(\lambda)$ can thus indeed be neglected in the studied devices.

3.6.6 Characteristics of typical directional couplers in SOI technology

This section is about typical characteristics of directional couplers in SOI technology. It addresses the influence of the waveguide and the gap on the coupling coefficient $s(\lambda)$ and it also addresses the strong dispersion in the couplers.

Influence of the width of the waveguides and the gap on the coupling

We studied the influence of the width of the waveguide and the size of the gap on the coupling coefficient s between the waveguides in the coupler. Directional couplers with narrow waveguides show a stronger coupling s than couplers with wider waveguides (see Fig. 3.11b). This is expected because the evanescent tail of the modes is larger for the narrower waveguides, so that these modes have more overlap with the other waveguide. Couplers with smaller gaps show stronger coupling than couplers with wider gaps (see Fig. 3.11c), as expected.

The correction ΔL due to the coupling in the bends shows little variation for the different width and gap combinations (see Fig.3.11d,e). We attribute these small variations to noise induced by fabrication, measurement, or fitting.

Dispersion in the coupler

Figure 3.11f shows the effect of dispersion in the couplers on the transmittance $|\tau(\lambda)|^2$. The colored areas shown are bounded by the maximum and the minimum transmission over a wavelength span from 1535 nm to 1565 nm. The maximum observed difference between the transmittance at 1535 nm and at 1565 nm varies from 0.12 to 0.18 for the different waveguide width/gap combinations. This is a very significant effect and it is nessecary to take this into account when designing photonic integrated circuits. One might, for example, use this effect to tune a ring resonator to critical coupling by changing the operation wavelength. However, this effect might also be very unfavourable when the functionallity of the device should be the same for a broader range of wavelengths. As alternative to a single directional coupler, it is possible to casade two directional couplers with 50/50 splitting, forming a Mach-Zehnder interferometer that is less wavelength dependent (see, for example, Ref. [120] where the functionality of the device demands a constant coupling coefficient over a broad wavelength range).

3.7 Large phase delay in directional cross-couplers

For a coupler with two identical waveguides and with effective length $\tilde{L}$ shorter than the length L_π for which all power transfers from one waveguide to the other, the phase delay may be approximated as the phase delay of an isolated waveguide ($\beta_b\tilde{L}$). However, there has been a recent interest in a more precise characterization of this phase delay because some devices such as ring-loaded Mach-Zehnder interferometers or cascaded ring resonators critically depend on this delay [111, 112]. In the previous Section 3.6, we measured the behavior of directional couplers by studying the transmission spectra of ring resonators. In this section, we focus on the coupling-induced phase delay for the case that nearly all light couples from one waveguide to the other, i.e., when the coupler operate as cross-coupler. For ring resonators with two couplers (add-drop configuration), the effect of this phase delay vanishes for a symmetric coupler consisting of two identical waveguides. We show that a tiny asymmetry δ between the waveguides causes a significant additional phase delay in the cross-coupling regime. This phase delay was observed as a significant change in the free-spectral-range (FSR) of the ring resonator.

In Sec. 3.2.2, we described the behavior of directional couplers with coupled mode theory and derived Eq. (3.2). The phase delay that is introduced by the coupling is given by the argument of τ in Eq. (3.2), i.e.,

$$\phi_\tau = -\beta_b(\lambda)\tilde{L} + \delta\tilde{L} + \arg\left\{\cos\left[s(\lambda)\tilde{L}\right] - \frac{\imath\delta}{s(\lambda)}\left[\sin s(\lambda)\tilde{L}\right]\right\}, \tag{3.15}$$

with arg{} the argument of a complex number. The right-hand-side of this equation has three terms. The first term, $-\beta_b\tilde{L}$ is the phase delay that is introduced by an isolated waveguide b of length $\tilde{L}$. The second term, $\delta\tilde{L}$, is small and may be neglected because δ is smaller than the uncertainty in β_b due to fabrication-induced variations. The third term, arg{...}, is what we refer to as the coupling-induced phase delay. This term is usually small or close to $-\pi$ as the real part of the term inside the argument is much larger than the imaginary part because δ/s is small. However, the real part vanishes around $\cos s\tilde{L} = 0$, hence this argument rapidly changes to $-\pi/2$. Equation (3.2) shows that the amplitude of τ is smallest at this point thus, at this point, most light is coupled from waveguide b to waveguide a.

We studied racetrack resonators with two directional couplers (i.e., in add-drop configuration). These resonators have round-trip phase delay $\theta = \phi_r + 2\phi_\tau$ with ϕ_r the phase delay due to the isolated waveguide and ϕ_τ the phase delay due to the coupler. Eq. (3.7) gives θ. For this configuration, the effect of the coupling-induced phase delay, $2\arg\{\cos s\tilde{L} - \imath(\delta/s)\sin s\tilde{L}\}$, vanishes for symmetric couplers ($\delta = 0$). A tiny asymmetry δ causes an additional phase delay in the cross-coupling regime and hence a change in the resonance wavelengths λ_m of the resonator.

Figure 3.9 (page 93) shows the transmission spectra of racetrack resonators for different coupler lengths L. In each spectrum the wavelength dependency of $s(\lambda)$ gives a wavelength dependency of $|\tau(\lambda)|^2$ (middle column in Fig. 3.9). The spectrum with $L = 14$ μm includes the cross-coupling regime (minimal $|\tau|^2$) and the coupling-induced phase delay is observed as a FSR which is different from the resonators with other coupler lengths.

DCM3 is based on Eq. (3.4 with 3.6 - 3.10) and includes this coupling-induced phase delay. It can be seen that the wavelengths λ_m of the resonances and hence also the particular FSR are well described by these equations (remember that the fitted transmission functions shown in Fig. 3.9 all have the same value for s_c, s'_c, ΔL, δ and n_g).

For the $L = 14$ μm spectrum, maximal coupling $|\tau|^2 \approx 0$ occurs at a wavelength of 1547 nm. The corresponding change in FSR from 5.0 nm to 6.4 nm is visible in the measured spectrum. This significant change is explained by a small difference between the propagation constants in the guides, $2\delta/\beta$, of 0.1% (β is computed with the numerical mode solver). To get a feeling for δ, we compute the difference in the widths of the waveguides that would give such an asymmetry. The corresponding difference between the widths of the waveguides would be $\Delta w \approx \partial w/\partial\beta \cdot 2\delta = 1$ nm, where $\partial w/\partial\beta$ was calculated using the FMM numerical mode solver and verified with the analytical approximate mode-solver [70]. This 1 nm difference is below the fabrication accuracy of the waveguides. Another explanation for the origin of δ lays in the asymmetry in the connecting waveguides of the coupler, as the upper waveguides are bent whereas the lower waveguides are straight.

The coupling coefficient s_c obtained from fitting the transmission spectra is much lower than the one we obtained with numerical simulations (see Sec. 3.10). This could be caused by imperfect PECVD deposition of the silicon-dioxide cladding, leaving low quality SiO_2 between the parallel waveguides of the coupler. We believe that this is unrelated to the observed large phase delay. This is because this particular phase delay was only observed in the cross-coupling regime ($|\tau|^2 \approx 0$) and shows a very strong wavelength-dependent or transmission-dependent behavior. A different cladding would not introduce such a strong wavelength dependent or transmission dependent effect. Moreover, all eleven measured spectra are simultaneously well described by Eq. (3.4 with 3.6 - 3.10), validating the theory of *DCM3*. Therefore the asymmetry in the waveguides is the most likely explanation of this particular phase delay.

In conclusion, we observed a coupler-induced phase delay by studying the resonance wavelengths of racetrack resonators. In a configuration with two couplers, this phase delay is only introduced when the waveguides of the coupler are not

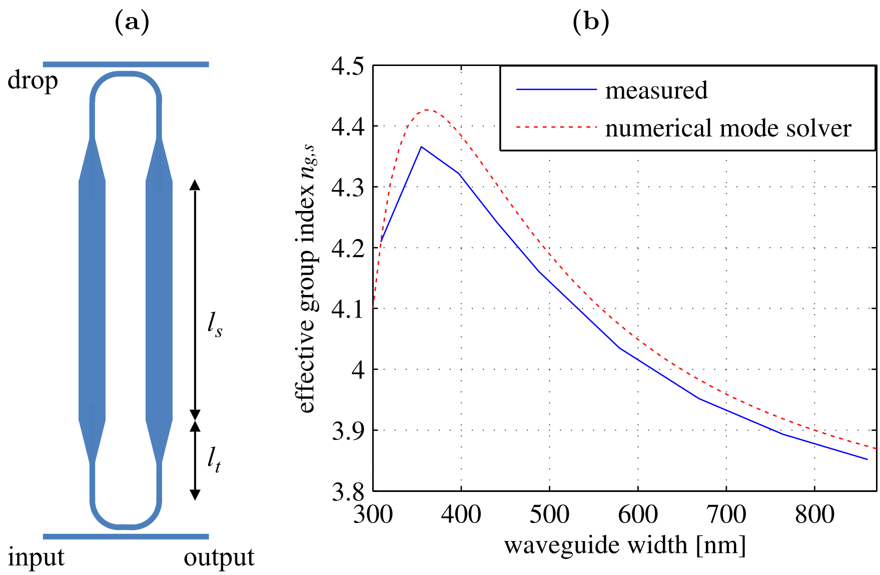

Figure 3.12: (a) Sketch of long racetrack resonator with in/output ports (not to scale). Long straight waveguide has length l_s and width w. Taper section has length $l_t = 64.35\ \mu$m (4.35 μm long waveguide of width 397 nm, taper with a length varying from 0 to 60 μm, followed by a waveguide of width w to close the space.) Coupler consists of two 10 μm long parallel guides (width ~397 nm, gap 222 nm), and bends with a radius of 5 μm. For each width w, a set of four racetracks with l_s = 250 μm, 500 μm, 750 μm, and 1000 μm were measured.
(b) Effective group index of rectangular silicon waveguides.

identical. We observed a 28% change in the free-spectral-range between two resonances due to a tiny asymmetry with a magnitude of that corresponds to a 1 nm difference between the widths of the two waveguides. In silicon-on-insulator ridge waveguides, such asymmetries are practically inevitable due to nanometer-scale variations in the fabrication process.

3.8 Waveguide group index

The effective group index of waveguides with different widths is characterized in this section. The transmission spectra of long resonators as shown in Fig. 3.12a were recorded. A small 5 nm span of this spectrum around λ = 1550 nm was analyzed so that the wavelength dependence of the effective index could be approximated as linear and the dispersion in the coupler could be neglected. The straight-through power of the couplers $|\tau|^2 = 0.41$, so that additional phase shift in the couplers due to δ could also be neglected. The shape of the transmission spectrum in Eq. (3.4 with 3.12) was fitted to the measured spectra, using the procedure described in Sec. 3.6.2 (*DCM2*). For this racetrack with varying waveguide width, the track-averaged effective index $\langle n_e \rangle$ and group index $\langle n_g \rangle$ were fitted.

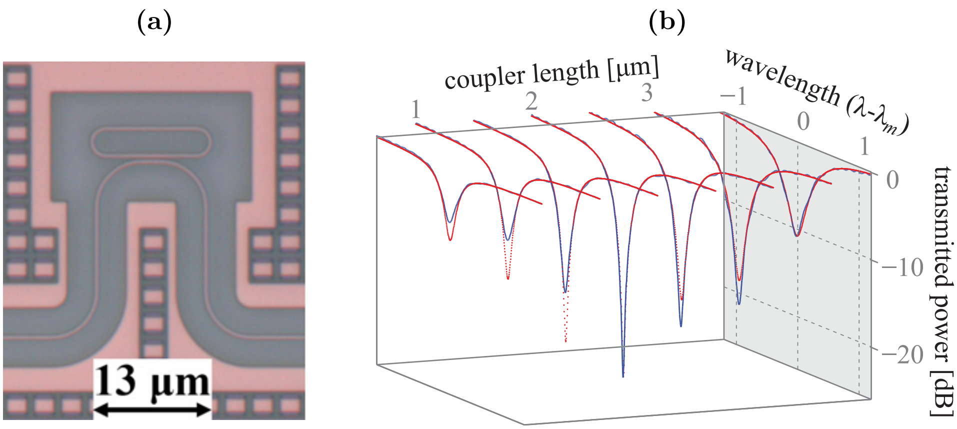

Figure 3.13: (a) Optical microscope photograph of a very small racetrack resonator with one coupled waveguide. **(b)** Transmission spectra of the racetrack resonators with different coupler lengths L are plotted at planes parallel to the backside of the box. Upper axis is the wavelength with respect to the wavelength of the resonance, $\lambda - \lambda_m$ [nm]. Measurements (solid, blue) and fits (dashed, red).

For each waveguide width, a set of four resonators were measured in which the long straight waveguides have different lengths l_s, while the tapers and couplers are identical. The track-averaged group index $\langle n_g \rangle$ times the track circumference l is then

$$\langle n_g \rangle l = 2n_{g,s} l_s + 2 \int n_g \mathrm{d}\rho, \tag{3.16}$$

where $n_{g,s}$ is the group index of the long straight section and where the integral runs over a section with the tapers, bends, and couplers. Plotting $\langle n_g \rangle l$ versus $2l_s$ and performing a linear fit gives $n_{g,s}$ as the tangent

$$\frac{\partial \langle n_g \rangle l}{\partial 2l_s} = n_{g,s}. \tag{3.17}$$

The group index is presented in Fig. 3.12b. We also computed the effective group index numerically using a mode solver and found good agreement with the measured group index (difference below 2%, see Fig. 3.12b). The FMM mode solver was used with the silicon-in-silica waveguides approximated as rectangular (see Sec. 2.8)

3.9 Critical coupling of ring resonators

This section presents an example of critical coupling. This example clearly illustrates the effect of critical coupling on the design of ring resonators, providing insight to the readers that are new to the design of resonators.

We designed a set of racetrack-shaped ring resonators (Fig. 3.13a) with a straight section of 10 μm, a very small bend radius of 1.5 μm, and circumference l =

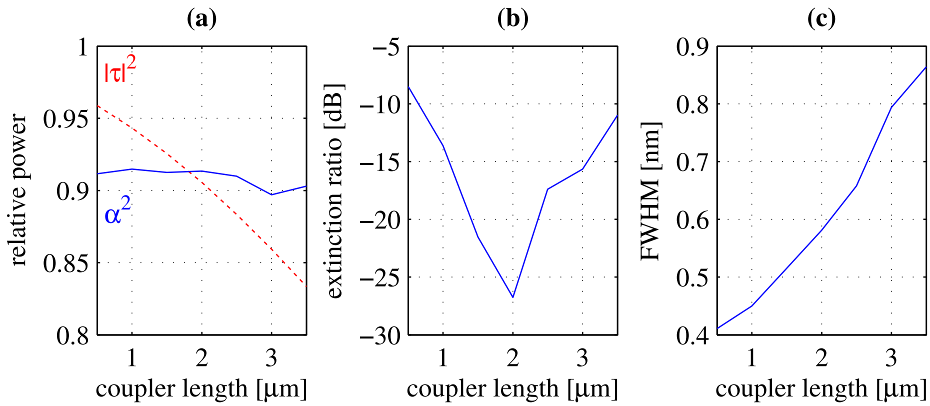

Figure 3.14: Characterization of very small racetrack resonators with one coupled waveguide. **(a)** Fitted round-trip power transmittance α^2, solid curve. Also showing $|\tau|^2$ from *DCM1* (Sec. 3.6.1). **(b)** Extinction ratio. **(c)** full-width at half-max (FWHM).

30 μm. Such a shape is required for specific applications such as local and directional sensing of mechanical strain (see Ch. 4). It has severe losses however. The racetracks have only one coupler (as in Fig. 2.20a) and the power in the output waveguide, $|b_1|^2$, may be computed from the power in the input waveguide, $|a_1|^2$, using Eqs. (2.173) and (2.174):

$$|b_1|^2 = \frac{\alpha^2 + |\tau|^2 - 2\alpha|\tau|\cos\theta}{1 + \alpha^2|\tau|^2 - 2\alpha|\tau|\cos\theta}|a_1|^2, \quad \text{with} \qquad (3.18)$$
$$\theta = \phi_r + \phi_\tau.$$

The extinction ratio r and the full-width at half-max $\Delta\lambda_{\text{FWHM}}$ of the resonance dips in the output spectrum are given by Eqs. (2.184) and (2.185):

$$r = \frac{(\alpha - |\tau|)^2(1 + \alpha|\tau|)^2}{(\alpha + |\tau|)^2(1 - \alpha|\tau|)^2}, \qquad \Delta\lambda_{\text{FWHM}} = \frac{\lambda^2}{\pi l n_g}\cos^{-1}\left[\frac{2\alpha|\tau|}{1 + \alpha^2|\tau|^2}\right]. \qquad (3.19)$$

Critical coupling means that the transmittance at resonance is zero ($r = 0$). This occurs when the power coupled to the racetrack is equal to the losses in the racetrack (i.e., when $|\tau|^2 = \alpha^2$). Transmittance spectra of the racetracks were recorded (30 nm span around $\lambda_c = 1550$ nm) and we fitted the ring transmission shape, Eq. (3.18 with 3.12), to these measurements. In this fitting, the coupler transmission $|\tau|^2$ (from *DCM1*) and track circumference l were fixed, while effective index n_e, group index n_g, power transmittance $|\alpha|^2$, and wavelength independent fiber-coupling power $P_0 = |a_1|^2$ were fitted.

The resonance dip closest to λ_c is shown in Fig. 3.13b, for a set of racetracks with a varying length of the directional coupler. It is clearly seen that under-coupling (small lengths) or over-coupling (long lengths) lead to shallow resonance

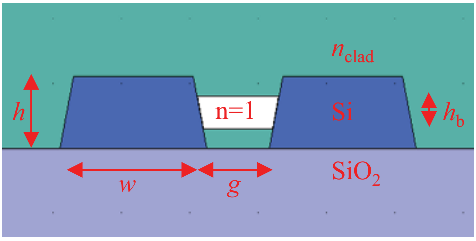

Figure 3.15: Sketch of directional coupler in mode-solver (cross-section). Silicon waveguides with 10° side-wall-angle, width w, height h, and gap g. Lower cladding (BOX) is silicon-dioxide, and upper cladding (deposited) has refractive index n_{clad}. Possible inclusion of a "bubble" with refractive index $n = 1$ and height h_b.

dips, while the close-to critical coupled racetracks shows an extinction of -25 dB. In Fig. 3.14a it can be seen that the fitted power transmission of one round-trip, α^2, is -0.4 dB and does not strongly depend on the coupler, as expected. The extinction ratio and FWHM were calculated from the fitted transmission shape employing Eqs. (3.19). Figure 3.14b clearly shows the effect of coupling on the extinction ratio, with critical coupling around coupler length $L = 2$ μm. Figure 3.14c shows the increasing FWHM for increasing coupling, this trend was predicted from Eqs. (3.19). The quality-factor, $Q = \lambda/\Delta\lambda_{\text{FWHM}}$, varies from 3800 to 1800 for increasing lengths of the coupler.

3.10 Comparison with numerical simulations

In this section, we compare the measured coupling with numerical simulations and we find a large difference between them. The coupling coefficients s were numerically computed using the eigenmode expansion method employing the FEM mode-solver (see Secs. 2.10.1). Fig. 3.15 depicts the simulated geometry consisting of two waveguides with a 10° side-wall-angle that are separated by a small gap. For the nominal simulations, there is no "bubble" ($h_{\text{b}} = 0$) and the upper cladding is silicon-dioxide ($n_{\text{clad}} = 1.444$). The measured and computed coupling coefficients s of the five sets of directional couplers are listed in Table 3.4, showing differences of about 20% .

We studied possible imperfections in fabrication that could explain this difference. We computed the coupling of directional couplers that might have been fabricated unintentionally (right block in Table 3.4). The studied imperfections are: a difference in the width of the waveguide Δw, a difference in the gap Δg, a different cladding n_{clad}, and an formation of a gas bubble in the gap between the waveguides of the coupler. First we consider the influence of the width of the waveguide w and the gap g. Figure 3.16 depicts the coupling s as a function of both waveguide width w and gap g. The measured coupling s is highlighted in Fig. 3.16b, and the change in waveguide width Δw or in gap Δg that correspond to the simulated s are shown. The five types of directional couplers are compared in Table 3.4, showing $\Delta w \approx 35$ nm and $\Delta g \approx 50$ nm. These differences are larger than our accuracy of the metrology of the devices, hence do not explain this difference. The PECVD deposition of the upper cladding might be imperfect, leading

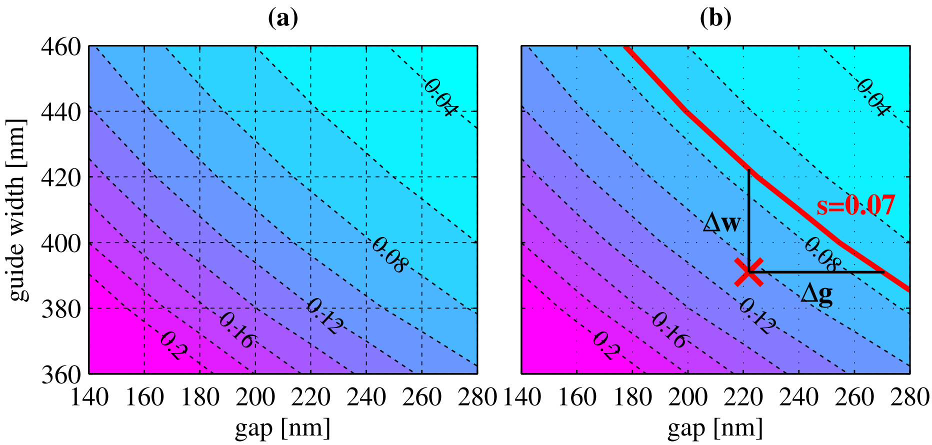

Figure 3.16: (a) Contour plot of computed coupling coefficients s [μm^{-1}] (wavelength 1550 nm). **(b)** also showing (a), but with a study of the measured directional coupler with width $w = 391$ nm and gap $g = 222$ nm (dimensions indicated with red X). The computed contour line corresponding to the measured coupling coefficient s is highlighted red and thick. The discrepancy between the measurement and the calculation is expressed in terms of width difference Δw or gap difference Δg.

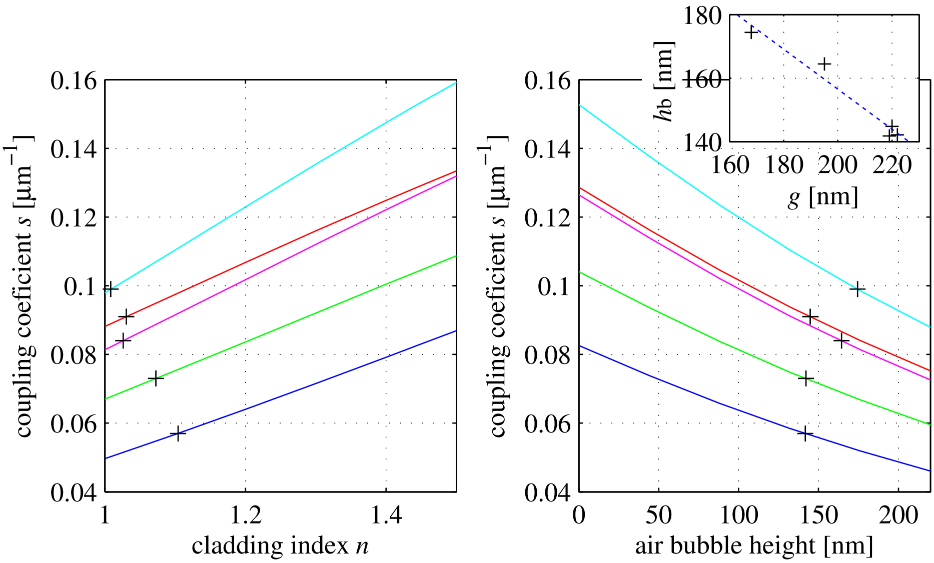

Figure 3.17: Possible effects of imperfect cladding deposition, see Fig. 3.15. Five sets of measured directional couplers. From top to bottom, the lines correspond to the waveguide width / gap combinations: 394/168, 375/220, 392/195, 391/222, and 413/219 [μm]. Black plusses show the value of n_{clad} or h_{b} that explains the measured coupling coefficients. **(a)** Upper cladding refractive index n_{clad}. **(b)** Inclusion of a bubble with refractive index $n = 1$ in the gap between the waveguides, height h_{b}. Inset shows the h_{b} corresponding to the measured coupling as function of the gap g.

coupler		coefficient s			corresponding geometry			
w	g	measured	calculated	Δs	Δw	Δg	n_{clad}	h_{b}
nm	nm	μm^{-1}	μm^{-1}	μm^{-1}	nm	nm	-	nm
391	222	0.073	0.105	0.032	31	49	1.073	142
413	219	0.057	0.083	0.026	36	48	1.104	142
375	220	0.091	0.130	0.039	29	49	1.031	145
392	195	0.084	0.128	0.044	39	55	1.026	164
394	168	0.099	0.154	0.055	43	57	1.008	174

Table 3.4: Comparison between measured and computed coupling coefficients s for five sets of directional couplers. Left block shows nominal waveguide width w and gap g. Wavelength $\lambda = 1550$ nm. Middle block shows measured and calculated coupling coefficient s, and their difference Δs. Right block shows the change in coupler geometry that could explain such a difference in s. Difference in width Δw, difference in gap Δg, upper cladding refractive index n_{clad}, or height of an included "bubble" h_{b}. Also see Figs. 3.15, 3.16 and 3.17.

to a lower quality of the SiO_2 of the upper cladding or leading to a vacuum "bubble" or gas "bubble" in the small gap between the waveguides. The effect of the cladding refractive index was studied by changing it in the numerical simulations, which shows that a cladding index which explains the measured coupling is around $n_{\text{clad}} = 1$, i.e., air (Fig. 3.17a). This is not a realistic explanation. The effect of an inclusion of an bubble in the cap is studied by including a strip with height h_{b} between the waveguides of the coupler. Such a bubble might be formed when the cladding starts growing from the corners of the waveguide surface and closes the gap before it is fully filled. A gap with height $h_{\text{b}} \approx 150$ nm would agree with the measured coupling (Fig. 3.17b). Although this is a large bubble, we believe that this is the most likely explanation of the discrepancy between the calculated and the measured coupling. The inset of Fig. 3.17b shows the height of the possible bubble h_{b} versus the width of the gap g, showing that the bubble is larger for smaller gaps, which is the expected trend.

3.11 Conclusion

In this chapter, we presented all necessities for the design, fabrication and characterization of silicon photonic micro-ring resonators. First, we discussed the fabrication via the ePIXfab platform that provides CMOS fabrication of the photonic chips. We discussed the in-house post-processing and metrology of these chips. Second, we presented a measurement setup that is capable of automatically measuring a series of devices with high repeatability. Third, we presented devices and a methodology to measure the important characteristics of silicon micro-ring resonators and their individual components. This included waveguides, directional couplers, and racetrack-shaped ring resonators. The obtained figures provide a reference for the typical behavior of silicon micro-ring resonators that are fabricated using contemporary semi-industrial CMOS fabrication. The probable inclusion of gas between the waveguides of the fabricated directional coupler unfortunately precludes the usage of the obtained figures as a reference for design of new sensors.

Especially the directional couplers were studied in detail. We provided a theory that agrees well with the measured characteristics. This intuitive description of the coupler was derived using coupled mode theory. In this theory, we approximated the wavelength-dependency of the coupling coefficient s as linear and we accounted for the coupling occurring in the bends of the coupler by introducing a wavelength-independent effective length of the coupler $\tilde{L}$. We observed an interesting effect in the cross-coupling regime where most light is coupled from one waveguide to the other. In this regime, the directional coupler introduces a surprisingly large additional phase delay.

We provided a clear example of critical coupling that clearly demonstrates the physics of ring resonators. The transmission at resonance is minimal when the amount of light that is coupled to the ring is equal to the amount of light during one round-trip in the ring because this gives perfect destructive interference in the output waveguide. The width of the resonances depends on the round-trip losses of the ring resonator, where the coupling from the ring to the connecting waveguide is also considered as loss. Our measurements provide a typical example of this behavior.

We believe that the methodology presented in this chapter and some of the obtained figures will be useful for designers of photonic chips. Moreover, this chapter provides understanding of the racetrack resonators that is necessary to study these devices as strain- or ultrasound sensors. These mechanical sensors will be the topics of the Chapters 4 and 5.

Chapter

4

Optical strain sensors based on silicon waveguides

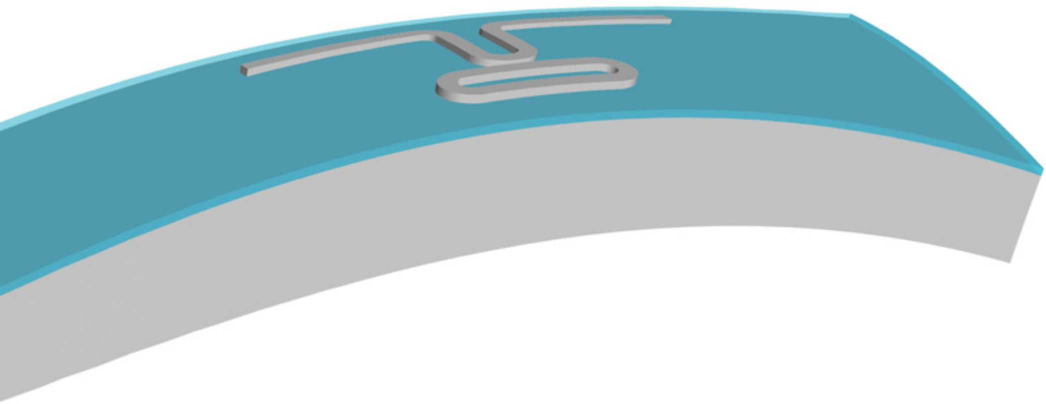

Abstract – Microscale strain gauges are widely used in micro electro-mechanical systems (MEMS) to measure strains such as those induced by force, acceleration, pressure or sound. We propose all-optical strain sensors based on micro-ring resonators to be integrated with MEMS. We characterized the strain-induced shift of the resonances of such devices. Depending on the width of the waveguide and the orientation of the silicon crystal, the linear wavelength shift per applied strain varies between 0.5 and 0.75 pm/microstrain for infrared light around 1550 nm wavelength. The influence of the increasing ring circumference is about three times larger than the influence of the change in waveguide effective index, and the two effects oppose each other. The strong dispersion in 220 nm high silicon sub-wavelength waveguides accounts for a decrease in sensitivity of a factor 2.2 to 1.4 for waveguide widths of 310 nm to 860 nm. These figures and insights are necessary for the design of strain sensors based on silicon waveguides.

4.1 Introduction

This chapter is about the relation between a strain applied to a micro-ring resonator and the shift in its resonance wavelengths. The ultrasound sensors that we will study in the next chapter have a complicated optical behavior and complicated mechanical behavior. Therefore we first use structures that behave mechanically in a well-defined manner to study the opto-mechanical relation.

Microscale strain gauges are widely used in micro electro-mechanical systems (MEMS) to measure strains such as those induced by force, acceleration, pressure or (ultra)sound. These sensors are traditionally based on a piezoresistive or piezoelectric material which transduces the strain to an electrical signal. Alternatively, we propose to use integrated optical silicon micro-ring resonators as sensing element (see Sec. 1.3). Any change in the size or in the refractive index of the waveguide of the ring resonator shifts its resonances, and this shift can be accurately recorded. Silicon-on-insulator technology allows the optical strain sensors, as well as their multiplexing circuit, to be integrated with silicon MEMS. Several groups have reported on sensor MEMS that are based on integrated optical ring resonators in SOI technology, such as strain gauges [16–18], pressure sensors [19–22], or accelerometers [121]. However, details of the relation between

This chapter is based on W.J. Westerveld, S.M. Leinders, P.M. Muilwijk, J. Pozo, T.C. van den Dool, M.D. Verweij, M. Yousefi and H.P. Urbach, “Characterization of integratd optical strain sensors based on silicon waveguides,” *IEEE Journal of Selected Topcis in Quantum Electronics*, vol. 20, no. 4, 2014, *to appear*.

Earlier results based on micro-ring resonator where we excited the fundamental TM-like mode of a 300 nm high silicon waveguide were published as W.J. Westerveld, J. Pozo, P.J. Harmsma, R. Schmits, E. Tabak, T.C. van den Dool, S.M. Leinders, K.W.A. van Dongen, H.P. Urbach, and M. Yousefi, “Characterization of a photonic strain sensor in silicon-on-insulator technology,” *Optics Letters*, vol. 37, no. 4, pp. 479–481, Feb 2012.

an applied strain and the shift in optical resonance of ring resonators have not been studied.

We characterized the shift of the resonance wavelengths that is caused by a well-defined strain. This includes a characterization of the change in the effective index of the sub-wavelength silicon waveguide. We studied the influence of the waveguide width and the influence of the orientation of the silicon crystal. This knowledge is required for the design of mechanical sensors based on silicon integrated optics, such as ring resonators or Mach-Zehnder interferometers. Also, we quantified the contribution of three physical effects: (1) the strain-induced change in circumference of the resonator, (2) the strain-induced change in effective index of the waveguide, and (3) the dispersion which is strong in sub-wavelength silicon waveguides.

This chapter is organized as follows: first we present the devices which are used to study the effect of strain on silicon optical waveguides (Sec. 4.2), then we derive opto-mechanical theory describing these devices (Sec. 4.3), after which we detail the experimental setup and methodology (Sec. 4.4). The characterization and the analysis of the devices are presented in Sec. 4.5 and Sec. 4.6, respectively, and we conclude in Sec. 4.7.

4.2 Devices

The integrated optical devices are in SOI technology with 220 nm thick silicon waveguides embedded in silica. From bottom to top, the chip consists of a 675 μm thick silicon substrate, a 2 μm thick SiO_2 (BOX) layer, the 220 nm thick silicon waveguide layer, and a 2 μm thick SiO_2 top cladding (see Sec. 3.3 for details).

We designed long racetrack-shaped ring resonators in an "add-drop" configuration (Fig. 4.1), and excite the "input" waveguide with infrared light with wavelengths λ around a center wavelength λ_c of 1550 nm. A directional coupler couples light from the "input/output" waveguide to the resonator, and an identical coupler is used half-way the racetrack to couple light to a "drop" waveguide. The transmitted spectrum $T(\lambda)$ in the "output" port has dips at the resonance wavelengths of the resonator. We characterized the couplers and found that 59% of the power is coupled from the waveguide to the track, such that the power which goes straight-through the coupler $|\tau|^2 = 41\%$. Having a strong coupling in a symmetric add-drop configuration gives resonance dips with good extinction ratio even for high losses in the racetrack or for fabrication-induced variations in coupling (see Sec. 2.13).

Silicon is anisotropic, so its deformation depends on the direction in which a force is applied. Therefore two sets of devices were designed, fabricated and characterized; one with the long side of the racetrack parallel to the $\langle 110\rangle$ direction of the silicon crystal and one with the long side parallel to the $\langle 100\rangle$ direction of the silicon crystal. Hopcroft *et al.* in [122] explain the crystal planes in a "(100) wafer" as we used. We characterized the influence of the width of the waveguide on the shift in resonance, therefore each set of devices consists of resonators with waveguide widths varying from 310 nm up to 860 nm. We only excited the fundamental mode of the waveguides.

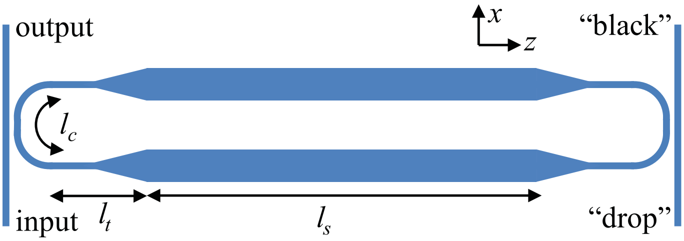

Figure 4.1: Sketch of racetrack resonator with in/output ports (not to scale). Long straight waveguide has length $l_s = 1000$ μm and width w. Taper section has length $l_t = 64.35$ μm (4.35 μm long waveguide of width 400 nm, taper with a length varying from 0 to 60 μm, followed by a waveguide of width w to close the space.) Coupler section has length l_c and consists of two 10 μm long parallel guides (width ~400 nm, gap 220 nm), and bends with a radius of 5 μm.

4.3 Theory

This section presents the theory of ring resonators such as presented in the previous section, i.e. a looped waveguide with a varying width. First, in Sec. 4.3.1, we briefly summarize the optical theory of ring resonators. Then in Sec. 4.3.2, the opto-mechanical theory is described. Sec. 4.3.3 applies the theory to the long racetrack resonators under study. The relations derived in this section are used as fitting function of the measured spectra, and as basis for the analysis of the measurements.

4.3.1 Ring and racetrack resonators

The fraction T of power that is transmitted from the input port to the output port of a micro-ring resonator with two lossless couplers in an add-drop configuration such as shown in Fig. 4.1 is, from Eqs. (2.175 and 2.176),

$$T = \frac{\alpha^2|\tau|^2 + |\tau|^2 - 2\alpha|\tau|^2\cos(\theta)}{1 + \alpha^2|\tau|^4 - 2\alpha|\tau|^2\cos(\theta)}, \tag{4.1}$$

where $|\tau|^2$ is the straight-through power of the coupler and α^2 is the power transmission due to one round-trip through the ring ($\alpha = 1$ means zero loss). T thus describes the fraction of optical power transmitted from the input to the output of the connecting waveguide, and is wavelength dependent primarily because θ is wavelength-dependent. The phase delay θ of one round-trip through the ring (including passing the couplers) is, from Eqs. (2.186 and 2.31)

$$\theta = \oint n_e(\rho, \lambda)\frac{2\pi}{\lambda}\mathrm{d}\rho = \langle n_e(\lambda)\rangle\frac{2\pi}{\lambda}l, \tag{4.2}$$

where the waveguide effective index $n_e(\rho, \lambda)$ is averaged over the position ρ in the track with circumference l as $\langle n_e(\lambda)\rangle \equiv \frac{1}{l}\oint n_e(\rho, \lambda)\mathrm{d}\rho$. The effective index in the coupler is approximated by the effective index of a single isolated waveguide. The strong modal dispersion in sub-wavelength silicon waveguides is approximated to be linear around the center wavelength λ_c, and is expressed in terms of the effective group index $n_g \equiv n_e - \lambda\frac{\partial n_e}{\partial \lambda}$, see (2.33). As λ and ρ are independent, the track-averaged effective index $\langle n_e(\lambda)\rangle$ is then given by

$$\langle n_e(\lambda)\rangle = \langle n_e\rangle + (\langle n_e\rangle - \langle n_g\rangle)(\frac{\lambda}{\lambda_c} - 1), \tag{4.3}$$

where n_e and n_g at the right-hand-side, denoted without λ dependence, are evaluated at λ_c.

Equation (4.1) with Eqs. (4.2) and (4.3) will be fitted to the measured resonance spectra to accurately obtain $\langle n_g\rangle$ and $\langle n_e\rangle$, from which the resonance wavelengths are calculated.

4.3.2 Strain-induced resonance shift of ring resonators

In this section we study the shift in the resonances of a ring resonator due to an applied mechanical strain. Four physical effects play a role when elongating a ring- or racetrack resonator. First, the circumference of the track l increases. Second, the cross section of the waveguide shrinks due to the Poisson effect. Third, the refractive indices of the silicon and SiO_2 change due to the photo-elastic effect. The latter two effects together influence the effective index n_e of the waveguide. Fourth, the shift in resonance is affected by the dispersion in the waveguide.

In our case, a homogeneous strain S_z is applied parallel to the long sides of the racetrack resonator (whose direction is referred to as the z-direction). The transmitted spectrum of the connecting waveguide shows dips at the resonance wavelengths λ_m when $\theta = m2\pi$, or

$$m\lambda_m = \oint n_e(\rho, \lambda_m, S_z)\,(1 + S_\rho(\rho, S_z))\,\mathrm{d}\rho. \tag{4.4}$$

The effective index of the waveguide depends on the mechanical deformation. The local strain in the direction of the track S_ρ is taken into account by stretching each element $\mathrm{d}\rho$ to $(1 + S_\rho)\mathrm{d}\rho$. For the straight waveguide of the racetracks as in Fig. 4.1, the z- and ρ-directions coincide, whereas they do not for the coupler sections. We found experimentally that the relation between an applied strain S_z and the shift in resonance wavelength is linear, which is explained by the fact that we applied small strains. A description of this linear influence can be found by taking the first derivative of Eq. (4.4) with respect to S_z,

$$m\frac{\partial \lambda_m}{\partial S_z} = \oint \left\{ \left(\frac{\partial n_e}{\partial S_z} + \frac{\partial n_e}{\partial \lambda_m}\frac{\partial \lambda_m}{\partial S_z} \right)(1 + S_\rho) + n_e\frac{\partial S_\rho}{\partial S_z} \right\} \mathrm{d}\rho,$$

which we evaluate at zero strain (i.e. $S_z = S_\rho = 0$). Solving this equation for $\partial\lambda_m/\partial S_z$, substituting m from Eq. (4.4), and dividing by track circumference l gives

$$\frac{\partial \lambda_m}{\partial S_z} = \frac{\lambda_c}{\langle n_g\rangle l} \oint \left(\frac{\partial n_e}{\partial S_z} + n_e\frac{\partial S_\rho}{\partial S_z} \right) \mathrm{d}\rho, \tag{4.5}$$

where λ_c is the resonance wavelength λ_m without deformation. In this work, we studied the resonace with a wavelength closest to a 1550 nm and we have approximated λ_c by 1550 nm. This gives a maximum error below below 0.01%. Equation (4.5) is easiest understood when considering a resonator with a uniform waveguide shape (i.e. $\langle n_e \rangle = n_e$ and $\langle n_g \rangle = n_g$). In that case,

$$\frac{\partial \lambda_m}{\partial S_z} = \underbrace{\frac{n_e}{n_g}}_{\text{dispersion}} \left\langle \underbrace{\frac{\lambda_c}{n_e}\frac{\partial n_e}{\partial S_z}}_{\text{eff. index}} + \underbrace{\lambda_c \frac{\partial S_\rho}{\partial S_z}}_{\text{track-length}} \right\rangle, \tag{4.6}$$

where the influence of the different physical effects are indicated. Without dispersion, $n_e/n_g = 1$. For the part of the track which is in the direction of the applied strain $S_\rho = S_z$, so $\partial S_\rho / \partial S_z = 1$, hence the contribution of the track-length change is simply λ_c.

4.3.3 Strain-induced resonance shift of long racetracks

We measured very (1 mm) long racetracks because this allows neglecting the influence of the tapers and the couplers (see Fig. 4.1). In the long racetrack resonators, Eq. (4.4) reads

$$\begin{aligned} m\lambda_m &= 2 l_s n_s (1 + S_z) \\ &\quad + \int_{\text{tapers}} n_e \left(1 + S_\rho\right) \mathrm{d}\rho + \int_{\text{couplers}} n_e \left(1 + S_\rho\right) \mathrm{d}\rho, \end{aligned} \tag{4.7}$$

where the contributions of the different sections of the track are separated (see Fig. 4.1, with l_s, l_t, and l_c indicating the straight, taper and coupler sections, respectively) and n_s is the effective index of the long straight waveguide. We calculate the first-order influence of strain on this racetrack similarly to Eq. (4.5), and rewrite the equation such that the influence of the tapers and the couplers is written as a correction to the shift caused by the long straight guides,

$$\begin{aligned} \langle n_g \rangle \frac{\partial \lambda_m}{\partial S_z} =& \lambda_c \left(\frac{\partial n_s}{\partial S_z} + n_s \right) \\ &+ \frac{\lambda_c}{l} \int_{\text{tapers}} \left(\frac{\partial n_e}{\partial S_z} + n_e \frac{\partial S_\rho}{\partial S_z} - \frac{\partial n_s}{\partial S_z} - n_s \right) \mathrm{d}\rho \\ &+ \frac{\lambda_c}{l} \int_{\text{couplers}} \left(\frac{\partial n_e}{\partial S_z} + n_e \frac{\partial S_\rho}{\partial S_z} - \frac{\partial n_s}{\partial S_z} - n_s \right) \mathrm{d}\rho. \end{aligned} \tag{4.8}$$

We will justify hereafter that the second and third term of the right-hand-side of this equation are small compared to the first one, and hence can be neglected, resulting in

$$\langle n_g \rangle \frac{\partial \lambda_m}{\partial S_z} \approx \lambda_c \left(\frac{\partial n_s}{\partial S_z} + n_s \right). \tag{4.9}$$

The taper is a waveguide in the z-direction with a width varying from 400 nm up to the width w of the long section waveguide. The second term at the right-hand-side of Eq. (4.8) is defined as the relative contribution of the taper to the resonance shift, with respect to the contribution of a waveguide with width w of the same length. The relative contribution of the taper is smaller than the relative contribution of a 400 nm wide waveguide of the same length. Using Eq. (4.9), it is thus found that the second term of the right-hand-side of Eq. (4.8) is smaller than

$$\frac{4l_t}{l}\left| \underbrace{\langle n_g\rangle \frac{\partial \lambda_m}{\partial S_z}}_{\text{width under study}} - \underbrace{\langle n_g\rangle \frac{\partial \lambda_m}{\partial S_z}}_{\text{width 400 nm}} \right|. \tag{4.10}$$

The third term of Eq. (4.8) comes from the effect of the couplers including the bend waveguides. This contribution can be either positive (as for the long waveguides) or negative (as the path-length might shrink due to the Poisson effect). We expect the magnitude of this term to be smaller than twice the effect of a straight waveguide of equal length that is strained in its long direction. Thus the 3rd term in Eq. (4.8) is smaller in magnitude than

$$2\frac{2l_c}{l}\left(\langle n_g\rangle \frac{\partial \lambda_m}{\partial S_z}\right). \tag{4.11}$$

As will be shown in Sec 4.5, the maximum measured difference in $\langle n_g\rangle(\partial\lambda_m/\partial S_z)$ for the devices under study with different waveguide widths is 10%. For these long racetracks, $4l_t/l = 11\%$, so the second term in Eq. (4.8) is smaller than 1.1%. The third term is smaller than $4l_c/l = 5\%$. Equation (4.9) is used in the characterization of the measurements. We characterized both $\langle n_g\rangle$ and $\partial\lambda_m/\partial S_z$. The effective index of the straight waveguide n_s is computed with a numerical mode solver, which allows us to extract the strain-induced change in effective index.

Similar to Eq. (4.6) in the more general Sec. 4.3.2, we indicate the effects of the different phenomena in Eq. (4.9)

$$\frac{\partial \lambda_m}{\partial S_z} = \underbrace{\frac{n_s}{\langle n_g\rangle}}_{\text{dispersion}} \left(\underbrace{\frac{\lambda_c}{n_s}\frac{\partial n_s}{\partial S_z}}_{\text{eff. index}} + \underbrace{\lambda_c}_{\text{track-length}} \right). \tag{4.12}$$

This result is used in the interpretation of the measurements in Sec. 4.6. In fact, we find that track-averaged group index $\langle n_g\rangle$ can be approximated as the group index n_g of the straight waveguide. We have used the numerical mode solver to show that this approximation is valid within 1%. In our analysis, we use the track-averaged group index which was accurately measured.

4.4 Methodology

We characterized the photonic chips in an automated setup in which they are bent such that the top layer with the racetrack resonators is strained. Transmission spectra of the resonators were recorded for elongations varying from 0 to

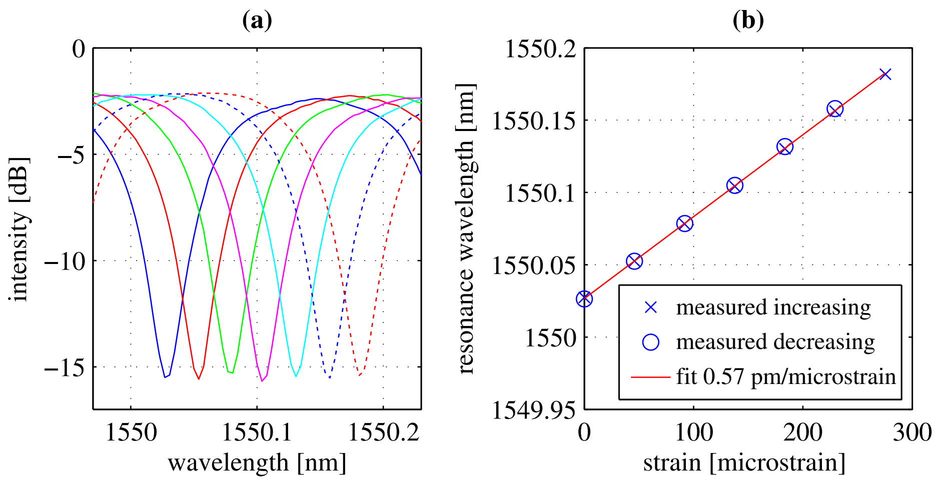

Figure 4.2: Example of resonance shift due to an applied strain. **(a)** Small wavelength span of 7 measured spectra for increasing values of applied strain. Resonance dips shift to the red. Racetrack is in the <100> crystalline direction, with waveguide width 400 nm. **(b)** The wavelengths of the resonance dips λ_m in (a) is plotted versus the applied strain S_z. The wavelengths of the resonance dips for decreasing values of strain are also plotted. Note that the observed relation is linear and that no hysteresis was observed. Resonance shift $\partial\lambda_m/\partial S_z$ is obtained from a linear fit.

275 microstrain. As example, Fig. 4.2a shows a resonance dip of the measured spectra for increasing strain. The resonance wavelengths, and the group index n_g, were extracted from fitting a relation for ring resonator transmission. Figure 4.2b shows the resonance wavelength λ_m plotted versus the applied strain.

4.4.1 Mechanical setup: four point bending

We designed and fabricated a mechanical setup in which the chips are bent such that the top layer with the photonic circuit is uniformly strained (Fig. 4.3). The setup is equipped with elastic elements to provide an accurate bending moment to the chip, without hysteresis or other non-linearities. Figure 4.3a-c explains the mechanics of the setup. A load L is applied at the lever. The upper beam acts as a lever so that total downwards force acting on the chip $L' = L \cdot a_1/a_2$ (Fig. 4.3b). This force is equally split between the two outer supports, which each provide a concentrated load $\frac{1}{2}L'$ on the chip such that the inner supports each have a reaction force $\frac{1}{2}L'$ upwards (Fig. 4.3c). The entire chip is in mechanical equilibrium, so that also a cross-section of the chip at arbitrary z-position is in equilibrium. The torque or *bending moment* $M(z)$ on a section is transmitted across it, and can be defined as "the sum of the moments about that section of all external forces acting to one side of that section". As the section is in equilibrium, either the left-hand-side of the section or the right-hand-side of the section result in

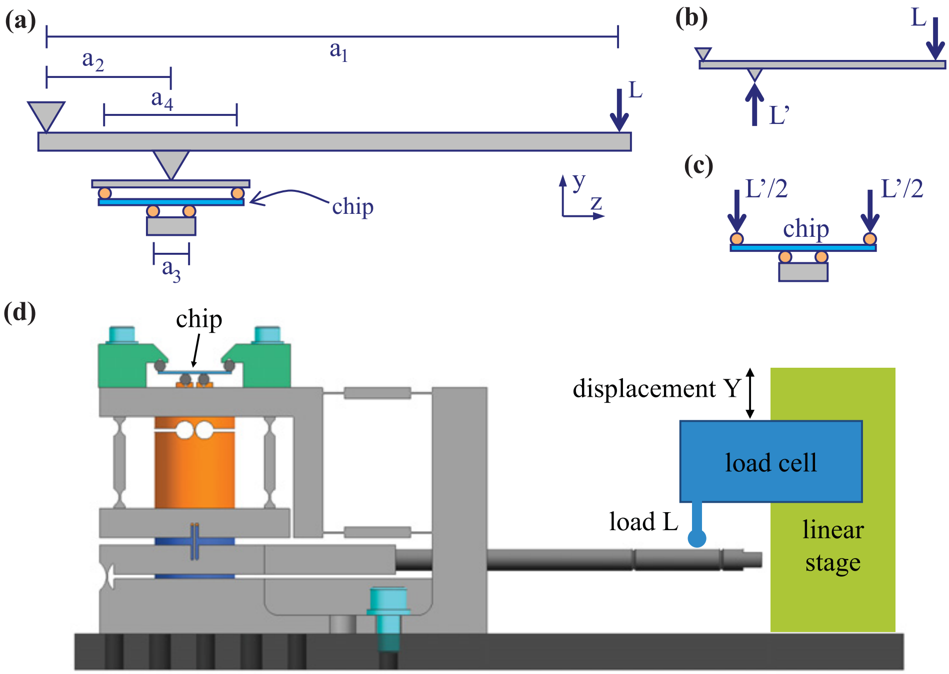

Figure 4.3: (a-c) Analysis of the mechanical setup. **(d)** Sketch of the mechanical setup. Composed of the CAD drawing that was used to fabricate the setup (left-hand-side), and a sketch of the linear stage with the load cell (right-hand-side). Appendix B presents photographs of this setup.

the same bending moment. The region of the chip between the two inner supports has a uniform bending moment $M = (a_4 - a_3)L'/4$, which is referred to as *pure bending* (see Fig. 5-4 in Ref. [123]). This gives

$$M = \frac{a_1(a_4 - a_3)}{4a_2} L, \tag{4.13}$$

The bending of the chip is described by plate bending theory for *thin plates with small deflections* [124], as its thickness H is small compared to its width W and length. An assumption in this theory is that the normal stresses in the x-direction can be neglected, so that there is no strain S_x in the x-direction and the width W of the chip does not change due to the applied load. Moreover, we neglect the influence of upper layers of the chip (BOX layer, waveguide layer, and cladding layer) as their total thickness of 4.220 μm is much smaller than the chip thickness of 675 μm. Hooke's law and plate bending theory give the relation between the stress σ_z and strain (relative elongation) S_z in the chip [122, 124]:

$$\sigma_z = \frac{E_z}{1 - \nu_{xz}\nu_{zx}} S_z, \tag{4.14}$$

with Young's modulus[1] E_z and anisotropic Poisson's ratios[2] ν_{xz} and ν_{zx}. Under the aforementioned assumptions, the deflection of the chip at considerable distance from its ends can be assumed to be cylindrical. The chip bends into a cylinder with curvature κ. The neutral axis of the chip experiences no strain, and the strain at a distance y above (or below, for negative y) the neutral axis is

$$S_z = \kappa y \tag{4.15}$$

The moment experienced by a small strip of the section with height dy is

$$\mathrm{d}M = \sigma_z(y)\, y\, W \mathrm{d}y. \tag{4.16}$$

Integrating over all small strips of the section gives the total bending moment on the section. Substituting Eqs. (4.14) and (4.15) in Eq. (4.16) and integrating over y from $-H/2$ to $H/2$ gives

$$M = \frac{\kappa E_z W H^3}{12(1-\nu_{xz}\nu_{zx})}. \tag{4.17}$$

The strain at the top surface, $y = H/2$, of the chip is given by Eqs. (4.15) and (4.17) as

$$S_z = \frac{6M(1-\nu_{xz}\nu_{zx})}{WH^2E_z}. \tag{4.18}$$

Combining Eqs. (4.13) and (4.18), the strain on the top surface of the chip in the mechanical setup is

$$S_z = \frac{3a_1(a_4-a_3)(1-\nu_{xz}\nu_{zx})}{2a_2WH^2E_z}L. \tag{4.19}$$

A precise linear stage (Newport MFA-CC) applies a force to the lever, while a load cell (Omega LECB5) measures the actual applied load L. It was observed that the relation between the displacement of the linear stage Y and the applied load L is linear in the regime of our measurements, and also that the repeatability of the linear stage position Y was higher than the repeatability of the load cell. Therefore, we extracted a single number for the resistance of the chip to bending, $\partial Y/\partial L$, from all the measurements performed on a chip.

4.4.2 Optical setup

The transmission spectra of the racetracks were measured with near infrared light around $\lambda_c = 1550$ nm. An amplified spontaneous emission light-source (OptoLink C-band ASE) was used to emit this light, and a 5 nm span of the spectra were recorded with an optical spectrum analyzer (Yokogawa AQ6370B). The input and output waveguides of the racetrack resonators are routed to out-of-plane grating couplers at convenient locations on the chip, and coupled to cleaved optical fibers via free-space (see Sec. 2.11). These fibers were mounted on stages with piezo

[1] E_i is the Young's modulus along axis i.

[2] ν_{ij} is the Poisson's ratio that corresponds to a contraction in direction j when an extension is applied in direction i.

positioning, and automatically actively aligned in the horizontal (x,z)-plane before recording a spectrum. All transmission spectra are normalized to the transmission spectrum of a reference waveguide, which was smoothened by convolution with a 1 nm wide Gaussian window to remove Fabry-Pérot resonances originating from reflections of the out-of-plane grating couples.

A relation for ring resonator transmittance, Eqs. (4.1)-(4.3), was fitted to the recorded spectrum (similar to the *DCM2* method in Sec. 3.6.2). The ring length l and straight-through power of the coupler $|\tau|^2 = 41\%$ were fixed, while the effective index $\langle n_e \rangle$, group index $\langle n_g \rangle$, resonator waveguide loss α^2 and fiber-coupling loss were fitted. The resolution bandwidth of the optical spectrum analyzer (OSA) was incorporated in this fitting by convoluting the calculated spectrum with a 20 pm wide Gaussian curve. For the zero-strain measurement, the mode number m of the resonance closest to λ_c was estimated from Eq. (4.4) where the effective index $n_e(\rho, \lambda_c, 0)$ was calculated using a mode solver (film mode matching method, see Sec. 2.8). This dip was followed over consecutive measurements. An accurate initial estimate of $\langle n_e \rangle$ and $\langle n_g \rangle$ (thus the wavelengths of the resonance dips) is necessary for the Levenberg-Marquardt fitting algorithm [119]. Therefore, the resonance dips were first found using *findpeaks* [118] and from this $\langle n_e \rangle$ and $\langle n_g \rangle$ were estimated via Eq. (4.4). This initial estimate allows for automated fitting of the spectra. With this fitting, the free parameters in Eqs. (4.1)-(4.3) could be obtained, and λ_m was calculated from Eq. (4.4) with an accuracy much higher than the resolution bandwidth of the OSA.

4.4.3 Measurements

We characterized chips with the racetracks in the <110> crystalline direction and with the racetracks in the <100> direction. The measurements were repeated several times for consistency and validation. First, the chip was manually placed in the setup. Then resonators with different widths of the straight waveguide were automatically measured. The strain of the racetrack was increased and decreased from 0 to approximately 275 microstrain, with 6 steps in each direction (see Fig. 4.2a). The transmittance spectrum was recorded for each applied strain, and the resonance position λ_m that started closest to λ_c was extracted. The effective group index $\langle n_g \rangle$ was also extracted from this spectrum. For each value of applied strain, the measured load L and the position of the linear stage Y were recorded. Per measurement-set of increasing and decreasing strain, the resonance shift per displacement of the load cell, $\partial\lambda_m/\partial Y$, was obtained from a linear fit, and so was the relation between the displacement and the applied load, $\partial Y/\partial L$. We observed that both relations were indeed linear in this regime. The strain-induced resonance shift is then

$$\frac{\partial \lambda_m}{\partial S_z} = \frac{\partial \lambda_m}{\partial Y} \cdot \frac{\partial Y}{\partial L} \cdot \frac{\partial L}{\partial S_z}, \tag{4.20}$$

in which the first two factors on the right-hand-side are measured and the last factor is calculated from Eq. (4.19).

The relation between the displacement of the load cell and the measured load can be interpreted as the resistance of the chip and setup to bending. The average value for the chip with the racetracks in the <110> direction is $\partial Y/\partial L = 0.128$ μm/mN and the average value for the chip with the racetracks in the <100> direction $\partial Y/\partial L = 0.135$ μm/mN.

4.4.4 Numerical mode solver

For the analysis of the measurements, we calculated the effective index at zero strain, $n_e(\rho, \lambda_c, 0)$ using the film mode matching method (see Sec. 2.8). Also the effective group index $n_g(\rho)$ at λ_c was calculated using this mode solver. The track-averaged effective index $\langle n_e \rangle$ and group index $\langle n_g \rangle$ are then straightforward to calculate.

4.4.5 Measurement uncertainty analysis

The uncertainty in the measurements was estimated following the guidelines of Ref. [125]. The relative errors of the three factors at the right-hand-side of Eq. (4.20) are added quadratically, as they are independent. The chips with the racetrack resonators in the <110> and <100> directions were placed in the mechanical setup and measured 6 and 5 times, respectively.

Uncertainty in $\partial \lambda_m/\partial Y$

The value for $\partial \lambda_m/\partial Y$ is averaged over the repetitive measurements, and the uncertainty is estimated by the standard deviation. The relative uncertainty did not significantly depend on the width of the waveguide, and the maximum relative uncertainty (of all widths) is used. The uncertainty in $\partial \lambda_m/\partial Y$ for the chips with the waveguides in the <110> and <100> directions are 3.1% and 1.1%, respectively. The measurement-to-measurement difference mainly originated from repositioning the chip in the setup, which was done before each measurement. Repeating a measurement without repositioning the chip in the setup gives a measurement-to-measurement difference which is negligible. We could not attribute this difference to a slight tilt of the chip with respect to the setup (around the y-direction). We do not fully understand why the uncertainty in the <110> direction is higher, but the strong angle dependency of Poisson's ratio around the <110> direction may play a role. Also, we had to reassemble the setup between various <110> measurements, while the measurements of the <100> chip were performed consecutively in a mainly empty laboratory.

Uncertainty in $\partial Y/\partial L$

The value of $\partial Y/\partial L$ did not significantly depend on the position of the chip in the setup. All measurements (for different widths of the waveguide, and repetitions of the measurements) are averaged to obtain $\partial Y/\partial L$. The statistical uncertainty (arising from random fluctuations) is estimated as the standard deviation, and the systematic uncertainty of the system (load cell, load cell voltage source, and A/D converter) is estimated as 3%. The standard deviation of the 30 measurements in the <110> direction is 2.8%, and the standard deviation of the 45 measurements

Table 4.1: Material properties, dimensions, and estimated uncertainties of mechanical setup

Quantity	Value	Uncertainty		
$E_z/(1-\nu_{xz}\nu_{zx})$, <110>	170 GPa[a]	4	GPa	2.5%[b]
$E_z/(1-\nu_{xz}\nu_{zx})$, <100>	141 GPa[a]	4	GPa	2.5%[b]
a_1	156 mm	0.3	mm	0.2%[c]
a_2	24 mm	0.03	mm	0.1%[d]
a_3	5 mm	0.03	mm	0.6%[d]
a_4	20 mm	0.03	mm	0.1%[d]
Chip W	24 mm	0.3	mm	1.2%[c]
Chip H	0.675 mm	0.01	mm	1.7%[e]
$\partial L/\partial S_z$, <110>	12.7 mN/μstrain	0.6	mN/μstrain	4.7%
$\partial L/\partial S_z$, <100>	10.5 mN/μstrain	0.5	mN/μstrain	4.7%

[a] From Ref. [122]
[b] Estimated.
[c] Measured with digital electronic calipers, maximum error 0.5 mm.
[d] Estimated fabrication uncertainty, maximum error 0.05 mm.
[e] Measured with digital electronic calipers, maximum error 0.02 mm.

in the <100> direction is 0.7%. This difference can be explained by the fact that we increased the integration time of the read-out of the load cell from 50 samples at 1 kHz for the <100> direction measurements to 1000 samples at 1 kHz for the <110> direction measurements. The output voltage of the load cell is a few mV, which required this longer integration time of our A/D converter (National Instruments USB-6251 DAQ). The uncertainties of $\partial Y/\partial L$ are thus 5.8% and 3.7% for the chips with the racetracks in the <110> and <100> directions, respectively.

Uncertainty in $\partial L/\partial S_z$

The mechanics of the setup is described by Eq. (4.19). The material properties, dimensions, and uncertainties that are used in this equation are listed in Table 4.1. The uncertainty σ of a quantity whose uncertainty is estimated as a maximum deviation u is given by $\sigma = u/\sqrt{3}$ [125]. In the computation of the uncertainty of $\partial L/\partial S_z$, we have treated all uncertainties as independent and approximated the influence of all the uncertainties as linear.

Uncertainty in the group index $\langle n_g \rangle$

We found that the track-averaged effective group index does not depend on the applied strain. Therefore all measurements of a device are averaged, and the uncertainty is estimated as the standard deviation. These where 78 and 65 measurements for the racetracks in the <110> direction and <100> directions, respectively. The relative uncertainty did not depend much on the width of the straight waveguide in the racetrack nor on the crystalline orientation, so that we have used the maximum of 0.03%.

Uncertainty in the effective index $\langle n_e \rangle$

In the analysis of the measurements, we calculated the effective index with a numerical mode solver. We do not know the uncertainty, as it is mostly related to the difference between the simulated waveguide and the fabricated waveguide. Therefore, we estimated the uncertainty in the effective index as the difference between the measured effective group index $\langle n_g \rangle$ and the track-averaged group index as calculated with the same mode solver (see Fig. 4.4b).

4.5 Characterization

We characterized two chips with long racetrack resonators; one chip with the resonators in the <110> silicon crystalline direction and one with the resonators in the <100> direction. A strain S_z was applied to the top surface of the chips, where the resonators are placed. The strain was increased to approximately 275 microstrain, and then decreased to zero strain in steps of approximately 45 microstrain. Per applied strain, the transmission spectrum of the resonator was recorded, as is shown in Fig. 4.2a. The wavelength of the resonance dip around 1550 nm is extracted from each of the spectra and it is plotted versus the applied strain in Fig. 4.2b. The shift per applied strain $\partial\lambda_m/\partial S_z$ is obtained from a linear fit. This is done for racetracks with different widths, and the resonance shifts per strain are presented in Fig. 4.4a. It can be seen that the racetracks in the <110> direction are slightly more sensitive than the tracks in the <100> direction, and that the resonators with wider waveguides are more sensitive to strain than the ones with narrower waveguides widths. The latter can be attributed to the dispersion in the waveguide, as shown in Sec. 4.6. The estimated uncertainties are with respect to the absolute value of λ_m/S_z, and a large part of the uncertainty is a systematic bias and equal for all measurements. Considering only the statistical (or random) uncertainties, we found that the racetracks in the <110> and <100> directions have a significantly different shift in resonance.

The track-averaged effective group indices $\langle n_g \rangle$ were also extracted from the spectra and are presented in Fig. 4.4b. Next to this, we calculated the effective group index with the numerical mode solver. The calculated and measured track-averaged effective group indices agree within 3%.

The change in effective index due to strain, $\partial n_s/\partial S_z$, is calculated using Eq. (4.9). We measured the resonance shift $\partial\lambda_m/\partial S_z$ and the effective group index $\langle n_g \rangle$, and we calculated the effective index n_s of the straight waveguide with the numerical mode solver. The resulting $\partial n_s/\partial S_z$ is shown in Fig. 4.4c.

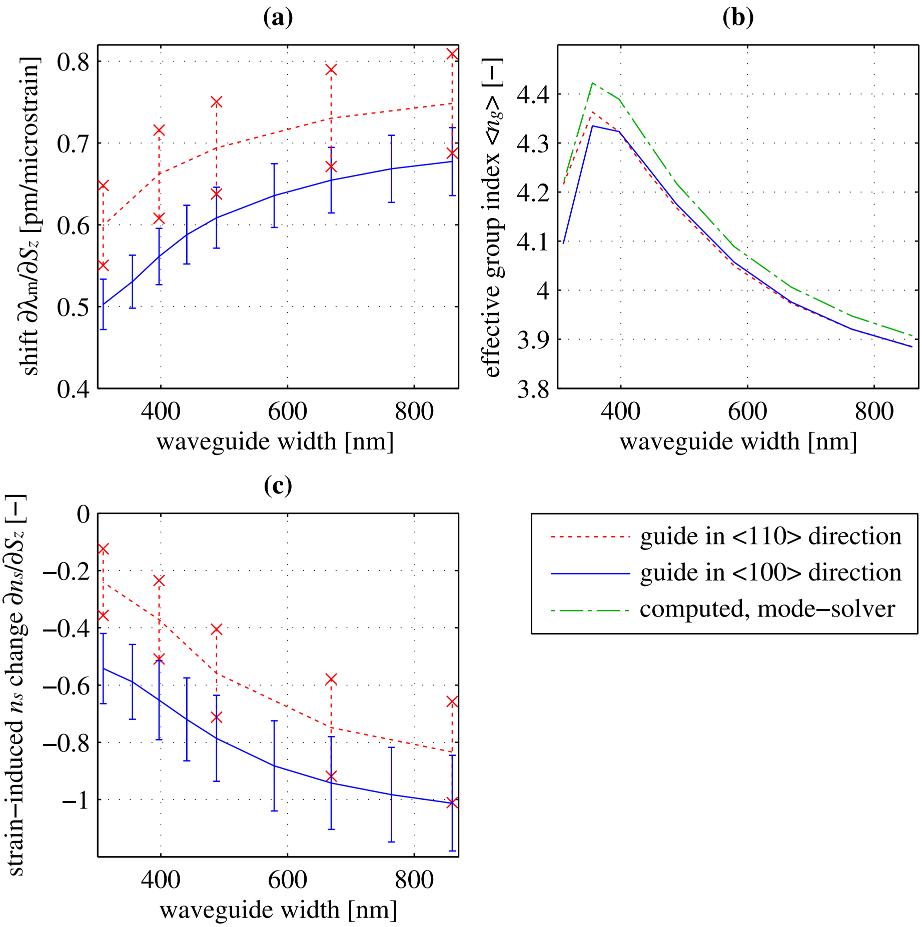

Figure 4.4: **(a)** Measured resonance shift per applied strain $\partial\lambda_m/\partial S_z$, with resonance wavelength λ_m and strain S_z. **(b)** Measured and calculated track-averaged effective group indices $\langle n_g \rangle$. Measured for racetracks in the <100> and in the <100> silicon crystalline directions. **(c)** Change in effective index of a straight waveguide, n_s, due to a strain, S_z, applied in the direction of the guide.

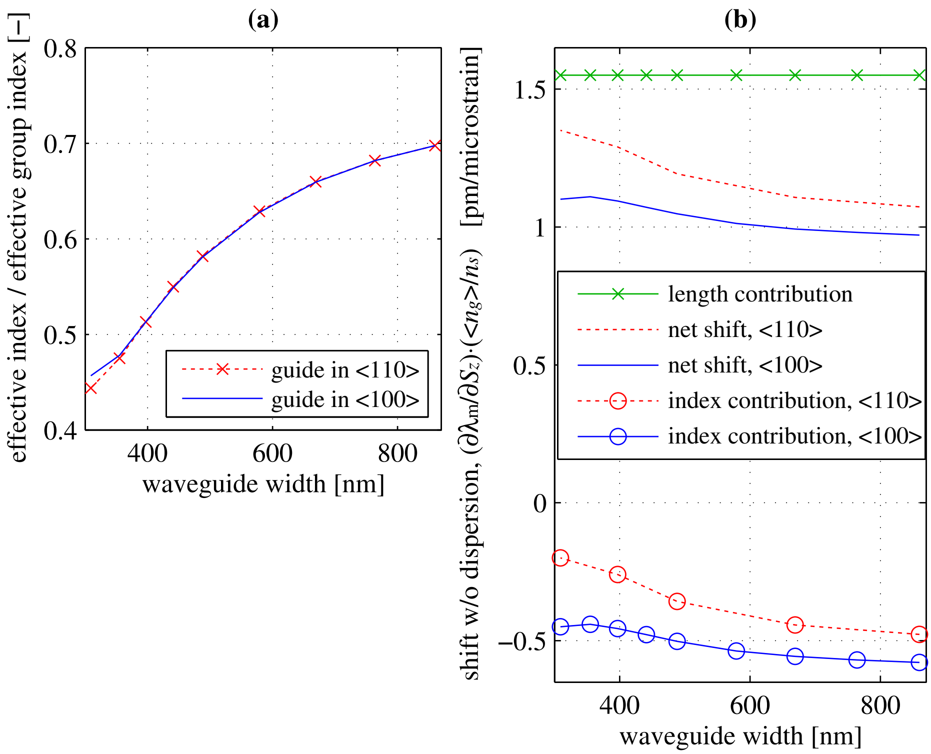

Figure 4.5: (a) Influence of dispersion on the strain-induced resonance shift, $n_s/\langle n_g\rangle$. Effective index n_s is calculated with a mode solver. Track-averaged effective group index $\langle n_g\rangle$ is measured. **(b)** The hypothetical strain-induced shift in resonance in which the dispersion is excluded. The two different contributions to this shift (track-length change and effective-index change) are shown. Results for the racetracks in the <110> and the <100> directions are shown

4.6 Analysis

In this section, we interpret the measured shift and indicate the contributions of different physical effects: the elongation of the track, the change in effective index and the dispersion of the waveguide. Equation (4.12) shows how these effects shift the resonance wavelength. The effect of the elongation of the track (λ_c) and the effect of the change in effective index are added. The change in effective index $\partial n_s/\partial S_z$ is negative, so the two effects oppose each other. The dispersion of the waveguide, n_s/n_g, is smaller than unity, and thus damps the shift. Figure 4.5a presents $n_s/\langle n_g\rangle$, in which it can be seen that this damping is stronger for small waveguides. Figure 4.5b presents the resonance wavelength shift with dispersion excluded. The shift due to the change in the effective index increases (in magnitude) with increasing width of the guide. The higher resonance shift $\partial\lambda_m/\partial S_z$ for wider waveguides is thus due to the dispersion, and not due to the change in effective index of the waveguide.

4.7 Conclusion

We measured the strain-induced shift of the resonances of optical racetrack resonators in silicon-on-insulator technology. For waveguides with a width of 400 nm, the resonance wavelength shift per applied strain is 0.55 pm/microstrain when the racetrack is parallel to the ⟨100⟩-direction of the silicon crystal, and 0.66 pm/microstrain when the racetrack is parallel to the ⟨110⟩-direction. We observed largest sensitivity for wider waveguides; a racetrack with 860 nm wide waveguides oriented in the ⟨110⟩-direction has a resonance shift of 0.75 pm/microstrain. We have studied elongations up to 275 microstrain, and observed a linear relation between the resonance wavelength and the applied strain.

The effect of the strain-induced increase in track circumference and the effect of the strain-induced change in waveguide effective index oppose each other. The effect of the strain-induced increase in circumference is about three times larger than the effect of the change in effective index. The strong dispersion in the sub-wavelength silicon waveguides lowers the change in wavelength shift approximately by a factor two. In fact, the lower dispersion of the wider waveguides is the reason that these devices are more sensitive.

In this work, we have characterized a novel type of optical strain sensors which can be integrated in micro-electro-mechanical systems (MEMS). As detailed in Sec. 1.3, we believe these sensors open opportunities in different fields of applications such as in the medical, petrochemical, or oil&gas markets, by offering specific advantages such as high-speed readout over kilometer distances, integrated optical multiplexing, and small device size. Moreover, by removing the need for galvanic connections, susceptibility to electromagnetic disturbance is eliminated.

The relation between strain and silicon waveguides is of broader interest than sensing alone. Electro-mechanical modulation of silicon optical resonators may be employed to modulate optical signals, for application in the field of telecommunication [126]. As alternative to using silicon waveguides-based ring-resonators, it is also possible to use photonic crystals cavities, which have their own dispersion relations [127]. Strain has also been used to modify the birefringence of larger SOI rib waveguides [128]. Strain is inevitable when using silicon photonic circuits on a flexible substrate [129]. Another interesting field of research is the strain-induced change in the electronic band-gap and the optical refractive index of silicon, with the possibility to introduce second-order nonlinearity [130,131]. All these fields of research might benefit from our analysis of the relation between an applied strain and the shift in resonance wavelengths of silicon micro-ring resonators.

Moreover, knowledge about the relation between an applied strain and the shift in resonance wavelength of racetrack-shaped ring resonators is necessary for design and understanding of the ultrasound sensors that we present in the next Chapter 5.

Chapter

5

An ultrasound microphone employing integrated photonic micro-ring resonators in silicon micro-technology

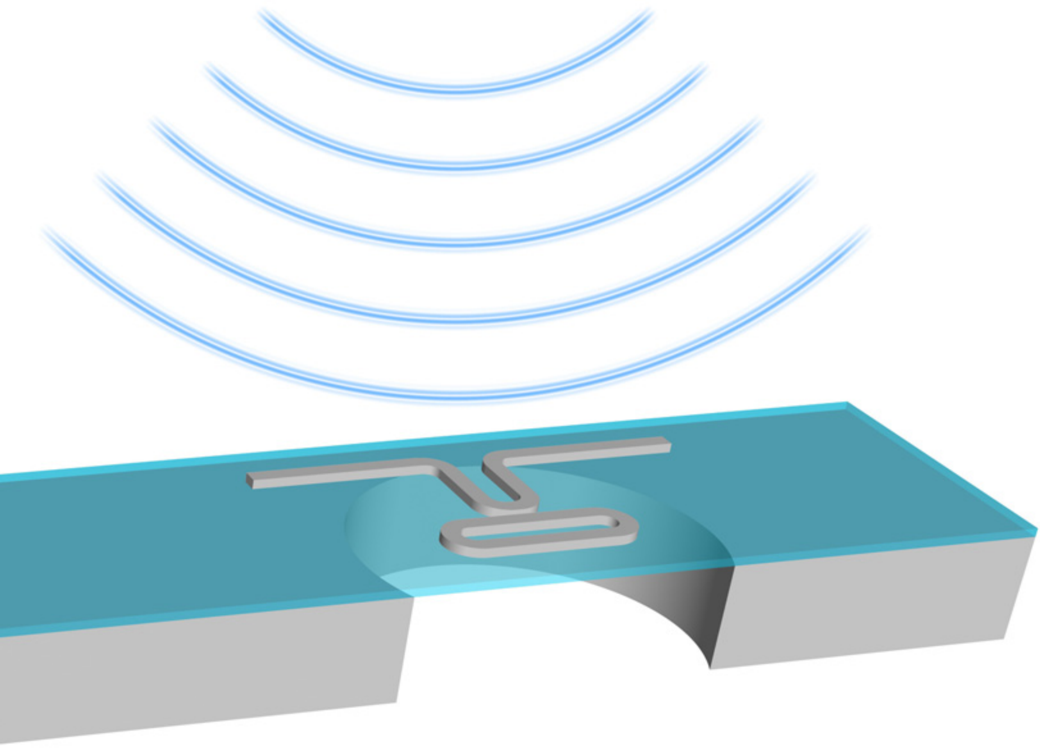

Abstract – Ultrasonography (imaging with ultrasound) is widely used in medical and industrial applications. Computation of sharp images using digital ultrasonic focusing requires an array of small microphones that have a size below half of the wavelength of the ultrasound. Fabrication of such small microphones and wiring of these microphones is challenging with traditional piezo-electric ultrasound transducers. We propose a new type of ultrasound microphone with photonic readout. Both the photonic circuit as well as the acoustical resonant membrane of this microphone were fabricated in wafer-scale silicon-on-insulator chip technology. Silicon photonic technology allows for devices with a small footprint such that wavelength-division multiplexers can be fabricated along with the microphone-resonator. This opens the possibility to read an array of sensors using one optical fiber. We have designed, fabricated, and measured a new type of ultrasonic microphone which is based on photonic micro-ring resonators. The microphone was designed to prove the operation principle of this microphone and the first prototype was fabricated. We demonstrated the operation principle of this new photonic microphone by measuring ultrasound around a frequency of 0.75 MHz. The sensitivity is 1.2 mV/Pa and the detection limit (NEP) is below 1 Pa. This is on the same order of magnitude as the state-of-the-art of conventional piezo-electric based ultrasound transducers. The measured -6 dB bandwidth of the acoustical resonator is 20%. Moreover, we report on the most basic configuration and we believe that there is much room for improvement and optimzation of this new type of microphone.

5.1 Introduction

Ultrasonography (imaging with ultrasound) is widely used in medical and industrial applications (Sec. 1.2). Ultrasonography is usually done either in an aqueous environment or using a liquid to enhance the acoustical coupling between the microphone and the object of interest (e.g. the human body or an oil pipe). Today's array technology allows the formation of images using digital focusing of the recorded signals. For such applications, it is desired to have an array of ultrasonic microphones that are spaced less than a half wavelength of the sound [92]. For sound waves in water (or blood), this corresponds to approximately 750 μm for an ultrasonic frequency of 1 MHz and to 37 μm for 20 MHz. This chapter is about a new type of microphone for the detection of ultrasound but we first give a short review of ultrasonic microphones that are currently used.

The most commonly used ultrasound transducers employ piezo-electric material to convert mechanical stress (or pressure) to an electric potential. However, fabricating transducer arrays is relatively difficult and expensive because the piezo-electric elements need to be wired individually. Over the last decades, there has been a substantial interest in micro-machined ultrasound transducers with capacitive read-out (cMUTs) [132,133]. These transducers consist of a flexible membrane that is above a fixed substrate. A pressure-induced deformation of the membrane

The design of the acoustical resonant membrane as reported in Sec. 5.4.1 is based on S. M. Leinders, W. J. Westerveld, J. Pozo, H. P. Urbach, N. de Jong, and M. D. Verweij, "Membrane design of an all-optical ultrasound receiver," in *Proceedings IEEE International Ultrasonics Symposium*, Prague, Jul. 2013, and the simulations in that section have been performed by the first author of that paper.

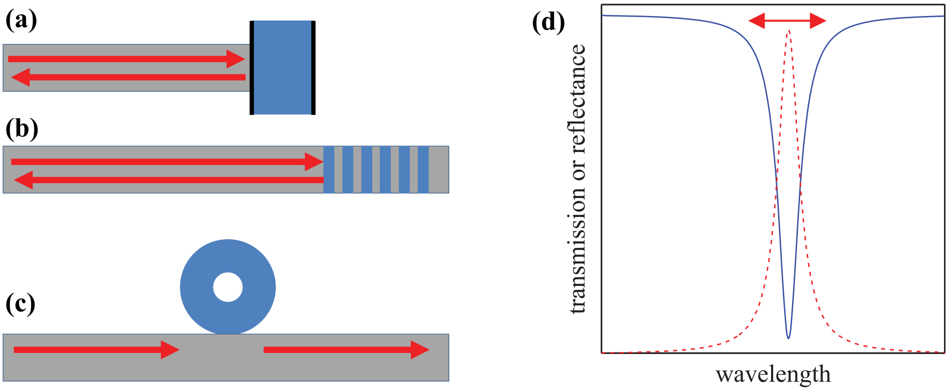

Figure 5.1: Sketch of optical ultrasound microphones. **(a)** Fabry-Pérot resonator at the facet of an optical fiber. **(b)** Distributed Bragg reflector (DBR) in the optical fiber. **(c)** Ring resonator that is coupled to the optical fiber or waveguide. **(d)** Sketch of the reflected or transmitted light. The wavelength of the resonance will shift when the resonator is deformed by ultrasonic pressure waves.

directly results in a change in the capacitance between the membrane and the substrate and this capacitance is continuously measured. An array of cMUTs can be simultaneously fabricated and wired using silicon micro-machining. This allows cost-effective wafer-scale fabrication in the CMOS infrastructure (see Sec. 1.4). Unfortunately, the sensitivity of cMUTs is generally lower than the sensitivity of piezo-electic devices [134]. Both piezo-electric transducers as well as cMUTs use electricity as carrier of information and normally need a coaxial wire for each sensor element. The bundle of wires requires substantial space which is not always available. For example in intravascular ultrasonic imaging, the wall of a blood vessel is imaged from a transducer inside the vessel and there is lack of space for wires (Sec. 1.2). Also, the capacitance of the wire scales with its length, thereby limiting the length of the wires for the high-frequent (MHz range) ultrasound.

As alternative, optical ultrasound transduces have been developed. In contrast to ultrasonic-electronic transducers, optical ultrasonic devices are usually not reciprocal. These are designed to either detect ultrasound (microphones) or generate ultrasound (sources or speakers). In the case of microphones, light is generated externally and the microphone modulates the lightwave with the acoustical signal. The examples hereafter are all based on the same sensing principle (see Fig. 5.1). Light is sent via an optical fiber or waveguide to an optical resonator. The light that is reflected from the resonator or the light that passes the resonator is recorded. Depending on the configuration, this light has minimal (dips) or maximal (peaks) transmission at the wavelengths that correspond to the resonances of the optical resonator (Fig. 5.1d). An incident acoustical soundwave will deform the resonator and change its refractive index which results in a shift of the resonance wavelengths. This shift is thus a direct measure for the ultrasonic signal and it can be recorded using an external interrogation system. One example of an optical ultrasound microphone consists of a Fabry-Pérot optical resonator at the end of the facet of an optical fiber (Fig. 5.1a). The Fabry-Pérot resonator is formed by two gold mirrors with a polymer spacing. Light is sent to the resonator via the fiber. Reflection of the light is minimal for optical wavelengths that correspond to the resonances of the Fabry-Pérot resonator. A hydrophone based on this principle is reported in Ref. [135] and commercially available from Precision Acoustics Ltd (Higher Bockhampton, Dorchester, UK). Another method to detect ultrasound via an optical fiber is by integrating a distributed Bragg reflector (DBR) in the fiber (Fig. 5.1b). This reflector has optical resonances such that it only reflects light around specific optical wavelengths. Similar to the previous method, the DBR can be stretched by ultrasonic waves due to which the optical resonance wavelengths shift [136].

Over the last decade, Guo and co-workers have reported on ultrasound microphones that are based on a polymer ring resonator (Fig. 5.1c) [137–142]. An ultrasonic wave incident on the polymer micro-ring resonator deforms the resonator and thereby shifts its resonance wavelengths. The devices reported in Ref. [141] have diameters 40 μm and 60 μm. The size of the ring resonators can not be very small because otherwise the losses in the highly curved bends are too high. This problem can be solved by using rings with waveguides that have a higher refractive index contrast. The polymer waveguides can be fabricated as a photonic integrated circuit on a planar substrate. In fact, Ref. [140] reports on a cascade of four ring resonators with distinct resonance wavelengths such that they can be interrogated via one optical fiber. The small device size and the planar integration make these devices attractive as microphone arrays for ultrasonography. The fabrication of these polymer photonic integrated circuits depends on special technologies. Recently, Rosenthal [143] and co-workers have reported an ultrasound microphone in silicon-on-insulator technology with waveguides similar to the ones we used. Their microphone is based on a π-phase-shifted Bragg grating formed by waveguide corrugation. In contrast to our ring-resonator, the grating is not placed in on a membrane and Ref. [143] does not report on the sensitivity of the sensor.

Ultrasonography requires an array of microphones but only a single acoustical source is, in fact, sufficient for the reconstruction of ultrasonic images. This source needs to be omnidirectional and deliver sufficient acoustical signal. This source can be a single piezo-electric element. Alternatively, it is possible to use the photo-acoustic effect to generate ultrasound, either in a well defined emitter or in the tissue to be imaged itself [3–7]. The latter is known photo-acoustic imaging. Photo-acoustic imaging has the additional advantage to provide a discrimination of different types of tissue by studying the absorbance of the light [8].

We propose the use of silicon photonic micro-ring resonators to sense ultrasound. Incident pressure waves will deform the optical resonator and hence shift its optical resonance wavelengths. These small silicon ring resonator can be integrated in a mechanical structure to enhance the sound-induced deformation. In particular, we study the use of an acoustical membrane such as is used in cMUTs. Pressure sensors based on this principle have been already been proposed in the 90's [144]. We are, to the best of our knowledge, the first to report the operation of such microphones for ultrasonic frequencies.

This microphone can be fabricated in silicon-on-insulator (SOI) technology. Both the photonic circuits with waveguides of sub-micron cross section as well as the acoustical membrane with a diameter of tens of microns can be fabricated in this technology. This allows for cost-effective wafers-scale fabrication of the microphones using existing CMOS fabrication infrastructure. An array of microphones including wiring can be simultaneously fabricated in this fabrication process. The photonic circuits in the devices that we report in this thesis are fabricated in a semi-industrial CMOS line (Sec. 3.3). Hereafter, we fabricated the membrane by lithography and etching from the back-side of the wafer as is common in MEMS fabrication (Sec. 5.5).

Photonic integrated circuits in SOI have a high refractive index contrast and a small footprint. Silicon micro-ring resonators can have diameters down to 10 μm without substantial radiation losses. This corresponds to an ultrasonic half-wavelength in water for a frequency of 75 MHz. Moreover, the small footprint of silicon photonic integrated circuits allows integration of small passive optical multiplexers for simultaneous readout of many microphones [1,2]. This opens the possibility for high-speed interrogation of an array of sensors via only one or two optical fibers. The height of the waveguiding layer is only a quarter of a micron and has little influence on the acoustical properties of the membrane. This gives the flexibility to optimize the membrane for the desired acoustical characteristics. Alternatively, another acoustical resonant or non-resonant structure could be used. This is different from piezo-electric transducers or cMUTS were the design of the transducer is a trade-off between the electric and acoustic characteristics.

We believe that our new type of ultrasound microphone is very promising for application in ultrasonography. Integrated passive optical multiplexers and the read-out of a sensor arrays at large distance via few optical fibers is highly attractive for certain applications. Moreover, the all-optical sensors do not suffer from electromagnetic interference so that they can be used in, for example, MRI scanners. Another advantage is that the all-optical signal does not produce electric sparks and hence does not have the danger to ignite gas explosions.

In this thesis, we present the proof-of-the-principle for this new type of ultrasound microphone. The design is optimized to proof the operation principle for sound waves with a frequency around 1 MHz. The aim of the optimization was twofold. First we wanted to obtain a device that is as simple as possible to be able to compare the experimental results with simulations. Secondly, the sensitivity was optimized as this was our biggest concern. We chose to integrate a silicon micro-ring resonator in an acoustically resonant membrane, similar to the membrane of a cMUT (Fig. 5.2 on page 132, or see the cover of this thesis).

This device was designed to proof the operation principle and the specifications are not yet tailored to a specific application. This makes it difficult to compare the performance with other types of sensors; however, we compare our results with two state-of-the art devices. A comparison of ultrasonic microphones needs to include at least the following figures: the noise equivalent power, the bandwidth and the surface area. The noise equivalent pressure (NEP) indicates the detection limit of the microphone and is defined as the acoustical pressure for which the signal-to-noise ratio is unity. The bandwidth is the frequency range in which the microphone is sensitive. A correct specification of the NEP also includes the bandwidth that is used to obtain the NEP. Usually, the noise scales with the root of the bandwidth. The total force acting on the microphone for a given acoustical pressure scales with the surface area.

Our sensor has maximal sensitivity at 0.75 MHz, a NEP below 1 Pa, a -6 dB bandwidth of 20% and a surface area of 0.03 mm^2. First, we compare our results with a transducer of PZT piezo-electric material that was recently developed for photo-acoustic breast tomography by Manohar and co-workers at the University of Twente [145]. This sensor operates at 0.9 MHz with a similar NEP of 0.5 Pa, a larger bandwidth of 80% but with a surface area of 25 mm which is two orders of magnitude larger than our sensor. Second, we compare our result with the latest microphones of Guo and co-workers based on polymer micro-ring resonators [141]. These sensors have a very wide bandwidth up to 75 MHz. For a bandwidth from 1 to 25 MHz, they reported a NEP of 10.5 Pa, one order of magnitude larger than our sensor, and a surface area of 0.01 mm^2 which is three times smaller than our microphone. Ultrasound microphones based on piezo-electic material and on polymer photonic ring resonators have experienced a century and a decade of development, respectively. We believe that the type of microphone reported in this thesis has a huge potential especially when considering the large room for improvement (Sec. 5.9).

This chapter is organized as follows. First we detail the choice of the SOI platform. Then we present the new microphone and the principle of the operation of interrogation (Sec. 5.3). Then we present the design (Sec. 5.4) and the fabrication process (Sec. 5.5). Then the characterization methodology (Sec. 5.6), results (Sec. 5.7), and analysis (Sec. 5.8) are presented. We conclude this chapter suggestions for improvements (Sec. 5.9) and the conclusions (Sec. 5.10).

5.2 Choice of the platforms

In this section, we detail requirements for the ultrasound sensor and the choices of mechanical platform, type of photonic resonator, and photonic platform.

The aim of this work was to proof the operation principle but the primary application that we had in mind is in intravascular ultrasonography. This gives the following requirements. (1) Operation should be extendable to at least 20 MHz meaning that the technology should allow for with sensing elements smaller than 40 μm. (2) The technology should allow for optical multiplexers with a footprint smaller than 1 mm x 2 mm. Moreover, the primary interest of the Acoustical Wavefield Imaging laboratory (TU Delft) and of TNO (a contract research institute) is in usage of this new type of microphone in applications. Therefore (3) the fabrication of the sensor should be reproducible without much difficulty and (4) the sensor should be strong enough for practical applications. Moreover, it was decided that (5) the technology should, as much as possible, be already available in order to limit the development of new fabrication processes within this project.

Silicon is the most commonly used material in MEMS and many processes have been developed for silicon micro-machining. Capacitive micro-machined ultrasound transducers (cMUTs) are mostly fabricated in silicon technology and often employ silicon-on-insulator (SOI) wafers. We therefore chose silicon technology for the micro-mechanical devices because it has been proven to work as ultrasound transducer, because of the knowledge on the mechanical behavior of silicon micro-structures, because of the known fabrication processes, and because of the favorable properties. Moreover, silicon micro-machining technology and experience was available in the Van Leeuwenhoek Laboratory which is a joint facility of TNO and Delft University of Technology.

There are different photonic platforms that use silicon wafers as substrate. We chose to use the photonic silicon-on-insulator platform because it matches with the five requirements listed before and because the research integrated photonics activity at TNO was focused at the silicon-on-insulator platform. Fabrication is offered by various institutions for affordable prices. We chose to use micro-ring resonators because these resonators are small enough to be applied for 20 MHz ultrasound sensors yet the size is large enough for reproducible fabrication. Photonic crystal cavities can be much smaller (about half a wavelength) but require more precise fabrication. We chose to use directional coupler to couple light to the ring resonators because they introduce little reflections and because arbitrary splitting ratios can be achieved, in contrast to multimode-interference (MMI) couplers [146, 147]. The drawback of directional couplers is that the coupling $|\kappa|^2$ strongly depends on the fabrication but this can be circumvented by designing a resonator whose response does not strongly depend on the coupling (see Sec. 2.13). Additional advantages of SOI are, for example, that it withstands large temperature fluctuations and radiation as may occur in industrial NDT applications and another advantage is that the materials are non-toxic which is favorable for medical applications.

A major drawback of the silicon-on-insulator platform for sensing is the strong elasto-optic effect of silicon, resulting in a shift of the resonance wavelength as large as 80 pm/degC [148]. From a practical point of view, slow drift of the resonance wavelength due to temperature would give a change in the sensitivity over time while faster fluctuations appear as noise in the measurements [25]. Fortunately, a measurement takes only 2.5 seconds including 500 averages and we are able to tune the interrogation system to the resonance wavelength in-between the measurements. Next to this, the bandwidth of the ultrasonic signal is limited and we used a high-pass filter at with a roll-off at 25 kHz. In Sec. 5.8, we find that the noise in the system is not dominated by changes in the resonance wavelengths of the ring and thus not by temperature fluctuations. Another drawback of the silicon-on-insulator platform is that the losses are relatively high as compared to, for example, glass or polymer. This loss ultimately determines the steepness of the flank of the resonator an thus the sensitivity of the system.

Alternative platforms that use a silicon wafer as substrate include silica-on-silicon technology [149], Si_3N_4-in-SiO_2-on-silicon technology [150], or polymer [137–142]. Silica-on-silicon devices typically have dimensions that are too large for our application (although different types of resonators might have smaller dimensions) [149]. When this project started the services offered by the ePIXfab consortium (SOI technology) were more mature than the fabrication services of Si_3N_4-in-SiO_2. Today, LioniX BV (Enschede, The Netherlands) also offers multi-

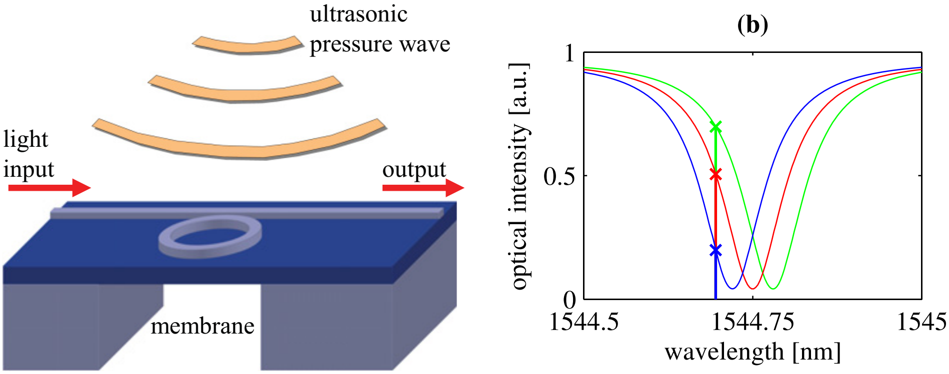

Figure 5.2: (a) Sketch of the new type of ultrasound microphone. Showing the photonic micro-ring resonator on top of a membrane. The actual device has a thin silicon dioxide top cladding to isolate the waveguide from the water. The actual device has a circular membrane. Light transmitted through the input/output waveguide is coupled to the resonator. The incident acoustical wave deforms the membrane and hence the resonator. **(b)** Sketch of the transmittance spectrum of the photonic micro-ring resonator. The interrogation system is depicted. Ultrasonic pressure shifts the photonic resonance as depicted by the three plotted spectra. The wavelength of the laser is chosen at the flank of the optical resonance such that a shift of the resonance directly translates into a modulation of the transmitted optical power.

project-wafer (MPW) services for Si_3N_4-in-SiO_2 waveguides based on their proprietary TriPleX™ technology [151]. Many research has been performed on platforms that can generate or detect light, such platforms based on indium-phosphide or gallium-arsenide but we are not interested in on-chip electro-optic conversion. The polymer platform is currently at the limit for applicability to 20 MHz ultrasound and depends on in-house technology (see Refs. [137–142] as discussed in Sec. 5.1). Alternative resonators include distributed Bragg gratings in waveguides, π-phase-shifted Bragg gratings in waveguides [143], or photonic crystal resonators [127]. Studying these alternatives was beyond the scope of this research.

5.3 The novel photonic ultrasound microphone

The sensing element of the microphone is a photonic ring resonator that is integrated in a membrane (Fig. 5.2). Incident acoustical pressure waves deform the membrane and hence the resonator. We used a racetrack shaped resonator. The deformation of the resonator causes a change in the circumference of the racetrack, a change in the cross-section of the waveguide and a change in the refractive index of the waveguide and the cladding (due to the photo-elastic effect). These changes result in a shift of the optical resonances. This shift is monitored using an external interrogation system. The microphone is fabricated in silicon-on-insulator (SOI) technology. We started with the fabrication of the photonic circuitry in a standard silicon-on-insulator platform. This yields a 220 nm thick silicon waveguides on top of a 2 μm thick SiO_2 buried oxide (BOX) layer on top of a 250 μm thick silicon substrate. The membrane was locally etched from the back-side of the substrate. We deposited an SiO_2 cladding of 0.5 μm to isolate the waveguide from the water.

The interrogation system that we used is based on a laser and a photo-diode. The laser emits coherent light with a center wavelength λ_l and with a very small bandwidth so that we may approximate the light as monochromatic. We tune the laser wavelength to the flank of a resonance of the silicon photonic ring resonator that is in the microphone (see Fig. 5.2b). The transmitted light is then usually about half the incident light. A shift in the wavelength of the resonance gives a change in the transmittance of the ring at this wavelength λ_l. The transmitted intensity is thus a direct measure of the shift of the resonance wavelength and hence a direct measure of the deflection of the membrane.

The optical transmission from the input to the output of the connecting waveguide is described by $T(\lambda)$. Equation (2.175) provides an expression for this transmission. An applied deformation results, in first order, in a wavelength shift $\Delta\lambda$ of the transmission, given by $T(\lambda) \approx T_0(\lambda + \Delta\lambda)$ where T_0 is defined as the transmission for zero deformation. For interrogation of the microphone, we use a laser to provide light in input waveguide with power I_0 and free-space wavelength λ_l. This wavelength is chosen at the flank of a resonance dip. The power in the output waveguide is then

$$I = T(\lambda_l)I_0 = T_0(\lambda_l + \Delta\lambda)I_0. \tag{5.1}$$

The expected change in resonance wavelength $\Delta\lambda$ is small and therefore we may approximate the behavior of the system as linear. The normalized sensitivity of the microphone to an applied pressure difference P may thus be written as

$$\frac{\partial T}{\partial P} = \frac{\partial T}{\partial \lambda}\frac{\partial \Delta\lambda}{\partial P}. \tag{5.2}$$

The actual sensitivity also depends on the optical input power,

$$\frac{\partial I}{\partial P} = \frac{\partial T}{\partial P}\frac{\partial P}{\partial I_0}. \tag{5.3}$$

5.4 Design

In this section, we describe how we designed the microphone to demonstrate the operation principle. We optimized the design for (1) simplicity of fabrication and analysis and (2) for sensitivity because this was our biggest concern. The microphone for the proof of the principle was designed for operation at 1 MHz. This relatively low frequency implies a relatively large size of the membrane which is easier to fabricate. Moreover, sensitivity is expected higher. But this frequency is also interesting for certain applications [145]. The microphone is designed for operation in water. Hereafter we explain the qualitative choices made for the shape of the acoustical resonant structure. Then in Secs. 5.4.1 and 5.4.2, we describe the design of the acoustical resonant membrane and of the optical resonator, respectively.

We chose to use an acoustically resonant membrane to achieve a large deformation of the optical ring resonator for a given acoustical pressure. The behavior of such membranes was studied for operation in cMUTs. We chose to use a circular membrane because this allowed us to use radial symmetry in the computations that were used for the design of the microphone. For a simple geometry it is also easier to understand the physics of the measured device. We chose to have air in the hole behind the membrane. When the back-side of the device containing the membrane is exposed to water, it is not know whether the water will fill the hole or an air bubble remains. Moreover, a given membrane has a higher resonance frequency when there is air below it compared to when there is water below it. We designed the structure to be resonant at 1 MHz and having air below the membrane implies a larger membrane. The chip was mounted on a glass plate so that the hole behind the membrane was closed.

The photonic ring resonator is sensitive to deformation which may be expressed in terms of strain (i.e., relative elongation). This sensor may be looked upon as a high-speed application of the strain sensor that was studied in the previous Chapter 4.

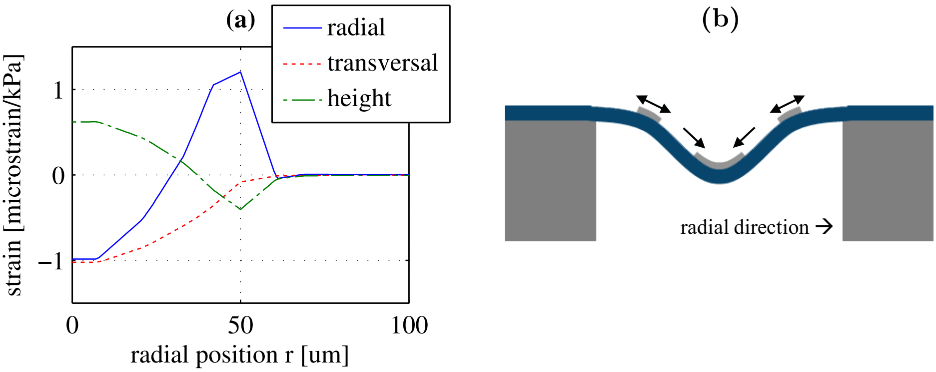

Figure 5.3: (a) Strain in the radial, transversal and height directions. The membrane diameter is 100 μm and has no silicon layer. The pressure above the membrane is 1 kPa. Strain and deflection are computed using the static FEM analysis (see Sec. 5.4.1, second step). The maximum deflection of the membrane is 17 nm which is much smaller than the height of the membrane (2.5 μm). **(b)** Sketch of the deflection and the strain in the radial direction for a layer that is above the neutral plane.

5.4.1 Design of the acoustical resonant membrane

The relation between the dimensions of the membrane and the pressure-induced strain in the ring resonator is nontrivial. First we consider static loading of the membrane under constant pressure (Fig. 5.3). The pressure-induced deflection of the membrane is expected small compared to the height of the membrane which allows us to use plate bending theory [124]. In the bending of membranes, there

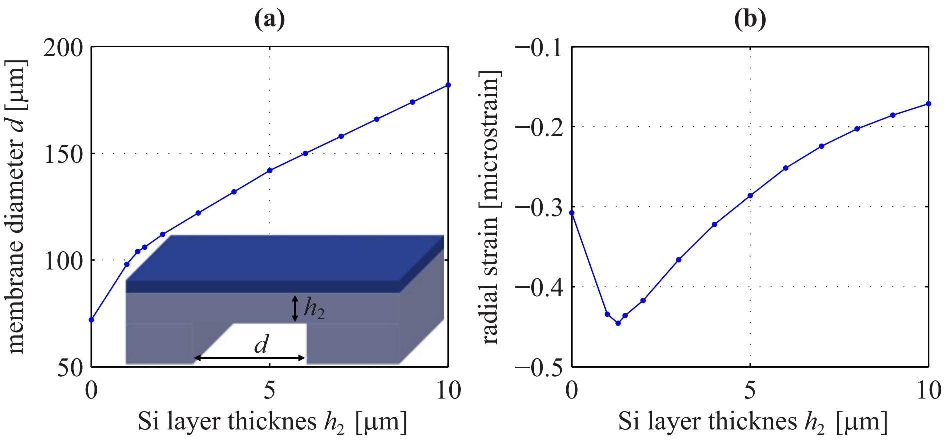

Figure 5.4: Design of the membrane. The membrane consist of a 2.5 μm thick silicon dioxide layer on top of a silicon layer with thickness h_2. **(a)** Diameter of the membrane as a function of the thickness h_2 for which the resonance is at 1 MHz (approximate analytical computation, Eq. 5.4). **(b)** Strain that is introduced by a static pressure of 1 kPa. Strain in the radial direction at the center of the membrane at a point located 0.5 μm below the surface as a function of the thickness h_w. For each h_2, the diameter of the membrane is chosen such that the membrane is resonant at 1 MHz using the curve presented in plot (a). The deformation of the membrane is computed using FEM simulations for static loading (COMSOL).The simulations include a substantial part of the thick substrate so that the deflection at the edges of the computational domain can be neglected. The clamping of the membrane in the chip is thus included in the FEM simulation.

is a neutral plane in which the deformation can be neglected.The curvature of the membrane results in a position-dependent strain that scales linearly with the distance from this neutral plane. The membranes that we consider have a minimal thickness h_1 of approximately 2.5 μm SiO_2 (neglecting the silicon waveguide layer). The strain sensor is located at a plane that is 0.5 μm below the surface. We are free to choose the thickness h_2 of the silicon layer below the SiO_2 layer. However, two effects oppose each other. Choosing a large thickness h_2 of this layer increases the distance of the strain sensor to the neutral plane which causes a higher strain for a given curvature. But by choosing a large thickness h_2 also the stiffness of the membrane increases so that for a given pressure the obtained curvature is lower. Knowing these difficulties, we designed the membrane with the procedure that is presented hereafter. The parameters to obtain are the membrane diameter d and silicon thickness h_2.

Membrane design: first step, resonance at 1 MHz

The first step of the design was to ensure resonance at 1 MHz. The acoustical resonance frequency of the membrane is determined by the geometry and the material properties[1]. For a given thickness of the silicon layer h_2 it is possible to choose the diameter d such that the fundamental resonance of the membrane is at 1 MHz. The resonance frequency f of a circular membrane may be approximated by [152–154].

$$f = \frac{1}{A}\frac{2}{\pi}\frac{\lambda_{\mathrm{M}}^2}{d^2}\sqrt{\frac{D}{\rho h}} \tag{5.4}$$

with $A = 1$ for a membrane in air, λ_{M} a value dependent on the mode shape and the boudary conditions of the membrane, d the diameter of the membrane, D the rigidity of the membrane, ρ the density of the membrane and h the thickness of the membrane. For a membrane consisting of one material, $D = Eh^3/(12(1-\nu))$ with Young's modulus E and Poisson's ratio ν. We used $\lambda_M = 4.977$ which corresponds to the fundamental resonance of a simply supported membrane (for $\nu = 0.3$) [152]. This is an approximation as the actual boundary conditions are expected somewhere between simply supported and clamped ($\lambda_M = 10.2$). The membranes that we studied consist of two layers. We have approximated the rigidity of the membrane using the following equation[2]

$$D \approx \frac{1}{2}(D_1' + D_2')h^3 + \frac{1}{2}(D_2' - D_1')(h_2 - h_1)^3, \tag{5.5}$$

with $D_i' = E_i/(12(1-\nu_i^2))$ where the i indicates the layer with corresponding Young's modulus E_i, Poisson's ratio ν_i and height h_i. The product of the height and density is approximated by $h\rho \approx (h_1\rho_1 + h_2\rho_2)$. Equation 5.4 with $A = 1$ is valid for a membrane in air while the membrane of the microphone has water above the membrane. This water damps the resonance. This damping is difficult to compute as movement and inertia of the water need to be taken into account. However, it is possible to approximate this damping by a single factor $A = f_a/f_w$ with f_a and f_w the resonance frequencies with air and water above the membrane, respectively. This factor A depends on the resonance mode of the membrane, the boundary conditions of the membrane, the geometry of the membrane, and the ratio of the density of water and the density of the membrane. We computed A using a numerical FEM analysis. The simulation included not only the membrane but also the substrate so that the boundary conditions of the membrane were included in the FEM analysis. The analysis was performed in the time-domain and the membrane was brought in motion using a very short pulse as boundary load at its top surface. Similar to the acoustical FEM analysis that are detailed

[1]

	density [kg/m^3]	Young's modulus (isotropic) [GPa]	Poisson's ratio (isotropic)
Silicon	2329	170	0.28
Silicon-dioxide	2200	70	0.17

[2] We follow Ref. [153]. The y-direction is defined normal to the membrane. The rigidity D of a plate is the relation between the bending moments per unit length and the deflection of the plate w. For the bending moment along x, M_x, this gives $M_x = -D\left(\frac{\partial^2 w}{\partial x^2} + \nu\frac{\partial^2 w}{\partial z^2}\right)$. The relation for M_z is identical but with x and z interchanged. Combining (4.2.16) and (4.2.12) of Ref. [153] gives $D = \int_{-h/2}^{h/2}(y^2E)/(1-\nu^2)dy$. This equation assumes that the neutral plane is in the middle of the membrane. We approximate that this is also the case for our two-layer membrane and arrive at Eq. (5.5).

hereafter (third design step), the strain was recorded as a function of time and the resonance of the membrane was found using a discrete Fourier transform. The resonance frequencies in air ($f_a = 2.9$ MHz) and water ($f_w = 1.6$ MHz) were computed for a membrane with only silicon-dioxide ($h_2 = 0$) and diameter $d = 80\mu$m. This gave $A = 2.4$. Equation 5.4 was used to compute the diameter of the membrane d for a given thickness of the silicon layer h_2 such that the membrane has a resonance frequency f_w of 1 MHz.

Membrane design: second step, silicon thickness h_2

The second step in the design was to choose the optimal thickness h_2 of the silicon layer provided that we use the corresponding membrane diameter d from Fig. 5.4a. The sensitivity of the microphone was studied using a static analysis so that the sensor acts as a pressure sensor. We expect that the geometry of the membrane that provides maximal sensitivity to static pressure also provides maximal sensitivity to ultrasonic pressure waves. The deformation of the membrane depends on the exact boundary conditions which are unknown. Therefore we numerically simulated the deformation of the membrane using a finite element method (implemented in COMSOL Multiphysics). The numerical model is of a 2D axis-symmetric domain exploiting the circular symmetry of the membrane. The influence of the 0.22 μm thick waveguide layer is neglected in this analysis. The model includes the substrate that support the membrane. The simulation domain has a radius of 300 μm so that the boundaries of the simulation domain are sufficiently far away from the membrane. The side of the substrate is clamped (no deformation) at the boundary of the simulation domain. For static loading, the result is not influenced by the type of fluid below the membrane (air or water). The microphone is loaded from the top with a static pressure of 1 kPa and we recorded the strain at a point 0.5 μm below the surface of the membrane at the center of the membrane. This is the position where the photonic resonator will be placed. We recorded the strain in the radial direction. Figure 5.4b presents this strain for a varying thickness h_2 of the the silicon layer with corresponding membrane diameter d. It can be seen that a thickness h_2 of 1.3 μm gives the optimal sensitivity. However, in the fabrication process of the membrane, the flatness and thickness of the silicon layer are difficult to control. A well defined fabrication can be achieved by completely removing the silicon layer of the membrane ($h_2 = 0$). In that case, the SiO_2 layer of the membrane is used as etch stop in a chemically selective etch process. Therefore we chose to completely remove the silicon below the membrane at the expense that the predicted sensitivity is 1.5 times lower.

Membrane design: third step, fine-tune diameter d

The third and final step was to determine the diameter of the membrane more precisely. This was done using acoustical FEM simulations in the time domain (also using COMSOL Multiphysics). The geometry of these simulations was similar to the static simulations and the same 2D axis-symmetry was used. The membrane consists only of the 2.5 μm thick SiO_2 layer. The etched “hole” behind the membrane is filled with air and the remaining part of the modeling domain is filled

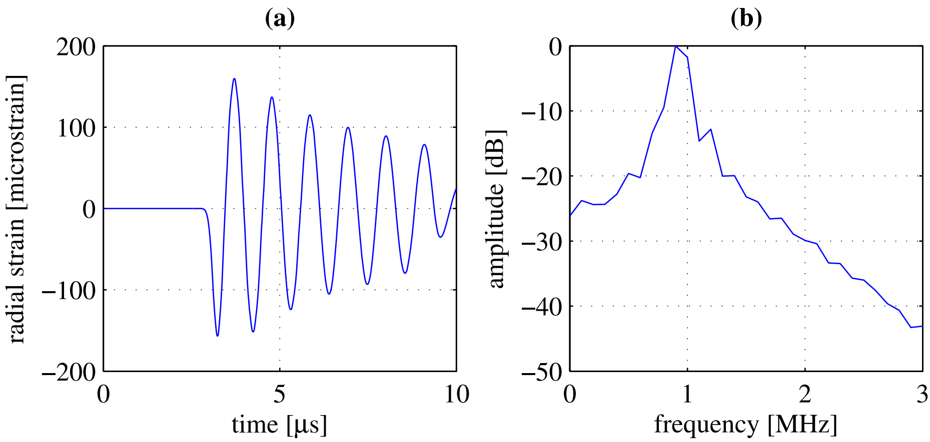

Figure 5.5: Time-domain acoustical FEM modeling of the membrane. An incident plane pressure-wave introduces a resonant vibration of the membrane. Silicon-dioxide membrane with thickness 2.5 μm and diameter 100 μm. **(a)** Radial strain in the center of the membrane, 0.5 μm below the top. **(b)** Spectrum of plot (a) showing a resonance at 0.9 MHz. This is the response of the chip to the incoming Gaussian pulse with a finite width of 0.6 μs.

with water. The discretization of the computational grid contained least 12 points per wavelength. The water domain is large enough to separate reflecting waves from the boundaries of the domain. The microphones were exited with an incident plane pressure-wave. This wave has a Gaussian shape with a maximal amplitude of 50 kPa and a pulse width of 0.6 μs. As in the static analysis, the radial strain at the center of the membrane and 0.5 μm below the surface was recorded. In this dynamical analysis, this strain is obviously time-dependent. The resonance of the membrane was found by computing the Fourier transform of this time signal. The duration of the simulation corresponded to a frequency accuracy of 0.1 MHz. Figure 5.5 shows the result of the simulation for the membrane with a diameter

Table 5.1: Response of the three microphone membrane for different diameters. Accuracy in the frequency is 0.1 Mhz.

membrane diameter [μm]	resonance frequency [MHz]
60	3.2
80	1.6
100	0.9
124	0.6

of 100 μm. We studied membrane diameters of 60 μm, 80 μm, 100 μm. The resonance frequencies for the different membrane diameters are listed in Table 5.1. For operation at a frequency of 1 MHz we chose a membrane diameter d of 100 μm.

Membrane design: summary

In this section, we presented the systematic design of the acoustically resonant membrane of the microphone. Many properties were dictated by the fabrication processes, such as the used materials and the thickness of the membrane. For operation at 1 MHz, we chose a diameter d of 100 μm.

5.4.2 Design of the photonic resonator for strain sensing

The photonic resonators were fabricated by a semi-industrial CMOS line in a multi-project-wafer run. Such a fabrication typically takes several months while many chips are simultaneously fabricated. Therefore the optical resonators were designed before the membrane design was finished. The chips contained 24 different ring and racetrack resonators. The design procedure for these resonators was presented in Sec. 2.13.

Sensor resonator design: first step, optical sensitivity

First we characterized the optical resonators to obtain the expected sensitivity of the interrogation system to a change in resonance wavelength $\Delta\lambda$ of the resonators. We measured the characteristics of racetrack resonators in the <100> crystalline direction using the methodology presented in Sec. 3.6.2 (*DCM2*). An example of the resonance of a resonator is plotted in Fig. 5.6a. The tangent of the flank is estimated by $\partial T/\partial\lambda \approx (1-r)/\lambda_{\mathrm{FWHM}}$ with optical power transmission T, wavelength λ, resonance extinction ratio r and resonance full-width at half-max λ_{FWHM}. A set of eight racetracks with different lengths of the straight section l_s was characterized and the steepness of the flank $\partial T/\partial\lambda$ is plotted in Fig. 5.6b. As expected, the flanks of resonators with a longer circumference are steeper and hence the sensitivity given a fixed change in resonance wavelength $\Delta\lambda$ is higher.

Sensor resonator design: second step, strain sensitivity

Secondly we estimate the expected change in resonance wavelength $\Delta\lambda$ per applied pressure P. The static mechanical analysis discussed in the previous Section 5.4.1 was used to compute the pressure-induced strain in the plane that is 0.5 μm below the top of the membrane. This strain profile is circular symmetric and given in Fig. 5.3a. We applied an analysis similar to the derivation in Sec. 4.3.2 but with the applied strain parameter S_z replaced by the applied pressure P. The resonators that we used consists of a waveguide with constant width and effective index over the full track. In this analysis, we neglected the change in effective refractive index, i.e., $\partial n_e/\partial P = 0$. This effect is difficult to compute as (1) details of the mechanical deformation of the waveguide are unknown because the cross-section of the stiff silicon waveguide does not necessarily follow the surrounding silicon-dioxide and

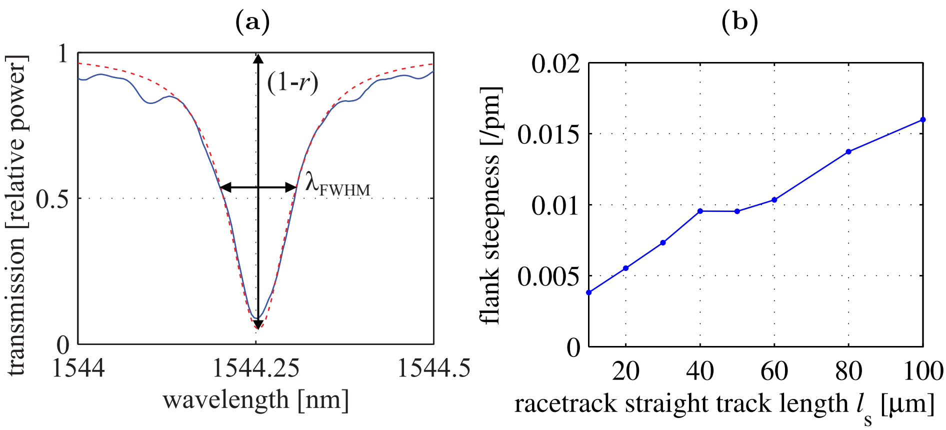

Figure 5.6: Optical properties of racetrack resonators. Characterization result of racetrack resonators as depicted in Fig. 2.20 (page 67). Bending radius 5 μm, waveguide width 400 nm (measured), length of the parallel waveguides in the directional coupler $L = 1\mu$m, coupler straight-through power $|\tau|^2 = 94\%$. **(a)** Measured transmission spectrum (blue solid line) and fitted transmission (dashed red line). Racetrack with straight track length $l_s = 40\mu$m. Exinction ratio r and full-width at half-max λ_{FWHM} are indicated. **(b)** Steepenes of the flank of the resonator approximated by $(1 - r)/\lambda_{\text{FWHM}}$ [relative power / pm]. Here r and λ_{FWHM} were obtained from the fitting as shown in (a).

(2) the optical properties of the waveguide are difficult to compute because the photo-elastic effect causes a non-homogeneous anisotropic refractive index profile of the waveguide and its cladding. For uniformly strained racetracks, the shift in the resonance wavelength is dominated by the change in the circumference of the racetrack and the contribution of the effective index was three times lower (see Ch. 4). We believe that neglecting this effect is justified in this analysis because the purpose is to find the most sensitive configuration and not to provide quantitative results. The pressure-induced shift of the resonance wavelengths is then given by

$$\frac{\partial \Delta\lambda}{\partial P} = \frac{n_e}{n_g}\frac{\lambda_c}{l}\oint \frac{\partial S_\rho}{\partial P}\mathrm{d}\rho, \tag{5.6}$$

with λ_c the resonance wavelength without deformation, n_e the effective index of the waveguide, n_g the effective group index of the waveguide, l the circumference of the racetrack, S_ρ the strain in the direction of the waveguide and the integral running along the track coordinate ρ. This integral was numerically evaluated by replacing it with a summation over discrete positions ρ_i with $\Delta\rho = 0.5$ μm. At each position, the strain tensor S is rotated to find the strain S_ρ in the direction of the waveguide. The contributions of all waveguide elements ρ_i are summed to compute $\partial\Delta\lambda/\partial P$. To obtain the position and length of the racetrack with maximum sensitivity to pressure, we computed the resonance shift per applied pressure for racetracks with different lengths of the straight waveguide l_s located at different positions of the membrane. In Fig. 5.7a, it can be seen that a short

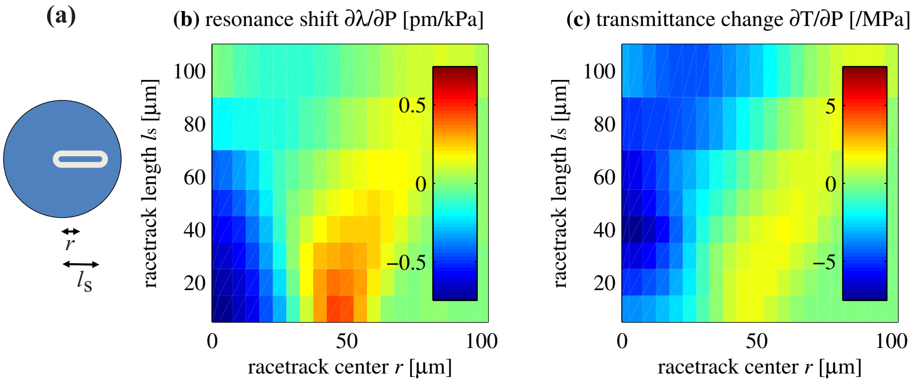

Figure 5.7: Design of the racetrack resonator in the membrane. The varied parameters are the length of the straight track of the racetrack (l_s) and the position of the racetrack on the membrane. The racetrack is horizontally displaced and r indicates the displacement of the center of the racetrack with respect to the center of the membrane. **(a)** Top-view of the circular membrane with a racetrack (length l_s, displacement r), sketch. **(b)** Expected shift in resonance wavelength due to a static pressure on the membrane. The change in effective index has been neglected. **(c)** Expected change in transmitted optical power due to a static pressure on the membrane. Normalized to incident optical power.

racetrack (straight track length $l_s = 10$ μm and bend radius 5 μm) located at the center of the membrane provides the maximal wavelengths shift per applied pressure.

Sensor resonator design: third and final step

Finally the previously obtained numbers are combined. For a maximal change in transmitted light per wavelengths shift ($\partial T/\partial \Delta\lambda$), it is desired to have a long racetrack resonator. For a maximal wavelength shift per applied pressure ($\partial \Delta\lambda/\partial P$), it is desired to have a short resonator. The change in transmitted power T per applied pressure P is given by Eq. 5.2. In Fig. 5.7b, it can be seen that the maximal sensitivity is expected for a racetrack with straight track length of 40 μm that is positioned at the center of the membrane. We also investigated the effect of a misalignment between the racetrack and the membrane. A misalignment of 5 μm results in an estimated decrease of the sensitivity of 4%. Figure 5.8 depicts the drawing of the final optimized resonator for the sensing of ultrasound.

5.5 Fabrication technology

This section is dedicated to the fabrication of the microphone. Both the photonic resonators as well as the membranes are fabricated in silicon-on-insulator technology. The fabrication process started with the photonic resonators including connecting waveguides and out-of-plane grating couplers. This fabrication was

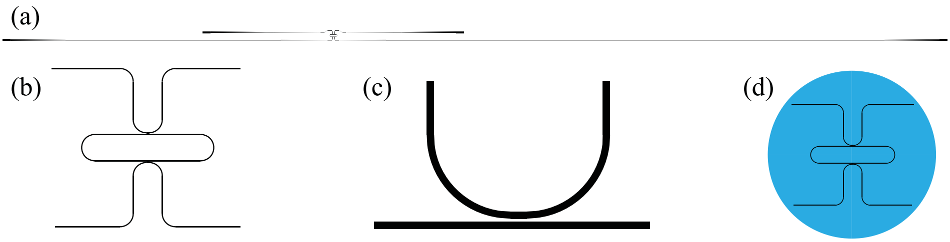

Figure 5.8: Drawing of the optimized photonic device for the sensing of ultrasound. From the GDSII file as used for the fabrication. **(a)** Device including connecting waveguides and out-of-plane grating couplers at the ends of the waveguides. Total width 6 mm. **(b)** Zoom-in of the resonator. Waveguide width 450 nm (400 nm fabricated), straight-track lenth 40 μm, bending radius 5 μm. **(c)** Zoom-in of the couplers of the resonator. Bending radius 5 μm, section of parallel waveguides 1 μm. **(d)** Overlay of the resonator and the membrane. Membrane diameter 100 μm.

done in the semi-industrial CMOS line of IMEC (Leuven, Belgium) via the ePIXfab platform (see Sec. 3.3). After the fabrication of the photonic circuits on wafers with a diameter of 200 mm, the wafers were thinned to a thickness of 250 μm and cut into dies of 51 mm by 57 nm. Each die contains 2 by 4 identical chips. Figure 5.8 shows the drawing of the resonator and Fig. 3.1 (page 79) shows the full chip design with over 300 devices.

The membranes were fabricated using standard MEMS processes in the Van Leeuwenhoek Laboratory (joint laboratory of Delft University of Technology and TNO). The membrane is etched from the back-side of the dies. The fabrication process is based on optical lithography with back-side alignment and deep reactive ion etching (DRIE). The Bosch etch process was used to etch deep with a high aspect ratio (holes of 250 μm deep and 100 μm diameter). Lithography was simultaneously done on the eight chips in one die and the dies are sawed to individual chip-dies before the etch process. Appendix D presents the details of this fabrication. Figure 5.9 depicts the resulting chip.

Before further handling we glued the chips on a glass plate. In fact, we glued the chips on a stack of two plates which each have a thickness of 1 mm. The first plate has a hole with a diameter of 4 mm that is below the membrane of the chip. This was done because direct gluing of the chip on a plate would have caused the adhesive to be sucked into the hole below the membrane by capillary forces. Figure 5.10 shows a sketch of the chip with the glass plates including their dimensions.

Connecting optical fibers to the photonic chip is referred to as *packaging* because it is usually part of the packaging process. Connecting optical fibers to the chip requires very precise alignment between the optical fibers and the photonic chip. We used out-of-plane grating couplers which still require alignment within a few micron (Sec. 2.11). These couplers require the fibers to have an angle of 8 degrees with respect to the normal of the surface of the chip. Packaging was done by Tyndall National Institute (Cork, Ireland) via the ePIXfab platform. Tyndall provides fiber-chip coupling for an array of optical fibers. These fibers end next to

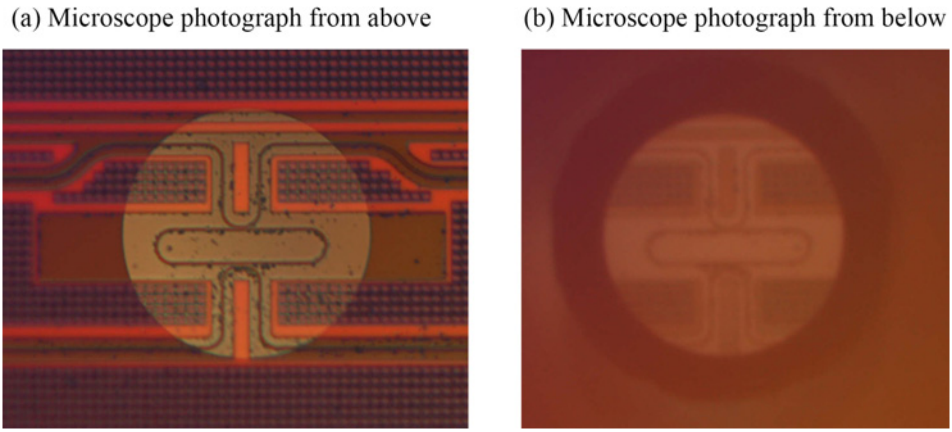

Figure 5.9: Microscope photograph of a membrane with optical resonator. Zoom 50x. This chip has a membrane with a diameter of 78 μm (measured). **(a)** Photo from above the chip. The circular membrane is visible because the microscope has a lamp that shines upwards from below the chip through the 2.5 μm thick membrane. **(b)** Photo from below the chip (chip up-side down). Focus of the microscope is at the membrane. The photonic circuit is visible through the silicon-dioxide (glass) membrane.

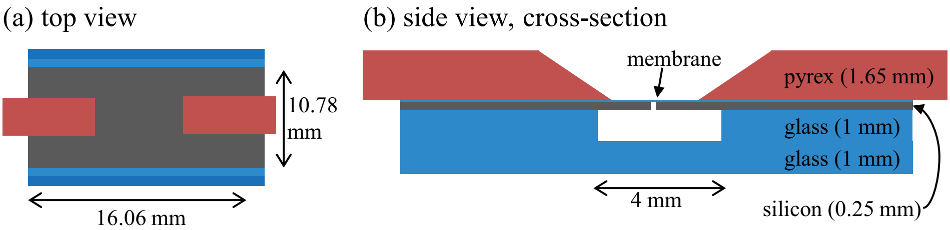

Figure 5.10: Prototype for the proof-of-the-principle of the new microphone (sketch not to scale). Includes dimensions of the device. In one direction the glass plates have the same length as the chip (a). In the other direction, the glass plates are 1 mm and 2 mm wider. Adhesive was gently applied at these ridges and capillary forces sucked the adhesive to form a sheet between the plates.

each other in a Pyrex (glass) block that has a slanted facet under an angle of 49 degrees. This facet reflects the light that leaves the fibers horizontally downwards to the grating couplers at the required angle (see Fig. 5.11, inset). Usually the glass-air interface gives total internal reflection of the ray of light but we emerge the chip in water which has a similar refractive index as glass. We gratefully acknowledge the researchers at Tyndall for developing a solution especially for our microphone. They have coated the end facets of the fiber array blocks with aluminum. This aluminum now acts as a mirror and reflects the light from the fiber to the chip. Figure 5.11 shows a photograph of the packaged chip.

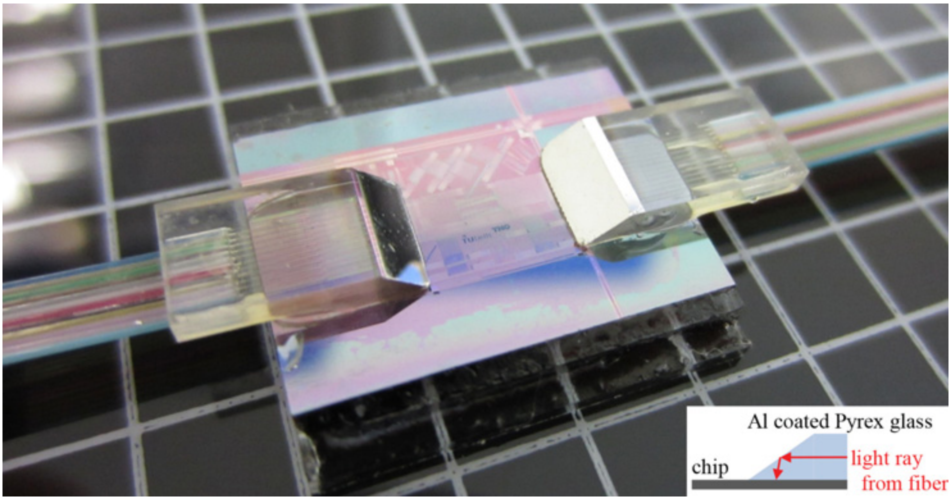

Figure 5.11: Photograph showing the microphone chip with optical fiber connections. Inset shows how the fiber array blocks reflect the light to the out-of-plane grating couples in the chip. Packaging was done by Tyndall National Institute (Cork, Ireland). Photograph by Brad Snyder.

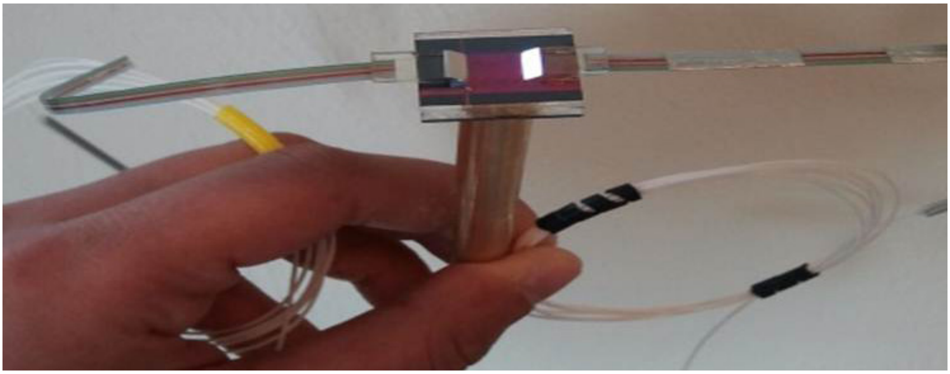

Figure 5.12: Photograph showing the microphone mounted on a brass rod.

Finally the chip was mounted on a brass rod for accurate and reproducible positioning of the chip in the setup (Fig. 5.12).

5.6 Characterization methodology

This section details the methodology that we used to characterize the sensors: the electro-optical interrogation system (Sec. 5.6.1), the acoustical setup (Sec. 5.6.2), the ultrasonic pressure signals (Sec. 5.6.3), and the measures (Sec. 5.6.4).

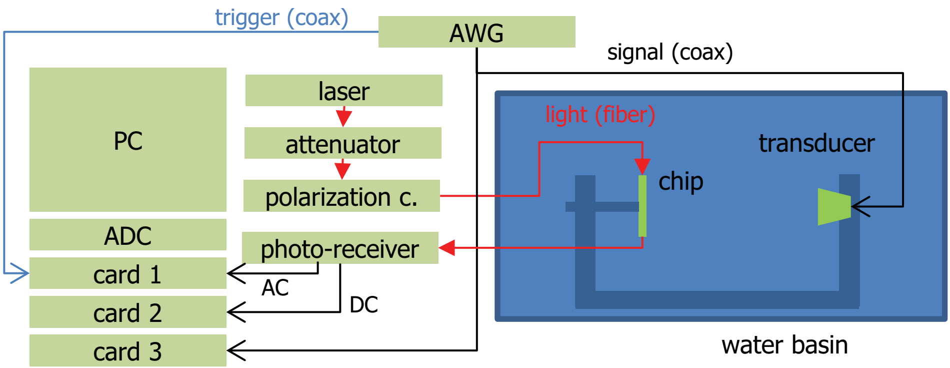

Figure 5.13: Schematics of the measurement setup. Abbreviations AWG (arbitrary waveform generator), ADC (analog to digital converter), coax (coaxial wire) and chip (our new microphone chip). Wires that send control information from the PC have been omitted from the drawing (PC – laser, PC – AWG and PC – ADC). Optical path starts with laser and ends with photo-receiver. Photographs of the setup are presented in Appendix C.

5.6.1 Interrogation of the photonic micro-ring resonator

The resonance shift of the photonic resonator is monitored by the following interrogation system (Fig. 5.13). A tunable laser is used to generate the light around a wavelength λ_l. The light passes through an in-fiber isolator, an in-fiber attenuator and an in-fiber polarization controller. The latter is required because the photonic chip only accepts one polarization state. This light is coupled to the chip where it is modulated by the photonic resonator and thus by the ultrasound. Light leaving the chip is measured with a photo-receiver that was designed to measured small fluctuations in signals with a large continuous-wave component. The photo-receiver includes a InGaAs photo-diode and an electronic circuit with two outputs. The AC output has a high-pass filter with a roll-off around 25 kHz and the DC output has a low-pass filter with a roll-of around 50 kHz. The AC output is used to measure the (ultrasonic) signal. The DC output is used to measure the spectrum of the resonator (by stepping the wavelength of the laser) and to position the laser at the flank of the resonance. Both outputs are connected to the analog-digital converters (ADC). The ADC has an electronic low-pass filter that was used to avoid aliasing of the recorded signal. We measured at a speed of 20 mega-samples per second. We took care in selecting equipment with high stability and low noise (see Table 5.2).

Throughout the measurements, we kept the laser power at 12 mW and we attenuated the light using the manual variable attenuator. We kept the optical power at the output of the system (at the photo-diode) at approximately 50 μW for a laser wavelength that is away from the resonance.

Silicon micro-ring resonators are very sensitive to temperature due to the strong thermo-optic effect in silicon. The temperature of the waveguide of the ring resonator is not only influenced by the environmental temperature but also by dissipa-

Table 5.2: List of equipment (optical, acoustical, electronic).

Tunable laser 81940A (Agilent, Santa Clara, California, USA). Wavelength span 1520 nm - 1630 nm; linewidth 100 kHz; wavelength resolution 1 pm; wavelength repeatability 1pm; wavelength stability (24 hours) ± 2.5 pm; power stability (1 hour) ± 0.01 dB.

Optical isolator OLISO-I-S155 (Opto-link Corporation Ltd., Hong-Kong). Isolation 32 dB.

Variable optical attenuator OLVAO-MN-155-2TA (Opto-link Corporation Ltd., Hong-Kong). Maximum attenuation -30 dB.

Fiber polarization controller FPC560 (Thorlabs, Newton, New Jersey, USA). Three paddles, diameter 56 mm.

Photo-receiver Newfocus 1811-FC-AC (Newport, Santa Clara, California, USA). InGaAs photo-diode; typical responsivity 1.0 μA/μW at 1550 nm wavelengt. AC output: high-pass filter with roll-off at 25 kHz and transimpedance gain of 40 mV/μA. DC output: low-pass filter with a roll-off around 50 kHz and a transimpedance gain of 10 mV/μA.

Digitizer (ADC) M3i4142-exp (Spectrum, Grosshansdorf, Germany). 16 bit; sampling up-to 250 MSamples/second. Includes electronic low-pass filter to avoid aliasing. Optional 50 Ohm or 1 MOhm impedance.

Arbitrary Waveform Generator (AWG) 33521A (Agilent, Santa Clara, California, USA). 30 MHz bandwidth. 250 MSa/s, 16-bit sampling rate for arbitrary waveforms.

Acoustical Transducer Panametrics V314 (Olympus NDT, Waltham, Massachusetts, USA). Center frequency 1 MHz (specs).

Hydrophone Needle hydrophone (Precision Acoustics Ltd, Higher Bockhampton, Dorchester, UK). 1 mm diameter.

tion of the optical power in the resonator. Therefore we obeyed long stabilization times before starting the measurements. At the beginning of the day the photonic microphone was placed in the water basin, the laser was connected, the laser was switched on and the system was left one hour to stabilize.

Before each set of measurements, we set the laser to a wavelength away from the resonance (λ_l = 1543.5 nm), we manually optimized the polarization control for maximum transmission through the system and we manually set the power at the output of the system at 50 μW (unless specified differently). The remainder of the measurements was automized. First the optical transmission spectrum of the photonic resonator was measured by stepping the laser from a wavelength of 1543.5 nm to 1544.0 nm in steps of 20 pm. The transmitted optical power was recorded for each wavelength. Then a Lorenzian curve was fitted through the spectrum and the laser wavelength was set at half-max of the left (blue) flank of the resonance. Then the system was left for 10 minutes to stabilize at this wavelength. This step was performed twice (although this turned out to be unnecessary). Hereafter we tried to optimize the laser wavelength by searching for the maximal signal-to-noise ratio (SNR) of the ultrasonic measurements. At each wavelength, an ultrasonic signal was measured and so was the noise of the system. The laser was stepped in steps of 2 pm in the direction of the highest SNR. However, we believe that this algorithm did not work properly and that noise caused the search to settle after only a few steps.

5.6.2 Acoustical setup and calibration

The acoustical setup consists of a signal generator and a ultrasound transducer. In the measurements, we used monotone-like ultrasonic signals that have a narrow frequency band around a central frequency.

The ultrasonic signals are generated using an arbitrary waveform generator (AWG). A digital arbitrary waveform can be loaded to the AWG and the AWG generates a voltage corresponding to this waveform at its output. The AWG may be looked upon ans the inverse of an analog-to-digital converter. This electronic signal is send to the ultrasound transducer which generates the pressure wave. This source transducer and the microphone chip were mounted in a mechanical U-frame. This allowed reproducible aliment of the microphone with respect to the transducer. Appendix C includes photos of the setup and of the the U-frame.

The setup was calibrated using a calibrated needle hydrophone that was placed at exactly the same location as the microphone chip (see Table 5.2). This hydrophone was used to calibrate the relation between the signal that was sent to the source transducer and the resulting acoustical pressure at the position of the microphone. We have used low acoustical pressures up to 3 kPa so that we may approximate the acoustical system as linear. By this we mean that the pressure that we generate at the position of the microphone chip scales linearly with the amplitude of the acoustical pulse that we load to the AWG. This requires linearity of the AWG, the source transducer and the propagation of the ultrasound. The calibration of the setup with the hydrophone confirmed linearity of the system (Sec. 5.7). The transfer function of the source transducer is not flat with respect to frequency. The setup is calibrated for different frequencies using monotone-like signals with exactly the same shape as the signals that were used for the measurements, but with a larger amplitude. We used the calibrated hydrophone data-sheet at the center frequency of the transmitted signal. The hydrophone has a specified accuracy of 8%.

We have measured the distance between the microphone and the transducer using an ultrasonic pulse-echo technique. From these measurements, we estimated that the uncertainty in the placement of the microphone was below 5 mm. We measured the pressure as a function of position using the hydrophone. A 5 mm change in the position of the hydrophone corresponded to a change of 3.8% in pressure. The combined uncertainty of the hydrophone specifications and the positioning of the microphone is 9% (quadratically summed as the two uncertainties are independent [125]).

5.6.3 Signals

The measurements have been performed with monotone-like signals at a certain frequency with a narrow bandwidth of 5%. These signals are loaded to the AWG and are transduced to pressure waves with little distortion. We have used a sine function with a Gaussian envelope. This function has a clean spectral content. This is important because the source transducer has a limited bandwidth which would cause distortion to signals with spectral content outside this bandwidth.

The signal has the shape [155]

$$s(t) = A \exp\left[-\left(\frac{t-\tau_d}{N/(2f_0)}\right)^2\right] \cdot \sin\left[2\pi f_0 t\right], \tag{5.7}$$

where s is the signal as a function of time t, A is the amplitude of the signal, τ_d is the time delay of the envelope, N is half the number of sine periods that are visible below the envelope and f_0 is the center frequency of the signal. The full-width at half-max in the time and frequency domains are $\Delta t_{\mathrm{FWHM}} \approx 1.2 \cdot N/f_0$ and $\Delta f_{\mathrm{FWHM}} \approx N/f_0$, respectively[3]. The spectrum of this signal is a Gaussian function centered at frequency f_0 with a bandwidth of Δf_{FHWM}.

We measured the microphones in a frequency range from 0.4 MHz to 1.4 MHz. We used long signals with $N = 20$ so that the bandwidth Δf_{FHWM} is maximal 0.07 MHz. This provides enough detail to resolve the spectral response of the microphone. This signal is short enough to prevent interfernce of the incoming signal with the signal that is reflected back from the U-frame.

5.6.4 Measures

This section details the measures that we use to characterize the device.

Maximum of the envelope (m.e.) of the signal

The signal that is measured with the photonic microphone does not have the same temporal shape as the incident pressure wave. The acoustical resonant membrane remains vibrating even when the pressure wave has already passed the chip[4]. Therefore it is not straightforward what the amplitude of the signal is. The quantity that we used to describe amplitude of a signal is the maximum value of the envelope of the signal, i.e., [155]

$$s_{\mathrm{m.e.}} = \max_t \left\{ \left| s(t) + \imath \mathcal{H}_t\left[s(t)\right] \right| \right\}, \tag{5.8}$$

where $s(t)$ denotes a signal, $s_{\mathrm{m.e.}}$ denotes the maximum of the envelope of the signal, and $\mathcal{H}_t\left[s(t)\right]$ denotes the temporal Hilbert transform of $s(t)$. The Hilbert transform was computed using the implementation in Matlab. The envelope was used because the signal $s(t)$ as defined in Eq. (5.7) does not necessarily have the maximum of the Gaussian shape coincident with a maximum of the sine. In practice, we did not observe a difference between the maximum of the envelope and the maximum of the absolute value of the signal. Throughout this work, we introduce the abbreviation m.e. to denote the maximum of the envelope of a signal as defined in Eq. (5.8).

[3] The characteristic time width of the envelope of the signal $\tau_w = N/f_0$, the full-width at half-max (FWHM) of the envelope in the time domain $\Delta t = N/(\sqrt{\ln 2} f_0)$. The FWHM of the envelope in the frequency domain $\Delta f_{\mathrm{FWHM}} = 4\sqrt{\ln 2}N/(\pi f_0)$.

[4] For example, Fig. 5.14a shows an incident pressure wave and Fig. 5.15a shows the corresponding response of the microphone. (The amplitude of the pressure wave in Fig. 5.15a was lower.)

The hydrophone showed an offset in the measured voltage. Therefore the signals (both of the hydrophone as well as the photonic microphone) were corrected for this offset by removing the mean of the signal.

The uncertainty in the measurements was decreased by averaging over 500 consecutive recordings. This improves the accuracy of the measured sensitivity and transfer function. This does not influence the specified noise equivalent pressure (NEP) as we did not average the noise measurements.

Sensitivity, linearity, and transfer function

The sensitivity was obtained by measuring the (maximum of the envelope of the) voltage [mV] at the AC output of the photo-receiver as function of the m.e. pressure [Pa]. Pressures were varied from 3.5 Pa to 35 Pa and the sensitivity [mV/Pa] was obtained using a linear fit through the origin (e.g., Fig. 5.15b).

The linearity was quantified as the pressure where the measured signal (voltage at the AC output of the photo-receiver) deviates more than 5% from the value that was predicted by the linear sensitivity (3.5 Pa to 35 Pa). Non-linearities may cause a difference in the minimum and the maximum of the signal. Therefore we presented the pressure when either the minimum or the maximum deviated more than 5% from the linearly predicted value.

The transfer function of the photonic microphone was obtained by measuring the sensitivity for signals with different center frequencies f_0. Low pressures were used so that the response of the microphone is linear. Therefore it was sufficient to measure the voltage signal of the microphone for only one pressure. The sensitivity is then simply the m.e. voltage signal divided by the m.e. pressure. The amplitude of the electric signal that was sent to the transducer was kept constant so that the actual pressures at the position of the chip varied between 4 Pa and 30 Pa for frequencies between 0.4 MHz and 1.4 MHz. The transfer function of the source system (i.e., mainly the transducer) showed a maximum at 1.14 MHz.

Noise equivalent pressure (NEP)

The noise equivalent pressure (NEP) is a measure of the minimum detection limit of the microphone. The NEP is defined as the pressure for which the signal-to-noise ratio is one. The NEP is obtained by dividing the root-mean-square (RMS) value of the noise [mV] by the sensitivity [mV/Pa] of the microphone. The noise was measured by recording the output of the photonic microphone (voltage at the AC output of the photo-receiver) for the case that there is no acoustical pressure induced. As in the signal measurements, 500 time-traces were recorded but here they are treated as one long recording. The offset was removed by subtracting the mean value. Then the RMS of this long noise signal was computed.

Distance from transducer to chip

The distance from the transducer to the chip was measured using an ultrasonic pulse-echo technique. In fact, we used one of the measurements that was also used to measure the photonic microphone (we used the measurement with 35 Pa m.e.

pressure). We recorded the voltage across the transducer with the ADC. First, this recording shows the signal that was sent from the AWG to the transducer. Later, this recording shows the pressure wave that was reflected from the surface of the microphone chip back to the transducer. As the transducers works as both source and receiver, the reflected pressure signal was transduced to a voltage. From both signals, we extracted the time at which the Gaussian envelope was maximum by computing the envelope of the signal (using the Hilbert transform) and smoothing this envelope to ensure that the sinusoidal modulation does not influence the time of the maximum. The time difference between the two pulses is the travel time of an ultrasonic pressure wave from the transducer to the chip and back. This is translated to the distance using the speed of the sound in the water.

The speed of ultrasound in the water was separately measured using a similar pulse-echo technique. This measurement used two conventional 5 MHz ultrasound transducers that are mounted in a U-frame with known distance of 20 cm between the transducers. An ultrasonic pulse is transmitted from one transducer to other and the speed of sound is computed from the pulse-echo time.

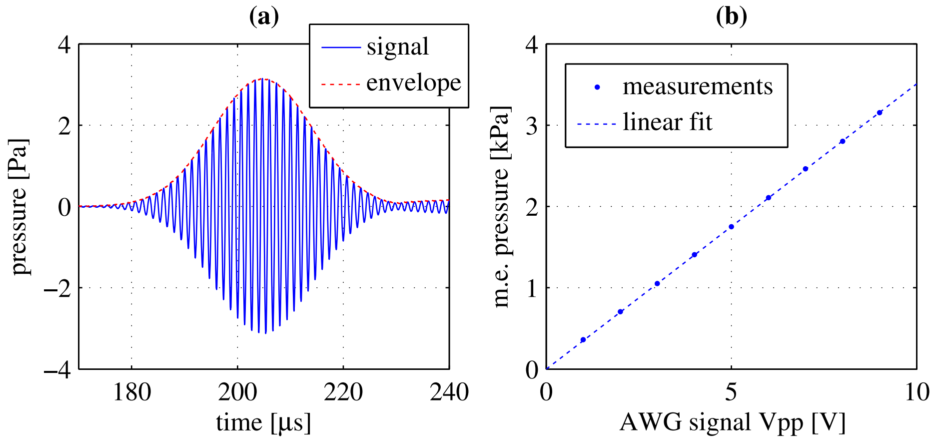

Figure 5.14: Measurement of the pressure wave using the hydrophone. Center frequency $f_0 = 0.75$ MHz. Distance from transducer to hydrophone is 24.2 cm. **(a)** Measured pressure versus time. The envelope of the signal is also shown. Vertical axis is computed using the value of the hydrophone calibration curve at f_0. **(b)** Measured maximum of the envelope of the pressure wave for different amplitudes of the signals that were sent to the transducer (Vpp). The AWG is designed to have a 50 Ohm termination while the impedance of the transducer is much higher. Therefore the actual voltage that is sent to the transducer is about half of the Vpp value as listed here. The transfer of the system is computed as the slope of the linear fit (351 Pa/Vpp).

5.7 Results

This section presents the results of the characterization: the calibration of the setup using the hydrophone, the actual dimensions of the fabricated microphone, the sensitivity, the NEP, and the transfer function of the photonic microphone.

The calibration of the setup with the hydrophone for center frequency $f_0 = 0.75$ MHz is shown in Fig. 5.14. The relation between the signal that is loaded to the AWG and the m.e. pressure is linear for the measured pressures up to 3 kPa.

We measured the diameter of the membrane of the fabricated microphone chip using a confocal optical microscope. The diameter of the fabricated membrane is 124 μm which is larger than designed.

Figure 5.15 presents characteristics of the photonic microphone. We observed a sensitivity of 1.3 mV/Pa, a noise equivalent pressure (NEP) of 0.8 Pa and a linearity up to 105 Pa. Plot (c) shows that the response of the photonic microphone is not symmetric, that is, the maximum and the minimum of the signal do not overlap whereas the input pressure is symmetric. This is because the flank of the resonance dip of the optical resonator is not linear (see, for example, Fig. 5.6 or Fig. 5.19). This is especially visible for the minimum of the signal. The resonance has shifted so far to the left (blue) that the minimum of the resonance dip is at the wavelength of the laser. Note that the signals in this regime are deformed by the high-pass filter (roll-off at 25 kHz) of the photo-receiver as non-linearity of the microphone may cause frequencies below 25 kHz.

The repeatability of the measurements was studied by performing the measurements several times. Before each measurement, the optical spectrum of the photonic resonator was measured and the laser was positioned at the flank of the resonance (see Sec. 5.6.1). The influence of repositioning the microphone was also studied by rotating the microphone along the axis of the brass rod. This also introduced variations in the distance between the microphone and the transducer. The maximum measured difference (using an ultrasonic pulse-echo technique) was only 3 mm. The variation in the measurements (linearity and NEP) was not larger when rotating the microphone. Therefore we treated the 12 measurements as one dataset and found a sensitivity of 1.2 mV/Pa and a NEP of 0.8 Pa with standard deviations of 7% and 20%, respectively. The total uncertainty may be estimated as the quadratic sum of these standard deviations and the uncertainty in the calibration of the setup. This gives an estimated uncertainty of 12% in the sensitivity and of 22% in the NEP.

The frequency dependent transfer function was measured by sending narrowband acoustical pulses with different center frequencies f_0. The sensitivity of the photonic microphone is obtained by dividing the recorded m.e. voltage signal by the m.e. pressure. Figure 5.16 presents the result. The photonic microphone has maximal sensitivity at 0.76 MHz and a -6 dB bandwith of 20%. This frequency is 22% of from the resonance frequency of the membrane that we predicted using numerical simulations (0.6 MHz, see Table 5.1).

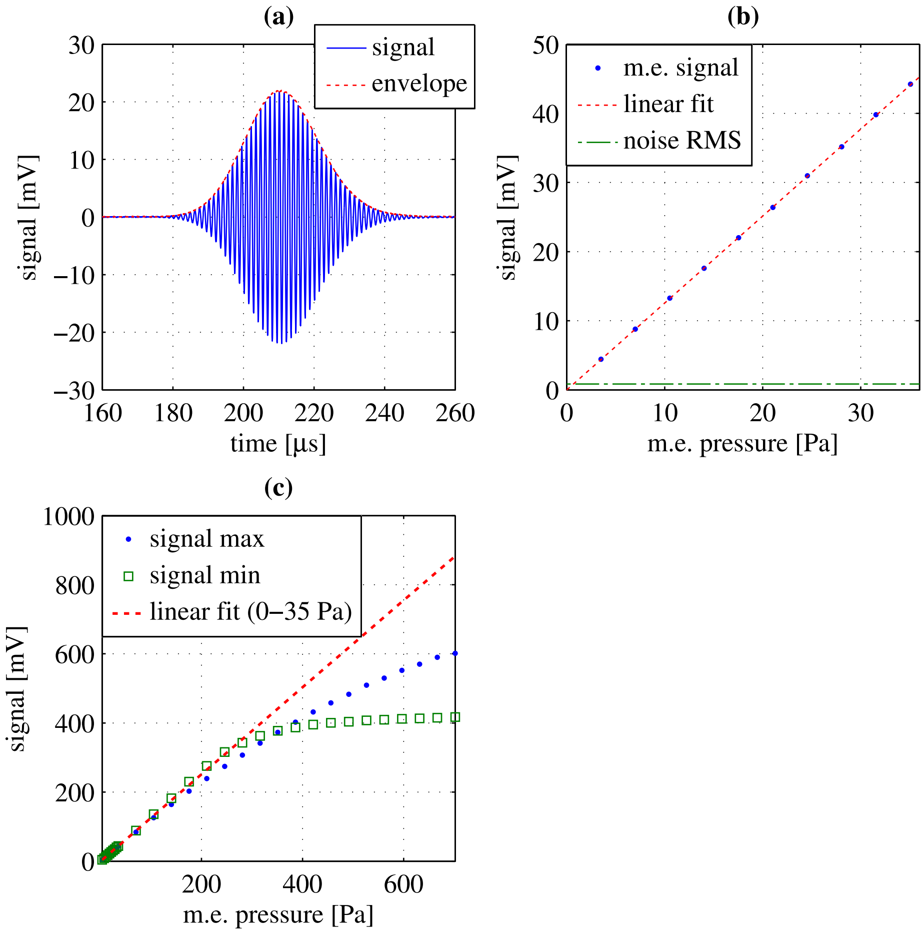

Figure 5.15: Measurement of the photonic microphone. Center frequency $f_0 = 0.75$ MHz at which the microphone has maximal sensitivity. **(a)** Measured signal versus time (photo-receiver AC output). The envelope of the signal is also shown. **(b)** Measured maximum of the envelope of the signal plotted versus calibrated maximum of the envelope of the pressure wave (blue dots). Linear fit through the origin with tangent 1.3 mV/Pa (red dashed line). Noise RMS = 0.8 mV (green dashed line). Crossing of the lines gives NEP at 0.7 Pa. **(c)** Measured maximum of the signal (blue dots) and minimum of the signal (green squares) plotted versus calibrated maximum of the envelope of the pressure wave. Also showing the linear fit of plot (b). The difference between the linear extrapolation and the measured maximum is above 5% at 105 Pa. The difference between the linear extrapolation and the measured minimum is above 5% at 281 Pa.

Table 5.3: Repeatability of the measurements. Power is the optical power that is transmitted through the resonator without ultrasound. Wavelength is the wavelength of the laser.

#	position	date	power [μW]	wavelength [nm]	sensitivity [mV/Pa]	NEP [Pa]	distance [cm]
1	1	6 Dec	24.075	1544.775	1.258	0.667	24.182
2	1	6 Dec	24.270	1544.804	1.265	0.661	24.068
3	1	6 Dec	25.781	1544.803	1.170	0.701	24.054
4	1	9 Dec	18.328	1544.616	1.041	0.920	24.158
5	1	9 Dec	26.220	1544.619	1.126	0.981	24.059
6	1	9 Dec	24.807	1544.632	1.205	0.876	24.056
7	1	9 Dec	20.380	1544.651	1.318	0.613	24.045
8	2	9 Dec	20.598	1544.664	1.308	0.698	24.191
9	3	9 Dec	24.480	1544.667	1.187	1.083	24.176
10	4	9 Dec	25.725	1544.677	1.145	1.027	23.975
11	5	9 Dec	23.304	1544.694	1.229	0.809	24.264
12	6	9 Dec	23.050	1544.704	1.223	0.726	24.052
mean					1.206	0.813	24.107
standard deviation					7 %	20 %	0.08 %

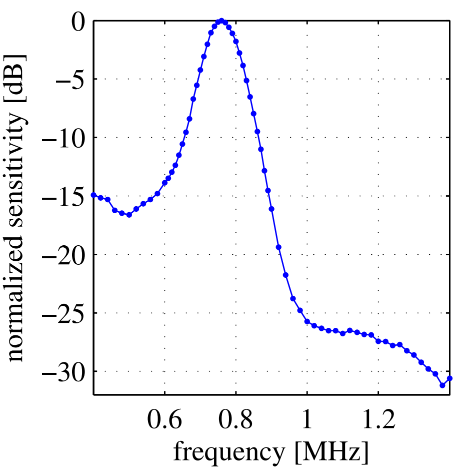

Figure 5.16: Normalized transfer function of the photonic microphone. This figure was measured by sending narrow-banded acoutical pulses at different center frequencies f_0 (horizontal axis). For each frequency, the m.e. signal [mV] of the photonic microphone was recorded and the m.e. pressure [Pa] was recorded (using the hydrophone). The two signals are divided to get the sensitivity [mV/Pa]. This quantity is plotted in the logarithmic decibel (power) scale.

5.8 Analysis of the interrogation system

The interrogation system was studied by stepping the wavelength of the laser. For each wavelength λ_l, the optical and acoustical properties are recorded. The optical powers as used for the measurements in this chapter caused heating of the waveguide of the ring resonator due to dissipation of the light in the ring resonator. Therefore we first study the ring resonator using lower optical power.

Interrogation system with low optical power

We stepped the laser output wavelength λ_l and measured the optical transmission as well as the acoustical characteristics at each wavelength. Figure 5.17a shows the transmitted optical power $I(\lambda_l)$ as a function of the wavelength of the incident light λ_l. The derivative $\partial I/\partial\lambda$ is also shown. Figure 5.17b shows the sensitivity of the microphone in units of micro-volt per pascal. We may compute the sensitivity expressed in optical power, $\partial I/\partial P$, using the transimpedance gain of the photo-receiver ($\sim$40 mV/μW). We expect that the sensitivity scales with the steepness of the flank of the optical resonance, $\partial I/\partial\lambda$. This can be seen in Eq. (5.2) multiplied by I_0, i.e., $\partial I/\partial P = (\partial I/\partial\lambda)\cdot(\partial\Delta\lambda/\partial P)$. Fig. 5.17b shows that these curves indeed show the same wavelength-dependecy and we computed $\partial\Delta\lambda/\partial P = (\partial I/\partial P)/(\partial I/\partial\lambda)$ as the ratio of the two curves. We computed the wavelength shift per ultrasonic pressure $\partial\Delta\lambda/\partial P = 67$ fm/Pa (at $f_0 = 0.75$ MHz). Figure 5.17c show the root-means-square value of the noise, i.e, the measured AC output of the photo-receiver for the case that there is no ultrasound. The noise follows the same trend as the optical power $I(\lambda)$ but with an offset that does not depend on the optical power. From this we may conclude that fluctuations in the resonance wavelength of the ring resonator do not dominate the noise in the measurements. Noise in the resonance wavelength of the ring, such as caused by random temperature fluctuations, would result in a higher noise for laser wavelengths at the flank of the resonator [25]. The NEP has a minimum value of 1.7 Pa which is higher than the NEP that could be obtained using higher optical power.

Interrogation system with higher optical power and heating of the ring

Figure 5.18 presents the influence of the laser wavelength for the case of higher optical power (50 μW transmission away from the resonance). This power was used for the ultrasonic measurements in this chapter because it provides a better signal-to-noise ratio. Figure 5.18b shows the sensitivity of the photonic microphone as a function of the wavelength of the laser. Figure 5.18c shows the RMS value of the noise. Figure 5.18d shows the NEP as a function of laser wavelength. The NEP has a minimal value of 0.43 Pa at wavelength $\lambda_l = 1544.830$ nm. Increasing the optical power by a factor 5 thus resulted in a decrease in the NEP by a factor 4.

Figure 5.18a shows the optical transmission as a function of laser wavelength. It seems that the resonance has an asymmetric lineshape, however, we believe that this asymmetry is due to heating of the ring. This asymmetric shape is thus not the instantaneous transmission of the resonator $T_0(\lambda)$ but it is due to the fact that the waveguide of the micro-ring resonator is heated by the incident light

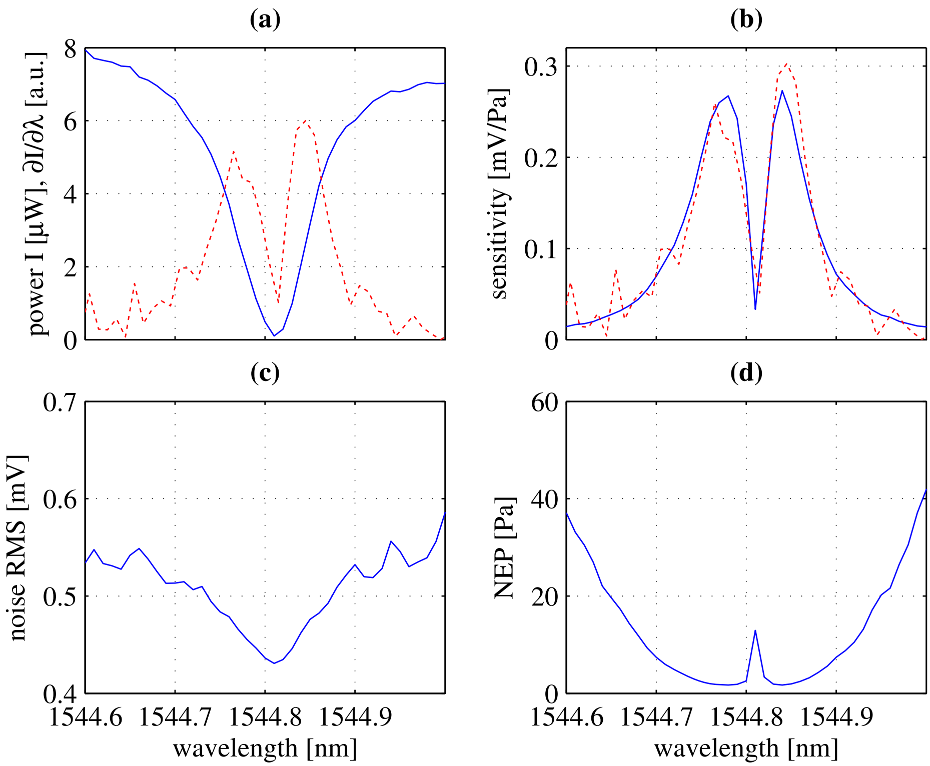

Figure 5.17: Characteristics of the photonic microphone as a function of the wavelength of the laser λ_l. Transmitted power away from the resonance $I_0 = 10\ \mu$W at $\lambda_l = 1543.5$ nm. This is lower than the optical power that was used in the other measurements in this chapter. Acoustical signal is kept constant: $f_0 = 0.75$ MHz with e.m. pressure 18 Pa. **(a)** Transmitted power I versus wavelength of the laser λ_l (solid blue curve). Also showing derivative with respect to wavelength $\partial I/\partial \lambda_l$ (dashed red curve, normalized for visibility). Same data as Fig. 5.19. **(b)** Sensitivity S in mV/Pa. Also showing the curve $A \cdot \partial I/\partial \lambda$ of (a) with factor A such that the squared difference between S and $A \cdot \partial I/\partial \lambda$ is minimal. We found $A = 67$ fm/Pa. **(c)** Root-mean-square value of noise [mV]. **(d)** Noise equivalent pressure (NEP) [Pa].

with a certain wavelength λ_l. The asymmetry was much smaller when we used lower optical input power (Fig. 5.17). The asymmetry was not observed when measuring the ring in a setup as was described in Sec. 3.4. In that setup, the optical input of the ring resonator is broadband and constant while the spectral response is measured using an optical spectrum analyzer (OSA) at the output of the ring. Silicon has a strong thermo-optic effect and the resulting shift in resonance wavelength is about 80 pm/°C [148]. The asymmetry is explained by heating of the ring due to dissipation of the light that is in the waveguide of the ring

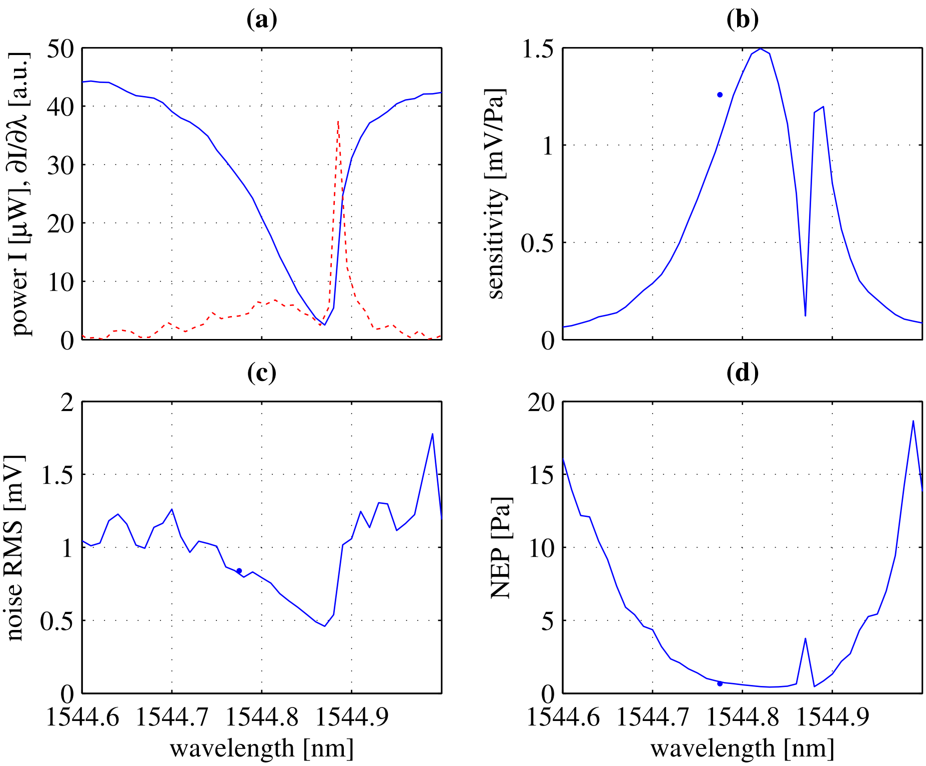

Figure 5.18: Characteristics of the photonic microphone as a function of the wavelength of the laser λ_l. Same measures as in Fig. 5.17 but with different optical input power: transmitted power away from the resonance $I = 50\ \mu$W at $\lambda_l = 1543.5$ nm. Acoustical signal is kept constant: $f_0 = 0.75$ MHz with e.m. pressure 18 Pa. Wavelength steps 10 pm. The stepsize 10 pm is not small enough to reveal all details, especially at the right (red) flank of the resonator. At least 20 s stabilization time after each step. **(a)** Transmitted optical power I versus wavelength of the laser λ_l (solid blue curve). Also showing derivative with respect to wavelength $\partial I/\partial\lambda_l$ (dashed red curve, normalized for visibility). **(b)** Sensitivity in mV/Pa. **(c)** Root-mean-square value of noise [mV]. **(d)** Noise equivalent pressure (NEP) [Pa]. Blue dots in (b-d) are the values as measured in Fig. 5.15.

resonator. The amount of light in the ring waveguide is maximal when the input wavelength is exactly at a resonance of the ring. The amount of light in the ring, and thus the dissipation, thus changes while measuring the transmittance of the ring resonator with a tunable laser. On the left (blue) flank of the resonance, the amount of light increases for increasing laser wavelength and the resonance thus shifts to the right while measuring. On the right (red) flank of the resonance, the amount of light decreases for increasing laser wavelength and the resonance thus shift to the left. This gives the asymmetric transmission as observed in Fig. 5.18.

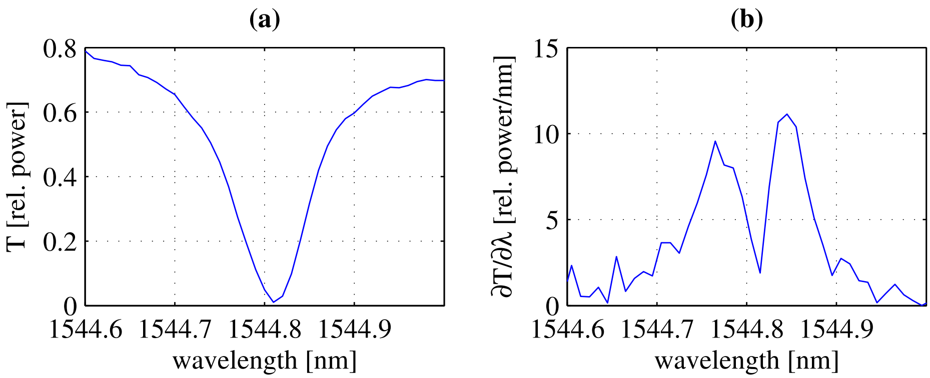

Figure 5.19: (a) Measured optical transmission spectrum $T(\lambda) = I(\lambda)/I_0$ of the racetrack resonator. Transmitted optical power away from the resonance $I_0 = 10\ \mu$W at $\lambda_l = 1543.5$ nm. Wavelength steps 10 pm. At least 20 s stabilization time after each step. **(b)** Derivative of (a) with respect to wavelength, $\partial T/\partial\lambda$.

As will be argued hereafter, we expect that the ultrasonic measurements are not influenced by the heating. The ultrasound-induced shift of the resonance wavelength is small and fast oscillating around a certain value. Figure 5.18b shows the sensitivity of the photonic microphone. Sensitivity is approximately equal for wavelengths at the left or at the right flank of the resonator. This sensitivity does not have the same trend as the steepness of the flank of the resonator, $\partial I/\partial\lambda_l$, when $I(\lambda_l)$ is measured with a tunable laser with high power. The fact that the sensitivity is approximately equal at the left flank and the right flank of the resonator suggests a symmetric resonance dip. Therefore we believe that the temperature of the ring during the ultrasonic measurements can be approximated constant. Typical measurements with 18 Pa m.e. pressure introduce only a small wavelength shift of approximately 1.2 pm. Also, the acoustical pressure has a mean value of zero and a fluctuation with a frequency of 0.75 MHz. The typical timescale for the change in the heating is thus only 0.7 μs.

We may introduced the heating-induced wavelength shift in Eq. (5.1) as

$$I(\lambda_l) = T\left(\lambda_l + \Delta\lambda(t) + \Delta\lambda_h(\lambda_l)\right) \cdot I_0 \tag{5.9}$$

with $\Delta\lambda(t)$ the ultrasound-induced wavelength shift and $\Delta\lambda_h(\lambda_l)$ the heating-induced wavelength shift. We neglected the influence of the ultrasound-induced change in the resonance wavelength on the heating ring resonator. This means that $\Delta\lambda_h$ is constant during the ultrasound measurements and only depends on the wavelength of the laser λ_l. When using low optical powers and without ultrasound, $\Delta\lambda_h$ may be neglected and Eq. 5.9 reduces to $I(\lambda) = T(\lambda) \cdot I_0$. We have used the measurement with low optical power ($I_0 = 10\ \mu$W) to measure $T(\lambda)$. The transmitted power $I(\lambda)$ was shown in Fig. 5.17a and the corresponding normalized optical transmission spectrum $T(\lambda)$ is presented in Fig. 5.19.

For low optical powers ($\Delta\lambda_h \approx 0$), Eq. (5.3) with Eq. (5.9) predict that the sensitivity $\partial I/\partial P$ of the microphone scales linearly with the optical power away form the resonance I_0. For higher optical powers, the relation between the sensitivity of the ultrasound measurements and the measured optical transmitted power $I(\lambda)$ is not as straightforward anymore. However, the maximum sensitivity of the ultrasound measurements $\partial I/\partial\Delta\lambda$ is still the maximum of $(\partial T/\partial\Delta\lambda)I_0$ but the maxima are not at the same wavelength λ_l due to the heating-induced shift $\Delta\lambda_h$. Using the data of the measurements with a low optical power ($I_0 = 10\ \mu$W), we predict the sensitivity of the measurements with high optical power ($I_0 = 50\ \mu$W) to be five times as high. This predicts a maximal sensitivity of 1.3 mV/Pa which is close to the maximal measured sensitivity of 1.5 mV/Pa.

Detection limit of the interrogator in terms of wavelength shift

It is interesting to know the detection limit of the interrogation system in terms of shift of the wavelength of the resonator. We may express this limit in terms of noise equivalent wavelength shift. We estimate the sensitivity of the interrogator as the steepness of the flank of the resonance, i.e. $\partial I/\partial\Delta\lambda = \partial T/\partial\lambda \cdot I_0$ (neglecting heating-induced wavelength shift). We measure the noise as the RMS value of the output of the system without induced ultrasound (ΔI_{noise}). Note that the electronic filters reduce the bandwidth from approximately 25 kHz to 20 MHz. The noise equivalent wavelength shift is then computed as $\Delta\lambda_{\text{noise}} = (\partial\lambda/\partial T) \cdot (\Delta I_{\text{noise}}/I_0)$. We use the left (blue) flank of the resonance as the ultrasonic measurements were performed at this flank. For low optical power $I_0 = 10\ \mu$W and at wavelength $\lambda_l = 1544.770$ we find RMS noise $\Delta I_{\text{noise}} \approx 12$ nW (Fig. 5.17c) and $\partial T/\partial\lambda = 9.6\ \text{nm}^{-1}$ (Fig. 5.19b) to arrive at $\Delta\lambda_{\text{noise}} \approx 121$ fm. For higher optical intensity, $I_0 = 50\ \mu$W, we know that $T(\lambda)$ and $I(\lambda)$ are not straightforwardly correlated due to the heating-induced shift of the resonance wavelength. Therefore we used wavelengths of maximal sensitivity. For $\partial T/\partial\lambda$ this is at $\lambda_l = 1544.770$ nm. The corresponding wavelength in the $I_0 = 50\ \mu$W data is estimated as the optical wavelength where the system has maximal sensitivity to ultrasound, i.e. 1544.820 nm from Fig. 5.18b. The corresponding noise $\Delta I_{\text{noise}} \approx 17$ nW (Fig. 5.18c) and $\Delta\lambda_{\text{noise}} \approx 36$ fm.

Summary

This section was mainly about the physics and the performance of the interrogation system. For lower optical powers, the system follows the characteristics as expected from Eqs. (5.1)-(5.3) and the sensitivity of the microphone scales with the steepness of the flank of the resonance. From these measurements we could compute the change in resonance wavelength due to the ultrasound. We found a m.e. wavelength shift per m.e. pressure $\partial\Delta\lambda/\partial P = 67$ fm/Pa (at $f_0 = 0.75$ MHz).

For high optical powers, dissipation of the light in the waveguide of the ring resonator heats this waveguide and thereby shifts the resonance depending on the amount of light that is coupled to the ring. However, we have shown that this does not influence the response of microphone to ultrasound. The microphone is most sensitive and has lowest NEP for the case of high optical power. We measured a NEP of 0.43 Pa. We computed the noise-equivalent-wavelength-shift of the interrogation system to be 36 fm.

5.9 Outlook

The studied microphone was designed for simplicity of fabrication and understanding and we believe that there is much room for the improvement of our new ultrasound microphone.

The sensitivity of the optical read-out system scales with the steepness of the flank of the optical resonator. Decreasing the full-width at half-max of the optical resonator gives an increase in sensitivity. We have estimated the sensitivity of the resonator as the ratio of the extinction ratio r and the full-width at half-max $\Delta\lambda_{\mathrm{FWHM}}$. For a racetrack resonator with a straight track length of 40 μm, we measured $r/\Delta\lambda_{\mathrm{FWHM}} = 0.01$ pm^{-1} (Fig. 5.1b). For a racetrack resonator with the same shape (straight track length 40 μm, bending radius 5 μm), with the same waveguide (400 nm by 220 nm), with a waveguide propagation loss of 2.5 dB/cm, but with only one coupler and with critical coupling, we find $r/\Delta\lambda_{\mathrm{FWHM}} = 0.1$ pm^{-1} which is one order of magnitude more sensitive. This number was computed using Eq. (2.184), Eq. (2.185) and the mode-solver presented in Sec. 2.7. Moreover, the sensitivity of the resonator increases with increasing length of the track. It is possible to fold the waveguide of the resonator on the membrane to increase the sensitivity of the resonator to ultrasound.

We have used off-the-shelf components for the interrogation system. Although the equipment was selected with care, a dedicated design for the lightsource, photoreceiver, and the electronic circuits thereof will most likely reduce the noise. Moreover, literature reports on a wide variety of interrogation concepts although not all of them operate at frequencies in the MHz range [25, 156–161].

The acoustical characteristics of a membrane with equal thickness were discussed in this chapter. The 2.5 μm silicon-dioxide membrane layer was kept constant and the only design parameters that were studied were the diameter d and the thickness h_2 of possible silicon layer in the membrane. However, it is possible to fabricate different membranes that translate a given pressure to a higher local strain. For example by using layers that are fabricated of different materials. Another approach that is used in MEMS pressure sensors is to have membranes with a height that varies over the membrane surface (e.g., a boss membrane). Such structures could be fabricated at the top surface of our chips by deposition and etching of the required materials and structures. A well controlled etch process from the back of the wafer could thin the silicon-dioxide layer behind the membrane.

Moreover, it is also possible to consider photonic resonators with their long direction in the same direction as the vibration of the longitudinal ultrasonic pressure wave (the y-direction). This requires cutting the dies into small stripes and rotating them by 90°. In general, many mechanical designs can be used as the optical circuit is small with respect to the mechanical structure.

5.10 Conclusion

We have designed, fabricated, and measured a new type of ultrasonic microphone which is based on photonic micro-ring resonators. The microphone was designed to proof the operation principle of this microphone and the first prototype was fabricated in silicon-on-insulator technology.

We demonstrated the operation principle of this new photonic microphone by measuring ultrasound around a frequency of 0.75 MHz. The sensitivity is 1.2 mV/Pa and the detection limit (NEP) is below 1 Pa. This is on the same order of magnitude as the state-of-the art of conventional piezo-electric based ultrasound transducers. The measured -6 dB bandwidth of the acoustical resonator is 20%.

We studied the interrogation system and found a detection limit (noise equivalent wavelength shift) of 36 fm. For higher optical powers, dissipation of the light in the waveguide of the ring resonator heats the ring which results in a measurable shift of the resonance wavelength. The ultrasound measurement is not influenced by this heating-induced shift. Moreover, we found that an ultrasonic pressure wave with a frequency around 0.75 MHz induced a wavelength shift of 67 fm/Pa.

We believe that there is much room for improvement of this new type of microphone as we report on the most simple design. Wafer-scale fabrication of the sensor is possible using silicon-on-insulator technology that is used in the electronic IC industry and the MEMS industry. One of the key features of this optical sensor is that wavelength-division multiplexing allows read-out of many microphone elements via one optical fiber. This is highly attractive for array technology such as is used in ultrasonography with applications in medical imaging or non-destructive inspection.

Chapter

6 Conclusions and outlook

We have demonstrated the use of silicon photonic micro-ring resonators as sensitive elements in strain sensors and in ultrasound sensors. The conclusions that are listed hereafter show the feasibility of the applications as introduced in Chapter 1. This section starts with a discussion of the ultrasound microphone and then continues with its components.

An ultrasound microphone based on silicon photonic ring resonators

Silicon photonic micro-ring resonators can be used as sensitive ultrasound microphones. The designed, fabricated and characterized microphone consists of a photonic racetrack-shaped resonator (footprint 50 μm by 10 μm, height 0.220 μm) that is integrated in an acoustically resonant silicon-dioxide membrane (diameter 0.124 mm, height 2.5 μm). This ultrasound microphone has a minimal detection level (noise equivalent pressure) below 1 Pa which is on the same order of magnitude as the state-of-the-art of piezo-electric based transducers [145]. The microphone showed an acoustical resonance around 0.75 MHz with a -6 dB bandwidth of 20% (Sec. 5.7).

The photonic micro-ring resonators were interrogated using a laser and a photoreceiver. The wavelength of the laser was tuned to the flank of a resonance of the ring resonator so that a shift in the resonance wavelength translates into a modulation of the transmitted light. This system showed a minimal detection limit of the wavelength shift (noise equivalent shift) of approximately 36 fm (bandwidth 25 kHz to 20 MHz, wavelength ~1550 nm, Secs. 5.3, 5.8).

We have studied the most simple form of this microphone and there is a lot of room for improvement of this sensor (Sec. 5.9). The acoustically resonant membrane may be replaced by an optimized resonant structure, the photonic resonators may be improved and more complex interrogation systems may be used. Next to general improvements of the microphone, future research will focus at specific applications. Designs are always a trade-off between different characteristics. For example, the sensor reported here has a very high sensitivity and a small size but it has a poor bandwidth. The application decides which characteristics are important and which are not. For application in medical intravascular echography it is necessary to increase the resonance frequency and the bandwidth of the acoustical resonant structure [11].

A variety of small wavelength-division multiplexers (WDM) in SOI technology have been reported the literature [1, 2]. However, to the best of our knowledge, interrogation of multiple silicon ring-resonators via one or two optical fibers has not been reported. This is probably because there was no interest, many research has been performed to integrate the light source, detectors and electronics in the same chip – this is exactly what we avoid [24, 56–61]. The largest bottleneck of the multiplexer is the inaccuracy of the fabrication of the photonic circuit. On the bright side, the requirements on this multiplexer are much lower than the requirements for telecommunications. The multiplexer should take care that each photonic resonator can be individually addressed using a specific wavelength but this wavelength is not fixed. The interrogation system can find this specific wavelength and tune to operation at this wavelength. A robust implementation could, for example, use a photonic resonators with a small free-spectral-range (e.g, a long ring circumference) combined with a multiplexer with a large channel spacing such that each channel contains a few resonances of the photonic resonator. In that configuration, the exact wavelength of the channels of the multiplexer is not important as the photonic resonator will always have a resonance in that channel. The semiconductor industry still develops rapidly by which the fabrication accuracy of silicon photonic circuits will increase.

We have demonstrated the principle of a new type of microphone. Application of this microphone will require packaging that is suited for specific applications. It is possible to cut (dice) silicon chips precisely to the required dimensions. We have used large fiber-array blocks to place the optical fibers above the out-of-plane grating couplers. However, single fibers can also be cut under the angle that is required to direct the light to the chip. Special fiber end-facets have been developed for intravascular optical coherence tomography [162]. Another point to consider is the price of the interrogation system. We have used a tunable external-cavity laser that is versatile for laboratory-purposes but which has a price of 20 thousand euro. Interrogation of the microphone does not need this wide tuning range and other specifications (e.g. absolute wavelength accuracy). Turn-key DFB laser systems[1] with a tunability of ∼1.7 nm are one order of magnitude cheaper and a special designed laser driver could probably reduce the price by another order of magnitude.

Characteristics and fabrication of silicon photonic ring resonators as strain sensors in micro-mechanical systems.

The relation between the deformation of the micro-ring resonator and the shift in the resonance wavelengths was studied in a well-defined static mechanical setup. Long racetrack resonators (1 mm long) were elongated in their long direction so that the effects of the bends and couplers could be neglected. Depending on the width of the waveguide and the orientation of the silicon crystal, the linear

[1]Vendors are, for example, Agilent (Santa Clara, California, USA), Thorlabs (Newton, New Jersey, USA), and Yenista (Lannion, France).

wavelength shift per applied strain varies between 0.5 and 0.75 pm/microstrain for infrared light around 1550 nm wavelength. The influence of the increasing ring circumference is about three times larger than the influence of the change in the propagation speed of the light through the waveguide (effective index), and the two effects oppose each other. The strong dispersion in silicon sub-wavelength waveguides (400 nm by 220 nm) accounts for a decrease in sensitivity of about a factor two (Ch. 4).

Fabrication of the microphone demonstrated successful integration of silicon photonic circuits in silicon micro-mechanical systems. First the photonic resonators and photonic wiring were fabricated in a semi-industrial CMOS line (at IMEC, Leuven, Belgium). The resulting SOI wafer consists of a thin silicon photonic circuit integrated in a 2.5 μm thick silicon-dioxide layer that is on top of a 250 μm thick silicon substrate. Second the membrane was fabricated by etching a hole from the back-side of the wafer until the only the thin silicon-dioxide membrane with integrated photonic resonator was left. This etching was done using a Bosch etch process which is often used in silicon micro-machining technology (Sec. 5.5).

We have measured the relation between the deformation of a ring resonator and the resulting shift in its resonance frequencies and we have identified the physical effects. What is missing is numerical simulations that predict the strain-induced change of the effective index (i.e., the propagation speed of the light through the waveguide). This change is not trivial to compute as (1) details of the mechanical deformation of the waveguide are unknown because the cross-section of the stiff silicon waveguide does not necessarily follow the surrounding silicon-dioxide and (2) the small optical changes in the waveguide are difficult to compute because the photo-elastic effect causes a non-homogeneous anisotropic refractive index profile of the waveguide and its cladding. This thesis provides accurate measurements to validate such simulations. Such simulations would lead to more accurate simulations of the ultrasound microphone and thus to better designs.

It was beyond the scope of this thesis to study the application of photonic micro-ring resonators in micro-mechanical systems other than ultrasound sensors. The results and insights obtained in this thesis are of broader interest. For example, researchers at TNO are studying the application of photonic micro-rings in the cantilever a atomic force microscope (AFM). Such microscope scans a sample with a micro-scale cantilever that is just above it. Traditionally, the deflection of the cantilever is measured by aligning a free-space laser beam to the cantilever and measuring the angle of the reflected beam. A strain sensor integrated in the cantilever could remove the need of this free-space optical system.

Optical characteristics of silicon photonic micro-ring resonators: experiments and theories

The optical characteristics of the micro-ring resonators and their components were extensively studied. Different methods to characterize directional couplers (direct and in ring-resonators) gave similar results. Most devices behaved as expected but it is probably interesting to note that the fabricated waveguides were 10%

smaller than designed. An interesting observation was that directional couplers introduce a large coupling-induced phase delay when nearly all light couples from one waveguide to the other. (See the abstract of Chapter 3 for more details.)

The devices characterized in this theses were fabricated in October 2011. At that time, fabrication of silicon photonic integrated circuits for universities was offered via the ePIXfab platform at IMEC (Leuven, Belgium) and at CEA-Leti (Grenoble, France). Today more microelectronic research institutes offer this service (see footnote 1 on page 12). There is a trend towards standardized components (e.g., ring resonators or multiplexers) that do not require the user to deliver a detailed design of the component but rather a functional requirement which is translated into a design by the fab. Currently early implementations of such standard components are part of the design kits for ePIXfab. Next to this, the fabrication of photonic integrated circuits benefits from the developments in the silicon semiconductor industry. The first trials on IMEC's newer 300 mm CMOS line outperformed the accuracy of their 200 mm CMOS line that is currently used for the fabrication of photonic circuits [163].

Most properties of silicon ring resonators and their components (waveguides and directional couplers) can be computed using approximate analytical theories. Many theories on integrated optics were originally derived for low-index-contrast waveguides like optical fibers ($\Delta n < 0.1$). We reviewed and revised those theories for application to silicon-on-insulator waveguides which have a very high index contrast ($\Delta n \approx 2$). This work was formulated such that it can be used in a university course with only basic theory of electrodynamics as prerequisite (Ch. 2).

Analytical theories allow fast computation of the behavior of photonic devices and circuits. This is especially important when circuits are designed that consist of many devices. Moreover, we believe that analytical theories provide insight in the physics of the system that is difficult to obtain with brute-force numerical simulations.

Final words

In this thesis, we demonstrated that silicon micro-ring resonators can be employed to sense mechanical properties such as strain or ultrasound. We demonstrated a new type of microphone that has a detection limit (NEP) on the same order of magnitude as the state of the art of piezo-electric ultrasound transducers. We believe that this new photonic microphone is a breakthrough for ultrasound array technology. First because optical multiplexing allows simultaneous reading of multiple microphones via one optical fiber and second because the silicon-on-insulator technology allows simultaneous cost-effective fabrication of multiple microphones and their photonic wiring.

This thesis is relevant for the scientific community as it includes new understanding of the physics of silicon photonic ring resonators and their components: analytical theories, measurements that demonstrate a previously unobserved phase delay in silicon directional couplers, and characterization of the physical effects that play a role when a ring resonator is deformed. Technological progress was made in the design, fabrication and characterization of the microphone in silicon-on-insulator technology.

We believe that this thesis can lead to better and possible cheaper ultrasonic images. Society will benefit from such images via, for example, better diagnoses of medical problems or better inspection of industrial plants.

Appendix

A Silicon-dioxide cladding deposition with PECVD

The silicon-dioxide top cladding of the photonic chips was deposited using plasma enhanced chemical vapor deposition (PECVD). We used the *Plasmalab 80+* PECVD system of Oxford Instruments GmbH (Wiesbaden, Germany), incorporating: full-diameter gas inlet shower-head, Edwards EH250/E2M40 pumping system, 4000C table with "PID" controller, 30/300 W 13.56 MHz solid state R.F. generator, digital close-coupled automatic impedance matching unit, and automatic process pressure control unit. We used the process parameters that was provided by the supplier:

100% SiH4 flow	8.5 sccm,
N_2 flow	162.5 sccm,
N_2O flow	710 sccm,
Pressure	1000 mTorr,
R.F. power	20 Watts @ 13.56MHz,
Temperature	300-4000C,

with the following process characteristics:

Deposition rate	$>$ 50 nm/min,
Refractive index	typically 1.46-1.47.

The deposition was performed in the Kavli NanoLab Delft (joint laboratory of Delft University of Technology and TNO).

Appendix

B Photos of strain characterization setup

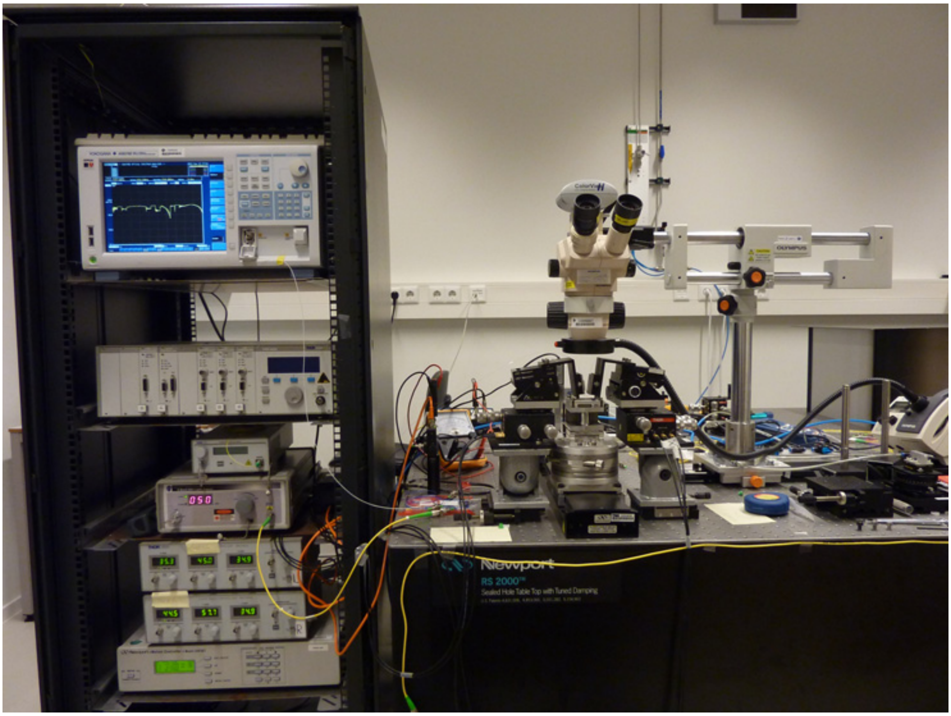

Figure B.1: Overview of the setup for the characterization of the influence of strain on photonic integrated circuits (see Sec. 4.4.1). Front view. Rack on the left-hand-side contains the equipment including Yokogawa optical spectrum analyzer (OSA, on top), two Thorlabs piezo-drivers and one Newport linear stage driver (on the bottom). Setup is built on a optical table (Newport). Microscope is placed above the chip in the setup. Zoom-in of the setup is shown in Fig. B.2.

(a) Side view

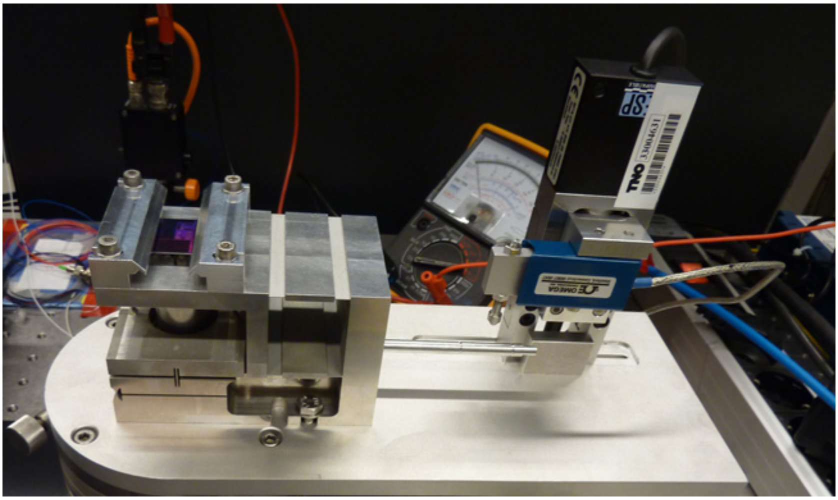

(b) Front view

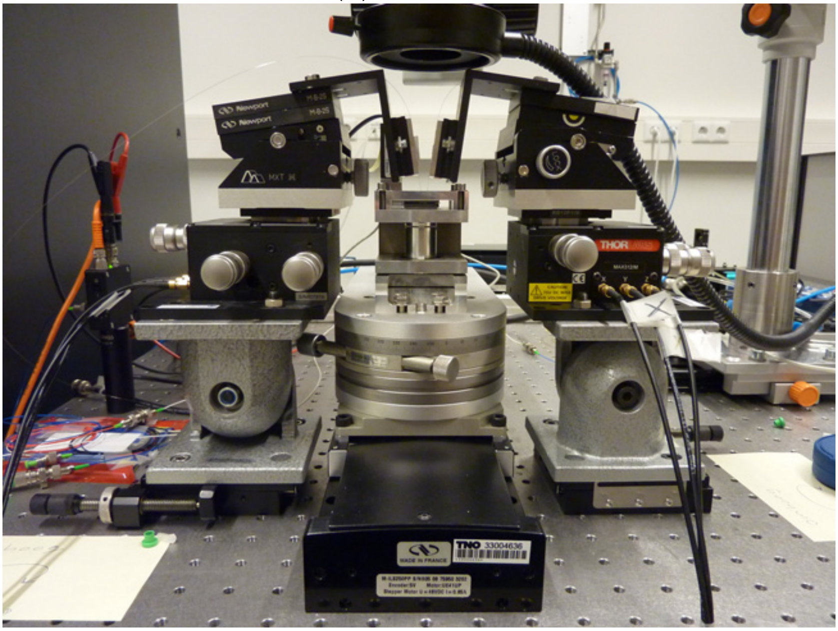

Figure B.2: Setup for applying strain and automated optical measurements. **(a)** side view, see Fig. 4.3. Tool for applying strain (metal) is mounted on a base plate (metal). Rectangular photonic chip (blue-ish) is loaded in the top of the tool. Lever is the rod on the right-hand-side of the tool. Automated strain application (blue load cell on a linear stage) is also mounted on the base plate. **(b)** Front view. Middle column from bottom to top: automated linear stage (black), manual rotation stage (metal), base plate (metal), tool for applying strain (metal), elbow-shaped fiber holders (black), microscope objective (black). Left and right columns from bottom to top: thin manual linear stages (black), height adjustment block (metal), precise x,y,z-stages (black), tilt stage (black), elbow-shaped fiber holders.

Appendix

C Photos of ultrasound characterization setup

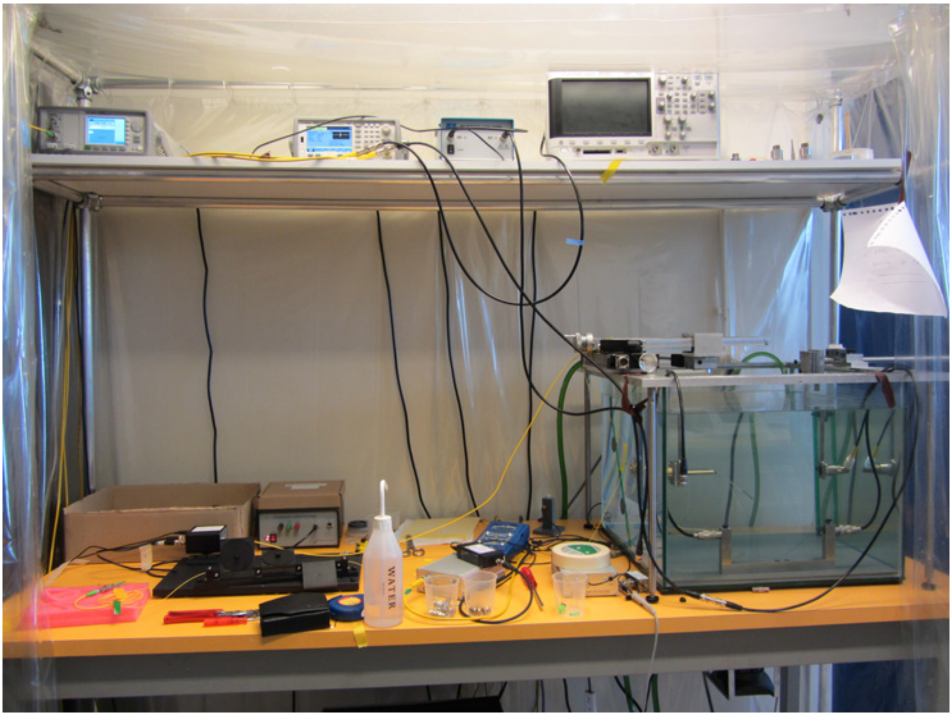

Figure C.1: Overview of the setup for the characterization of the photonic ultrasound microphone. On the top shelf: laser (left) and arbitrary waveform generator (AWG, middle). Water basin is placed on the right-hand-side of the table. In this photo, the chip microphone is not mounted in an U-frame but in a movable frame. The U-frame in the water basin is for to measure the speed of sound. The light from the fiber passes the manual variable attenuator (MVA, in the pinkish foam on the left of the table), then the polarization control (three black paddles), then the chip microphone (in water basin), then it ends in the photo-diode (black box on the corner of the optical breadboard on the table).

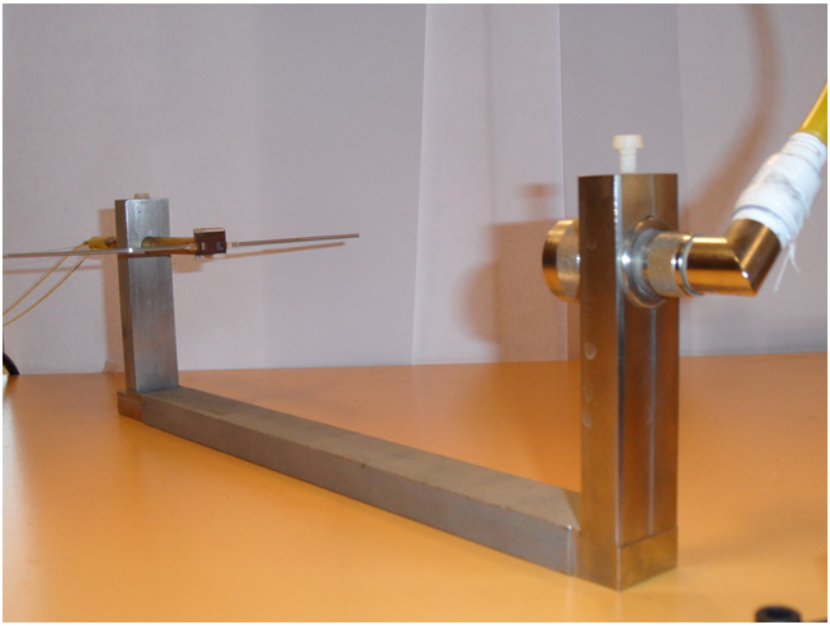

Figure C.2: U-frame with the photonic chip microphone on a brass rod (left) and traditional piezo-electric ultrasound transducer (right). Optical fibers leave the chip on the left-hand-side and on the right-hand-side.

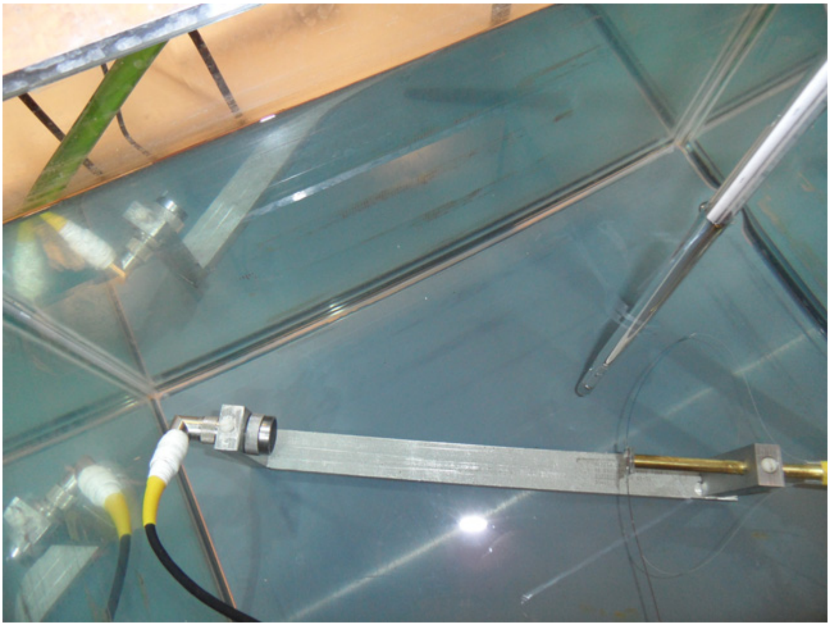

Figure C.3: Top-view of the water basin with the U-frame with the photonic chip microphone (right) and traditional ultrasound transducer (left). The pole sticking from above into the water is a thermometer.

Appendix

D Fabrication of the membrane

This appendix describes the procedure that was used for the fabrication of membrane. The photonic circuitry was first fabricated in silicon-on-insulator (SOI) technology using wafer-scale CMOS fabrication. Hereafter, we etched the membranes from the back of these wafers using processes that are typical in MEMS fabrication (Fig. D.1). The fabrication of the membrane was performed in the Van Leeuwenhoek Laboratory (joint laboratory of Delft University of Technology and TNO).

The fabrication of the photonic circuitry was done by IMEC via the ePIXfab platform (see Sec. 3.3 and Sec. 5.5). This circuitry has typical dimensions that are two orders of magnitude smaller than the membranes. At IMEC, the substrate of the wafer was thinned to a thickness of 250 μm. This is a non-standard procedure and we gratefully acknowledge IMEC for making this possible. In this fabrication process, many photonic chips are fabricated simultaneously on a single wafer. Our chips have a size of 12.7 mm by 6.3 mm and they are spaced with a horizontal pitch of 25.870 mm and a vertical pitch of 13.850 mm. According to our specifications, the wafer was diced at IMEC into dies of 2 by 4 chips so that the dies are 51.740 mm by 55.400 mm. This is the minimal die size that we could handle in the mask aligner (2"). The layout of the wafer is shown in Fig. D.2.

The fabrication process is based on optical lithography with back-side alignment and deep reactive ion etching (DRIE). A Bosch etching process was used to etch the hole from the backside of the silicon wafer. This is a DRIE process that alternates repeatedly between plasma etching and passivisation. This process was developed to etch deep with a high aspect ratio. We etched the silicon with sulfur

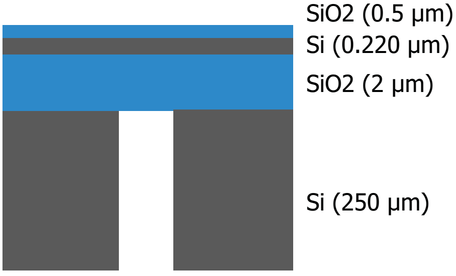

Figure D.1: Sketch of the microphone. The circular membrane is etched from the back of the wafer die and the photonic circuitry is inside the membrane.

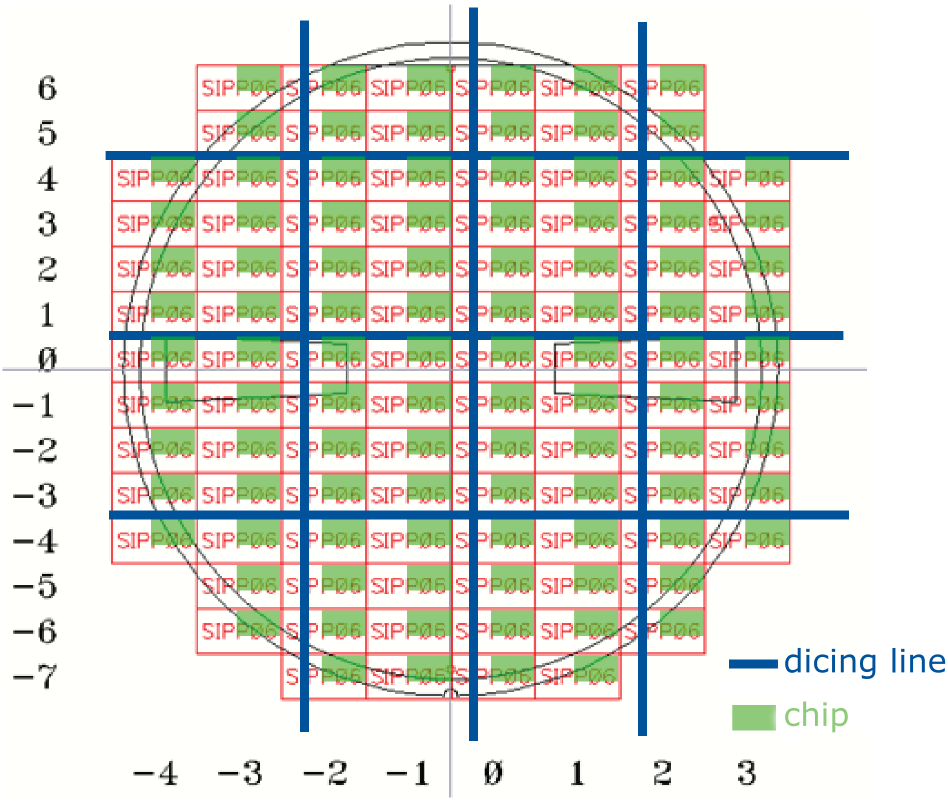

Figure D.2: Layout of the wafer with chips. The dicing lines for the first dicing are indicated. Wafer has a diameter of 200 mm.

hexafluoride (SF_6) which etches silicon at a much higher rate than silicon dioxide. This allowed us to use the SiO_2 membrane as etch-stop. In our cleanroom, the etch rate was unstable because it critically depends on how well the fresh etchant is able to enter the hole. This etch rate depends on parameters such as the position of the die in the chamber and the application of the thermal joint compound. Precise etching of the membrane was achieved by alternating etching and inspection of the etch dept until the membrane had reached the desired depth.

We performed the following steps to fabricate the membranes: (1) deposit 500 nm SiO_2 at the top-side of the die, (2) deposit 2500 nm SiO_2 on the back-side of the die as hard mask for the etching, (3) spin photoresist at the back-side of the die, (4) define the patterns in the photoresist using optical lithography and develop the photoresist, (5) etch through the photoresist and the SiO_2 hard-mask, (6) saw the dies into individual chips and (7) etch through the silicon substrate. The dicing of the chips is done after the lithography but before the etching of the membranes because some of the membranes broke as when we tried to saw a die with multiple chips into smaller dies.

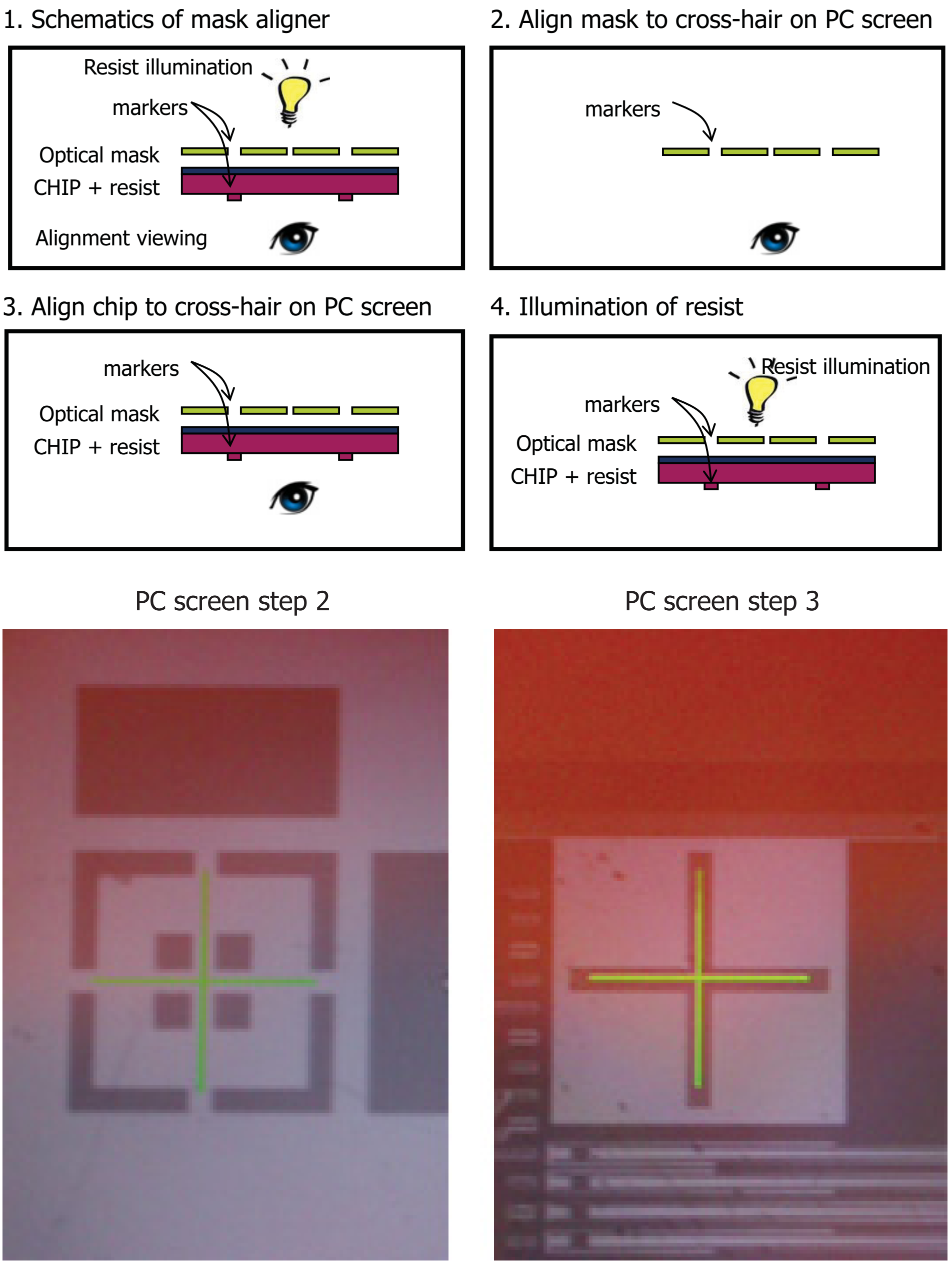

Figure D.3: Steps of the back-side aligment process: (1) schematics of the mask aligner, (2) align mask to cross-hair on PC screen, (3) align chip to cross-hair on PC screen and (4) illumination of the photoresist. Lower two photos show the PC screen in steps (2) and (3).

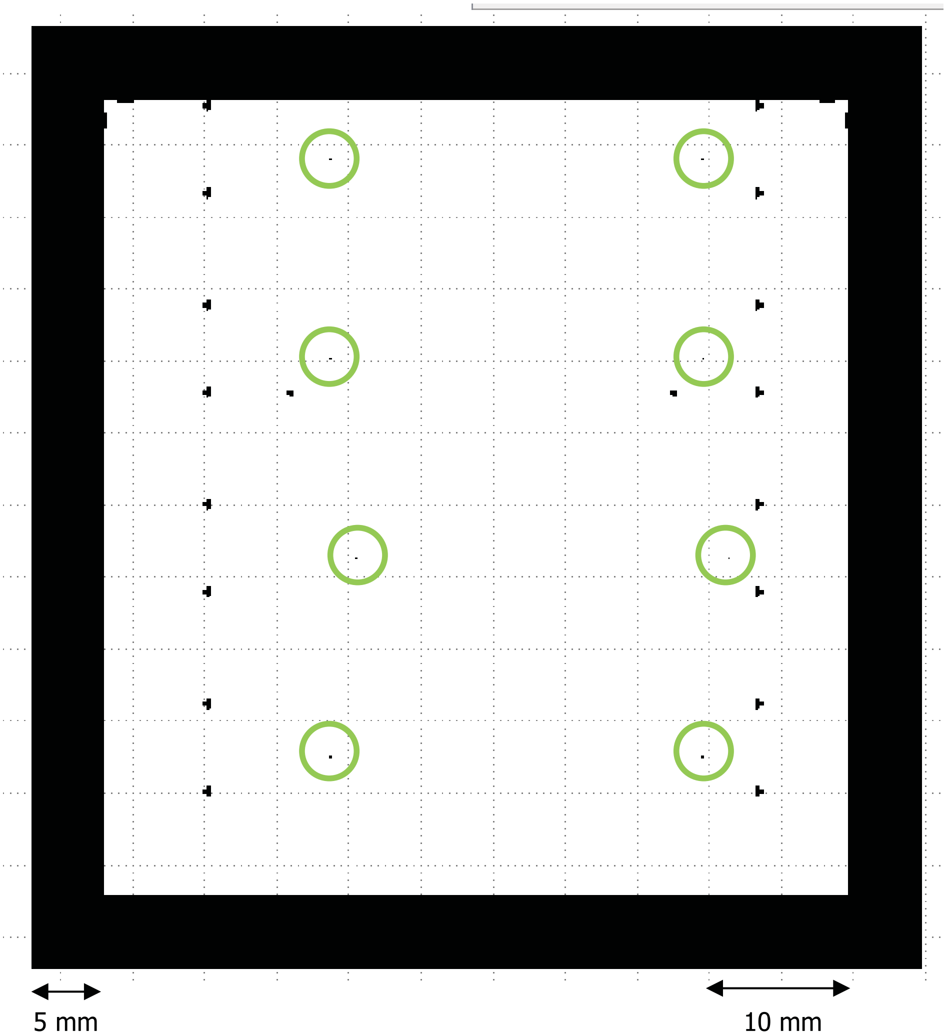

Figure D.4: Mask for the fabrication of the membranes. The border is such that the die of 2 by 4 chips fits exactly in this border. This can be used for coarse alignment. The membranes are hardly visible in this scale but the locations of the membranes are indicated by the light-green circles. The other features are markers for alignment.

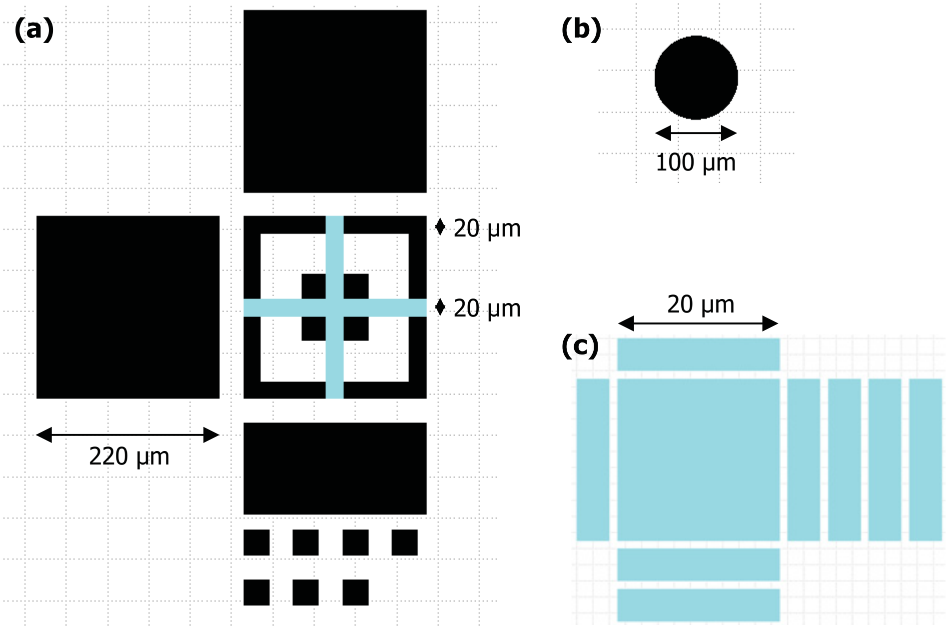

Figure D.5: Details of the mask for the fabrication of the membranes. Black is the optical mask. Cyan is the marker that is the 220 nm high silicon layer of the photonic cicruitry at the top of the die. **(a)** Alignment marker. The large squares are there so that the markers are easier to find when operating the mask aligner. The seven small squares below the marker indicate the position of the marker on the mask. **(b)** Membrane. Same scale as (a). **(c)** Zoom-in of the marker at the top of the die (in the same layer as the photonic circuitry).

D.1 Optical lithography with back-side alignment

Figure D.3 explains the procedure for aligning the lithographic mask to the other side of the die. First, the lithographic mask is aligned to cross-hairs that are visible on the PC screen. Then the chip is placed below the mask with the photonic circuitry facing down (step 2). Note that a transparent chuck should be used to position the chip here. Now the chip is aligned to the cross-hairs on the PC screen. Using this procedure, the optical mask is effectively aligned to the photonic circuitry that is on the other side of the chip.

The mask that is used in the optical lithography is shown in Figs. D.4 and D.5. The mask contains a large border that indicates the outline of the chip for coarse alignment. The mask contains markers to align this mask to the photonic circuitry at the top of the die. The camera view in the mask aligner is magnified using objective lenses. In the back-side alignment mode, the objectives have a fixed zoom. This limits the field of view and also limits the focal depth. This makes it difficult to find the alignment markers. To solve this issue, the alignment markers contain large square blocks (0.220 mm by 0.220 mm) so that the markers are still visible when the chip is not in focus.

D.2 Recipe for fabrication of the membranes

- Equipment
  - Plasma-enhanced chemical vapor deposition (PECVD). Plasmalab 80+ PECVD system from Oxford Instruments GmbH (Wiesbaden, Germany)
  - Deep reactive-ion-etcher (DRIE). Adixen AMS-100 from Adixen / Pfeiffer Vacuum GmbH (Asslar, Germany)
  - Mask aligner with option for back-side alignment. EVG 620 mask aligner from EVG Group (St.Florian am Inn, Austria)
  - Wafer dicer. DAD 3320 from Disco (Tokyo, Japan)
  - Laser confocal microscope. LEXT from Olympus (Tokyo, Japan)
- Start
  - Dies of photonic circuitry in SOI technology (51.740 mm by 55.400 mm).
  - Layers top-to-bottom: protective resist layer, 220 nm thick silicon layer with photonic circuitry, 2 μm thick silicon-dioxide BOX layer, 250 μm thick silicon substrate.
- Cleaning
  - Clean chip with acetone a few minutes to remove resist
  - Rinse with acetone
  - Rinse with IPA (Isopropyl alcohol)
  - Dry with nitrogen gun
- PECVD SiO_2 500 nm on front-side (waveguide cladding)
  - PECVD program silicon oxide 300 degrees C, see Appendix A
  - Soft pump 60 seconds
  - PECVD 7.5 minutes
- Cleaning
  - Clean chip with acetone a few minutes
  - Rinse with acetone
  - Rinse with IPA
  - Dry with nitrogen gun
- PECVD SiO_2 2500 nm back-side (hard mask)
  - PECVD program silicon oxide 300 degrees, see Appendix A
  - Soft pump 60 seconds
  - PECVD 37.5 minutes
- Spin photoresist
  - Spin primer HMDS; 3000 rpm, 2 minutes hotplate; 175 degrees C
  - Spin photoresist AZ5214; 1500 rpm; soft bake 30 minutes in oven at 90 degrees C (layer thickness 2.4 um)

  - Leave the chip for one day
- Lithography
  - Backside alignment procedure described in Sec. D.1.
  - Mask aligner EVG 620
  - Exposure 8 seconds
  - Develop 150 seconds in MF321 (Micropozit); 30 seconds in H_2O
  - Hard bake 30 minutes in oven at 120 degrees C
- Etching I: Opening of the hard mask.
  - Before the thermal joint compound was applied, AZ5214 photoresist was used as protection layer. Use a swab to apply the AZ5214 on the device side of the phtonic chip in SOI technology. Next bake substrate in oven for 15 minutes at 90 degrees C. Cool down and apply the thermal joint compound with a swab. Stick the chip on a 4 inch wafer with a 2 μm thick oxide layer.
  - Opening oxide hard-mask
    * Adixen AMS-100 etcher with recipe *Oxide Etchen VII* (Sec. D.3)
    * Duration 14+1 minutes
  - Photoresist removal
    * Adixen AMS-100 etcher with recipe *Clean recipe* (Sec. D.3)
    * Duration 8 minutes
- Dicing
  - Using DAD 3320 wafer dicer
  - Saw the die in individual chips. The horizontal size of the chip-die was chosen such that the out-of-plane grating couplers are 6 mm from the edge of the chip-die. This size is nessecary for the pyrex fiber-chip coupling block that was used (see Sec. 5.5). The vertical size of the die was chosen such that the membrane is approxiately in the center of the chip-die.
- Etching II: Etching the silicon hole
  - Adixen AMS-100 etcher with recipe *Silicon etching* (Sec. D.3)
  - Apply thermal joint compound using the description in Etching I.
  - The etch rate is unstable. Therefore we consecutively etched and inspected the depth of the etched hole. Etch rate depends on the diameter of the hole so different membranes need to be checked individually.
  - Inspection of the etched depth using the LEXT laser confocal microscope.
  - Note that the etch rate depends on the diameter of the hole.
  - Typical example of the etch process (hole diameters 100 μm and 120 μm)
    First step 40 minutes etch $\rightarrow$ depth 196 μm; etch rate 5.0 μm/minute
    Second step 13 minutes etch $\rightarrow$ depth 248 μm; etch rate 3.9 μm/minute
    Third step 7 minutes etch $\rightarrow$ oxide layer visible

– Gently remove thermal joint compound with a clean room clove sucked with IPA. Dry with nitrogen gun.

D.3 Recipes for deep reactive-ion-etcher Adixen AMS-100

D.3.1 Recipe for etching silicon-dioxide (Oxide etsen VII)

Temperature SH	0 degrees C,
Position SH	200 mm,
Pressure	2.6E-3 mbar position 100%,
RF1	2500 W,
SH RF2	300 W,
Bias	37.5 V,
Gas flow	C4F8 20 sccm,
	H_2 100 sccm,
	CH_4 10 sccm,
Etch rate Oxide	216 nm/min,
Etch rate AZ5214	131 nm/min.

D.3.2 Recipe for photoresist removal (Clean receipt)

Temperature SH	10 degrees C,
Position SH	120 mm,
Pressure	8E-2 mbar position 12.7%,
RF1	2000 W,
SH RF2	30 W,
Bias	37.5 V,
Gas flow	O_2 200 sccm,
Cleaning rate photoresist	196 nm/min.

D.3.3 Bosch etching recipe for silicon (Silicon etching)

Temperature SH	10 degrees C,
Position SH	200 mm,
Etch pulse	SF_6, 200 sccm, 7 sec,
Passivation pulse	C_4F_8 100 sccm, 2 sec,
RF1	2000 W,
Position	25%,
LF2	80 W;
	High power 80W; High time 10 msec;
	Low power 0W; Low time 90 msec,
Etch rate AZ5214	40-50 nm/min,
Etch rate Oxide	26 nm/min.

Bibliography

[1] W. Bogaerts, S. Selvaraja, P. Dumon, J. Brouckaert, K. De Vos, D. Van Thourhout, and R. Baets, "Silicon-on-insulator spectral filters fabricated with cmos technology," *Selected Topics in Quantum Electronics, IEEE Journal of*, vol. 16, no. 1, pp. 33–44, 2010. DOI:10.1109/JSTQE.2009.2039680

[2] W. Shi, X. Wang, W. Zhang, H. Yun, C. Lin, L. Chrostowski, and N. A. F. Jaeger, "Grating-coupled silicon microring resonators," *Applied Physics Letters*, vol. 100, no. 12, p. 121118, 2012. DOI:10.1063/1.3696082

[3] F. P. Wieringa and R. A. Bezemer, "Ultrasound lumen cleaning technique," World A1 WO2 006 031 106 (A1), 9 13, 2005.

[4] Y. Hou, J.-S. Kim, S. Ashkenazi, M. O'Donnell, and L. J. Guo, "Optical generation of high frequency ultrasound using two-dimensional gold nanostructure," *Applied Physics Letters*, vol. 89, no. 9, 2006. DOI:10.1063/1.2344929

[5] B.-Y. Hsieh, S.-L. Chen, T. Ling, L. J. Guo, and P.-C. Li, "Integrated intravascular ultrasound and photoacoustic imaging scan head," *Optics Letters*, vol. 35, no. 17, pp. 2892–2894, Sep 2010. DOI:10.1364/OL.35.002892

[6] H. Won Baac, J. G. Ok, H. J. Park, T. Ling, S.-L. Chen, A. J. Hart, and L. Jay Guo, "Carbon nanotube composite optoacoustic transmitters for strong and high frequency ultrasound generation," *Applied Physics Letters*, vol. 97, no. 23, pp. 234 104–234 104–3, 2010. DOI:10.1063/1.3522833

[7] B.-Y. Hsieh, S.-L. Chen, T. Ling, L. J. Guo, and P.-C. Li, "All-optical scanhead for ultrasound and photoacoustic dual-modality imaging," *Optics Express*, vol. 20, no. 2, pp. 1588–1596, Jan 2012. DOI:10.1364/OE.20.001588

[8] K. Jansen, A. F. W. van der Steen, H. M. M. van Beusekom, J. W. Oosterhuis, and G. van Soest, "Intravascular photoacoustic imaging of human coronary atherosclerosis," *Optics Letters*, vol. 36, no. 5, pp. 597–599, Mar 2011. DOI:10.1364/OL.36.000597

[9] (2013, 11) Volcano corporation— ivus imaging: Overview. [Online]. http://eu.volcanocorp.com/products/ivus-imaging/

[10] C. D. Liapis, K. Balzer, F. Benedetti-Valentini, and J. Fernandes e Fernandes, *Vascular Surgery*, ser. European Manual of Medicine. Berlin: Springer, 2007.

[11] C. L. de Korte, H. H. G. Hansen, and A. F. W. van der Steen, "Vascular ultrasound for atherosclerosis imaging," *Interface Focus*, vol. 1, no. 4, pp. 565–575, 2011. DOI:10.1098/rsfs.2011.0024

[12] R. S. C. Cobbold, *Foundations of Biomedical Ultrasound*. New York: Oxford University Press, 2007.

[13] E. J. Alles, G. J. van Dijk, A. F. W. van der Steen, A. Gisolf, and K. W. A. van Dongen, "An axial array for three-dimensional intravascular ultrasound," in *Ultrasonics Symposium (IUS), 2012 IEEE International*, 2012, pp. 1153–1156. DOI:10.1109/ULTSYM.2012.0287

[14] J. Bryzek, S. Roundy, B. Bircumshaw, C. Chung, K. Castellino, J. R. Stetter, and M. Vestel, "Marvelous mems," *Circuits and Devices Magazine, IEEE*, vol. 22, no. 2, pp. 8–28, 2006. DOI:10.1109/MCD.2006.1615241

[15] A. A. Barlian, W.-T. Park, J. R. Mallon, A. J. Rastegar, and B. L. Pruitt, "Review: Semiconductor piezoresistance for microsystems," *Proceedings of the IEEE*, vol. 97, no. 3, pp. 513–552, March. DOI:10.1109/JPROC.2009.2013612

[16] D. Taillaert, W. Van Paepegem, J. Vlekken, and R. Baets, "A thin foil optical strain gage based on silicon-on-insulator microresonators," in *Proc. SPIE*, vol. 6619, 2007, p. 661914. DOI:10.1117/12.738412

[17] G. N. Pearson and P. E. Jessop, "Silicon-on-insulator interferometric strain sensor," in *Proc. SPIE (Photonics Packaging and Integration III)*, vol. 4997, Jun. 2003, p. 242. DOI:10.1117/12.476663

[18] Y. Amemiya, Y. Tanushi, T. Tokunaga, and S. Yokoyama, "Photoelastic effect in silicon ring resonators," *Japanese Journal of Applied Physics*, vol. 47, pp. 2910–2914, Apr. 2008. DOI:10.1143/JJAP.47.2910

[19] X. Zhao, J. M. Tsai, H. Cai, X. M. Ji, J. Zhou, M. H. Bao, Y. P. Huang, D. L. Kwong, and A. Q. Liu, "A nano-opto-mechanical pressure sensor via ring resonator," *Optics Express*, vol. 20, no. 8, pp. 8535–8542, Apr 2012. DOI:10.1364/OE.20.008535

[20] E. Hallynck and P. Bienstman, "Integrated optical pressure sensors in silicon-on-insulator," *Photonics Journal, IEEE*, vol. 4, no. 2, pp. 443–450, April. DOI:10.1109/JPHOT.2012.2189614

[21] S. M. C. Abdulla, P. J. Harmsma, R. A. Nieuwland, J. Pozo, M. Lemmen, H. Sadeghian, J. H. van den Berg, P. Bodis, and P. Buskens, "Soi based mechano-optical pressure sensor using a folded microring resonator," in *Proc. 9th Nanomechanical sensing workshop, NMC 2012*, Mumbai, India, Jun. 2012, pp. 80–81.

[22] K. Benaissa and A. Nathan, "IC compatible optomechanical pressure sensors using Mach-Zehnder interferometry," *Electron Devices, IEEE Transactions on*, vol. 43, no. 9, pp. 1571–1582, Sep 1996. DOI:10.1109/16.535351

[23] (2013, Aug) The history of the integrated circuit. Nobelprize.org. Nobel Media AB. [Online]. http://www.nobelprize.org/educational/physics/integrated_circuit/history/index.html

[24] P. Dumon, W. Bogaerts, A. Tchelnokov, J.-M. Fedeli, and R. Baets, "Silicon nanophotonics," *Future Fab International*, vol. 25, pp. 29–36, Apr. 2008.

[25] P. J. Harmsma, H. Sadeghian, S. M. C. Abdulla, and R. A. Nieuwland, "Wavelength noise in ring resonator sensors," in *Proceedings Symposium IEEE Photonics Society Benelux Chapter*, Mons, 2012.

[26] J. Pozo, P. Kumar, D. M. R. Lo Cascio, A. Khanna, P. Dumon, D. Delbeke, R. Baets, M. Fournier, J. Fedeli, L. Fulbert, L. Zimmermann, B. Tillack, H. Tian, T. Aalto, P. O"Brien, D. Deptuck, J. Xu, X. Zhang, and D. Gale, "Essential: Epixfab services specifically targeting (sme) industrial takeup of advanced silicon photonics," in *Transparent Optical Networks (ICTON), 2012 14th International Conference on*, 2012, pp. 1–3. DOI:10.1109/ICTON.2012.6254391

[27] H. Kogelnik, "2. theory of dielectric waveguides," in *Integrated Optics*, ser. Topics in Applied Physics. Springer Berlin Heidelberg, 1975, vol. 7, pp. 13–81. DOI:10.1007/BFb0103618

[28] D. Marcuse, *Theory of dielectrically optical waveguides*, 2nd ed. San Diego: Academic Press Inc, 1991.

[29] ——, *Light transmission optics*, 2nd ed. New York: Van nostrand reinhold company, 1982.

[30] E. A. J. Marcatili, "Dielectric rectangular waveguide and directional coupler for integrated optics," *The Bell System Technical Journal*, vol. 48, pp. 2071–2121, Mar. 1969.

[31] A. Hardy and W. Streifer, "Coupled mode theory of parallel waveguides," *Lightwave Technology, Journal of*, vol. 3, no. 5, pp. 1135–1146, Oct. 1985. DOI:10.1109/JLT.1985.1074291

[32] A. Hardy, "A unified approach to coupled-mode phenomena," *IEEE Journal of Quantum Electronics*, vol. 34, no. 7, pp. 1109–1116, Jul. 1998. DOI:10.1109/3.687851

[33] A. W. Sneyder and J. D. Love, *Optical Waveguide Theory.* London, United Kingdom: Chapman and Hall Ltd, 1983.

[34] E. A. J. Marcatili and S. E. Miller, "Improved relations describing directional control in electromagnetic wave guidance," *The Bell System Technical Journal*, vol. 48, pp. 2161–2188, Mar. 1969.

[35] A. Yariv, "Coupled-mode theory for guided-wave optics," *Quantum Electronics, IEEE Journal of*, vol. 9, no. 9, pp. 919–933, 1973. DOI:10.1109/JQE.1973.1077767

[36] A. Yariv and M. Nakamura, "Periodic structures for integrated optics," *IEEE Journal of Quantum Electronics*, vol. 13, no. 7, pp. 233–251, Jul. 1977. DOI:10.1109/JQE.1977.1069323

[37] W. Streifer, D. R. Scifres, and R. D. Burnham, "Analysis of grating-coupled radiation in gaas:gaalas lasers and waveguides," *IEEE Journal of Quantum Electronics*, vol. 12, no. 7, pp. 422–428, Jul. 1976. DOI:10.1109/JQE.1976.1069175

[38] R. G. Hunsperger, *Integrated Optics*, 5th ed. Berlin Heidelberg New York: Springer, 2002.

[39] G. T. Reed, Ed., *Silicon Photonics: The state of the art.* Chichester, UK: John Wiley & Sons Ltd, 2008.

[40] D. J. Griffiths, *Introduction to Electrodynamics*, third, international ed. New Jersey: Preice-Hall Inernational, Inc, 1999.

[41] (2013, Aug.) Photonics. Wikipedia. [Online]. http://en.wikipedia.org/wiki/Photonics

[42] R. C. Alferness, "Integrated optics: Technology and system applications converge," *Optics and Photonics News*, vol. 8, no. 9, p. 16, Sep 1997. DOI:10.1364/OPN.8.9.000016

[43] "Corning® SMF-28™ optical fiber: Product information," Corning Incorporated, April 2002.

[44] R. Soref and J. Lorenzo, "Single-crystal silicon: a new material for 1.3 and 1.6μm integrated-optical components," *Electronics Letters*, vol. 21, no. 21, pp. 953–954, October 1985. DOI:10.1049/el:19850673

[45] B. N. Kurdi and D. G. Hall, "Optical waveguides in oxygen-implanted buried-oxide silicon-on-insulator structures," *Optics Letters*, vol. 13, no. 2, pp. 175–177, Feb 1988. DOI:10.1364/OL.13.000175

[46] E. Cortesi, F. Namavar, and R. A. Soref, "Novel silicon-on-insulator structures for silicon waveguides," in *SOS/SOI Technology Conference, 1989., 1989 IEEE*, Oct 1989, p. 109. DOI:10.1109/SOI.1989.69790

[47] G. Abstreiter, "Engineering the future of electronics," *Physics World, UK*, vol. 5, pp. 36–39, Mar 1992.

[48] R. A. Soref, "Silicon-based optoelectronics," *Proceedings of the IEEE*, vol. 81, no. 12, pp. 1687–1706, Dec 1993. DOI:10.1109/5.248958

[49] L. Vivien and L. Pavesi, Eds., *Handbook of Silicon Photonics.* Boca Raton, Forida, USA: Taylor & Francis, 2013.

[50] J. Rattner. (2013, May) Keynote at intel developer forum bejing 2013. [Online]. http://www.intel.com/content/www/us/en/research/intel-labs-idf2013-justin-rattner.html

[51] S. Assefa, S. Shank, W. Green, M. Khater, E. Kiewra, C. Reinholm, S. Kamlapurkar, A. Rylyakov, C. Schow, F. Horst, H. Pan, T. Topuria, P. Rice, D. Gill, J. Rosenberg, T. Barwicz, M. Yang, J. Proesel, J. Hofrichter, B. Offrein, X. Gu, W. Haensch, J. Ellis-Monaghan, and Y. Vlasov, "A 90nm cmos integrated nano-photonics technology for 25gbps wdm optical communications applications," in *Electron Devices Meeting (IEDM), 2012 IEEE International*, 2012, pp. 33.8.1–33.8.3. DOI:10.1109/IEDM.2012.6479162

[52] Y. Vlasov, "Silicon cmos-integrated nano-photonics for computer and data communications beyond 100g," *Communications Magazine, IEEE*, vol. 50, no. 2, pp. s67–s72, 2012. DOI:10.1109/MCOM.2012.6146487

[53] "Quad small form-factor pluggable plus (qsfp+) psm4 active optical cables (product brochure)," Molex, Lisle, Illinois, USA, 2013. [Online]. http://www.molex.com

[54] (2013, 12) Crx - integrated coherent receiver (product brochure). Teraxion. [Online]. http://www.teraxion.com/en/crx

[55] Y. Painchaud, M. Poulin, J.-F. Gagne, and C. Paquet, "Ultra-compact si-photonic dqpsk demodulator," in *Optical Fiber Communication Conference and Exposition (OFC/NFOEC), 2012 and the National Fiber Optic Engineers Conference*, 2012.

[56] S. Assefa, F. Xia, W. M. J. Green, C. Schow, A. Rylyakov, and Y. Vlasov, "Cmos-integrated optical receivers for on-chip interconnects," *Selected Topics in Quantum Electronics, IEEE Journal of*, vol. 16, no. 5, pp. 1376–1385, 2010. DOI:10.1109/JSTQE.2010.2048306

[57] S. Assefa, F. Xia, and Y. A. Vlasov, "Reinventing germanium avalanche photodetector for nanophotonic on-chip optical interconnects," *Nature*, vol. 464, no. 4, pp. 80–85, Mar. 2010.

[58] J. Michel, J. Liu, and L. C. Kimerling, "High-performance ge-on-si photodetectors," *Nature Photonics*, vol. 4, pp. 527–534, 8 2010. DOI:10.1038/nphoton.2010.157

[59] D. Liang and J. E. Bowers, "Recent progress in lasers on silicon," *Nature Photonics*, vol. 4, pp. 511–517, 8 2010. DOI:10.1038/nphoton.2010.167

[60] M. Heck, J. Bauters, M. Davenport, J. Doylend, S. Jain, G. Kurczveil, S. Srinivasan, Y. Tang, and J. Bowers, "Hybrid silicon photonic integrated circuit technology," *Selected Topics in Quantum Electronics, IEEE Journal of*, vol. 19, no. 4, pp. 6 100 117–6 100 117, 2013. DOI:10.1109/JSTQE.2012.2235413

[61] G. Roelkens, L. Liu, D. Liang, R. Jones, A. Fang, B. Koch, and J. Bowers, "Iii-v/silicon photonics for on-chip and intra-chip optical interconnects," *Laser & Photonics Reviews*, vol. 4, pp. 751–779, 2010. DOI:10.1002/lpor.200900033

[62] K. Bourzac, "Photonic chips made easier," *Nature*, vol. 483, p. 388, Mar. 2012. DOI:10.1038/483388a

[63] "Imec SiPhotonics process handbook - release 0.1," distributed with ePIXfab IMEC08 Design Kit, IMEC-Ghent University, 3 2011.

[64] S. K. Selvaraja, W. Bogaerts, and D. V. Thourhout, "Loss reduction in silicon nanophotonic waveguide micro-bends through etch profile improvement," *Optics Communications*, vol. 284, no. 8, pp. 2141 – 2144, 2011. DOI:10.1016/j.optcom.2010.12.086

[65] F. Morichetti, A. Canciamilla, M. Martinelli, A. Samarelli, R. M. De La Rue, M. Sorel, and A. Melloni, "Coherent backscattering in optical microring resonators," *Applied Physics Letters*, vol. 96, no. 8, p. 081112, 2010. DOI:10.1063/1.3330894

[66] J. Leuthold, C. Koos, and W. Freude, "Nonlinear silicon photonics," *Nature photonics*, vol. 4, pp. 535–544, July 2010.

[67] G. T. Reed and A. P. Knights, *Silicon Photonics: An Introduction*. Chichester, UK: John Wiley & Sons Ltd, 2004.

[68] G. Woan, *The Cambridge Handbook of Physics Formulas*. Cambridge: Cambrige University Press, 2000.

[69] E. W. Weisstein. (2013, Aug.) Divergence theorem. MathWorld–A Wolfram Web Resource. [Online]. http://mathworld.wolfram.com/DivergenceTheorem.html

[70] W. J. Westerveld, S. M. Leinders, K. W. A. van Dongen, H. P. Urbach, and M. Yousefi, "Extension of marcatili's analytical approach for rectangular silicon optical waveguides," *Lightwave Technology, Journal of*, vol. 30, no. 14, pp. 2388–2401, 2012. DOI:10.1109/JLT.2012.2199464

[71] W. J. Westerveld, S. M. Leinders, K. W. A. van Dongen, M. Yousefi, and H. P. Urbach, "Extension of marcatili's analytical approach for 220 nm high waveguides in soi technology," in *Annual Symposium of the IEEE Photonics Society Benelux Chapter*, Mons, Belgium, Nov. 2012, pp. 25–28.

[72] T. Aalto, "Microphotonic silicon waveguide components," Ph.D. dissertation, Helsinki University of Technology, Espoo, Finland, Dec. 2004, published by VTT Information Technology. [Online]. http://aaltodoc.aalto.fi

[73] A. Melloni, D. Roncelli, F. Morichetti, A. Canciamilla, and A. Bakker, "Statistical design in integrated optics," in *CLEO/Europe and EQEC 2009 Conference Digest*. Optical Society of America, 2009, p. JSI1_4.

[74] W. J. Westerveld. (2013, Mar.) RECTWG: Matlab implementation of the extended marcatili approaches for rectangular silicon optical waveguides (free open-source software). Distributed in *RECTWG package for Matlab – Version 0.1*. Delft University of Technology. [Online]. http://waveguide.sourceforge.net

[75] L. D. Landau and E. M. Lifshitz, *Quantum Mechanics*, 3rd ed. Pergamon Press Ltd., 1977, sec. 79.

[76] "Material database and material models," distributed with FimmWave software package, Photon Design Ltd, Oxford, United Kingdom, Jan. 2011.

[77] A. S. Sudbo, "Improved formulation of the film mode matching method for mode field calculations in delectric waveguides," *Pure and Applied Optics: Journal of the European Optical Society Part A*, vol. 3, pp. 381–388, 1994. DOI:10.1088/0963-9659/3/3/021

[78] Photon Design (Oxford, UK). (2012, 9) Fimmwave, a powerful waveguide mode solver. [Online]. http://www.photond.com/products/fimmwave.htm

[79] W. Bogaerts, P. De Heyn, T. Van Vaerenbergh, K. De Vos, S. Kumar Selvaraja, T. Claes, P. Dumon, P. Bienstman, D. Van Thourhout, and R. Baets, "Silicon microring resonators," *Laser & Photonics Reviews*, vol. 6, no. 1, pp. 47–73, 2012. DOI:10.1002/lpor.201100017

[80] A. Taflove and S. C. Hagness, *Computational Electrodynamics: The Finite Difference Time Domain Method*, 3rd ed. Norwood, Massachusetts, USA: Artech House, Inc, 2005.

[81] O. Janssen, "Rigorous simulations of emitting and non-emitting nano-optical structures," Ph.D. dissertation, Technische Universiteit Delft, Delft, Nov. 2010.

[82] *CrystalWave Manual*, Version 4.5 ed., Photon Design, Oxford, UK, 2010.

[83] A. Yariv and P. Yeh, *Photonics: optical electronics in modern communications*, ser. The Oxford Series in Electrical and Computer Engineering Series. Oxford University Press, Incorporated, 2007.

[84] A. Hardy and M. Ben-Artzi, "Expansion of an arbitrary field in terms of waveguide modes," *Optoelectronics, IEE Proceedings -*, vol. 141, no. 1, pp. 16–20, Feb. 1994. DOI:10.1049/ip-opt:19949691

[85] M. L. Dakss, L. Kuhn, P. F. Heidrich, and B. A. Scott, "Grating coupler for efficient excitation of optical guided waves in thin films," *Applied Physics Letters*, vol. 16, no. 12, pp. 523–525, Jun. 1970. DOI:10.1063/1.1653091

[86] D. Taillaert, W. Bogaerts, P. Bienstman, T. Krauss, P. van Daele, I. Moerman, S. Verstuyft, K. de Mesel, and R. Baets, "An out-of-plane grating coupler for efficient butt-coupling between compact planar waveguides and single-mode fibers," *IEEE Journal of Quantum Electronics*, vol. 38, no. 7, pp. 949–955, Jul. 2002. DOI:10.1109/JQE.2002.1017613

[87] D. Taillaert, F. van Laere, M. Ayre, W. Bogaerts, D. van Thourhout, P. Bienstman, and R. Baets, "Grating couplers for coupling between optical fibers and nanophotonic waveguides," *Japanese Journal of Applied Physics*, vol. 45, no. 8A, pp. 6071–6077, Aug. 2006. DOI:10.1143/JJAP.45.6071

[88] G. Roelkens, D. Vermeulen, S. Selvaraja, R. Halir, W. Bogaerts, and D. Van Thourhout, "Grating-based optical fiber interfaces for silicon-on-insulator photonic integrated circuits," *Selected Topics in Quantum Electronics, IEEE Journal of*, vol. 17, no. 3, pp. 571–580, 2011. DOI:10.1109/JSTQE.2010.2069087

[89] W. J. Westerveld, H. P. Urbach, and M. Yousefi, "Optimized 3-d simulation method for modeling out-of-plane radiation in silicon photonic integrated circuits," *Quantum Electronics, IEEE Journal of*, vol. 47, no. 5, pp. 561–568, May 2011. DOI:10.1109/JQE.2010.2099645

[90] J. Goodman, *Introduction to Fourier Optics.* New York: McGraw-Hill Book Co., 1968.

[91] F. Shen and A. Wang, "Fast-fourier-transform based numerical integration method for the rayleigh-sommerfeld diffraction formula," *Applied Optics*, vol. 45, no. 6, pp. 1102–1110, Feb. 2006. DOI:10.1364/AO.45.001102

[92] D. Gisolf and E. Verschuur, *The Principles of Quantitative Acoustical Imaging.* Houten, The Netherlands: Eagle Publications B.V., 2010.

[93] D. Taillaert, P. Bienstman, and R. Baets, "Compact efficient broadband grating coupler for silicon-on-insulator waveguides," *Optics Letters*, vol. 29, no. 23, pp. 2749–2751, Dec. 2004.

[94] D. Vermeulen, S. Selvaraja, P. Verheyen, G. Lepage, W. Bogaerts, P. Absil, D. V. Thourhout, and G. Roelkens, "High-efficiency fiber-to-chip grating couplers realized using an advanced cmos-compatible silicon-on-insulator platform," *Optics Express*, vol. 18, no. 17, pp. 18 278–18 283, Aug. 2010. DOI:10.1364/OE.18.018278

[95] X. Chen, C. Li, C. Fung, S. Lo, and H. Tsang, "Apodized waveguide grating couplers for efficient coupling to optical fibers," *Photonics Technology Letters, IEEE*, vol. 22, no. 15, pp. 1156–1158, Aug. 2010. DOI:10.1109/LPT.2010.2051220

[96] F. Van Laere, W. Bogaerts, D. Taillaert, P. Dumon, D. Van Thourhout, and R. Baets, "Compact focusing grating couplers between optical fibers and silicon-on-insulator photonic wire waveguides," in *Optical*

Fiber Communication and the National Fiber Optic Engineers Conference, 2007. OFC/NFOEC 2007. Conference on, 2007, pp. 1–3. DOI:10.1109/OFC.2007.4348869

[97] D. Vermeulen, Y. D. Koninck, Y. Li, E. Lambert, W. Bogaerts, R. Baets, and G. Roelkens, "Reflectionless grating couplers for silicon-on-insulator photonic integrated circuits," *Optics Express*, vol. 20, no. 20, pp. 22 278–22 283, Sep. 2012. DOI:10.1364/OE.20.022278

[98] Y. Li, D. Vermeulen, Y. D. Koninck, G. Yurtsever, G. Roelkens, and R. Baets, "Compact grating couplers on silicon-on-insulator with reduced backreflection," *Opt. Lett.*, vol. 37, no. 21, pp. 4356–4358, Nov 2012. DOI:10.1364/OL.37.004356

[99] Y. Li, L. Li, B. Tian, G. Roelkens, and R. Baets, "Reflectionless tilted grating couplers with improved coupling efficiency based on a silicon overlay," *Photonics Technology Letters, IEEE*, vol. 25, no. 13, pp. 1195–1198, Jul. 2013. DOI:10.1109/LPT.2013.2261484

[100] A. Yariv, "Universal relations for coupling of optical power between microresonators and dielectric waveguides," *Electronics Letters*, vol. 36, no. 4, pp. 321 –322, feb 2000. DOI:10.1049/el:20000340

[101] L.-W. Lee, N. Ophir, C. Chen, L. H. Gabrielli, C. B. Poitras, K. Bergman, , and M. Lipson, "Simultaneous mode and wavelength division multiplexing on-chip," Jun 2013, arXiv:1306.2378 [physics.optics]. [Online]. http://arxiv.org/abs/1306.2378

[102] G. T. Reed, G. Mashanovich, F. Y. Gardes, and D. J. Thomson, "Silicon optical modulators," *Nature Photonics*, no. 4, pp. 518 – 526, Jul 2010. DOI:10.1038/nphoton.2010.179

[103] K. D. Vos, J. Girones, S. Popelka, E. Schacht, R. Baets, and P. Bienstman, "{SOI} optical microring resonator with poly(ethylene glycol) polymer brush for label-free biosensor applications," *Biosensors and Bioelectronics*, vol. 24, no. 8, pp. 2528 – 2533, 2009. DOI:10.1016/j.bios.2009.01.009

[104] S. Feng, T. Lei, H. Chen, H. Cai, X. Luo, and A. Poon, "Silicon photonics: from a microresonator perspective," *Laser & Photonics Reviews*, vol. 6, no. 2, pp. 145–177, 2012. DOI:10.1002/lpor.201100020

[105] A. Melloni, A. Canciamilla, C. Ferrari, F. Morichetti, L. O'Faolain, T. F. Krauss, R. De La Rue, A. Samarelli, and M. Sorel, "Tunable delay lines in silicon photonics: Coupled resonators and photonic crystals, a comparison," *Photonics Journal, IEEE*, vol. 2, no. 2, pp. 181–194, April 2010.

[106] F. Morichetti, C. Ferrari, A. Canciamilla, and A. Melloni, "The first decade of coupled resonator optical waveguides: bringing slow light to applications," *Laser & Photonics Reviews*, vol. 6, no. 1, pp. 74–96, 2012. [Online]. http://dx.doi.org/10.1002/lpor.201100018. DOI:10.1002/lpor.201100018

[107] W. Bogaerts and S. Selvaraja, “Compact single-mode silicon hybrid rib/strip waveguide with adiabatic bends,” *Photonics Journal, IEEE*, vol. 3, no. 3, pp. 422–432, 2011. DOI:10.1109/JPHOT.2011.2142931

[108] W. Bogaerts, “Nanophotonic waveguides and photonic crystals in silicon-on-insulator,” Ph.D. dissertation, Universiteit Gent, Belgium, April 2004.

[109] P. Dumon, “Ultra-compact integrated optical filters in silicon-on-insulator by means of wafer-scale technology,” Ph.D. dissertation, Universiteit Gent, Belgium, March 2007.

[110] K. de Vos, “Label-free silicon photonics biosensor platform with microring resonators,” Ph.D. dissertation, Universiteit Gent, Belgium, April 2010.

[111] S. Darmawan, L. Y. M. Tobing, and T. Mei, “Coupling-induced phase shift in a microring-coupled mach-zehnder interferometer,” *Opt. Lett.*, vol. 35, no. 2, pp. 238–240, Jan 2010. DOI:10.1364/OL.35.000238

[112] M. Popovic, C. Manolatou, and M. Watts, “Coupling-induced resonance frequency shifts in coupled dielectric multi-cavity filters,” *Optics Express*, vol. 14, no. 3, pp. 1208–1222, Feb. 2006. DOI:10.1364/OE.14.001208

[113] J. Orloff, Ed., *Handbook of Charged Particle Optics.* Boca Raton, Florida, USA: CRC Press, Taylor & Francis Group, 2009.

[114] D. J. Maas, E. W. Van Der Drift, E. Van Veldhoven, J. Meessen, M. Rudneva, and P. F. A. Alkemade, “Nano-engineering with a focused helium ion beam,” in *Materials Research Society Symposium Proceedings*, vol. 1354, 2012, pp. 33–46. DOI:10.1557/opl.2011.1407

[115] P. F. A. Alkemade, E. M. Koster, E. van Veldhoven, and D. J. Maas, “Imaging and nanofabrication with the helium ion microscope of the van leeuwenhoek laboratory in delft,” *Scanning*, vol. 34, no. 2, pp. 90–100, 2012. DOI:10.1002/sca.21009

[116] P. Dumon, Sep 2013, private communications.

[117] M. Heck, “On the fabry-pérot fringes in transmission and insertion loss measurements,” Jan 2013, private communications.

[118] T. O’Haver. (2012, 9) Findpeaks matlab function by Tom O’Haver. [Online]. http://terpconnect.umd.edu/~toh/

[119] J. J. Moré, “The levenberg-marquardt algorithm: Implementation and theory,” in *Numerical Analysis*, ser. Lecture Notes in Mathematics, G. Watson, Ed. Springer Berlin Heidelberg, 1978, vol. 630, pp. 105–116. DOI:10.1007/BFb0067700

[120] L. Zhuang, M. Hoekman, W. Beeker, A. Leinse, R. Heideman, P. van Dijk, and C. Roeloffzen, “Novel low-loss waveguide delay lines using

vernier ring resonators for on-chip multi- microwave photonic signal processors," *Laser & Photonics Reviews*, vol. 7, no. 6, pp. 994–1002, 2013. DOI:10.1002/lpor.201300053

[121] A. Llobera, J. A. Plaza, I. Salinas, J. Berganzo, J. Garcia, J. Esteve, and C. Domínguez, "Technological aspects on the fabrication of silicon-based optical accelerometer with arrow structures," *Sensors and Actuators A: Physical*, vol. 110, p. 395400, Feb 2004. DOI:10.1016/j.sna.2003.10.053

[122] M. A. Hopcroft, W. D. Nix, and T. W. Kenny, "What is the young"s modulus of silicon?" *IEEE/ASME Journal of Microelectromechanical Systems*, vol. 19, no. 2, pp. 229–238, Apr. 2010. DOI:10.1109/JMEMS.2009.2039697

[123] J. Gere and S. Timoshenko, *Mechanics of Materials*, 4th SI ed. London: Stanley Thornes, 1999.

[124] S. Timoshenko and S. Woinowsky-Krieger, *Theory of Plates and Shells*, 2nd Reissued ed. New York: McGraw-Hill, 1987.

[125] S. E. Angad Gaur and E. Lagendijk, "Inleiding practicum technische natuurwetenschappen," Lecture notes, Delft University of Technology, Faculty of Applied Sciences, Delft, The Netherlands, 2002, English title: Introduction Practicals Applied Sciences. These lecture notes follows the Guide to the Expression of Uncertainty in Measurement (ISO/IEC Guide 98:1993).

[126] C. W. Wong, P. T. Rakich, S. G. Johnson, M. Qi, H. I. Smith, E. P. Ippen, L. C. Kimerling, Y. Jeon, G. Barbastathis, and S.-G. Kim, "Strain-tunable silicon photonic band gap microcavities in optical waveguides," *Applied Physics Letters*, vol. 84, no. 8, pp. 1242–1244, 2004. DOI:10.1063/1.1649803

[127] B. T. Tung, H. M. Nguyen, D. V. Dao, S. Rogge, H. W. M. Salemink, and S. Sugiyama, "Strain sensitive effect in a triangular lattice photonic crystal hole-modified nanocavity," *Sensors Journal, IEEE*, vol. 11, no. 11, pp. 2657–2663, 2011. DOI:10.1109/JSEN.2011.2157122

[128] W. N. Ye, D.-X. Xu, S. Janz, P. Cheben, M.-J. Picard, B. Lamontagne, and N. G. Tarr, "Birefringence control using stress engineering in silicon-on-insulator (soi) waveguides," *Lightwave Technology, Journal of*, vol. 23, no. 3, pp. 1308–1318, 2005. DOI:10.1109/JLT.2005.843518

[129] L. Fan, L. T. Varghese, Y. Xuan, J. Wang, B. Niu, and M. Qi, "Direct fabrication of silicon photonic devices on a flexible platform and its application for strain sensing," *Optics Express*, vol. 20, no. 18, pp. 20 564–20 575, 2012. DOI:10.1364/OE.20.020564

[130] R. S. Jacobsen, K. N. Andersen, P. I. Borel, J. Fage-Pedersen, L. H. Frandsen, O. Hansen, M. Kristensen, A. V. Lavrinenko, G. Moulin, H. Ou, C. Peucheret, B. Zsigri, and A. Bjarklev, "Strained silicon as a new electro-optic material," *Nature*, vol. 441, pp. 199–202, 2006. DOI:10.1038/nature04706

[131] M. Cazzanelli, F. Bianco, E. Borga, G. Pucker, M. Ghulinyan, E. Degoli, E. Luppi, V. Vniard, S. Ossicini, D. Modotto, S. Wabnitz, R. Pierobon, and L. Pavesi, "Second-harmonic generation in silicon waveguides strained by silicon nitride," *Nature Materials*, vol. 84, pp. 148–154, 2012. DOI:10.1038/nmat3200

[132] B. T. Khuri-Yakub and O. Oralkan, "Capacitive micromachined ultrasonic transducers for medical imaging and therapy," *Journal of Micromechanics and Microengineering*, vol. 21, no. 5, p. 054004, 2011. DOI:doi:10.1088/0960-1317/21/5/054004

[133] D. Lemmerhirt, X. Cheng, R. White, C. Rich, M. Zhang, J. Fowlkes, and O. Kripfgans, "A 32 x 32 capacitive micromachined ultrasonic transducer array manufactured in standard cmos," *Ultrasonics, Ferroelectrics and Frequency Control, IEEE Transactions on*, vol. 59, no. 7, pp. 1521–1536, 2012. DOI:10.1109/TUFFC.2012.2352

[134] I. Wygant, "A comparison of cmuts and piezoelectric transducer elements for 2d medical imaging based on conventional simulation models," in *Ultrasonics Symposium (IUS), 2011 IEEE International*, 2011, pp. 100–103. DOI:10.1109/ULTSYM.2011.0025

[135] P. Morris, A. Hurrell, A. Shaw, E. Zhang, and P. Beard, "A fabry-pérot fiber-optic ultrasonic hydrophone for the simultaneous measurement of temperature and acoustic pressure," *The Journal of the Acoustical Society of America*, vol. 125, no. 6, pp. 3611–3622, 2009. DOI:10.1121/1.3117437

[136] G. Wild and S. Hinckley, "Acousto-ultrasonic optical fiber sensors: Overview and state-of-the-art," *Sensors Journal, IEEE*, vol. 8, no. 7, pp. 1184–1193, 2008. DOI:10.1109/JSEN.2008.926894

[137] S. Ashkenazi, C.-Y. Chao, L. J. Guo, and M. O'Donnell, "Ultrasound detection using polymer microring optical resonator," *Applied Physics Letters*, vol. 85, no. 22, pp. 5418–5420, 2004. DOI:10.1063/1.1829775

[138] C.-Y. Chao, S. Ashkenazi, S.-W. Huang, M. O'Donnell, and L. Guo, "High-frequency ultrasound sensors using polymer microring resonators," *Ultrasonics, Ferroelectrics and Frequency Control, IEEE Transactions on*, vol. 54, no. 5, pp. 957–965, 2007. DOI:10.1109/TUFFC.2007.341

[139] S.-W. Huang, S.-L. Chen, T. Ling, A. Maxwell, M. O'Donnell, L. J. Guo, and S. Ashkenazi, "Low-noise wideband ultrasound detection using polymer microring resonators," *Applied Physics Letters*, vol. 92, no. 19, 2008. DOI:10.1063/1.2929379

[140] A. Maxwell, S.-W. Huang, T. Ling, J.-S. Kim, S. Ashkenazi, and L. Jay Guo, "Polymer microring resonators for high-frequency ultrasound detection and imaging," *Selected Topics in Quantum Electronics, IEEE Journal of*, vol. 14, no. 1, pp. 191–197, 2008. DOI:10.1109/JSTQE.2007.914047

[141] T. Ling, S.-L. Chen, and L. J. Guo, "High-sensitivity and wide-directivity ultrasound detection using high q polymer microring resonators," *Applied Physics Letters*, vol. 98, no. 20, 2011. DOI:10.1063/1.3589971

[142] ——, "Fabrication and characterization of high q polymer micro-ring resonator and its application as a sensitive ultrasonic detector," *Optics Express*, vol. 19, no. 2, pp. 861–869, Jan 2011. DOI:10.1364/OE.19.000861

[143] A. Rosenthal, M. Omar, H. Estrada, S. Kellnberger, D. Razansky, and V. Ntziachristos, "Embedded ultrasound sensor in a silicon-on-insulator photonic platform," *Applied Physics Letters*, vol. 104, no. 2, 2014. DOI:10.1063/1.4860983

[144] G. N. De Brabander, J. T. Boyd, and G. Beheim, "Integrated optical ring resonator with micromechanical diaphragms for pressure sensing," *Photonics Technology Letters, IEEE*, vol. 6, no. 5, pp. 671–673, 1994. DOI:10.1109/68.285575

[145] W. Xia, D. Piras, J. C. G. van Hespen, S. van Veldhoven, C. Prins, T. G. van Leeuwen, W. Steenbergen, and S. Manohar, "An optimized ultrasound detector for photoacoustic breast tomography," *Medical Physics*, vol. 40, no. 3, p. 032901, 2013. DOI:10.1118/1.4792462

[146] L. B. Soldano and E. C. M. Pennings, "Optical multi-mode interference devices based on self-imaging: principles and applications," *Lightwave Technology, Journal of*, vol. 13, no. 4, pp. 615–627, 1995. DOI:10.1109/50.372474

[147] D. J. Thomson, Y. Hu, G. T. Reed, and J.-M. Fedeli, "Low loss MMI couplers for high performance MZI modulators," *Photonics Technology Letters, IEEE*, vol. 22, no. 20, pp. 1485–1487, 2010.

[148] P. Dumon, G. R. A. Priem, L. R. Nunes, W. Bogaerts, D. V. Thourhout, P. Bienstman, T. K. Liang, M. Tsuchiya, P. Jaenen, S. Beckx, J. Wouters, and R. Baets, "Linear and nonlinear nanophotonic devices based on silicon-on-insulator wire waveguides," *Japanese Journal of Applied Physics*, vol. 45, no. 8B, pp. 6589–6602, Aug. 2006. DOI:10.1143/JJAP.45.6589

[149] C. Holmes, L. G. Carpenter, J. C. Gates, and P. G. R. Smith, "Miniaturization of bragg-multiplexed membrane transducers," *Journal of Micromechanics and Microengineering*, vol. 22, no. 2, p. 025017, 2012. DOI:10.1088/0960-1317/22/2/025017

[150] A. Gondarenko, J. S. Levy, and M. Lipson, "High confinement micron-scale silicon nitride high q ring resonator," *Optics Express*, vol. 17, no. 14, pp. 11 366–11 370, Jul 2009. DOI:10.1364/OE.17.011366

[151] (2014, 1) Triplex mpw. LioniX BV. [Online]. http://www.lionixbv.com/triplexmpw.html

[152] A. W. Leissa, *Vibrations of plates*. Washington D.C.: National aeronautics and space administration U.S.A., 1969.

[153] K. F. Graff, *Wave Motion in Elastic Solids*. New York: Dover Publications, 1991.

[154] M. K. Kwak, "Vibration of circular membranes in contact with fluid," *Journal of Sound and Vibration*, vol. 178, pp. 688–690, 1994. DOI:10.1006/jsvi.1994.1516

[155] J. Huijssen, "Modeling of nonlinear medical diagnostic ultrasound," Ph.D. dissertation, Technische Universiteit Delft, Delft, Oct. 2008.

[156] P. J. Harmsma, J.-P. Staats, D. M. R. Lo Cascio, and L. K. Cheng, "Three-port interferometer in silicon-on-insulator for wavelength monitoring and displacement measurement," in *Lasers and Electro-Optics Europe (CLEO EUROPE/EQEC), 2011 Conference on and 12th European Quantum Electronics Conference*, M unchen, 2011. DOI:10.1109/CLEOE.2011.5943282

[157] C. Mesaritakis, A. Argyris, E. Grivas, A. Kapsalis, and D. Syvridis, "Adaptive interrogation for fast optical sensing based on cascaded micro-ring resonators," *Sensors Journal, IEEE*, vol. 11, no. 7, pp. 1595–1601, 2011. DOI:10.1109/JSEN.2010.2086057

[158] N. Yebo, W. Bogaerts, Z. Hens, and R. Baets, "On-chip arrayed waveguide grating interrogated silicon-on-insulator microring resonator-based gas sensor," *Photonics Technology Letters, IEEE*, vol. 23, no. 20, pp. 1505–1507, 2011. DOI:10.1109/LPT.2011.2162825

[159] J. Song, L. Wang, L. Jin, X. Xia, Q. Kou, S. Bouchoule, and J.-J. He, "Intensity-interrogated sensor based on cascaded fabry-perot laser and microring resonator," *Lightwave Technology, Journal of*, vol. 30, no. 17, pp. 2901–2906, 2012. DOI:10.1109/JLT.2012.2209401

[160] T. Claes, W. Bogaerts, and P. Bienstman, "Vernier-cascade label-free biosensor with integrated arrayed waveguide grating for wavelength interrogation with low-cost broadband source," *Optics Letters*, vol. 36, no. 17, pp. 3320–3322, Sep. 2011. DOI:10.1364/OL.36.003320

[161] L. Jin, M. Li, and J.-J. He, "Optical waveguide double-ring sensor using intensity interrogation with a low-cost broadband source," *Optics Letters*, vol. 36, no. 7, pp. 1128–1130, Apr. 2011. DOI:10.1364/OL.36.001128

[162] X. Yang, D. Lorenser, R. A. McLaughlin, R. W. Kirk, M. Edmond, M. C. Simpson, M. D. Grounds, and D. D. Sampson, "Imaging deep skeletal muscle structure using a high-sensitivity ultrathin side-viewing optical coherence tomography needle probe," *Biomedical Optics Express*, vol. 5, no. 1, pp. 136–148, Jan 2014. DOI:10.1364/BOE.5.000136

[163] W. Bogaerts, Nov 2013, private communications.

List of acronyms

1D	One dimensional
2D	Two dimensional
3D	Three dimensional
III-V	Material compounds with elements of group III and group IV of the periodic table of elements (e.g., indium phosphide, gallium arsenide).
AC	Alternating Current
ADC	Analog to digital converter
AFM	Atomic force microscope
ASE	Amplified spontaneous emission
AWG	Arbitrary waveform generator
BOX	Buried oxide layer
C-band	wavelength range 1530-1565 nm
CMOS	Complementary Metal Oxide Semiconductor
cMUT	Capacitive micro-machined ultrasound transducer
COAX	Coaxial wire
CPU	Central processing unit
DBR	Distributed Bragg reflector
DC	Direct current
DFB	Distributed feedback
DCM1	Directional coupler characterization method 1 (see Sec. 3.6)
DRIE	Deep reactive ion etching
DRC	Design rule check
EIM	Effective index method
EMI	Electromagnetic interference
EME	Eigenmode expansion method
EU	European union
FDTD	Finite difference time domain
FEM	Finite element method
FFT	Fast Fourier transform
FMM	Film mode-matching method
FWHM	Full-width at half-max
FSR	Free spectral range

GDSII	Graphic Database System file format II, owned by Cadence Design Systems (San Jose, California, USA)
HIM	Helium ion microscope
IC	Integrated circuit
IPA	isopropylalcohol
IVUS	Intravascular ultrasonography
MC	Medical center
m.e.	Maximum of the envelope of
MEMS	Micro electro-mechanical system
MRI	Magnetic resonance imaging
MUT	Micro-machined ultrasound transducer
NDT	Nondestructive testing
NEP	Noise equivalent pressure
OSA	Optical spectrum analyzer
PECVD	Plasma enhanced chemical vapor deposition
PIC	Photonic integrated circuit
Q-factor	Quality factor
RF	Radio frequency
RMS	Root mean square
SiO_2	Silicon dioxide
SNR	Signal to noise ratio
SOI	Silicon on insulator
TE	Transverse electric
TM	Transverse magnetic
UV	Ultraviolet
WDM	Wavelength division multiplexing

About the author

Wouter Jan Westerveld (Wouter) was born on Easter Monday April 23, 1984, in Goes, a city in the Province of Zeeland in the southwestern Netherlands. In Goes, he followed primary education at the Prinses Ireneschool and he followed secondary education at the highest level (VWO) at the Buys Ballot College. He went to Delft University of Technology to study applied physics and he received the Master of Science degree, cum laude, in 2009. He spent five months in 2007 as exchange student at Queens University Belfast, Northern Ireland, via the Erasmus Programme. He worked in the fields of sound control (B.Sc. thesis project), ultrasonic imaging for non-destructive testing (M.Sc. industrial internship at Applus RTD, Rotterdam), and silicon integrated photonics (M.Sc. thesis project at TNO, Delft). In September 2009, he started his Ph.D. research as collaboration between the integrated nano-photonics activity of lead scientist dr. Mirvais Yousefi at TNO and the Optics Research Group of prof. Paul Urbach at Delft University of Technology. This research has led to this Thesis.

He has had various part-time and summer jobs such as freelance web-designer and web-developer, programmer at TNO Building and Construction in Delft, and researcher at Varibel BV in Arnhem, where he continued his B.Sc. project until implementation in high-tech hearing aids. As of January, he holds the position of laser scientist at Mach8 Lasers in Breda.

Ir. Westerveld was member of the board of the Student Association for Applied Physics Students at Delft University of Technology from 2004 to 2005 (Vereniging voor Technische Physica). He was Secretary (2011) and Chairman (2012) of the Student Board of the IEEE Photonics Society Benelux Chapter. He is certified Project Management Associate (IPMA Level D).

Wouter has two “little” sisters and he lives with his girlfriend Mirjam in The Hague where they own a house nearby the sea.

Publications of the author

Journal publications

- W. J. Westerveld, J. Pozo, S. M. Leinders, M. Yousefi, and H. P. Urbach, "Demonstration of large coupling-induced phase delay in silicon directional cross-couplers," *IEEE Journal of Selected Topics in Quantum Electronics*, vol. 20, no. 4, 2014, *to appear*. DOI:10.1109/JSTQE.2013.2292874

- W. J. Westerveld, S. M. Leinders, P. M. Muilwijk, J. Pozo, T. C. van den Dool, M. D. Verweij, M. Yousefi, and H. P. Urbach, "Characterization of integrated optical strain sensors based on silicon waveguides," *IEEE Journal of Selected Topics in Quantum Electronics*, vol. 20, no. 4, 2014, *to appear*. DOI:10.1109/JSTQE.2013.2289992

- W. J. Westerveld, S. M. Leinders, K. W. A. van Dongen, H. P. Urbach, and M. Yousefi, "Extension of Marcatili's analytical approach for rectangular silicon optical waveguides," *Journal of Lightwave Technology*, vol. 30, no. 14, pp. 2388–2401, 2012. DOI:10.1109/JLT.2012.2199464

- W. J. Westerveld, J. Pozo, P. J. Harmsma, R. Schmits, E. Tabak, T. C. van den Dool, S. M. Leinders, K. W. A. van Dongen, H. P. Urbach, and M. Yousefi, "Characterization of a photonic strain sensor in silicon-on-insulator technology," *Optics Letters*, vol. 37, no. 4, pp. 479–481, Feb 2012. DOI:10.1364/OL.37.000479

- W. J. Westerveld, H. P. Urbach, and M. Yousefi, "Optimized 3-D simulation method for modeling out-of-plane radiation in silicon photonic integrated circuits," *IEEE Journal of Quantum Electronics*, vol. 47, no. 5, pp. 561–568, May 2011. DOI:10.1109/JQE.2010.2099645

- We are preparing two more journal publications, one on Chapter 2 and one on Chapter 5.

Conference contributions

- W. J. Westerveld, J. Pozo, S. M. Leinders, M. Yousefi, and H. P. Urbach, "Characterization of silicon micro-ring resonators," in *18th Annual Symposium of the IEEE Photonics Society Benelux Chapter*, Eindhoven, Nov. 2013, pp. 37–40.

- W. J. Westerveld, "Ultrasound sensing with silicon photonic micro-ring resonators," presented at *Symposium Fotonica of IOP Photonic Devices*, Leiden, Nov. 2013 *(invited).*

- S. M. Leinders, W. J. Westerveld, J. Pozo, H. P. Urbach, N. de Jong, and M. D. Verweij, "Membrane design of an all-optical ultrasound receiver," in *Proceedings IEEE International Ultrasonics Symposium*, Prague, Jul. 2013, IUS5-PD-6.

- W. J. Westerveld, J. Pozo, P. M. Muilwijk, S. M. Leinders, P. J. Harmsma, E. Tabak, T. C. van den Dool, K. W. A. van Dongen, M. Yousefi, and H. P. Urbach, "Characterization of optical strain sensors based on silicon waveguides," in *Conference on Lasers and Electro-Optics Europe 2013 and the European Quantum Electronics Conference (CLEO Europe - EQEC 2013)*, München, May 2013, CH3.4.

- W. J. Westerveld, S. M. Leinders, J. Pozo, K. W. A. van Dongen, M. Yousefi, N. de Jong, M. D. Verweij, and H. P. Urbach, "All-optical ultrasound receiver in silicon-on-insulator technology," in *Optics in Cardiology*, Rotterdam, Mar. 2013.

- S. M. Leinders, W. J. Westerveld, J. Pozo, M. Yousefi, H. P. Urbach, and K. W. A. van Dongen, "Membrane design of an all-optical ultrasound receiver in silicon-on-insulator technology," in *4th Dutch Bio-Medical Engineering Conference*, Egmond aan Zee, The Netherlands, Jan. 2013.

- W. J. Westerveld, S. M. J. Pozo, Leinders, K. W. A. van Dongen, M. Yousefi, and H. P. Urbach, "Extension of Marcatilis analytical approach for 220 nm high waveguides in SOI technology," in *17th Annual Symposium of the IEEE Photonics Society Benelux Chapter*, Mons, Nov. 2012, pp. 25–28. [Online]. http://www.photonics-benelux.org

- W. J. Westerveld, J. Pozo, R. A. Nieuwland, S. M. Leinders, K. W. A. van Dongen, and M. Yousefi, "Experimental confirmation of universal relations for microring resonators in SOI technology," in *European Optical Society Annual Meeting (EOSAM 2012)*, Aberdeen, Sep. 2012, Presentation nr. 5995.

- W. J. Westerveld, "Silicon integrated optomechanical sensors," presented at *38th European Conference on Optical Communication (ECOC), Workshop 7: Low-Cost Open Access to Photonic Integration Technology (4th European Photonic Integration Forum)*, Amsterdam, Sep. 2012 *(invited).*

- W. J. Westerveld, J. Pozo, R. A. Nieuwland, S. M. Leinders, K. W. A. van Dongen, M. Yousefi, and H. P. Urbach, "Experimental confirmation of universal relations for microring resonators in SOI technology," in *16th European Conference on Integrated Optics (ECIO)*, Barcelona, Apr. 2012, Oral Nr. 187.

- W. J. Westerveld, J. Pozo, P. J. Harmsma, R. Schmits, E. Tabak, S. M. Leinders, K. W. A. van Dongen, H. P. Urbach, and M. Yousefi, "Characterization of the effects that play a role in photonic strain sensors in silicon-on-insulator technology," in *16th Annual Symposium of the IEEE Photonics Society Benelux Chapter*, Gent, Dec. 2011, pp. 69–72. [Online]. http://www.photonics-benelux.org

- R. Hagen, J. Pozo, A. Kaźmierczak, W. J. Westerveld, P. J. Harmsma, J. H. van den Berg, R. Schmits, M. Yousefi, M. Cabezon, A. Villafranca, D. Izquierdo, and J. I. Garces, "Vertical interconnection of SOI photonic integrated circuits," in *16th Annual Symposium of the IEEE Photonics Society Benelux Chapter*, Gent, Dec. 2011, pp. 237–240. [Online]. http://www.photonics-benelux.org

- J. Pozo, W. J. Westerveld, P. J. Harmsma, S. Yang, P. Bodis, R. Nieuwland, M. Lagioia, D. M. R. Lo Cascio, J. Staats, R. Schmits, H. van den Berg, E. Tabak, K. Green, H. P. Urbach, L. K. Cheng, and M. Yousefi, "Silicon on insulator photonic integrated sensors: On-chip sensing and interrogation," in *13th International Conference on Transparent Optical Networks (ICTON)*, Stockholm, Jun. 2011, Th.A4.5. DOI:10.1109/ICTON.2011.5970854

- W. J. Westerveld, P. J. Harmsma, R. Schmits, E. Tabak, J. Pozo, H. P. Urbach, and M. Yousefi, "Characterization of the influence of strain on the optical properties of waveguides and microresonators in silicon-on-insulator technology," in *Conference on Lasers and Electro-Optics Europe 2011 and the European Quantum Electronics Conference (CLEO Europe - EQEC 2011)*, München, May 2011, CH2.5. DOI:10.1109/CLEOE.2011.5943062

- W. J. Westerveld, H. P. Urbach, and M. Yousefi, "Optimization of an out-of-plane grating coupler using a novel 3d simulation scheme," in *15th Annual Symposium of the IEEE Photonics Society Benelux Chapter*, Delft, Nov. 2010, pp. 153–156. [Online]. http://www.photonics-benelux.org

- E. van Zeijl, R. Schmits, J. H. van den Berg, P. J. Harmsma, W. J. Westerveld, M. Lagioia, P. Bodis, R. P. Ebeling, R. A. Nieuwland, S. Yang, D. M. R. Lo Cascio, K. Agovic, E. J. Enderink, R. E. van Vliet, and M. Yousefi, "Commercial SOI sensor technology," in *15th Annual Symposium of the IEEE Photonics Society Benelux Chapter*, Delft, Nov. 2010, pp. 249–252. [Online]. http://www.photonics-benelux.org

- W. J. Westerveld, P. J. Harmsma, R. Schmits, D. M. R. Lo Cascio, A. E. Duisterwinkel, K. Agovic, R. E. van Vliet, H. P. Urbach, and M. Yousefi, "A path towards short-term commercialization of integrated nanophotonic sensors," in *Proceedings URSI Forum 2010*, Brussels, May 2010, p. 51.

- W. J. Westerveld, H. P. Urbach, and M. Yousefi, "An alternative to full 3D simulations of out-of-plane grating couplers based on 2D FDTD simulations, the effective index method and the Rayleigh II integral," in *Proceedings 14th IEEE Photonics Society Benelux Annual Workshop*, Gent, Apr. 2010.

- W. J. Westerveld, M. J. Engelmann, R. Schmits, P. J. Harmsma, K. Agovic, J. H. van den Berg, R. E. van Vliet, H. P. Urbach, and M. Yousefi, "Design of a photonic integrated circuit for a chaotic integrated broadband light source," poster presented at *MicroNanoNed Conference 2009*, Delft, Nov. 2009.

- W. J. Westerveld, P. J. Harmsma, R. Schmits, H. P. Urbach, and M. Yousefi, "Chaotic integrated broadband laser lightsource," in *Proceedings URSI Benelux Forum 2009*, Delft, Jun. 2009.

- P. J. Harmsma, M. J. Engelmann, R. Schmits, W. J. Westerveld, J. H. van den Berg, K. Agovic, R. E. van Vliet, and M. Yousefi, "Photonic pressure sensor in silicon on insulator," in *Conference on Lasers and Electro-Optics Europe 2009 and the European Quantum Electronics Conference (CLEO Europe - EQEC 2009)*, München, Jun. 2009.
DOI:10.1109/CLEOE-EQEC.2009.5196279

- W. J. Westerveld, M. J. Engelmann, R. Schmits, P. J. Harmsma, K. Agovic, J. H. van den Berg, R. E. van Vliet, H. P. Urbach, and M. Yousefi, "Integrated nano photonic sensors @ TNO," poster presented at *Fotonica Evenement 2009*, Nieuwegein, The Netherlands, Apr. 2009.

- W. J. Westerveld, M. J. Engelmann, R. Schmits, H. P. Urbach, and M. Yousefi, "A commercial integrated broadband and coherent light source," poster presented at *MicroNanoNed Conference 2008*, Ede, The Netherlands, Nov. 2008.

Theses, reports, software and more

- W. J. Westerveld, "RECTWG: Matlab implementation of the extended Marcatili approaches for rectangular silicon optical waveguides," distributed in *RECTWG package for Matlab – Version 0.1*, free open-source software, Mar. 2013. [Online]. http://waveguide.sourceforge.net

- W. J. Westerveld, J. Pozo, M. Yousefi, and H. P. Urbach, "Critical coupling of optical microring resonators for opto-mechanical sensors," in *Europractice IC Service Activity Report 2011*, EUROPRACTICE IC Service (office at IMEC, Kapeldreef 75, Leuven, Belgium), Jan. 2012, pp. 22–23. [Online]. http://www.europractice-ic.com/docs/Annual_report_2011.pdf

- W. J. Westerveld, "Design of a photonic integrated circuit (PIC) in silicon on isolator (SOI) technology for a novel chaotic integrated laser light source (CHILL)," Master's thesis, Delft University of Technology, supervisors dr. M. Yousefi and prof. dr. H. P. Urbach, Jul. 2009.

- ——, "Interpreting 2D IWEX images of girth weld defects using a property model, forward calculations and an iterative scheme," Applus RTD, Delftweg 144, Rotterdam, The Netherlands, Internship Report, supervisors ir. K. Chougrani, ir. C. H. P. Wassink, and prof. dr. ir. A. Gisolf, Aug. 2008.

- ——, "Reductie van windruis bij de hoorbril," Bachelor's thesis, Delft University of Technology, supervisors dr. ir. M. M. Boone and prof. dr. A. Gisolf, Jun. 2007.